

REPORT DOCUMENTATION PAGE			Form Approved OMB No. 0704-0188	
Public reporting burden for this collection of information is estimated to average 1 hour per response, including the time for reviewing instructions, searching existing data sources, gathering and maintaining the data needed, and completing and reviewing the collection of information. Send comments regarding this burden estimate or any other aspect of this collection of information, including suggestions for reducing this burden, to Washington Headquarters Services, Directorate for Information Operations and Reports, 1215 Jefferson Davis Highway, Suite 1204, Arlington, VA 22202-4302, and to the Office of Management and Budget, Paperwork Reduction Project (0704-0188), Washington, DC 20503.				
1. AGENCY USE ONLY (Leave Blank)	2. REPORT DATE September 1997	3. REPORT TYPE AND DATES COVERED Final Technical Report: 5/01/92 - 4/30/97		
4. TITLE AND SUBTITLE Control of Interactions between Wake and Blades		5. FUNDING NUMBERS N00014-92-J-1731		
6. AUTHORS Chih-Ming Ho				
7. PERFORMING ORGANIZATION NAME(S) AND ADDRESS(ES) Mechanical and Aerospace Engineering Department University of California , Los Angeles 420 Westwood Plaza Los Angeles, CA 90095-1597		8. PERFORMING ORGANIZATION REPORT NUMBER		
9. SPONSORING / MONITORING AGENCY NAME(S) AND ADDRESS(ES) Navy/Office of Naval Research 800 North Quincy Street Arlington, VA 22217-5000		10. SPONSORING / MONITORING AGENCY REPORT NUMBER		
11. SUPPLEMENTARY NOTES				
12a. DISTRIBUTION / AVAILABILITY STATEMENT Unlimited		12b. DISTRIBUTION CODE N/A		
<div style="border: 1px solid black; padding: 5px; text-align: center;"> DISTRIBUTION STATEMENT A Approved for public release Distribution Unlimited </div>				
13. ABSTRACT (Maximum 200 words) <p>This investigation of rotor-stator interaction noise originated from an interest in reducing a ventilation-noise problem. This type of noise is generated aerodynamically by the flow interaction between the rotor and stator. In order to reduce this interaction noise thoroughly along the pipe, an efficient method is to remove noise sources aerodynamically in the interaction flow region by means of active flow control. This method suggests that we need to identify the active noise source region before attempting to implement the noise reduction. On this account, we shall employ measurement techniques for this identification process by correlating both the interaction-flow field (cause) and the corresponding acoustic field (effect). Therefore, the motive of the present study is to provide a general basis for locating the noise sources experimentally and to pave the road for possible application of the active rotor-stator interaction-noise control in the future.</p>				
14. SUBJECT TERMS Wake-blade Interaction Noise, Surface pressure distribution			15. NUMBER OF PAGES 142	
			16. PRICE CODE	
17. SECURITY CLASSIFICATION OF REPORT Unrestricted	18. SECURITY CLASSIFICATION OF THIS PAGE Unrestricted	19. SECURITY CLASSIFICATION OF ABSTRACT Unrestricted	20. LIMITATION OF ABSTRACT None	

19971007 173

Final Report

Control of Interactions between Wake and Blades *N00014-92-J-1731*

Abstract

This investigation of rotor-stator interaction noise originated from an interest in reducing a ventilation-noise problem. This type of noise is generated aerodynamically by the flow interaction between the rotor and stator. In order to reduce this interaction noise thoroughly along the pipe, an efficient method is to remove noise sources aerodynamically in the interaction flow region by means of *active flow control*. This method suggests that we need to identify the active noise source region before attempting to implement the noise reduction. On this account, we shall employ measurement techniques for this identification process by correlating both the interaction-flow field (*cause*) and the corresponding acoustic field (*effect*). Therefore, the *motive* of the present study is to provide a general basis for locating the noise sources experimentally and to pave the road for possible application of the active rotor-stator interaction-noise control in the future.

1.1. Theories regarding the Present Study

The theory of 'aeroacoustics' or 'sound generated aerodynamically' is built upon the governing equations of a fluid flow, i.e., the continuity and momentum equations. There are two approaches to the study of aeroacoustics (Goldstein 1976): one is to directly solve the linearized governing equations specifically for sound generation due to pressure fluctuations on a solid boundary in a moving medium (Kaji and Okazaki 1970, Myers and Kershen 1995), the other is to follow Lighthill's acoustic analogy (Lighthill 1952, 1954, 1962) deduced from the governing equations (Powell 1960, Meecham 1965, Ffowcs Williams and Hawkings 1969a, 1970, Fujita and Kovasznay 1974). We will follow the second approach to investigate the noise generated by rotor-stator interaction.

Based on Lighthill's theory, Ffowcs Williams and Hawkings (1969b) have established a more general aeroacoustic theory for a moving solid boundary in a nonstationary medium. Their theory provides a basis for noise generation due to rotor-stator interaction. However, in the reported experimental papers, a transient stator response is usually responsible for the majority of the interaction-noise generation (Fujita and Kovasznay 1974, Ho and Kovasznay 1976a, Zandbergen 1988, Simonich *et al.* 1993). Since the stator is stationary in the flow, we may simplify Ffowcs Williams-Hawkings theory in order to obtain a relationship between the stator response and the noise generation. The sound field radiated by a stationary solid body in a moving medium (Fig. 1-1) is

$$\rho - \rho_0 = \frac{I}{4\pi a_0^2} \left\{ \frac{\partial^2}{\partial x_i \partial x_j} \int_V \frac{T_{ij}(\mathbf{y}, t - R/a_0)}{R} d\mathbf{y} - \frac{\partial}{\partial x_i} \int_S \frac{f_i(\mathbf{y}, t - R/a_0)}{R} dS(\mathbf{y}) \right\}, \quad (1.1)$$

where $R \equiv |\mathbf{x} - \mathbf{y}|$. Eq.(1.1) was first derived by Curle (1955) based on Lighthill's theory.

The volume integral in Eq.(1.1) is exactly the solution of Lighthill's equation (Lighthill 1952) and represents a sound field produced by a volume distribution of quadrupoles. Similarly, the surface integral depicts an equivalent system to the sound generated in a stationary medium by a distribution of dipoles of strength f_i per unit area, where f_i is the fluctuating force per unit area exerted by the solid boundaries on the fluid in the x_i direction. Therefore, the surface integral term is known as *Curle's supplementary formula* to the sound field with the existence of a stationary solid boundary in a moving medium (Clark and Ribner 1969, Siddon 1973, Fujita and Kovasznay 1974).

It should be noticed that $t - R/a_0$, the so-called '*retarded time*', represents the time at which the sound received at time t by a sensor at the point \mathbf{x} was radiated from the source at the point \mathbf{y} , where $R = |\mathbf{x} - \mathbf{y}|$, as illustrated in Fig. 1-1. In other words, an *event* (sound) happening at time $t - R/a_0$ shall be observed at time t by an *observer* (sensor) located at a distance R .

By neglecting the quadrupole term based on an order-of-magnitude comparison, Curle (1955) imposed a far-field condition on Eq.(1.1) and came to an estimate of the *far-field noise* or *radiation field* for low Mach-number flow with the presence of a solid body in the form

$$\rho - \rho_0 = \frac{I}{4\pi a_0^3} \frac{x_i}{x^2} \frac{\partial}{\partial t} F_i(t - R/a_0), \quad (1.2)$$

where $F_i(t - R/a_0) = \int_S f_i(\mathbf{y}, t - R/a_0) dS(\mathbf{y})$ is the summation of fluctuating forces per unit area exerted by the solid surface on the fluid.

Therefore, Eq.(1.2) is a simplified Curle's supplementary formula for the far-field noise.

Clark and Ribner (1969) have proven the validity of Eq.(1.2) experimentally by finding the direct correlation between far-field sound and fluctuating lift on an airfoil in turbulent flow. In parallel with the work of Clark and Ribner, Siddon (1973) established a formal cross-correlation method, from Eq.(1.2), to calculate surface dipole strength from both the unsteady pressure on an airfoil in a jet flow and the corresponding far-field noise. Siddon's result indicates that the distribution of surface dipole strength is identified locally on the solid boundary and does not necessarily correspond to the pressure distribution on the same boundary. This is because, from Eq.(1.2), only the $\partial F_i / \partial t$ part, i.e., the time derivative of pressure fluctuations, not F_i itself, contributes to the far-field noise. However, for those measuring positions in the near field, Eq.(1.2) is no longer satisfied. The near-field noise should be obtained by reconsidering Eq.(1.1).

For the near field, Fujita and Kovasznay (1974) defined a less restrictive condition, that is, only *the square of the sound-propagating distance is much larger than that of the dimensions of the source region*. Under this assumption, they were able to re-derive, from Curle's supplementary formula, a simplified equation for noise prediction in the near field. They found that the results obtained from noise prediction were in good agreement with those measured from experiments. This simplified equation for free-space, near-field dipole sound is

$$p - p_0 = \frac{q_0 A \cos \theta}{4\pi x^2 a_0^2} \cdot \left\{ C_L(t - R/a_0) + \frac{x}{a_0} \frac{dC_L(t - R/a_0)}{dt} \right\}, \quad (1.3)$$

where $q_0 = \frac{1}{2} \rho U_0^2$, is the freestream dynamic pressure with freestream speed U_0 , $\cos \theta = x_i / x$ the directivity of the dipole sound, R / a_0 the time delay due to the propagating distance of sound wave between source and detector, A the area of stator, and C_L the lift coefficient of the stationary body. In fact, this simplification for the near-field noise has been already examined by Lighthill (1962) in an explanation of sound generation by a simple dipole in a non-moving medium. Similar to Lighthill's description, the first term on the right-hand side of Eq.(1.3), with C_L which represents the total lift fluctuation, is identified as the *near-field noise*, while the second term, the *radiation field* or *far-field noise*, of the same as that shown in Eq.(1.2).

In light of the above theoretical results, we will be able to investigate the interaction noise from a rotor-stator stage. Before delving deeper into the current research interest, a brief discussion will be made about the features of the rotor-stator interaction noise.

1.2. Characteristics of Rotor-Stator Interaction Noise

A typical sound-pressure-level spectrum of the microphone signal of rotor-stator interaction noise is shown in Fig.1-2, for an arrangement with a two-blade rotor and a two-blade stator. The blade passing frequency (BPF) is 50Hz with a rotor rotation of 25Hz, and is identified by a clear spike at 50Hz in Fig. 1-2. We also observe, from Fig.1-2, that there exist discrete spikes at 100, 150, 200 and 250 Hz, respectively, which shows that the sound radiation due to the rotor-stator interaction is at discrete frequencies that are multiples of the *blade passing frequency* (Kaji and Okazaki 1970, Hanson 1973, Goldstein 1976, Blake 1986).

Since the wave energy, in Fig. 1-2, is mainly distributed at the multiple BPF's, the signal in the time domain should be, by definition, *complex periodic data whose waveform repeats itself at regular intervals* (Bendat and Piersol 1986). In addition, the signals measured from the flow properties (for example, surface pressure, velocity field, etc.) around the rotor-stator stage are also complex periodic due to the rotor's rotation. A phase-averaging technique, hence, is applicable to the current study, and will be introduced in Chapter 2.

After the sound radiates from the rotor-stator interaction region, it propagates through the pipe in both directions, upstream and downstream. For the sound propagating downstream, a vortical shear flow induced by the rotor's rotation will refract the sound from its propagating path and may also attenuate it a little by heat or viscous dissipation (Ho and Kovasznay 1976b, Goldstein 1976). The theory of *ray tracing* for geometric acoustics is devoted to such a wave propagation through a shear flow (Pridmore-Brown 1962, Thompson 1971, Lighthill 1978, Pierce 1989). When flow velocities are much smaller than the sound speed, the interaction between the sound wave and the vortical shear flow is involved with very gradual changes (Lighthill 1978). Since in this study the flow is incompressible, this interaction hence will be ignored.

Another point of special interest in the rotor-stator interaction noise is regarding the noise resource in the interaction-flow field. The transient stator response due to the passing wake of the rotor used to be deemed as the noise resource (Fujita and Kovasznay 1974, Ho and Kovasznay 1976a, Zandbergen 1988, Simonich *et al.* 1993). Nevertheless, still very little is known about the details of how this noise source is influenced by the interaction-flow field. Therefore, the current investigation will merely employ the experimental methods to identify the noise-source region from the associated interaction-flow field.

The *gap* between the rotor and stator also plays a very important role on the interaction-noise generation (Sugeng and Fiedler 1986). We may expect that the shorter the gap, the stronger the flow interaction, and hence the louder the noise. For simplicity, we shall confine a fixed gap for investigating the noise-generation mechanism in this study.

Inasmuch as this research interest stems from analyzing the noise generation in a ventilation system, the flow concerned in the current study will be incompressible. Nevertheless, the results should be helpful as a basis for elucidating the mechanism of the interaction-noise generation in a more complicated turbomachinery system.

1.3. Goal of the Present Study

The *goal* of this research work is to understand, by experiments, the physical mechanism of noise generation due to rotor-stator interaction in an incompressible pipe flow. The approach of this experimental study is attempting to correlate the measured acoustic field at a certain cross-section of the pipe to the aerodynamic field observed in the flow region of the rotor-stator interaction. There are three different measurements involved with this investigation; they are *downstream noise measurements*, *surface pressure measurements on the stator*, and *velocity measurements around the stator*. Since the raw data from all measurements are periodic based on BPF, the results from these data will be finalized by a phase-averaging technique.

After this experimental investigation, we should be able to determine the *active interaction phase interval*, to identify the *active noise source region* in the interaction-flow field, and to understand the *physical mechanism of noise generation* from the rotor-stator interaction.

CHAPTER 2

EXPERIMENTAL CONFIGURATION

2.1. Wind Tunnel and Test Section

A blow-down open-loop wind tunnel with an anechoic settling chamber was employed for the experimental setup (Fig. 2-1). The maximum freestream speed is about 15 m/s. The test section is a circular plexiglass pipe with dimensions of 0.7 m in length and a 0.178 m inner diameter (7" I.D.). A detachable plexiglass section is connected to the rear end of the test section for microphone measurements, as illustrated in Fig. 2-1.

Rotor and Stator

For simplicity, a test stage consisting of a two-blade-rotor and a two-blade-stator combination in a circular pipe has been set up for this study (Fig.2-1 & 2-2). The stator was located at a distance 0.71 m upstream as measured from the end of the rear pipe section to the leading edge of the stator blade (Fig.2-1).

Instead of a circular cylinder for the rotor which was commonly used in the reported experimental studies (Fujita and Kovasznay 1974, Ho and Kovasznay 1976a, Sugeng and Fiedler 1986, Zandbergen 1988, Simonich *et al.* 1993), a fan-type-profile propeller, with variation in both chord-length and pitch along the span, has been adopted as the rotor, which facilitates a variety of operating conditions for investigation.

Accordingly, a 6-inch-pitch, 7-inch-diameter, 2-blade model-plane propeller (from the Master Airscrew Series made by Windsor Propeller Co.) is chosen for the rotor. The rotor was driven by a DC motor and operated below 4000 RPM. In contrast to the selection of the rotor, the stator consists of two constant-NACA0016-profile blades with a small, bronze hub (with 0.026m O.D. and 0.035m in length) between them. Each stator blade has a chord length of 0.05 m and a span of 0.076 m. Comparing the dimensions of the stator blades and the hub, it can be asserted that the noise generated by the hub should be much smaller than the noise from the rotor-stator interaction in this experimental setup. Hence, the noise generated by the rotor-stator interaction has been mainly investigated in this study. The *pressure side* of the stator is defined as the side facing the approaching rotor, and, in turn, the *suction side* of the stator is on the leeward side (Fig.2-3).

Definitions of phase angle, ϕ , at 0° and $\pm 180^\circ$

The output of a micro-switch sensor attached on the rotor's driving motor is used as a phase reference signal based on the rotor's rotation. With this reference, a phase-averaging technique can be applied to process raw data from three different measurements, and will be described in Section 2.3.1.

The reference signal is a pulse related to the instant at which the rotor's trailing edge passes in front of the stator's leading edge. Since the stator's angle of attack (AoA)

is changed from case to case in this study, this signal, therefore, is triggered relative to the stator's position at zero-degree AoA, as shown in Fig.2-2(b). With this arrangement, we will be able to define a time reference named *zero degree phase angle*, i.e., $\phi = 0^\circ$, in order to assist data analysis. The phase angle ϕ at $\pm 180^\circ$ is defined as the rotor rotating to a vertical position relative to the stator, as illustrated in Fig. 2-2(b).

Stator's angle of attack, α_s , & rotor's effective angle of attack, β_e

With respect to the freestream direction, the *stator's angle of attack (AoA)*, α_s , is in a positive sense when the stator is turned to its pressure side, in Fig. 2-3.

An *effective angle of attack*, β_e , of a rotor-blade section at a certain radius of the rotor is determined by the freestream velocity U_o , the rotor's velocity U_r , and the zero-lift-line angle θ of the same rotor section, as illustrated in Fig.2-3. This relationship is written in the following form

$$\beta_e = \theta - \tan^{-1}(U_o / U_r). \quad (2.1)$$

In this study, a cross section on the stator at 55% radius of rotor has been selected for both surface pressure and velocity measurements (Fig. 2-2(a)). The zero-lift-line angle, θ , at rotor's 55%R section is approximated as 26° . Meanwhile, the corresponding chord length of rotor at 55%R is measured to be 1.8 cm.

Gap between Rotor and Stator

The gap between the rotor and stator is fixed in all investigated cases but changes along the rotor's spanwise direction due to the variation in both chord-length and incidence of the rotor's blades. Approximately, the gap varied from 0.5 cm to 0.865 cm along the direction from the rotor's root to its tip. Hence, a constant distance, instead of the gap, is measured to be 1 cm between the center-chord-line along the rotor's span and the leading edge of stator blade, as shown in Fig.2-3. The gap at 55%R of rotor is measured as 0.71 cm. Thus, this gap is 39% of the corresponding rotor's chord length (1.8 cm) and 14% of the stator's chord length (5cm).

It is noticed that, from the setup sketched in Fig.2-3, this rotor and stator arrangement is a typical stage in an axial compressor (Turton 1984).

2.2. Measurements

Three types of measurements have been conducted in this research. They are *downstream noise measurement, unsteady surface pressure measurement on the stator, and velocity measurement around the stator.*

2.2.1. Downstream Noise Measurement

In order to identify the downstream noise signature, the microphone measurements are set up at two different pipe-sections downstream from the rotor-stator stage, as illustrated in Fig. 2-2(c). First downstream measurement is accomplished by a quarter-inch-diameter Bruel & Kjaer (B&K) type-4135 condenser microphone flush-mounted on the pipe wall which was 0.7 m distant from the stator's leading edge. In addition, two quarter-inch-diameter B&K (Type 4135 and Type 4136) condenser microphones are placed 90° apart and also flush-mounted on the pipe wall which is 0.23 m downstream from the leading edge of stator.

2.2.2. Surface Pressure Measurement

A total of 37 pressure holes on both sides of the stator blades are used for the surface pressure measurement: 19 pressure holes on the pressure sides and 18 on the suction sides. They are located at the mid-span of a single stator blade which was 55% radius of rotor distant from the center line of the test section. These pressure holes are drilled to meet channels underneath the stator blade, and these channels terminate up with connections to metal tubes at the end side of the stator blade (Fig. 2-4(a)). The pressure holes are typically in two different diameters: 0.254 mm (0.01 inch) around the leading edge and 0.508 mm (0.02 inch) otherwise on both sides. Due to the difficulty of drilling the channels near the trailing edge, it was unable to measure the surface pressure at the rear 15%C on both sides of stator (Fig. 2-4(a)). Fortunately, this deficiency does not influence the current study since the flow interaction happens mainly around the stator's leading-edge portion, as we will see in later chapters.

By connecting to each pressure hole, the surface pressure measurement on the stator consists of two separate parts: 1) *mean pressure* measured by a static-pressure tube with a 1-torr-range, differential-type MKS pressure transducer, and 2) *pressure fluctuation* measured by a quarter-inch-diameter B&K type-4136 condenser microphone via a transmission line. The transmission line is composed of the surface channel in the stator blade from the pressure hole to the end-side metal tube and a Tygon tube (1/16" I.D., 9.7 cm in length) connecting the metal tube to a well-sealed microphone adapter for the B&K condenser microphone, in Fig. 2-4(a).

Before taking surface pressure measurements, a calibration process for the transmission line (Fig. 2-4(a)) should be conducted in advance. This is due to energy loss and phase lag of the pressure wave propagating through the transmission line. The pressure-fluctuation measurements by the condenser microphone should be compensated in order to recover the distorted signal back to the actual signal on the stator surface. Accordingly, gain and phase *characteristics* or *frequency responses* for the transmission line should be determined prior to the compensating process. There are 37 pressure holes used for surface pressure measurement; hence, 37 sets of gain and phase responses should be compensated in order to yield the correct pressure distributions on the stator surface.

Experimental Procedure for Pressure-Fluctuation Compensation

A conceptual description to the calibration process of obtaining the frequency responses for a transmission line is illustrated in Fig. 2-4(b). In the real setup, a 7"D sub-woofer is chosen for the sound source and attaches to one end of the 7"I.D. plexiglass pipe. It generates sinusoidal waves in a frequency range from 35 to 3000 Hz and is driven by a wave generator. The blade with a transmission line, as illustrated in Fig. 2-4(a), and a reference microphone are both placed at the same pipe section which is 19 cm downstream from the sub-woofer. On the plane of this pipe section, a plane acoustic wave has been detected and checked by the reference microphone. Both microphone signals were recorded via analog-to-digital converter to the computer. By varying the frequencies, we are able to measure both reference and testing signals from two microphones for determination of frequency responses of this transmission line. The procedure to obtain the frequency responses will be described in Section 2.3.2. A single-input/single-output model is illustrated to describe the transmission-line system in Fig. 2-4(c). Fig. 2-4(d) schematically illustrates a linear-system-identification process by a finite-duration-impulse-response (FIR) filter for compensating the distorted pressure-fluctuation signals, which will be discussed in detail later in Section 2.3.3.

2.2.3. Velocity Measurement

A special, single-component hot-wire probe, with broaches bent 45° from their original, straight positions, has been utilized in the velocity measurements around the stator, as shown in Fig.2-2(a) & 2-5. This special probe expedited velocity measurement, especially around the region adjacent to the leading edge of stator. In this study, the wire between two broaches on the probe was set parallel to the spanwise direction of the stator (Fig. 2-5). When the hot-wire probe was moved close to the stator surface, this setup provided a better evaluation of the streamwise velocity component because of the physical weakness of the normal velocity component close to a solid boundary and the poor resolution of the spanwise velocity component due to the worst flow heat-transfer effect along the wire (Blackwelder 1981).

A three-axis traverse system was used to support and move the hot-wire probe, and it was driven by PC through a three-axis controller manufactured by Anaheim Automation, Inc.

Since the stator blades possessed both a constant NACA0016-cross-section and constant incidence along its span, we may select cross sections away from both the hub and the tunnel wall to investigate the unsteady flow field mainly induced by rotor-stator interaction. The velocity measurements were taken specifically around the front 30% chord length of stator's blade at 55% radius of rotor. The measurements were accomplished by generating a fine mesh of approximately 4500 hot-wire stations which will be shown in the later chapters.

2.3. Data Processing Technique

The data acquisition system includes a PC 486DX50 and a Dell Pentium 90 with a 12-bit, 16-channel analog-to-digital board manufactured by RC Electronics, Inc. The maximum sampling frequency is 1 MHz. This maximum sampling frequency is sufficient enough for sampling data in this study because the maximum value of blade passing frequency (BPF) will not exceed 133Hz (8000 RPM) for rotor RPM less than 4000.

2.3.1. Phase-Averaging Technique

As mentioned previously, a square-wave reference related to the rotor's motion can be employed for data analysis with a phase-averaging technique. Typical square-wave reference and measurement signals in this study are shown in Fig.2-6(a).

Phase-Averaging Algorithm

The phase-averaging technique is introduced for extracting the deterministic part of the signal. Basically, it has a resemblance to the ensemble averaging method except that the phase average is based on an intrinsic period, for example, T_p in Fig.2-6(a).

The phase-averaging algorithm is defined as, (Fujita and Kovasznay 1974),

$$\hat{f}(t) = \lim_{N \rightarrow \infty} \frac{1}{N} \sum_{n=1}^N f(t + nT_p),$$

where T_p is the period, and N is the number of cycles or samples for phase-averaging. In practice, the choice of cycle number depends on a compromise between the accuracy of the result and the time length available to accomplish one experiment. Generally speaking, $500 < N < 1000$ is the typical range of cycle number chosen. Fig. 2-6(b) shows the phase-averaging results of the signals shown in Fig. 2-6(a), by using approximately 600 cycles to smooth out the random fluctuation. At first sight of the raw signals, it is noticed that the noise shown in part (a) of Fig. 2-6 has no significantly distinguishable repeating pattern as the other signals. However, in Fig. 2-6(b), a high peak in the phase-averaged noise signature emerges from the random fluctuations which are mostly the pressure fluctuations due to small eddies passing by the flush-mounted microphones (Lighthill 1962, Goldstein 1983). The random fluctuations are filtered by phase-averaging technique.

In the present study, 150, 500 and 1000 cycles were adopted for phase-averaging the velocity, surface pressure and noise signals, respectively.

2.3.2. Frequency Responses of Transmission Line

In Section 2.2.2, we learn that, in order to compensate the distorted pressure-fluctuation signals, the frequency responses of transmission lines (Fig. 2-4(a)) should be determined in advance. Both the reference- and testing-microphone signals (Fig. 2-4(b) to (d)) were used to obtain both the gain and phase frequency responses.

The *gain response* at a certain frequency can be obtained by taking the ratio of both microphone signal magnitudes which are calculated from their energy spectra by a *fast Fourier transform* (FFT) technique (Brigham 1988, Proakis and Manolakis 1992). Meanwhile, the *phase lag* or *response* at the same testing frequency is acquired by directly computing the phase angle of the one-sided cross-spectral density function from both signals (Bendat and Piersol 1986).

The gain and phase responses for two typical pressure holes (diam.=0.254 mm and 0.508 mm) are plotted in Fig. 2-7.

2.3.3. Compensating Procedure for Pressure Fluctuation

Three processes are needed to accomplish the compensation of transmission distortion: (I) the *linear-inverse-system identification process for a transmission line* (Proakis and Manolakis 1992), which uses a *digital finite-duration impulse response* (FIR) filter to identify a linear system as an inverse system of the gain response of a transmission line, (II) the *gain-compensating process of pressure fluctuation* due to both energy loss and phase lag in the transmission line, which mainly applies a convolution process between the raw signal of pressure fluctuation and the compensating FIR filter obtained in PROCESS(I), and (III) the *phase-compensating process of pressure fluctuation* due to phase lag in the transmission line, which transforms the gain-

compensated signal of the pressure fluctuation to the frequency domain by *Fourier transform*, after PROCESS(II), in order to subtract the phase lag at each frequency, and then obtain the well-compensated signal of pressure fluctuation in the time domain by *inverse Fourier transform*.

With knowledge of the frequency responses for all transmission lines, we may start to drive the compensating filters for each transmission line. A *digital finite-duration impulse response*, FIR, filter (McClellan *et al.* 1975, Rabiner *et al.* 1975, Rabiner and Gold 1975) is employed as a linear, time-invariant (LTI) system to accomplish the *linear-inverse-system identification process for a transmission line* (Fig. 2-4(d)). The major advantage of adopting the digital FIR filter is that it possesses exact linearity of phase. This makes both the gain- and phase-compensating processes easier and more feasible, specifically in the phase compensation part. It should be noticed that a low-pass filter used in this procedure, as will be described later in this section, was also designed by the FIR filter technique.

The *convolution technique* is used for processing the raw pressure-fluctuation signal via FIR filters, including the low-pass FIR filter, described in the preceding subsection. Next, by transforming the gain-compensated signal with a *fast-Fourier-transform* (FFT) technique, the fully compensated signal was recovered by directly subtracting the phase lag at each frequency with the phase response information, and could be obtained by using an *inverse-fast-Fourier-transform* (IFFT) technique (Brigham 1988, Proakis and Manolakis, 1992).

Steps of the Compensating Procedure

The steps of the compensating procedure for pressure-fluctuation signals are listed as follows:

- (1) find the digital compensating filter for each transmission line within the desired frequency range,
- (2) start the gain compensating for each pressure-fluctuation signal obtained from each transmission line by taking the convolution of the signal and its corresponding digital compensating filter,
- (3) use a low-pass FIR filter to keep the gain-compensated signals within the desired frequency range,
- (4) multiply an appropriate constant to obtain the correct gain for signals obtained in STEP (3),
- (5) take the FFT of the gain-compensated single to obtain both amplitude and phase angle spectra in the frequency domain,
- (6) get the phase angle at each frequency and subtract the corresponding phase lag measured by the same transmission line, and
- (7) take IFFT of both amplitude and phase-compensated spectra to yield the fully-compensated pressure-fluctuation signals in time domain.

In this procedure, STEP(1) is the linear-inverse-system identification process, using a FIR filter, for a transmission line. STEP(2) to (4) are related to the gain-compensating process of pressure fluctuation due to the frequency loss in transmission

lines, while STEP(5) to (7) are the phase-compensating process for pressure fluctuation. The gain responses in Fig. 2-7(a), for two typical pressure holes in this study, are compensated right after STEP(4) and plotted in Fig. 2-8. The flat lines in Fig. 2-8(a) & (b) represent the well-compensated gain responses which were obtained by multiplying the gain responses in Fig. 2-7(a) with the linear-inverse-system function by FIR filters. An example used to demonstrate the compensating procedure can be found in Hu and Ho's report (1997).

CHAPTER 3

NOISE MEASUREMENT

In Section 2.2.1, we have described that the microphone measurements were conducted for identifying the sound wave at two pipe sections which were 0.23m and 0.7m downstream from the stator's leading edge. Since the plane pressure wave measured by microphones at the 0.23m pipe section did not propagate at the acoustic speed (Hu and Ho 1997), hence it can not be recognized as the sound wave. Meanwhile, due to identifying a plane acoustic wave arriving at the 0.7m pipe section (Hu and Ho 1997), only the noise signatures were measured by Microphone A at position # 3 of this pipe section (Fig. 2-2(b)).

Delay Time, R/a_0 , and phase advancing

Since these noise signatures are measured at the pipe section 0.7m downstream from the stator's leading edge, the delay times, R/a_0 , for this pipe section (as indicated in Chapter 1) is calculated to be 2.06 msec, based on the value of sound speed of 340 m/s in air at 20°C. This delay time are needed to advance the measured noise signals in order to be correlated with the unsteady flow field around the rotor-stator stage. Notice that the noise signatures in this study will be plotted against the dimensionless axis of phase angle ϕ . Thus, we have to advance this delay time in phase angle ϕ , i.e. a normalized time. The phase advancing is calculated by $(\text{delay time} / T_p) \cdot 360^\circ$, where T_p is defined as the period based on BPF. The noise signatures after the phase advancing are shown in Fig.3-1 through 3-4.

In this chapter, we will define an *active phase interval* by comparing noise signatures measured *with* and *without* the presence of the stator. This active phase interval will be utilized to correlate the acoustic field to the unsteady flow field in the later chapters.

3.1. Operating Conditions for Noise Measurements

In this investigation, there are four freestream speeds, five rotor speeds at 55%R, and six different stator's AoA chosen in the downstream noise measurement, and therefore

Table 3-1. β_e and U_t at 55%R of rotor for noise measurements.

U_r @ 55%R of rotor (m/s)	U_o (m/s)							
	4.66		5.62		8.43		11.24	
	β_e *	U_t **	β_e	U_t	β_e	U_t	β_e	U_t
				15				

U_r @ 55%R of rotor (m/s)	U_o (m/s)							
	4.66		5.62		8.43		11.24	
	β_e^*	U_t^{**}	β_e	U_t	β_e	U_t	β_e	U_t
6.11	-11.33°	7.68	-16.61°	8.30	-28.07°	10.41	-35.47°	12.79
7.65	-5.35°	8.96	-10.30°	9.49	-21.78°	11.38	-29.76°	13.60
12.23	5.14°	13.09	1.32°	13.46	-8.58°	14.85	-16.58°	16.61
15.29	9.05°	15.98	5.82°	16.29	-2.87°	17.46	-10.32°	18.98
19.11	12.30°	19.67	9.61°	19.92	2.20°	20.89	-4.46°	22.17

we have one-hundred-and-twenty operating conditions set up for studying the interaction-noise signatures in a range of $-35.5^\circ < \beta_e < 12.5^\circ$ and $-15^\circ < \alpha_s < 10^\circ$.

The freestream speeds and the rotor speeds are shown in Table 3-1 & Fig. 3-5. The six stator's AoA α_s are 0° , $\pm 5^\circ$, $\pm 10^\circ$ and -15° , respectively.

3.2. Noise Signatures

After being phase-averaged and advanced with the delay time, the noise signatures are shown in Figures 3-1, 3-2, 3-3 and 3-4. In these figures, the horizontal axis is a non-dimensionalized time axis in phase angle, ϕ , while the vertical axis represents noise magnitude with a dimensional unit, Pa . The *phase angle*, ϕ , shown in Fig.4-3, is normalized by the individual T_p value of each case and re-scaled from -180° to 180° . The phase angle ϕ at 0° is defined as when the rotor's trailing-edge position is aligned with the stator leading edge which is at 0° AoA (Fig.2-2(b) and Fig.2-7(b)). Similarly, ϕ at $\pm 180^\circ$ is defined as rotor's position perpendicular to the stator, as shown in Fig. 2-7(b).

3.2.1. Noise Peak

By carefully examining the noise signatures in Figures 3-1 through 3-4, a prominent noise peak is consistently observed before the zero-degree phase angle for cases where $\beta_e > -22^\circ$ with all six stator's AoA. This noise peak is an indicator for both event time and strength of noise generation due to rotor-stator interaction.

Alignment of Noise Peaks for Cases: $\beta_e > -22^\circ$

The first observation, from noise signatures in Fig. 3-1 to 3-4, is an alignment of noise peaks at about -30° phase angle in all cases where $\beta_e > -22^\circ$. In other words, the *time* when the peak noise happens is irrelevant to U_o , U_r and β_e , for all cases where $\beta_e > -22^\circ$. This result is probably due to both the similar flow fields and the fixed gap between the rotor and the stator in this study. For those cases where $\beta_e < -22^\circ$, the unsteady flow fields corresponding to the interaction-noise generation might be fairly different from those in $\beta_e > -22^\circ$. Accordingly, in this study, the operating conditions for $-22^\circ < \beta_e < 12^\circ$ is used for a comprehensive survey of interaction-noise signatures.

Noise Peaks vs. Velocities for Cases: $\beta_e > -22^\circ$

Our next interest is to look for a relationship between the noise-peak value and the velocities. In general, for the cases where $\beta_e > -22^\circ$, the peak-noise value goes up as long as one or both of U_o and U_r increase under a fixed stator's AoA, α_s , by looking into the noise signatures in Fig. 3-1 to 3-4. Although the event time of the noise peaks appear irrelevant to both U_o and U_r in these cases, we still expect a relationship between noise-peak values and the velocity magnitudes. A simple relation between peak values and velocities can be found by a *power-fitting* method as follows:

$$Y = a X^b, \quad \text{or} \quad \log(Y) = b \log(X) + A, \quad \text{where } A = \log(a). \quad (3.1)$$

Choosing Y for the peak value, the coefficients a 's and power b 's are listed in Table 3-2 with X for freestream velocity U_o , rotor's velocity U_r at 55%R, and the resultant velocity U_t at 55%R, respectively, under different stator's AoA, α_s .

Table 3-2. $Y = (\text{peak value})$ & $X = \text{Velocities}$ in Eq.(3.1) for cases: $\beta_e > -22^\circ$.

α_s^*	$X = U_o$		$X = U_r @ 55\%R$		$X = U_t @ 55\%R$	
	a	b	a	b	a	b
-15°	0.0163	2.031	0.0098	1.739	0.0015	2.339
-10°	0.0210	1.828	0.0077	1.787	0.0013	2.347
-5°	0.0146	1.941	0.0090	1.664	0.0014	2.263
0°	0.0141	1.975	0.0414	1.063	0.0077	1.629
5°	0.0077	2.229	0.0234	1.241	0.0038	1.853
10°	0.0072	2.195	0.0208	1.237	0.0035	1.829

* α_s : the stator's AoA.

From Table 3-2, it shows that the power b 's have average values of 2.03, 1.43 and 2.03 for velocities U_o , U_r at 55%R, U_t at 55%R, respectively. This means that noise-peak value increases as any of the velocities increases. Since U_t is the resultant velocity of both U_o and U_r , hence we may assert that it directly contributes to the noise-peak magnitude. Fig. 3-6 shows the relationship between peak value and U_t . Thus, the peak value is proportional to U_t^2 , i.e.,

$$\text{Peak Value} \propto U_t^2 \quad (3.2a)$$

or,

$$\text{Peak Value} \propto q_t, \quad (3.2b)$$

where q_t is a *local dynamic pressure* defined as $\frac{1}{2}\rho_0 U_t^2$. Physically, it follows that the peak noise is directly related to the local flow field, i.e. q_t , due to rotor-stator interaction.

Table 3-3. $Y = (\text{Peak Value} / q_t)$ & $X = \text{Velocities}$ in Eq.(3.1) in cases: $\beta_e > -22^\circ$.

	$X = U_o$	$X = U_r @ 55\%R$	$X = U_t @ 55\%R$
--	-----------	-------------------	-------------------

α_s^*	a	b	a	b	a	b
-15°	7.66×10^{-4}	1.087	4.47×10^{-3}	0.116	2.23×10^{-3}	0.370
-10°	1.16×10^{-3}	0.817	3.66×10^{-3}	0.156	2.10×10^{-3}	0.357
-5°	6.62×10^{-4}	1.012	4.35×10^{-3}	0.011	2.22×10^{-3}	0.265
0°	5.63×10^{-4}	1.110	1.90×10^{-2}	-0.570	1.13×10^{-2}	-0.338
5°	5.11×10^{-4}	1.128	1.10×10^{-2}	-0.376	6.34×10^{-3}	-0.146
10°	3.81×10^{-4}	1.196	9.17×10^{-3}	-0.368	5.31×10^{-3}	-0.140

* α_s : the stator's AoA.

If we normalize the peak values with their corresponding q_t 's for the cases where $\beta_e > -22^\circ$, then we can apply the power-fitting equation (3.1) again to find the relationship between normalized peak values and velocities. The corresponding coefficient a 's and power b 's are listed in Table 3-3.

From Table 3-3, average values of power b 's for U_o , U_r and U_t are 1.06, -0.17 and 0.06, respectively. It is apparently that the freestream velocity U_o remains linearly proportional to the noise-peak values at different stator's AoA. This power relationship between normalized peak value and freestream velocity U_o at different stator's AoA is plotted in Fig.3-7, and can be expressed as

$$(Peak Value / q_t) \propto U_o \quad (3.3a)$$

or

$$Peak Value \propto q_t U_o \quad (3.3b)$$

Before discussing the physical significance of Eq. (3.3), we should examine if there still exists any power dependency between peak values and velocities. Once again, the coefficient a 's and power b 's for $Y = (Peak Value / q_t U_o)$ are listed in Table 3-4.

Table 3-4. $Y = (Peak Value / q_t U_o)$ & $X = Velocities$ in Eq.(3.1) in cases: $\beta_e > -22^\circ$.

α_s^*	$X = U_o$		$X = U_r @ 55\%R$		$X = U_t @ 55\%R$	
	a	b	a	b	a	b
-15°	0.0010	-3.06×10^{-14}	0.0010	-6.54×10^{-15}	0.0010	-1.49×10^{-14}
-10°	0.0010	-3.06×10^{-14}	0.0010	-6.54×10^{-15}	0.0010	-1.49×10^{-14}
-5°	0.0010	-3.06×10^{-14}	0.0010	-6.54×10^{-15}	0.0010	-1.49×10^{-14}
0°	0.0014	-0.142	0.0014	-0.121	0.0017	-0.179
5°	0.0010	1.79×10^{-15}	0.0010	-2.39×10^{-15}	0.0010	-1.27×10^{-14}
10°	0.0010	-2.15×10^{-14}	0.0010	-1.69×10^{-14}	0.0010	-4.58×10^{-15}

* α_s : the stator's AoA.

From Table 3-4, we observe that all the power b 's approach zero for three velocities except for $\alpha_s = 0^\circ$. In other words, Eq.(3.3b) shows a general power relationship between noise-peak magnitude and velocities for cases where $\beta_e > -22^\circ$. We may rewrite Eq.(3.3) as

$$\text{Peak Value} = \text{const. } q_t U_0 \quad (3.4)$$

In general, Eqs.(3.3) and (3.4) not only describe an amplitude relationship between noise-peak values and velocities but also provide a pressure parameter, q_t , for non-dimensionalizing the noise signatures for those cases where $\beta_e > -22^\circ$ in Fig. 3-1, 3-2, 3-3 and 3-4. In addition, from both equations, it also shows that these dimensionless peak amplitudes are still proportional to the freestream velocity U_0 . In other words, this implies that the dimension of the proportional constant in Eq.(3.4) has a unit as *an inverse of a velocity scale*. Furthermore, from Eq.(3.4), we observe that the contribution to the noise-peak values from the rotor's velocity U_r is implicitly included in q_t which is equal to $\frac{1}{2}\rho_0 U_t^2$ or $\frac{1}{2}\rho_0 (U_0^2 + U_r^2)$.

Noise Peak vs. β_e for Cases: $\beta_e > -22^\circ$

Since β_e is directly related to the velocity ratio U_0/U_r and defined, in Eq.(2.1), as

$$\beta_e = \theta - \tan^{-1}(U_0 / U_r),$$

or

$$U_0/U_r = \tan(\theta - \beta_e), \quad (3.5)$$

we can derive, from Eq.(3.3), a form that relates the peak value to β_e in the following.

For U_t is the resultant velocity of both U_0 and U_r , then we can rewrite Eq.(3.3b) as

$$\begin{aligned} \text{Peak Value} \propto q_t U_0 &= \frac{1}{2} \rho_0 U_t^2 U_0 \\ &= \frac{1}{2} \rho_0 (U_0^2 + U_r^2) U_0 \\ &= \frac{1}{2} \rho_0 U_0^2 (1 + U_r^2/U_0^2) U_0. \end{aligned}$$

By substituting Eq.(3.5) for the velocity ratio U_r/U_0 , we obtain

$$\text{Peak Value} \propto q_0 \left(1 + \frac{1}{\tan^2(\theta - \beta_e)}\right) U_0 \quad (3.6)$$

where $q_0 = \frac{1}{2} \rho_0 U_0^2$ is the *freestream dynamic pressure*. Comparing Eq.(3.6) and Eq.(3.3), we have

$$q_t = q_0 \left(1 + \frac{1}{\tan^2(\theta - \beta_e)}\right). \quad (3.7)$$

From Eq.(3.6) and (3.7), it turns out that the contribution to the noise-peak value from the rotor's effective AoA β_e is *implicitly* included in the local dynamic pressure, q_t , like the rotor's velocity, U_r . Since, in the present study, β_e at 55%R ranges from -22° to 12° , with a fixed θ of 26° at the same radius, the value in the parentheses on the right-hand side of Eq.(3.6) varies from 1.8 to 17.1, respectively. Apparently, from Eq.(3.6), *the noise-peak magnitude increases as β_e increases with a constant θ , for all cases where $\beta_e > -22^\circ$.*

Peak Noise vs. α_i for Cases: $0^\circ < \beta_e < 10^\circ$

One interesting thing observed from noise signatures in Fig. 3-1 to 3-4 is that, for cases that $0^\circ < \beta_e < 10^\circ$, the noise peak increases as the stator's AoA α_i decreases. However, there does not exist a similar relationship between the peak values and α_i in these cases as Eq.(3.6). Nevertheless, this observed phenomenon still reveals that α_i is an important parameter to the noise generation for cases where $0^\circ < \beta_e < 10^\circ$. Further investigation of the unsteady flow field induced by rotor-stator interaction is necessary to understand this phenomenon.

3.2.2. Interaction Period for Cases: $\beta_e > -22^\circ$.

As indicated previously, the noise peak represents a maximum noise generated by rotor-stator interaction for cases where $\beta_e > -22^\circ$. Its existence indicates a reference phase angle for the active interaction period. Since most noise peaks, for the cases where $\beta_e > -22^\circ$, lie in an interval of phase angle $-27^\circ \pm 3^\circ$, we may, for the sake of simplicity, choose a phase angle -30° as the *upper bound* of the active interaction-noise period. Meanwhile, a sudden rise exists commonly at $\phi = -60^\circ$. We choose this phase angle as the *lower bound* of the interaction period. We, hence, define an *interaction period* from a phase angle -60° to -30° for the remainder of this study.

3.2.3. Two Typical Noise Patterns in Cases: $\beta_e > -22^\circ$.

In this subsection, we are going to compare two typical noise patterns observed from cases where $\beta_e > -22^\circ$. Two representative noise signatures are plotted in Fig. 3-8.

These two signatures are normalized by their corresponding local dynamic pressure q_i and chosen from cases where $\beta_e = -10.30^\circ$ in Fig. 3-2(b) and $\beta_e = 9.61^\circ$ in Fig. 3-2(b) with a fixed $\alpha_s = 10^\circ$. Simply, we use $\beta_e = \pm 10^\circ$ to distinguish these two cases for discussion.

In Fig. 3-8, we observe that these two normalized noise signatures are apparently different in both magnitude and pattern. The dimensionless noise magnitude in the case $\beta_e = -10^\circ$ is obviously higher than the one in the case $\beta_e = 10^\circ$. For the case $\beta_e = -10^\circ$, the noise starts decreasing before phase angle $\phi = -90^\circ$, reaches a valley at $\phi = -60^\circ$, and then rises abruptly to a peak at $\phi = -30^\circ$. However, for the case $\beta_e = 10^\circ$, the noise rises gradually from a valley at $\phi = -90^\circ$, and then, after reaching a higher-noise level at $\phi = -48^\circ$, increases rapidly to a peak at $\phi = -30^\circ$. Differences observed in both the magnitude and the pattern suggest that there may be two distinct mechanisms which generate the interaction noise during the rotor's passage in the vicinity of the stator's leading edge. These two typical noise signatures generally exist in two categories where $\beta_e < 0^\circ$ and $\beta_e > 0^\circ$, respectively. Further discussion will be postponed until investigation of the interaction-flow fields in the later chapters.

3.3. Active Interaction Phase Interval

In sub-section 3.2.2, we have already defined the interaction period, for $\beta_e > -22^\circ$, by locating a sudden rise of peak noise from -60° to -30° in phase angle ϕ . In order to confirm the relationship of this peak noise to the rotor-stator interaction noise, we have to examine noise signatures which are measured *with* and *without* the presence of a stator for two cases: $\beta_e = -10.30^\circ$ and 5.82° .

Comparison of noise signatures with and without Stator

In Fig.3-9(a) and (b), it is obvious that, without the stator, the peak noise does not exist for both cases. Accordingly, from Fig.3-9, the peak noise, with the presence of stator, is identified as the rotor-stator interaction noise.

Active interaction-noise phase interval for $\beta_e > -22^\circ$

As a consequence, from Fig.3-9, the interaction noise arises abruptly from a valley to a peak before the zero-degree phase angle, when compared to the noise measured without a stator. Therefore, the active time interval of noise interaction or the *active interaction phase interval* is defined between the corresponding phase angles of these two values, and can be found in Fig. 3-9. Therefore, from Fig. 3-9(a) & (b), the active interaction phase interval for both cases ranges from -60° to -30° in phase angle ϕ .

3.4. Summary

According to the discussion in previous sections, we may summarize as follows. First, it is noted that the active interaction phase interval is similar in all cases where $\beta_e > -22^\circ$ and commonly ranges from $\phi = -60^\circ$ to -30° in which a rise in the noise peak is associated with the interaction-noise generation. This implies that, for $\beta_e > -22^\circ$ and $-15^\circ < \alpha_s < -10^\circ$, *the interaction period is irrelevant to changes in operating conditions, or, precisely, to changes of parameters in the freestream speed, the rotor's RPM and the stator's AoA.*

Secondly, from the observation of the noise-peaks' alignment for cases where $\beta_e > -22^\circ$, the effective rotor's AoA β_e is irrelevant to the timing of the noise peaks. Nevertheless, *the peak-noise magnitude does increase as β_e increases.*

Next, by inspecting the peak values during the interaction period from cases where $\beta_e > -22^\circ$, it turns out that there exists a direct relationship between the peak value of the interaction noise and the local resultant velocity U_t which is defined, in Fig.2-3, by the freestream speed U_o and the rotor's speed U_r at 55% R of the rotor. It is shown in Table 3-2 and Fig. 3-6 that the peak value is proportional to the square value of U_t , i.e., U_t^2 . This indicates that *the peak value shown in each noise signature is directly proportional to the local dynamic pressure, q_t , which is equal to $\frac{1}{2}\rho_o U_t^2$ with a constant ρ_o in this study.* However, Fujita and Kovasznay (1974) pointed out that the peak value due to the rotor-stator interaction is proportional to the freestream dynamic pressure q_o defined as $\frac{1}{2}\rho_o U_o^2$, as shown in Eq.(1.3). This is because, in Fujita and Kovasznay's study, the only freestream speed U_o adopted was 38 m/s which is close to the value of 41 m/s for the local resultant speed, U_t , with a fixed rotor's speed at 15.7 m/s (a circular-cylinder rod rotates at 300 rpm). Since the values of both U_o and U_t are too close to be distinguished, it was misleading to use q_o in their study. Therefore, a correction for both the calculation of the noise prediction (Fujita and Kovasznay 1974) and non-dimensionalization of the measured noise (Ho and Kovasznay 1976) should be taken by the local dynamic pressure q_t instead of the freestream dynamic pressure q_o .

CHAPTER 4

STATOR RESPONSE TO FLOW DISTURBANCES

As mentioned in Chapter 1, Fujita and Kovasznay (1974) studied the rotor-stator interaction noise in a free space. They simplified Curle's supplementary formula to relate a transient stator response (i.e., the lift fluctuations) to the corresponding *free-space*, near-field dipole sound (Eq. (1.3)). In this study, the sound field were measured in a confined region by the pipe. Accordingly, the Fujita-Kovasznay formula (Eq.(1.3)) may not be directly applied in the current circumstance. Nevertheless, the local flow interaction results in a net-force variation acting on the stator, which induces the noise generation. In other words, the noise is produced by the change of both C_L and dC_L/dt , but the proportional constant in the equation will not hold.

4.1. Stator Response

Stator response within a complete period based on BPF is the time trace of the resultant aerodynamic force on the stator surface. Since the flow incidence relative to the stator is varied with time, hence it is hardly to determine the instantaneous lift- and drag-forces' directions case by case. Therefore, the stator response is resolved into the *normal* and *tangential* components instead of the lift and drag for investigation. In this chapter, we are about to review 36 cases for the relationship between the stator response and interaction noise in a range of $-22^\circ < \beta_e < 0^\circ$ and $-15^\circ < \alpha_e < 10^\circ$.

4.1.1. Operating Conditions

In Section 3.1, we have one hundred and twenty operating conditions to investigate the interaction-noise signatures. In order to examine the dependency between both the acoustic fields and stator responses, thirty-six conditions for the surface pressure measurements are chosen from them, and are described as follows.

There are six different rotor's effective AoA β_e which are -10.30° , 1.32° , 5.82° , 9.61° , -21.78° and 2.20° with their corresponding incident velocities U_i at 55%R of 9.49, 13.46, 16.29, 19.92, 11.38 and 20.89 m/s, respectively, as listed in Table. 3-1. Also from Table 3-1, the first four values of β_e are set up by four different rotor's RPMs at 1500, 2400, 3000 and 3750, with a fixed freestream velocity U_o at 5.62 m/s, which present four corresponding rotor's velocities U_i at 55%R of 7.65, 12.23, 15.29 and 19.11 m/s, respectively. However, the latter two values of β_e , -21.78° and 2.20° , correspond to the two rotor RPMs at 1500 and 3750, in turn, with a fixed freestream velocity U_o at 8.43 m/s. Based on these β_e values, we will survey the relationship between the stator response and interaction noise for the cases where $-22^\circ < \beta_e < 10^\circ$.

With six stator's AoA, α_e , at -15° , $\pm 10^\circ$, $\pm 5^\circ$ and 0° , we hence have 36 operating conditions for a comprehensive investigation.

4.1.2. Force Coefficients : C_N & C_T

To evaluate the components of the stator response, the stator's pressure distributions on both sides must be integrated. It is straightforward to choose the positive direction for the tangential force component as pointing toward the trailing edge in parallel with the stator's chordwise direction. Since the stronger impact happens on the pressure side during the flow interaction for the cases that $-22^\circ < \beta_e < 0^\circ$, the normal force component is calculated by subtracting the resultant force on the suction side from the one on the pressure side: hence its positive direction shall be normal to the chordwise direction and pointing outward from the pressure side. A schematic description for the senses of both force components is illustrated in Fig. 4-1, where \mathbf{N} and \mathbf{T} represent the normal and tangential forces, respectively.

From Chapter 3, we know that the peak-noise value is proportional to the local dynamic pressure q_i for the entire surveying range. We may define the *normal force coefficient*, C_N , and the *tangential force coefficient*, C_T , as follows:

$$C_N \equiv \frac{N}{q_i A} = \frac{N}{\frac{1}{2} \rho U_i^2 \cdot c \cdot 1} \quad (4.1a)$$

and

$$C_T \equiv \frac{T}{q_i A} = \frac{T}{\frac{1}{2} \rho U_i^2 \cdot c \cdot 1} \quad (4.1b)$$

where N and T are magnitudes of the normal and tangential forces, respectively, q_i is defined as $\frac{1}{2} \rho_0 U_i^2$ with the local resultant velocity U_i , and A is the planform area. Since, at present study, the stator response is calculated on the blade section at 55%R of the rotor, the planform area, A , for a certain section of the stator blade is given by a product of its chord, c , and a unit span in Eq.(4.1).

Accordingly, the normal and tangential forces, C_N and C_T , acting on the stator are calculated and plotted for thirty six cases in Fig. 4-2 through 4-7. We shall discuss these results in two categories: $-22^\circ < \beta_e < 0^\circ$ and $0^\circ < \beta_e < 10^\circ$.

Fluctuations of C_N and C_T curves in $-22^\circ < \beta_e < 0^\circ$

There exists a resemblance among the C_N curves in the category of $-22^\circ < \beta_e < 0^\circ$, as shown in Fig. 4-2 and 4-3. In general, a rising slope in each C_N curve is consistently observed during the interaction period from $\phi = -60^\circ$ to -30° , and ends up with reaching a maximum. However, it is hardly to find, from these figures, a unique trend from the variations of the C_T curves in this category.

Meanwhile, from Fig. 4-2 & 4-3, we observe that the fluctuation magnitude of each C_N curve is greater than that of the corresponding C_T curve. This shows that the majority of surface pressure fluctuation contributes to the normal force rather than to the tangential one. In other words, the *sound radiation from the stator surface is mainly consequent on the normal force fluctuation*. The discussion will be subsequently focused on the normal force coefficient C_N for this category.

Fluctuations of C_N and C_T curves in $0^\circ < \beta_e < 10^\circ$

Both the C_N and C_T curves in the category of $0^\circ < \beta_e < 10^\circ$ are plotted from Fig. 4-4 to 4-7. For the smaller β_e cases, i.e., $\beta_e = 1.32^\circ$ and 2.20° , a similar tendency of rising slopes in the C_N curves occurs during the interaction period in Fig. 4-4 & 4-5. It is noticed that the magnitudes of these rising slopes are apparently smaller than those for $-22^\circ < \beta_e < 0^\circ$ in Fig. 4-2 & 4-3. However, this tendency in the C_N curves is invalid for the higher β_e cases. For $\beta_e = 5.82^\circ$, the rising slopes in the C_N curves become vague during the interaction period in Fig. 4-6, and turn themselves into declining slopes for $\beta_e = 9.61^\circ$ in Fig. 4-5. Besides, the magnitudes of the C_N curves for these two cases are smaller than those in the smaller β_e cases in Fig. 4-4 & 4-5.

For the C_T curves in this category, there does not exist a consistent trend from their variations on Fig. 4-4 through 4-7. Meanwhile, from these figures, we observe again that the fluctuation magnitude of each C_N curve is greater than that of the corresponding C_T curve, which means that the normal force indicates the main part of the stator response.

The above observations imply that the stator response in the category of $0^\circ < \beta_e < 10^\circ$ is weak and not responsible for the majority of the interaction-noise generation, especially in the higher β_e cases.

4.1.3. Fluctuations : \tilde{C}_N & $\frac{R}{a_0} \frac{d\tilde{C}_N}{dt}$

Since sound radiation results from the pressure fluctuation, a new coefficient, \tilde{C}_N , will be introduced in the following sections to represent the fluctuation part of the normal force coefficient C_N . Accordingly, the time traces of the new coefficient, \tilde{C}_N , are plotted in part (a) of Fig. 4-8 to 4-13. Each \tilde{C}_N curve is simply the fluctuation portion of its corresponding coefficient C_N , except that the C_N fluctuations for $\beta_e = 9.61^\circ$ in Fig. 4-7 are inverted and plotted in Fig. 4-13. This exception is made since we have no knowledge about the influence of the force orientation to the directivity of the acoustic field (note that we only know that the acoustic wave arriving at 0.7 m downstream becomes a plane wave.) Hence, in Fig. 4-13, the inverted \tilde{C}_N curves show a consistent rising slope during the interaction period from $\phi = -60^\circ$ to -12° .

However, the peaks of \tilde{C}_N in part (a) of Fig. 4-8 to 4-13 do not coincide with the corresponding peak noises observed in Fig. 3-2 (b), (c), (d) & (e) and Fig. 3-3 (b) & (e). We will discuss it later in this section.

Another fluctuation item in which we are interested is the time derivative of \tilde{C}_N itself. From Fujita-Kovaszny simplified formula in Chapter 1, the lift-fluctuation term contributes mainly to the near-field noise, while its time-derivative term dominates the

far-field noise (Lighthill, 1962). Meanwhile, since we have the normal force instead of the lift force, the Fujita-Kovaszny formula is rewritten in terms of \tilde{C}_N as following:

$$S.P. = k_1 \left\{ \underbrace{\tilde{C}_N}_{\text{near field}} + \underbrace{\frac{R}{a_0} \frac{d\tilde{C}_N}{dt}}_{\text{far field}} \right\}, \quad (4.2)$$

where $k_1 = \frac{A}{4\pi R^2} \cos\theta$, as defined in Chapter 1. Note that, given $R = 0.7$ m and $a_0 = 340$ m/s, then R / a_0 is 0.00206 sec. Time traces of $\frac{R}{a_0} \frac{d\tilde{C}_N}{dt}$ are subsequently obtained and plotted in part (b) of Fig. 4-8 through 4-13.

First, from these figures, both fluctuation magnitudes of the \tilde{C}_N and $\frac{R}{a_0} \frac{d\tilde{C}_N}{dt}$ curves decrease as β_e decreases. Secondly, for a fixed β_e , the magnitude of \tilde{C}_N is of the same order as that of $\frac{R}{a_0} \frac{d\tilde{C}_N}{dt}$. Therefore, the \tilde{C}_N term in Eq.(4.2) contributes as much to the sound radiation from the stator surface as the $\frac{R}{a_0} \frac{d\tilde{C}_N}{dt}$ term calculated at 0.7 m. Thirdly, we also observe that the rising slope occurring in each $\frac{R}{a_0} \frac{d\tilde{C}_N}{dt}$ curve during the interaction period is more correlated with the peak noise from the measurements than that in the corresponding \tilde{C}_N curve. This observation is in agreement with the fact that $\frac{R}{a_0} \frac{d\tilde{C}_N}{dt}$ governs the far-field noise for the free space as R approaches infinity, as described in Chapter 1.

In the light of Eq.(4.2), we can calculate the resultant contribution from both fluctuation terms which will be discussed in the next section.

4.2. Source Term vs. Measured Noise

We define the *source term* by the summation of both terms in curly brackets on the right-hand side of Eq.(4.2), i.e., $\{\tilde{C}_N + \frac{R}{a_0} \frac{d\tilde{C}_N}{dt}\}$. Then, the source-term curves are plotted with the measured noise signatures from Fig. 4-14 to 4-19.

For $-22^\circ < \beta_e < 0^\circ$ in Fig. 4-14 & 4-15, there is a good agreement in peak value between both the source-term and measured results during the interaction period. It is surprising because the sound propagation in the pipe is not influenced so much due to the confined geometry as we expected. For $0^\circ < \beta_e < 10^\circ$ in Fig. 4-16 to 4-19, the peak values in the source-term results become smaller than those in the measured-noise results specifically as β_e increases.

Note that the source term is calculated based on the stator response. Therefore, the stator response becomes the dominant resource for the interaction-noise generation if the rotor's effective AoA, β_e , is negative. If β_e is positive, it becomes less responsible for the majority of the interaction-noise generation with increasing β_e .

4.2.1. Amplitude factor κ vs. interaction angle γ

An *amplitude factor*, κ , is defined as a ratio of the source-term peak value to the peak noise, and can be easily obtained by measuring and comparing the peak values from Fig. 4-14 to 4-19, during the interaction-noise generation. For each κ , there exists both the corresponding values of α_i and β_i which enable us to define an *interaction angle*, γ , via a simple triangular relationship illustrated in Fig. 4-20.

In Chapter 3, we found that, from Eq.(3.4), the noise-peak value is also proportional to the freestream velocity, U_o , for the cases that $\beta_i > -22^\circ$. In addition, as mentioned in Section 6.1, the thirty-six operating conditions for surface pressure measurements are chosen based on two freestream velocities at $U_o = 5.62$ and 8.43 m/s. The κ - γ diagrams are, hence, plotted for both of them in Fig.4-21(a) & (b), respectively.

Generally in Fig.4-21(a) & (b), for a fixed stator's AoA α_i , the amplitude factor κ increases as the interaction angle γ increases. According to the definition of κ , the higher the κ , the stronger the noise generation from the stator response. From Fig.4-20, for a fixed α_i , the rotor's effective AoA β_i decreases while the interaction angle γ increases.

Note that, as κ approaches unity for $-22^\circ < \beta_i < 0^\circ$ in Fig. 4-21 (a) & (b), there exists a high dependency between both the peak values of the source terms and measured noises, which suggests that the stator response is the major resource to the noise generation. Since the source term is calculated from the pressure distributions on the stator's blade section at 55%R, the good agreement between both of the peak values implies that the stator response at 55%R is typical of the entire stator response along the span with a factor κ , essentially.

For $0^\circ < \beta_i < 10^\circ$, the value of κ decreases as β_i increases with a fixed α_i in Fig. 4-21 (a) & (b). In other words, the stator response in this category does not contribute so much to the noise generation as that in $-22^\circ < \beta_i < 0^\circ$. Hence, it implies that a transient rotor response becomes responsible for the majority of interaction-noise generation for $0^\circ < \beta_i < 10^\circ$.

4.3. Summary

In this chapter, we may summarize as follows.

- In the light of the Fujita-Kovaszny formula [Eq.(4.2)], we find that the source terms calculated from the stator's surface pressure distributions agree with the measured noise signatures for the category of $-22^\circ < \beta_e < 0^\circ$, while, for $0^\circ < \beta_e < 10^\circ$, this dependency becomes less as β_e increases.
- Meanwhile, by defining two parameters, i.e., the amplitude factor κ and the interaction angle γ , we have reached the following conclusion: *For a fixed stator's AoA, α , the interaction-noise generation highly depends upon the stator response as the interaction angle γ increases, while, if γ decreases, the rotor response shall be mainly responsible for the interaction-noise generation.*

CHAPTER 5

FLOW FIELD AROUND THE STATOR

One of the main tasks in the present study is to understand the physical mechanism of the rotor-stator interaction-noise generation by correlating both the acoustic field (*effect*) and the corresponding aerodynamic field (*cause*). In this chapter, we will examine the local flow fields in detail and qualitatively correlate them to the interaction noise. Note that the active interaction phase interval for the cases where $\beta_i > -22^\circ$ is previously identified as the phase angle ϕ from -60° to -30° . Nevertheless, we may as well extend the investigation interval from $\phi = -60^\circ$ up to -12° for study in order to understand more details about the unsteadiness of the interaction flow field.

Meanwhile, since the peak value of the interaction noise increases with the rotor's effective AoA β_i for cases where $\beta_i > -22^\circ$ (Chapter 3), it is convenient to investigate the flow field categorized by β_i in this chapter.

5.1. Operating Conditions for Surface Pressure and Velocity Measurements

There are thirty-six operating conditions for the surface pressure measurements which are same as described in sub-section 4.1.1.

For the velocity measurements, sixteen conditions are selected from those conditions in surface pressure measurements. Except only choosing $\alpha_i = 0^\circ$ for case of $\beta_i = -21.78^\circ$, three α_i 's are set up at 0° and $\pm 10^\circ$ for the remaining five β_i 's, i.e. -10.30° , 1.32° , 5.82° , 9.61° and 2.20° . Fig. 5-1 shows three meshes of hot-wire stations at $\alpha_i = 10^\circ$, 0° and -10° used for velocity measurements around the stator's FIRST 30%C. Each mesh has approximately 4,500 hot-wire stations.

In the following sections, the results of these two measurements will be discussed and correlated to the noise results in order to survey the noise-generation mechanism due to rotor-stator interaction for cases where $-22^\circ < \beta_i < 10^\circ$.

5.2. Categorization of Interaction Flow Fields by β_i

Recall that, in sub-section 3.2.3, two typical noise patterns have been observed within $-22^\circ < \beta_i < 10^\circ$ and distinguished by cases: $\beta_i = \pm 10^\circ$. Moreover, from sub-section 3.2.1, it has been pointed out that, for cases where $0^\circ < \beta_i < 10^\circ$, the noise-peak value increases as the stator's AoA α_i decreases. Therefore, the zero degrees of β_i which represent the rotor's zero-lift AoA will be a somewhat rough but good dividing line for categorizing the cases. Accordingly, we may easily survey the interaction flow fields with two categories: $-22^\circ < \beta_i < 0^\circ$ and $0^\circ < \beta_i < 10^\circ$.

In the following, two cases, i.e. $\beta_t = -10.30^\circ$ and 9.61° , will be utilized to represent both categories for investigation. The experimental results regarding the rest cases can be found in Hu and Ho's report (1997).

5.3. The Flow Fields for Cases: $-22^\circ < \beta_t < 0^\circ$.

The cases for investigation in $-22^\circ < \beta_t < 0^\circ$ are $\beta_t = -10.30^\circ$ with $-15^\circ < \alpha_t < 10^\circ$.

5.3.1. Characteristics of surface pressure results for $\beta_t = -10.30^\circ$

Unsteady surface pressure distributions for $\beta_t = -10.30^\circ$ are shown in Fig. 5-2, with six stator's AoA during $-60^\circ < \phi < -12^\circ$. The pressure distributions in Fig. 5-2 are non-dimensionalized by the local dynamic pressure q , i.e. $\frac{1}{2}\rho_0 U_t^2$, and plotted against the normalized chordwise coordinate, x/c . As mentioned previously, the pressure distributions on both sides are shown up to 85%C due to the limitation of measurements (Chapter2).

The physical significance of Fig.5-2 is described as follows. First, for all six stator's AoA α_t 's, the pressure distributions on the stator's pressure side fluctuate more drastically than those on its suction side during the interaction period. This seems consequent to the fact that the pressure side is the side facing to the rotor's approach (Fig. 2-3) and is supposed to experience the most impact during the interaction period.

Secondly, we will look into how the surface pressure varies during the interaction period on the stator's pressure side. For $\alpha_t > 0^\circ$, which means the stator is tilted to its pressure side for a positive angle of attack, most of the pressure side experiences negative pressure, shown in Fig. 5-2(a) & (b), and the dramatic change observed is a diminishing region of negative pressure gradient from 20%C down to 2%C due to a decrease of the surface pressure. For $\alpha_t = 0^\circ$, a similar progress is observed in Fig. 5-2(c). The difference is that the negative-pressure-gradient region shrinks from 45%C at $\phi = -60^\circ$ down to 5%C at $\phi = -12^\circ$, which causes a strong pressure drop on the pressure side. For $\alpha_t < 0^\circ$, the pressure distributions on the pressure side are mostly positive, as shown in Fig. 5-2(d), (e) & (f), and the highest pressure indicates the stator's *front stagnation point* is observed and located within the first 5%C of the pressure side. In a like manner, a diminishing and decreasing negative-pressure-gradient region occurs from 50%C down to 10%C on this side within a phase interval: $\phi = -60^\circ$ to -12° .

These results show that, for all six stator's AoA α_t 's with $\beta_t = -10.30^\circ$, a negative-pressure-gradient region on the stator's pressure side diminishes during the rotor-stator interaction and is identified as the *active interaction region* on the stator.

5.3.2 The flow fields for $\beta_t = -10.30^\circ$ at six α_t 's

It is noticed that this pressure decrease is simultaneously accompanied by a sudden drop of the negative pressure gradient in the same active region for the case: $\beta_t = -10.30^\circ$ with all six α_t 's. This active region generally ranges from the stator's leading

edge up to 30%C on its pressure side. Hence, the following velocity results will be confined in this active region (Fig. 5-1). We should inspect the cause of the drastic drop in both the surface pressure and its corresponding negative gradient during the interaction period. This discussion will be initiated with the case: $\alpha_i = 10^\circ$ for $\beta_i = -10.30^\circ$, and extended to the rest α_i 's at $5^\circ, 0^\circ, -5^\circ, -10^\circ$ and -15° .

5.3.2.1 Case : $\alpha_i = 10^\circ$.

Fig. 5-3 shows a history of velocity contours for $\alpha_i = 10^\circ$ and $\beta_i = -10.30^\circ$ from phase angle $\phi = -60^\circ$ to -12° . Each velocity contour at a certain phase angle is cross-plotted from phase-averaged time-trace data measured at different hot-wire stations (Fig. 5-1(a)). It should be borne in mind that, since the velocity measurements were done by a single hot-wire probe which measures the heat-transfer effect in the normal direction to the hot wire, hence the magnitude $U(x,y,\phi)$ of velocities measured, as shown in Fig. 5-3, is the resultant, $(u^2 + v^2)^{1/2}$, of two velocity components, u and v , in a Cartesian or x - y coordinate system as plotted in Fig. 5-3. This indicates that the contour lines shown in Fig. 5-3 are not the instantaneous streamlines so that we can not apply them to identify the local flow directions. Despite this drawback, these velocity-contour plots still provide us profound information about the interaction flow field as pictures obtained by flow-visualization methods.

We shall investigate the velocity-contour plots in Fig. 5-3 in parallel with the corresponding surface pressure distributions from Fig. 5-2(a). At $\phi = -60^\circ$ in Fig. 5-3, the rotor's wake which is shaded by a low-speed region is clearly entering in the left-bottom corner of the velocity-contour plot in Fig. 5-3. We also observe that, at this moment, another low-speed region occurs around the leading edge on the stator's suction side. This low-speed region is recognized as the *instantaneous front-stagnation-flow* regime on the stator, and is also validated by the existence of a maximum and positive pressure on the suction side at $\phi = -60^\circ$ in Fig. 5-2(a). This front stagnation point located on the suction side is subsequently on the positive stator's AoA α_i , which is rotated 10° to the pressure side. On the pressure side, there exists a high-speed spot marked by a 10 m/s contour line from the leading edge to approximate 10%C. As we will see later, this high-speed spot is a strongly accelerated flow region which is an inviscid effect caused by the separated rotor's wake approaching to the stator in the present case. In this flow acceleration region, a pressure drop, i.e. a negative pressure gradient region, is consistently observed at $\phi = -60^\circ$ on the pressure side in Fig. 5-2(a).

Next, at $\phi = -54^\circ$, the flow field does not change too much by observing both Fig. 5-2(a) and 5-3, except that the rotor's wake moves upwards and appears clearer. The wake behind the rotor is separated due to a negative rotor's AoA β_i of -10.30° . At this circumstance, the rotor itself serves as a bluff body, and the boundary layer on its pressure side has already separated to form a thick wake behind.

Between $\phi = -48^\circ$ and -12° , it is observed that a strong interaction happens in the flow field by inspecting the consecutive velocity contours in Fig. 5-3. At $\phi = -48^\circ$, the inviscid wake behind the rotor apparently approaches to the stator's pressure side. The

contour lines become squeezed within a narrowing region formed by the margin between the rotor's wake and the stator's pressure-side surface, especially near the stator's leading edge. This indicates that around the highly-curved leading edge portion there occurs a stronger velocity gradient at the present phase than that at the previous phase. Meanwhile, it is also noticed that the 10 m/s-high-speed spot on the pressure side shrinks at $\phi = -48^\circ$ due to the rotor's wake approaching.

Three sequential velocity-contour plots of $\phi = -42^\circ$, -36° and -30° clearly show that an interaction process takes place as the rotor's wake (the separated, inviscid flow) breaks in the stator's boundary layer (an attached, viscous flow). This process is the *impinging wake* phenomenon identified by Fujita and Kovasznay (1974). During the interaction process, we observe that the rotor's wake starts to disappear and to connect itself to the stator's leading-edge flow regime. This suggests that an active region on the stator's surface will erupt from its originally attached boundary layer due to the impingement of the rotor's wake.

Boundary layer at stator's leading edge

This eruption of the laminar boundary layer is validated by an inspection of time variations of velocity distributions along two lines: one line is normal to the leading edge and the other normal to the point at 2%C on the pressure side, as illustrated in Fig. 5-4(a). The temporal variations of velocity contours along the specific line normal to the leading edge is plotted in Fig. 5-5(a), while the normal coordinate, n , has been non-dimensionalized by the gap distance d_{gap} of 0.71cm at 55%R. Meanwhile, Fig. 5-6(b) shows a portion of Fig. 5-6(a) which is 10% of d_{gap} from the leading edge. The velocity-contour values are also non-dimensionalized by the freestream velocity U_o , 5.62 m/s for the present case, in Fig. 5-6(a) and (b), where the *solid contour lines* represent the *values greater than or equal to one* and the *dashed lines* values *less than one*.

Since both the rotor's and stator's positions are perpendicular to each other at phase angle $\phi = \pm 180^\circ$, the flow field around the stator's leading edge portion in Fig. 5-4(b) looks like the stator sitting in a uniform stream with less disturbance from the most faraway rotor's position within a revolution cycle. Hence, before the strong interaction happens at about $\phi = -60^\circ$, the contour line with value one in Fig. 5-5(b) indicates the boundary layer thickness at the stator's leading edge in a certain sense, and has an estimated thickness with an edge velocity U_o at $\phi = -180^\circ$ is about $0.015 d_{gap}$, as observed in Fig. 5-5(b).

From $\phi = -180^\circ$ to -60° in Fig. 5-5(b), the boundary layer at the stator's leading edge is attached and laminar. It is noticed that this boundary layer is suppressed by the presence of a flow acceleration process on the leading edge marked by a set of centered solid lines from $\phi = -105^\circ$ to -60° , in Fig. 5-5 (a) & (b). The flow-acceleration process ends with the boundary-layer thickness reaching a minimum value of $0.01 d_{gap}$ at $\phi = -60^\circ$ in Fig. 5-5(b). This is also supported by an observation of a 10 m/s-high-speed spot from the leading edge to 10%C on the stator's pressure side at $\phi = -60^\circ$ in Fig. 5-3. This flow-acceleration process is due to a contraction formed instantaneously by the rotor's separated wake margin and the curved leading edge geometry on the stator's pressure

side (as illustrated in Fig. 5-7(a)). A flow deceleration on the leading edge is observed from $\phi = -60^\circ$ to -42° in Fig. 5-5(b), while the boundary layer grows a little during this process. This deceleration process is also validated with the diminishing of the 10 m/s-high-speed spot from $\phi = -60^\circ$ to -42° in Fig. 5-3. After $\phi = -42^\circ$, the boundary layer at the stator's leading edge suddenly erupts and extends along the normal direction to the rotor's surface, as shown in Fig. 5-5(a) & (b). This boundary layer eruption is due to an impingement of the rotor's wake onto the stator's surface, in Fig. 5-3 and Fig. 5-5(a) & (b). This process is a *viscous-inviscid interaction* between a viscous, attached flow (the stator's boundary layer) and an inviscid, separated flow (the rotor's separated wake) (Didden and Ho 1985).

In Fig. 5-2(a), we observe that a pressure drop is accompanied with a decrease of negative pressure gradient (i.e., $\partial p / \partial s < 0$) at first 5%C of the stator's pressure side. Since a pressure gradient along the surface is necessary to sustain a flux of vorticity into the fluid (Panton 1984), the Navier-Stokes equation along the streamwise direction on a solid surface for a 2-D flow becomes

$$\frac{\partial \omega_z}{\partial n} = - \frac{1}{\mu} \frac{\partial p}{\partial s} \Big|_{\text{on the surface}},$$

where $\frac{\partial \omega_z}{\partial n}$ is the vorticity gradient. Hence, both time traces of the normalized surface pressure and the normalized surface vorticity gradient, dw^*/dn^* (calculated by $-1/\mu (\partial p / \partial s) \cdot (d_{gap})^2 / U_t$), at the leading edge are plotted in Fig. 5-5 (c)&(d), respectively.

Fig. 5-5(c) and (d) show that, from $\phi = -60^\circ$ to -30° , a sudden pressure drop at the leading edge (Fig. 5-5(c)) obviously accompanies with a vorticity flux (i.e., an increase of vorticity gradient) into the fluid flow (Fig. 5-5(d)). Accordingly, a *strong* flow interaction between the rotor and stator happens at $\phi = -60^\circ$, from which proceeds a sudden flux of vorticity into the fluid around the stator's leading edge portion.

Moreover, the boundary layer eruption at the leading edge continues until the phase angle $\phi = 0^\circ$ after which the boundary layer is gradually recovered by the rotor's passing, and it reattaches to the stator's leading edge after $\phi = 30^\circ$ in Fig. 5-5(a) & (b).

Boundary layer at 2%C on stator's pressure side

On a similar basis, Fig. 5-6(a) & (b) shows the time-trace contour along the normal line originated from the point at 2%C on the stator's pressure side. Since the flow is accelerated by the favorable pressure gradient to overcome the curved geometry around the leading edge at $\phi = -180^\circ$ in Fig. 5-4(b), an edge velocity U_e of the boundary layer at the current point should be larger than that at the leading edge. It is such a short distance from the leading edge to the current point at 2%C that the laminar boundary layer thickness over this distance should grow very little at $\phi = -180^\circ$. Hence, at $\phi = -180^\circ$ in Fig. 5-6(b), the contour line with a constant value of 1.5 is capable of indicating a boundary layer thickness of $0.015 d_{gap}$ (note that an approximate value of U_e at the edge

of the leading-edge boundary layer has been adopted earlier with $0.015 d_{gap}$ as a boundary layer thickness at $\phi = -180^\circ$.) From Fig. 5-6(b), we observe that a thin boundary layer at this point is mostly attached during one cycle except a phase interval in which an eruption of the boundary layer happens due to the flow interaction. Thus, following the contour line of 1.5 in Fig. 5-6(b), the boundary-layer thickness starts decreasing at $\phi = -90^\circ$ due to the flow acceleration above and reaches a minimum thickness at $\phi = -66^\circ$. In the meantime, the rotor's wake clearly shows up at $\phi = -90^\circ$ on the top of Fig. 5-6(a), and approaches to the point at 2%C on the pressure side. A flow-deceleration process above the occurs from $\phi = -66^\circ$ to -42° in Fig. 5-6(b), which is also observed in Fig. 5-3. The boundary layer grows up during the flow-deceleration process, and eventually erupts, after $\phi = -42^\circ$, due to an impingement of the rotor's wake at this point. The eruption of the boundary layer lasts until about $\phi = 15^\circ$ at which flow reattachment is observed in Fig. 5-6(b).

Fig. 5-6(c) and (d) show the time variations of surface pressure and vorticity gradient at the current point. In these figures, a dramatic pressure drop and a sudden rise of vorticity gradient are observed again from $\phi = -60^\circ$ to -30° . Therefore, it follows that the approaching wake is responsible for the sudden drop in the surface pressure about the stator's leading edge, which causes an interaction process between a viscous flow (the stator's boundary layer) and an inviscid flow (the rotor's wake).

Since this *viscous-inviscid-interaction* process happens exactly during a sudden rise of the interaction noise in Fig. 3-2(b), it is directly responsible for the interaction-noise generation in the present case. The interaction process from $\phi = -90^\circ$ to -30° is illustrated in Fig. 5-7 (a)&(b).

Post-interaction-noise period

After the interaction process in Fig. 5-3, the rotor's wake is completely cut off as shown in the velocity-contour plot at $\phi = -24^\circ$. Then, an attachment of the rotor's wake onto the stator's leading-edge portion are shown in contour plots at $\phi = -18^\circ$ and -12° .

5.3.2.2. A brief summary for $\beta_t = -10.30^\circ$ with six α_t 's

The velocity-contour plots for $\beta_t = -10.30^\circ$ and α_t 's at 0° and -10° are shown in Figs. 5-8 and 5-9, respectively. Generally speaking, the interaction-noise generation is due to the surface-pressure fluctuations on the stator's pressure side for all six α_t 's with $\beta_t = -10.30^\circ$, and these fluctuations are induced by the flow separation around the stator's leading edge while the rotor's wake approaches to the stator's pressure side. It is interesting to point out that the surface-pressure fluctuations are different in two categories (Fig. 5-2). For $\alpha_t < 0^\circ$, a negative-pressure drop in the active region on the stator's pressure side is esteemed as the surface-pressure fluctuation, while a positive-pressure drop, in contrast, is observed for $\alpha_t > 0^\circ$. An accompanying negative-pressure-gradient decrease is also observed in each α_t 's case. This is very important, as we shall see later, when we try to seek a unique mechanism for the interaction-noise generation for $-22^\circ < \beta_t < 0^\circ$.

5.4. Vorticity Flux vs. Sound Radiation for $-22^\circ < \beta_r < 0^\circ$

From the above discussion of both the surface pressure and velocity results, it is obvious that, around the stator's leading edge, the impingement of the rotor's wake causes locally, in the main, a strong surface pressure fluctuation which radiates sound wave. In other words, the unsteady stator response induced by this pressure fluctuation is the source of sound radiation for the category: $-22^\circ < \beta_r < 0^\circ$ and $-15^\circ < \alpha_r < 10^\circ$. We also find that whatever this surface pressure fluctuation varies case by case, a drop of negative surface pressure gradient is consistently observed in each case during the interaction period. This surface pressure gradient is directly associated to the surface vorticity gradient, as described in the previous section. Therefore, in the following, a unique description based on the concept of *vorticity flux* is developed to summarize the relationship of the negative pressure gradient to the stator response and the sound radiation.

5.4.1. Concept of vorticity flux

The concept of vorticity flux is due to Lighthill (1963). He pointed out that: *'The tangential-vorticity source strength has a simple relation to pressure gradient, at least for flow over a stationary plane surface. ..., and because at a solid surface transfer of momentum by convection is absent, so that transfer by diffusion must exactly balance transfer by pressure gradient.'* Furthermore, the balance between both the vorticity generation and transport is mainly the cause to change the vorticity field in an unsteady flow (Reynolds and Carr 1985, Shih and Ho 1994). Thus, for $-22^\circ < \beta_s < 0^\circ$, the separated flow behind the rotor induces the unsteadiness of the vorticity field around the stator's leading-edge surface to produce the vorticity into the fluid and hence the sound.

On the basis of this statement, a relationship can be obtained between vorticity flux (i.e., the tangential-vorticity source strength) and pressure gradient on a solid surface. First, we derive this relationship, and then take advantage of it to explore a connection of the surface vorticity flux to the noise generation.

Vorticity flux is used to phrase the vorticity generation across a solid surface into the flow. Consider a local s - n - z coordinate system on the stator surface as illustrated in Fig. 5-10, where s and n represent the streamwise and the normal coordinates which are tangential and perpendicular to the surface, respectively, and z the coordinate which is bi-normal to both s - and n - coordinates on the surface.

The z -component of a positive *vorticity flux vector* σ across a surface with the normal \mathbf{n} is defined as (Panton 1984)

$$\sigma_z \equiv -\frac{\partial \omega_z}{\partial n} = \frac{1}{\mu} \frac{\partial p}{\partial s} \Big|_{\text{on the surface}} \quad (5.1)$$

Eq.(5.1) shows a relationship between vorticity flux and surface pressure gradient. Since the surface pressure measurements have been conducted to present study, their results enable us to calculate the vorticity flux from the surface pressure gradient via Eq.(5.1).

Note that σ_z is equal to the negative value of $\partial \omega_z / \partial n$. In other words, if $\partial p / \partial s < 0$ and $\partial \omega_z / \partial n > 0$, then $\sigma_z < 0$: a *negative vorticity* is generated from the surface to the fluid. Namely, the surface is a vorticity source. Conversely, if $\partial p / \partial s > 0$ and $\partial \omega_z / \partial n < 0$, then $\sigma_z > 0$: a *negative vorticity* enters into the surface from the fluid; hence the surface a vorticity sink.

5.4.2. Contour and Surface Plots of $\partial \omega_z / \partial n$: for $-22^\circ < \beta_s < 0^\circ$

Since the most active region during the interaction period is typically located on the first 25%C of the stator's pressure side for $-22^\circ < \beta_s < 0^\circ$, hence we may calculate the

vorticity flux for this specific region from the surface-pressure results to see its variation within one BPF harmonic.

For $\beta_c = -10.30^\circ$, the surface-vorticity-gradient contour and surface plots are shown in Fig. 5-11 at six stator's AoA α_c 's. Two non-dimensionalized base axes plotted in Fig. 5-11 are the *temporal* and *spatial* coordinates in terms of the phase angle ϕ and the normalized streamwise coordinate, s^* , respectively. Note that, in this figure, the normalized streamwise coordinate, s^* , is confined from the stator's leading edge up to 25%C of the pressure side, which contains the active region for the flow interaction. The contour plot is stacked upon the surface one for the convenience of inspecting the variation of vorticity flux within a complete cycle in the active region. The height of both contour and surface plots represents $\partial\omega_z^*/\partial n^*$, the dimensionless magnitude of *surface vorticity gradient* $\partial\omega_z/\partial n$ on the stator surface, which is obtained by calculating $-1/\mu(\partial p/\partial s)$ in Eq. (5.1) and normalizing it by $(d_{gap})^2/U_c$, where p is the surface pressure and d_{gap} the gap between the rotor and stator at 55%R.

The contour and surface plots for $\beta_c = -10.30^\circ$ and $\alpha_c = 10^\circ$ are shown in Fig. 5-11(a). From Fig. 5-11(a), it is apparent that the active region is concentrated on the first 10%C of the stator's pressure side. Inside this region, a surface vorticity gradient $\partial\omega_z/\partial n$ abruptly rises during the interaction period, as we observed in Fig. 5-5(d) & 5-6(d). Hence, the stator's loading due to the surface-vorticity generation is highly related to the noise generation sound in this case. It turns out that, during the interaction period, a strong surface vorticity is generated into the flow on the pressure side for $-22^\circ < \beta_c < 0^\circ$ at six stator's AoA.

Since the surface-vorticity generation will simultaneously increase the stator's lift, a transient stator response, hence, induced by the vorticity fluctuation becomes the source to radiate the sound for $-22^\circ < \beta_c < 0^\circ$ and $-15^\circ < \beta_c < 10^\circ$.

5.4.3. Cause and effect of rotor-stator interaction for $-22^\circ < \beta_c < 0^\circ$

Therefore, for the cases that $-22^\circ < \beta_c < 0^\circ$, the *cause* of the rotor-stator interaction noise is as follows: During the interaction period, the incoming rotor's wake interacts with the stator's boundary layer to cause a sudden pressure drop on the first 10%C of the stator's pressure side. And hence the *effect*: A strong vorticity generation by the surface-pressure drop is the major source of a transient stator response and hence the interaction-noise radiation.

A schematic description of the noise-generation mechanism for $-22^\circ < \beta_c < 0^\circ$ and $-15^\circ < \alpha_c < 10^\circ$ is illustrated in Fig. 5-12.

5.5. The Flow Fields for Cases: $0^\circ < \beta_r < 10^\circ$.

In the rest of this chapter, we are about to survey the second category of $0^\circ < \beta_r < 10^\circ$. The $\beta_r = 9.61^\circ$ case will be investigated for the category of $0^\circ < \beta_r < 10^\circ$.

5.5.1. Characteristics of surface pressure results for $0^\circ < \beta_r < 10^\circ$

In Fig. 5-13, surface pressure distributions are plotted within $-60^\circ < \phi < -12^\circ$, for $\beta_r = 9.61^\circ$ at six different α_r 's. We find, from Fig. 5-13, that, at each α_r , the surface pressure fluctuations on both sides of stator are much less than those that we observed previously in the $\beta_r = -10.30^\circ$ case ($-22^\circ < \beta_r < 0^\circ$), as shown in Fig. 5-2. Meanwhile, the variations of surface-pressure distributions on both sides for $-15^\circ < \alpha_r < 10^\circ$ are apparently too small to distinguish which side (or both) shall be the active region for the noise-generation resource, as shown in Fig. 5-13(a) through (f). These suggest that, during the interaction period, the noise generation may not be consequent on the stator's surface-pressure fluctuations for $\beta_r = 9.61^\circ$ and $-15^\circ < \alpha_r < 10^\circ$.

In other words, the surface pressure variations show that the stator response is apparently *not* the major interaction-noise resource for $0^\circ < \beta_r < 10^\circ$ and $-15^\circ < \alpha_r < 10^\circ$, which is exactly disclosed in Chapter 4.

5.5.2. The flow fields for $0^\circ < \beta_r < 10^\circ$ and $-15^\circ < \alpha_r < 10^\circ$

The velocity-contour plots for $\beta_r = 9.61^\circ$ at $\alpha_r = 10^\circ$, 0° and -10° are shown in Fig. 5-14, 5-15 and 5-16, respectively. Generally speaking, since the rotor's effective AoA β_r is between 0° and 10° , the rotor's wakes observed in these figures are apparently thinner than those in $-22^\circ < \beta_r < 0^\circ$. Moreover, the wakes' angles are steep and close to the rotor's rotational plane, as schematically described in Fig. 5-17. These characteristics of the rotor's wakes reveal more or less that a noise-generation mechanism for the current case may differ from that in $-22^\circ < \beta_r < 0^\circ$.

An overview of the velocity-contour plots for $0^\circ < \beta_r < 10^\circ$ and $-15^\circ < \alpha_r < 10^\circ$ show that a slight variation of the flow field in the vicinity of the stator surface through the entire interaction period (Hu and Ho 1997). This agrees to the surface pressure results in this category. Since the noise generation still occurs during the interaction period from $\phi = -60^\circ$ to -30° (for example, in Fig. 3-2(c), (d) & (e) and Fig. 3-3(e)), this implies that the interaction-noise generation may be from the a *transient rotor response*.

5.6. Summary

The physical mechanism of the interaction-noise generation for $-22^\circ < \beta_r < 10^\circ$ and $-15^\circ < \beta_r < 10^\circ$ has been surveyed. For $-22^\circ < \beta_r < 0^\circ$ and $-15^\circ < \beta_r < 10^\circ$, the flow interaction is based on the first 10%C of the stator's pressure side during the interaction period from $\phi = -60^\circ$ to -30° . This interaction causes a surface-vorticity generation from the stator into the flow; hence, a transient stator response is induced to radiate sound. For $0^\circ < \beta_r < 10^\circ$ and $-15^\circ < \beta_r < 10^\circ$, the experimental results reveal that the flow interaction is irrelevant to the stator response, which suggests that a transient rotor response may be the cause of interaction-noise generation.

As a summary, if β_r decreases, the rotor's wake will be tilted more toward the stator and become broader in width, and hence the strong flow interaction will take place adjacent to the stator surface. Namely, for a fixed α_r , the stator response increases as β_r increases, and it decreases as β_r decreases. On the other hand, while β_r decreases, the majority of the interaction-noise generation is from the rotor response, as discussed in Chapter 4.

CHAPTER 6 CONCLUSION

The noise generated from a rotor-stator assembly placed in an incompressible pipe flow has been experimentally investigated. The focus of this study is to understand the physical mechanism of the interaction-noise generation by correlating the acoustic field to the unsteady flow field around the rotor-stator stage. From the measured noise signatures, a sudden rise in the noise level is consistently observed and identified as the interaction-noise generation from -60° to -30° in phase angle, ϕ , for $-22^\circ < \beta_r < 10^\circ$ and $-15^\circ < \alpha_r < 10^\circ$ (Chapter 3). In these noise signatures, two noise patterns can be easily distinguished at $\beta_r = -10^\circ$ and 10° , which implies that there exist two different mechanisms for the noise generation in the survey range.

Based on the Lighthill's acoustic analogy, Curle (1955) first derived the sound field radiated by a stationary solid body in a moving medium. Fujita and Kovaszny (1974) simplified Curle's result to study the rotor-stator interaction noise generated by a transient stator response in a free space. Since, in current study, the fluid flow is confined in a circular pipe, the proportional constant in Fujita-Kovaszny formula, Eq.(4.2), is no longer valid. Therefore, we can only calculate the source term, i.e., the summation of

\tilde{C}_N and $\frac{R}{a_0} \frac{d\tilde{C}_N}{dt}$ in Eq.(4.2), from the unsteady stator response. By comparing the calculated source term with the measured noise, both of them are in good agreement in peak value as β_r decreases, which means that a transient stator response is the major resource of the interaction noise generation (Chapter 4). On the other hand, as β_r increases, such an agreement between both peak values decreases. This suggests that the unsteady stator response contributes less to the noise generation as β_r increases; hence, most of the noise generation are from a transient rotor response. In other words, different mechanisms for the interaction-noise generation results from a variety of the flow-incidence angles to the rotor, i.e., β_r . This is because β_r determines the flow structure behind the rotor's wake which interacts with the stator to generate the noise. From the velocity results, a separated wake behind the rotor observed in $\beta_r < 0^\circ$ has a strong flow interaction with the boundary layer around the stator's leading edge during the interaction-noise generation. At this interaction period, an abrupt decrease of surface pressure on the first 10%C of the stator's pressure side induces unsteady vorticity-flux production into the fluid flow, which causes a transient stator response and hence sound radiation. For $\beta_r > 0^\circ$, the rotor's wake is thinner and tilted to the rotor's side, as observed from the velocity-contour plots, and the experimental results show that small surface-pressure and velocity fluctuations occur around the stator during the interaction-noise generation. Accordingly, the transient rotor response becomes the major resource of the interaction-noise generation for $\beta_r > 0^\circ$.

FIGURES

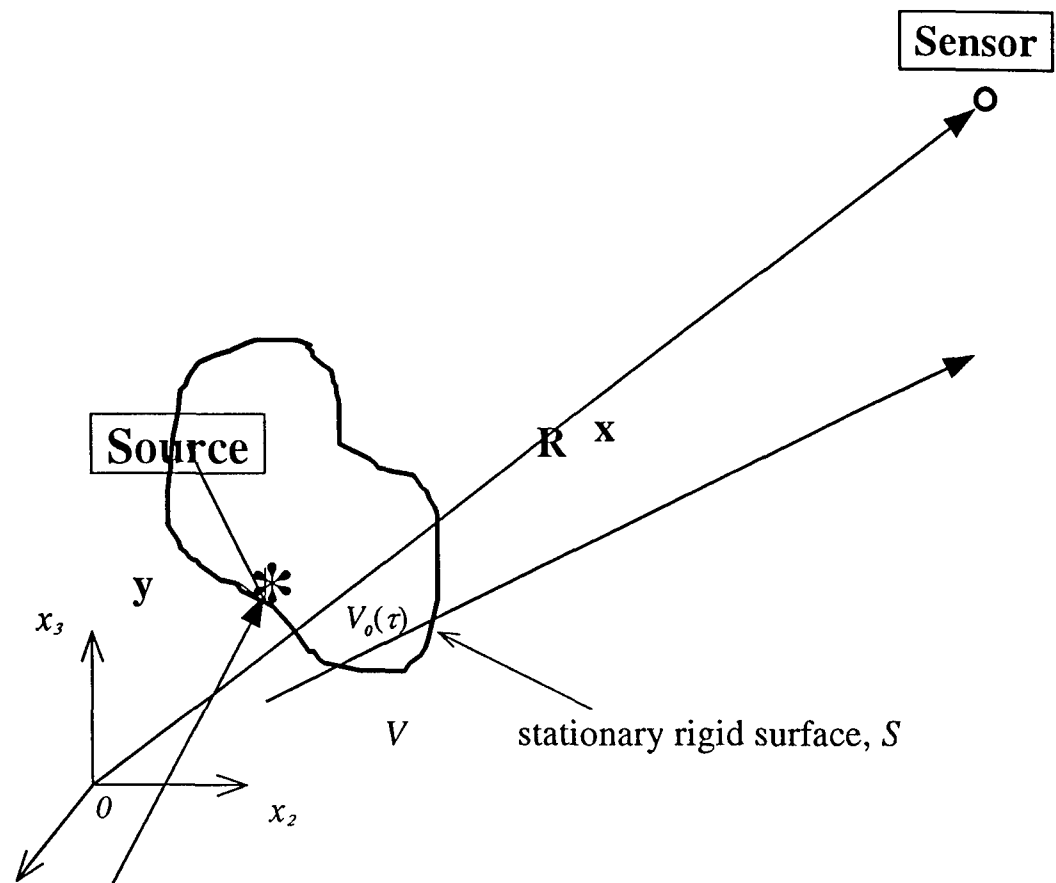


Fig. 1. A fixed coordinate system, x_i . The surface S is rigid and stationary, and divides an interior volume V_o from an exterior one V . $R = |x - y|$.

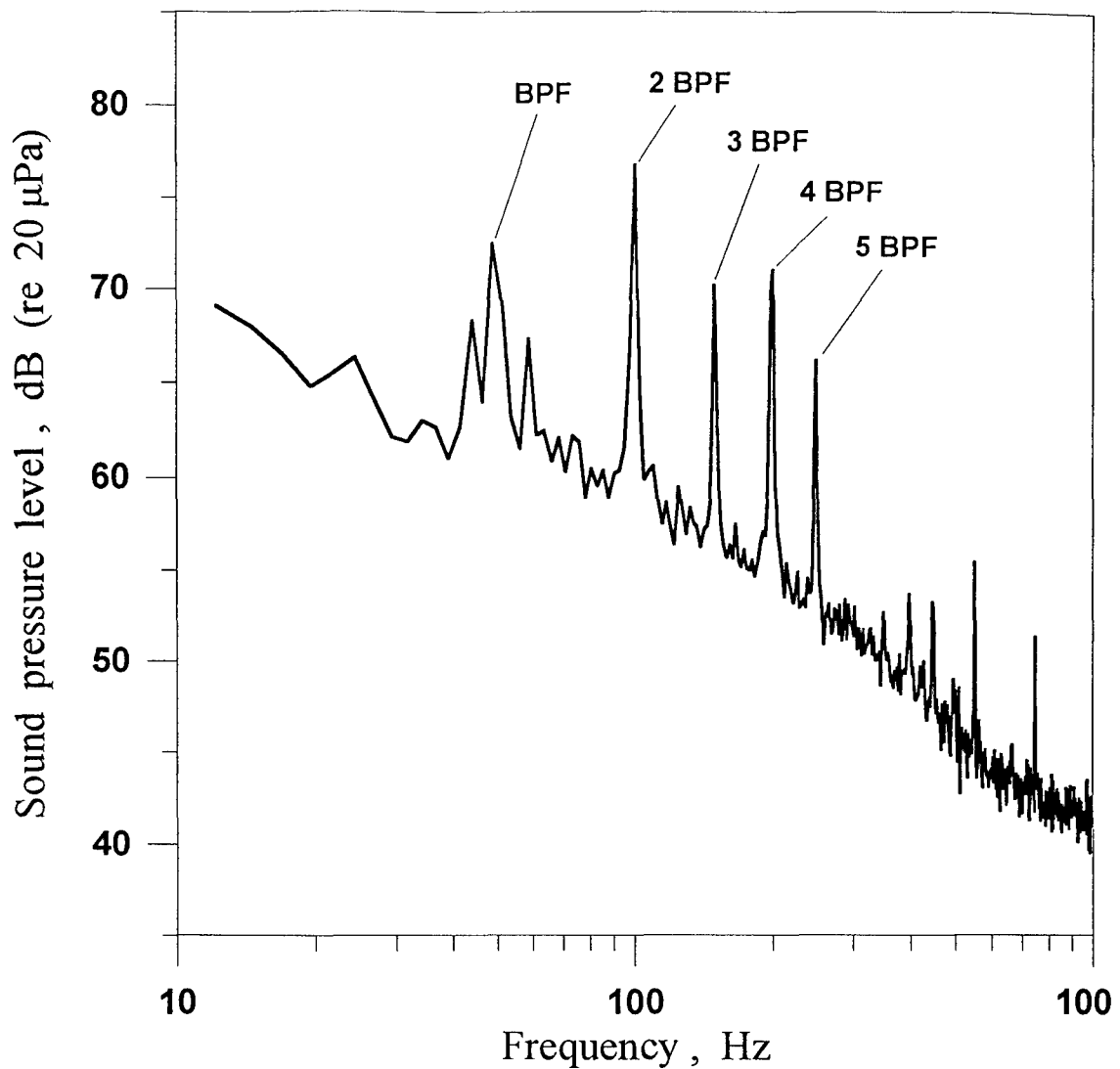


Fig. 1-2. A typical sound-pressure-level spectrum of the signal from the microphone attached on the pipe wall occurs in study of the rotor-stator interaction noise. Both the rotor and stator are two-bladed; hence, the *blade passing frequency* (BPF) is 50Hz with a rotor's rotation at 25Hz.



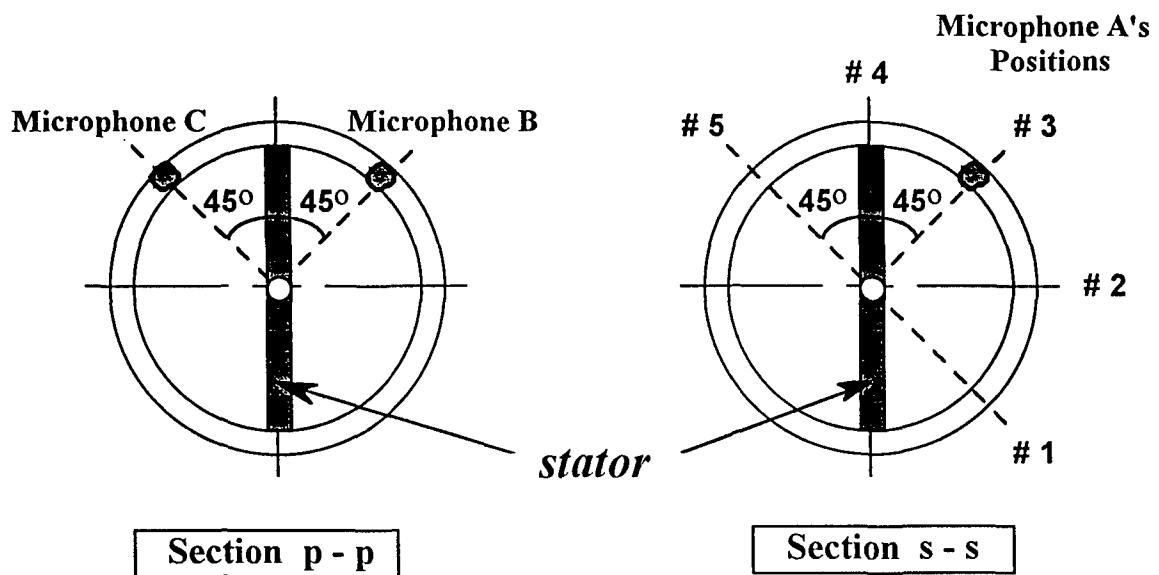


Fig. 2-2 (c)

Fig.2-2 Arrangement of the rotor and stator (a), definitions of phase angle ϕ at 0° and $\pm 180^\circ$ (b), and the microphone measurements (c).

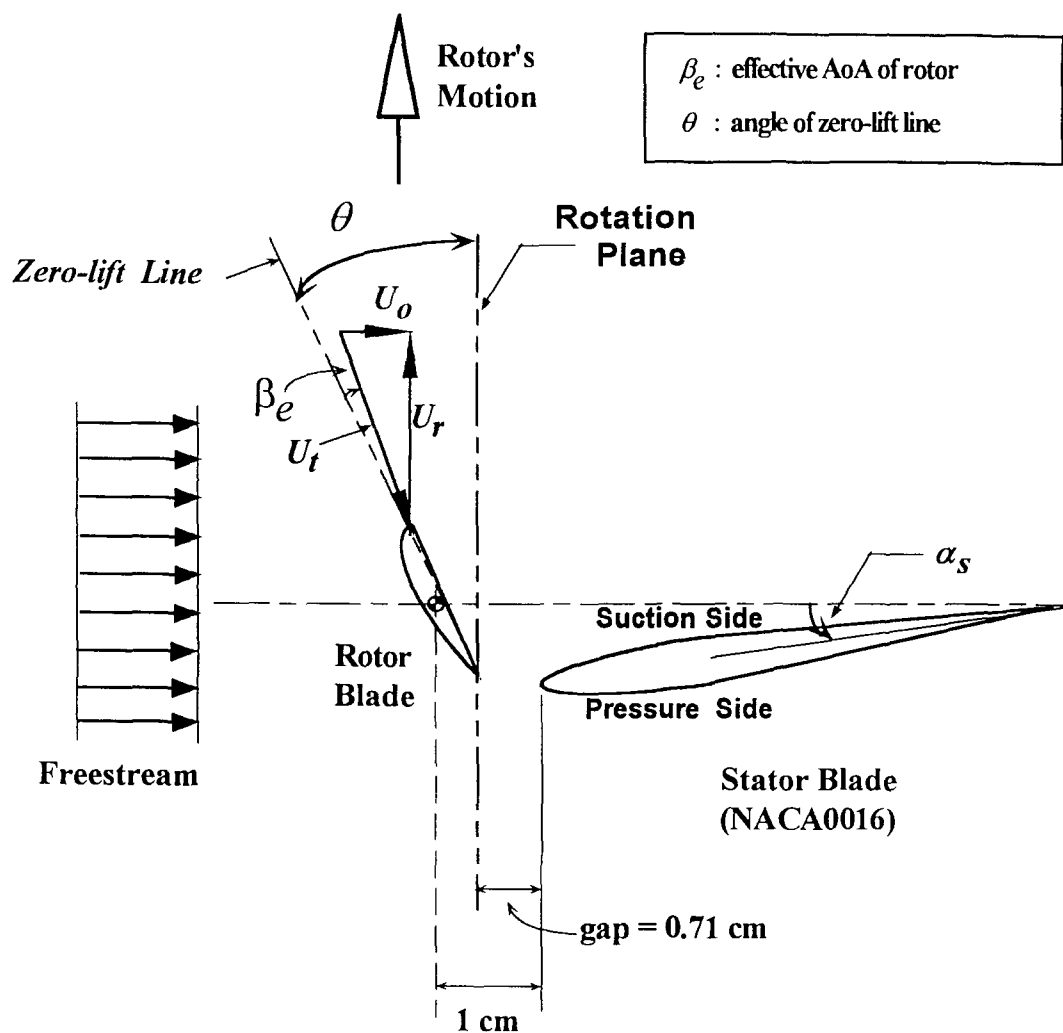


Fig.2-3. Operating condition at 55% radius of the rotor. Note that both α_s and β_e are plotted in the positive sense.

DTIC QUALITY INSPECTED

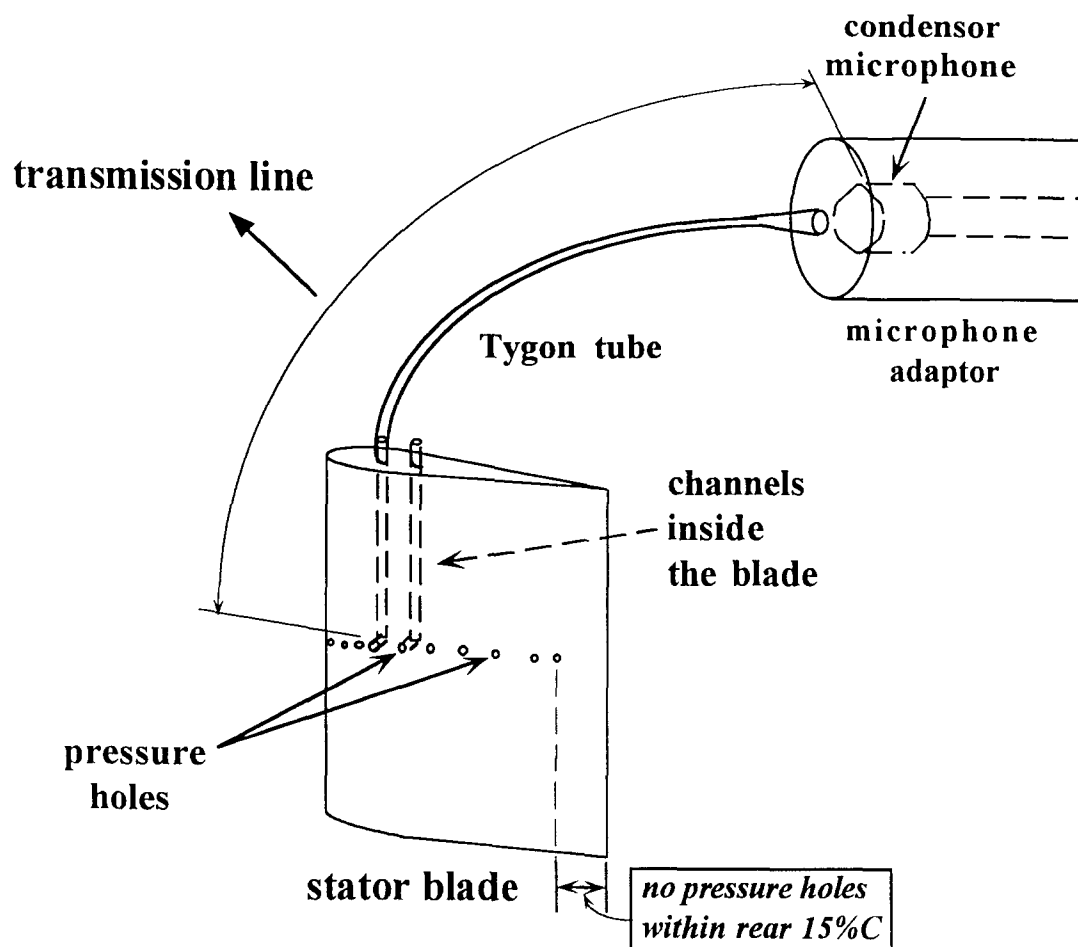


Fig. 2-4(a) Configuration of a transmission line to the stator blade.

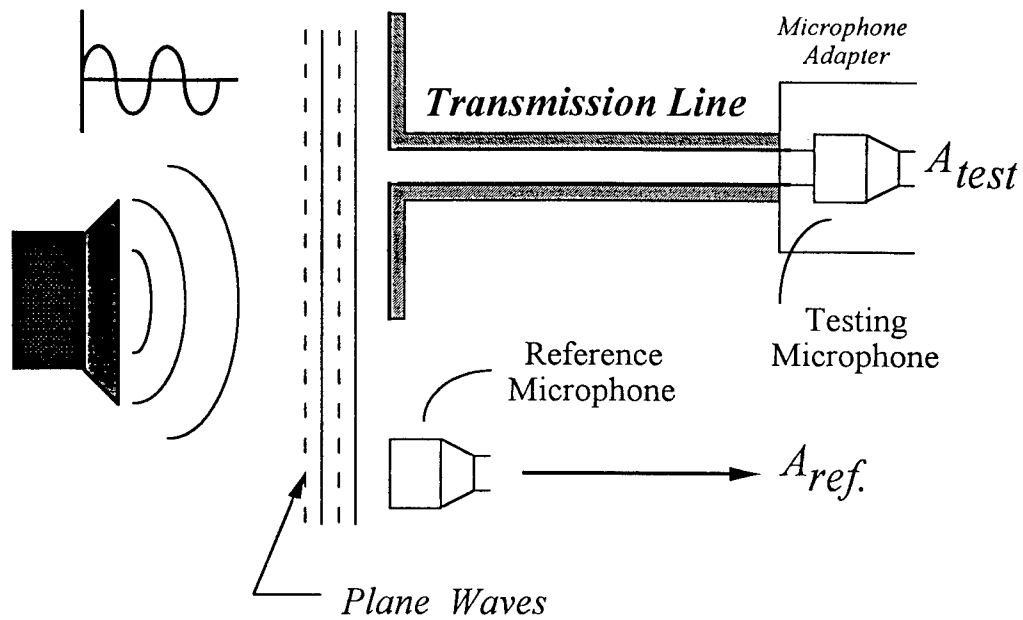


Fig. 2-4(b) A conceptual explanation for obtaining the frequency responses of a transmission line.

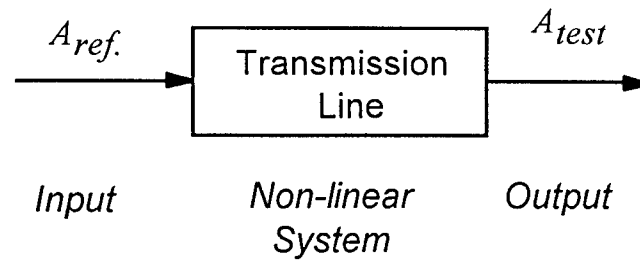


Fig.2-4(c) A single-input / single-output model for the transmission-line system.

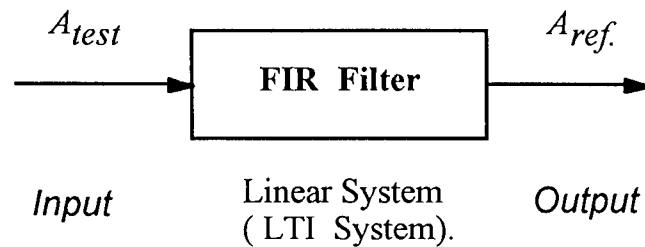
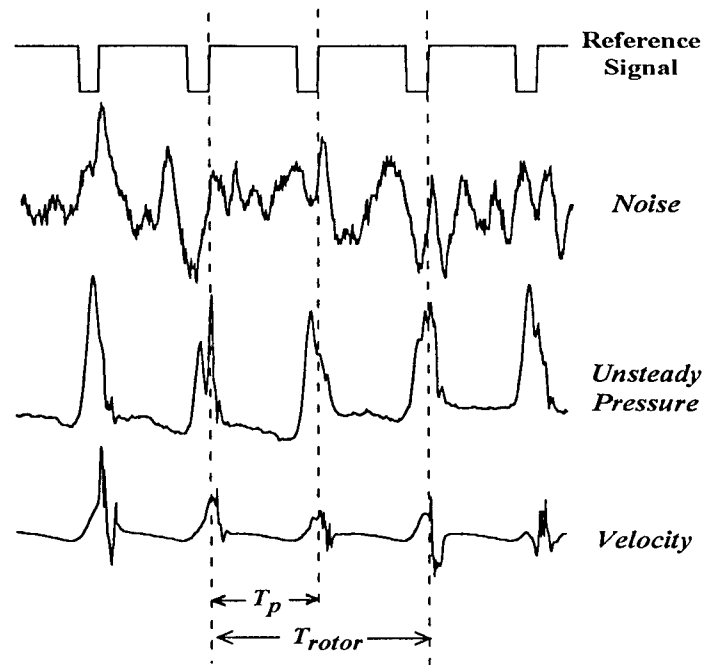
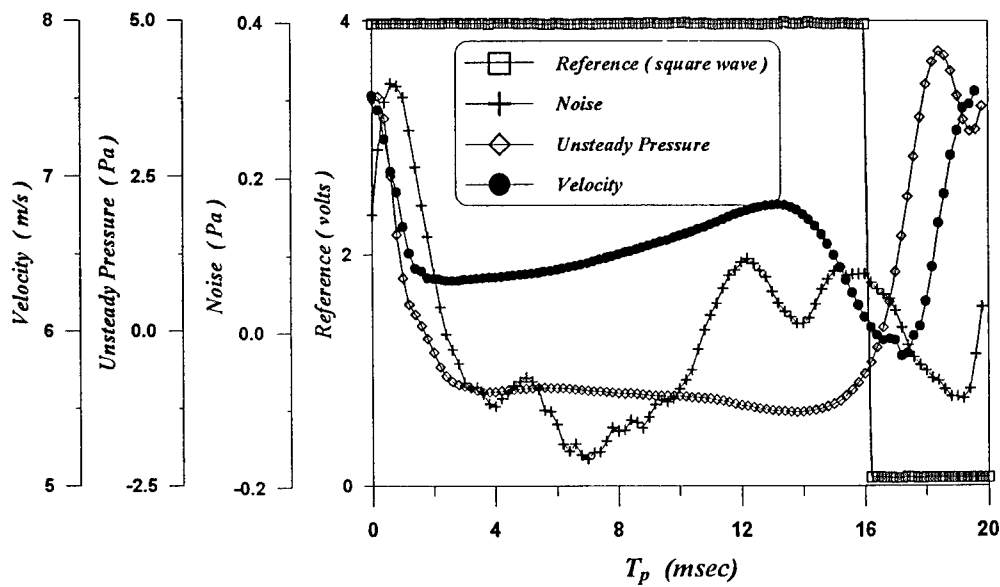


Fig.2-4(d) Compensation of signal by FIR filters.

Fig.2-5 Configuration of the hot-wire probe and the velocity measurement: a typical measuring region on the 55%R cross-section as shown in Fig. 2-2(a).



(a)



(b)

Fig.2-6 (a) Time trace of the reference and the corresponding signals from measurements; (b) phase-averaged results of the signals shown in part (a).

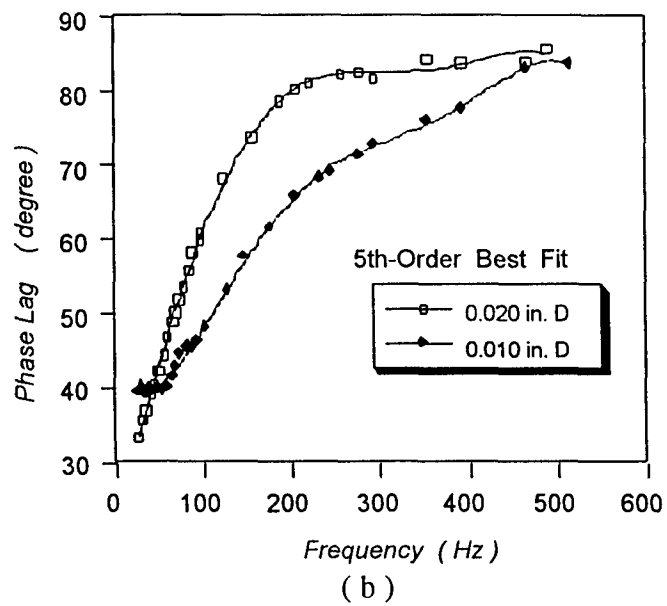
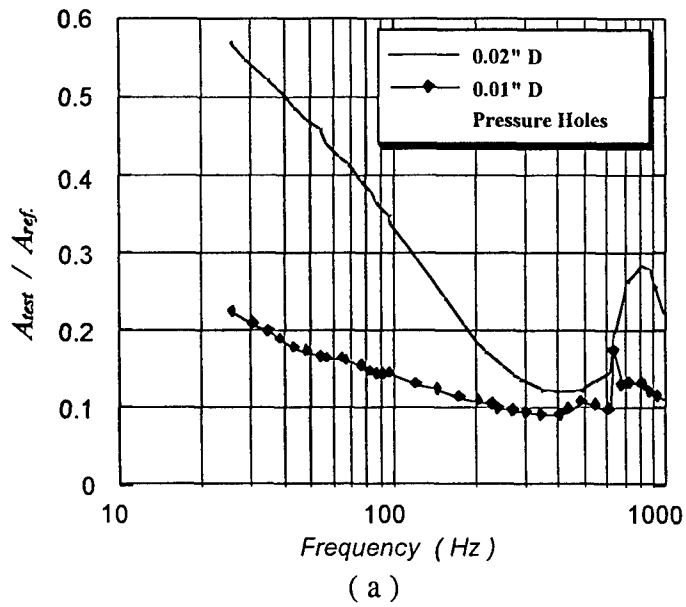


Fig.2-7. Gain and phase responses for two typical pressure holes: diam.= (a) 0.01" (0.254mm) and (b) 0.02" (0.508mm).

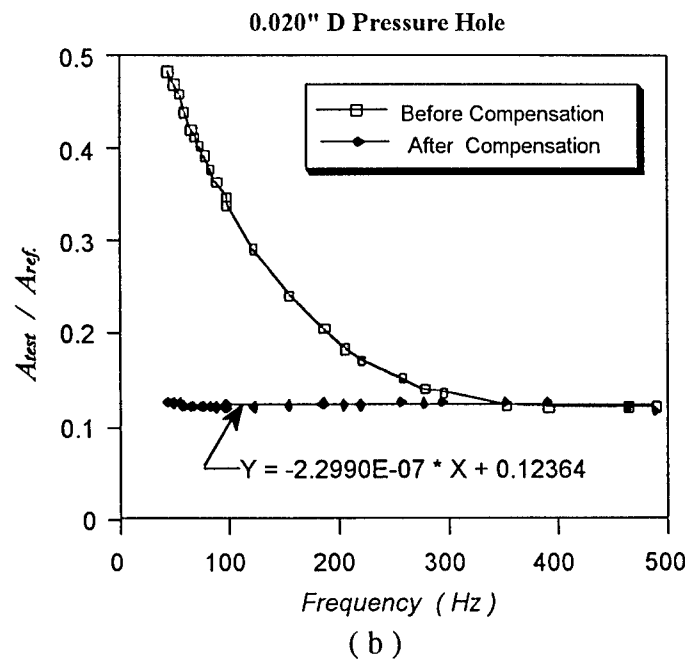
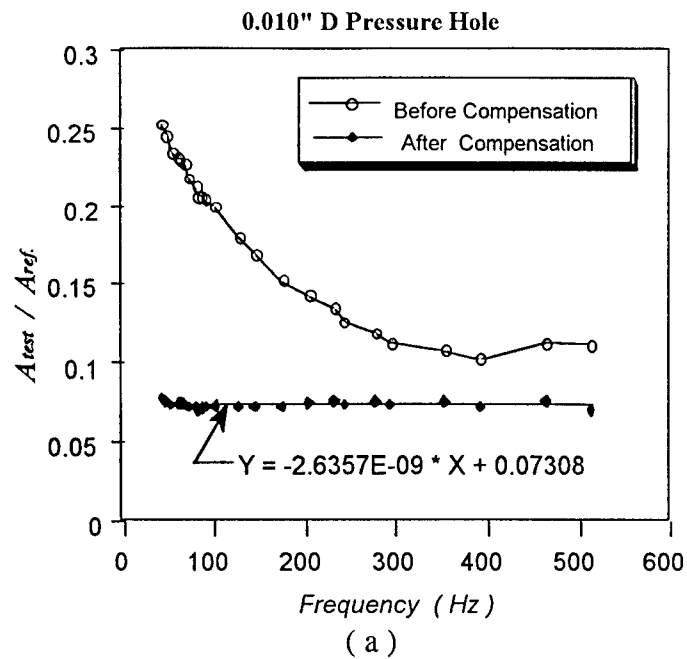


Fig.2-8. Compensation of gain response of transmission lines by FIR filters for two typical pressure holes: (a) 0.01"D, (b) 0.02"D.

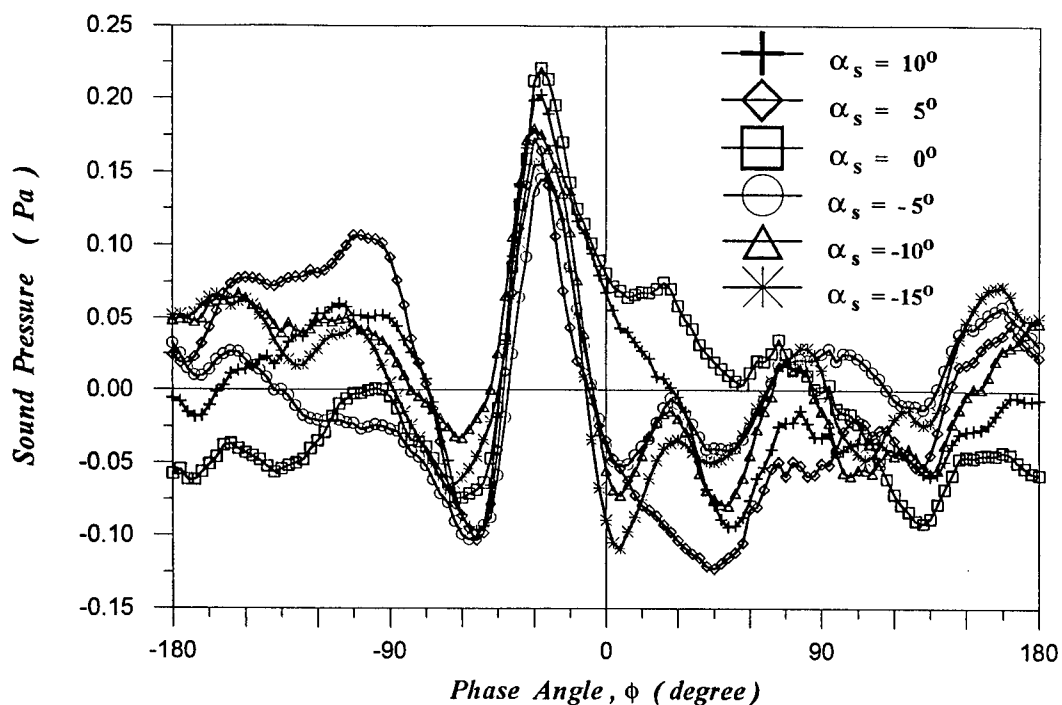


Fig. 3-1(a) ($U_0 = 4.66$ m/s, $U_r@55\%R = 6.11$ m/s : $\beta_e = -11.33^\circ$, $U_t@55\%R = 7.68$ m/s.)

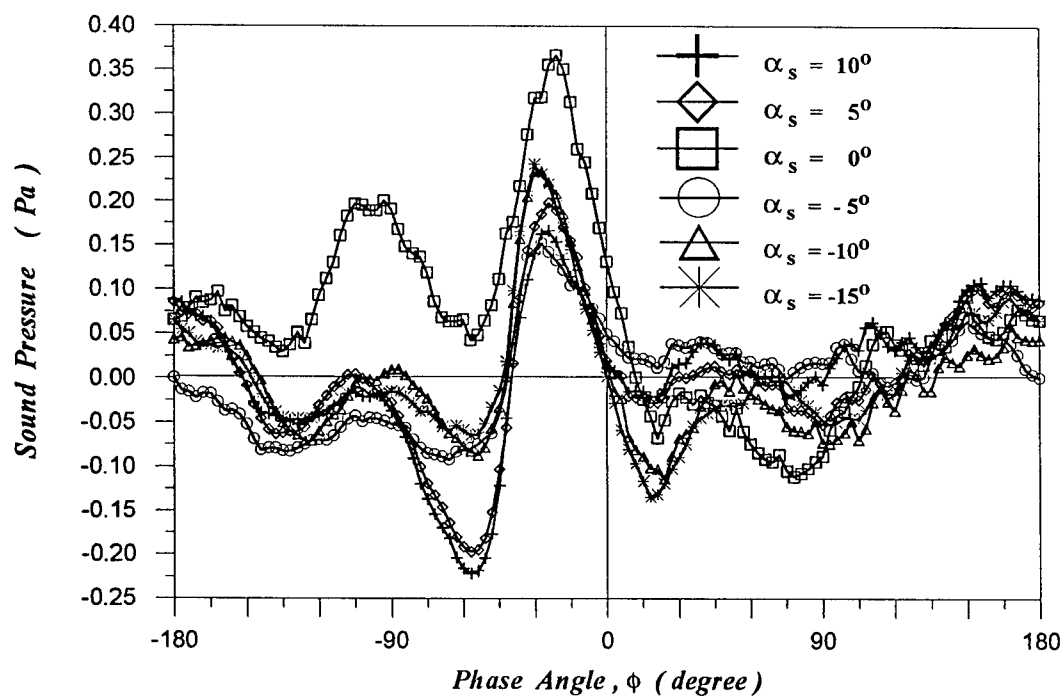


Fig. 3-1(b) ($U_0 = 4.66$ m/s, $U_r@55\%R = 7.65$ m/s : $\beta_e = -5.35^\circ$, $U_t@55\%R = 8.96$ m/s.)

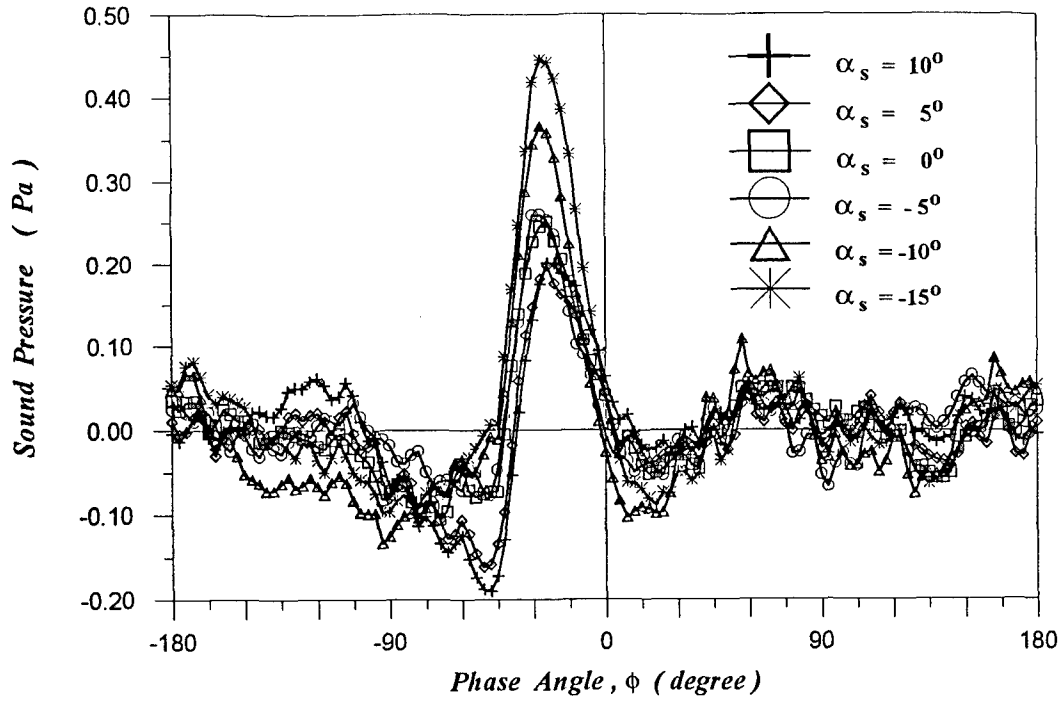


Fig. 3-1(c) ($U_0 = 4.66$ m/s, $U_r@55\%R = 12.23$ m/s : $\beta_e = 5.14^\circ$, $U_t@55\%R = 13.09$ m/s.)

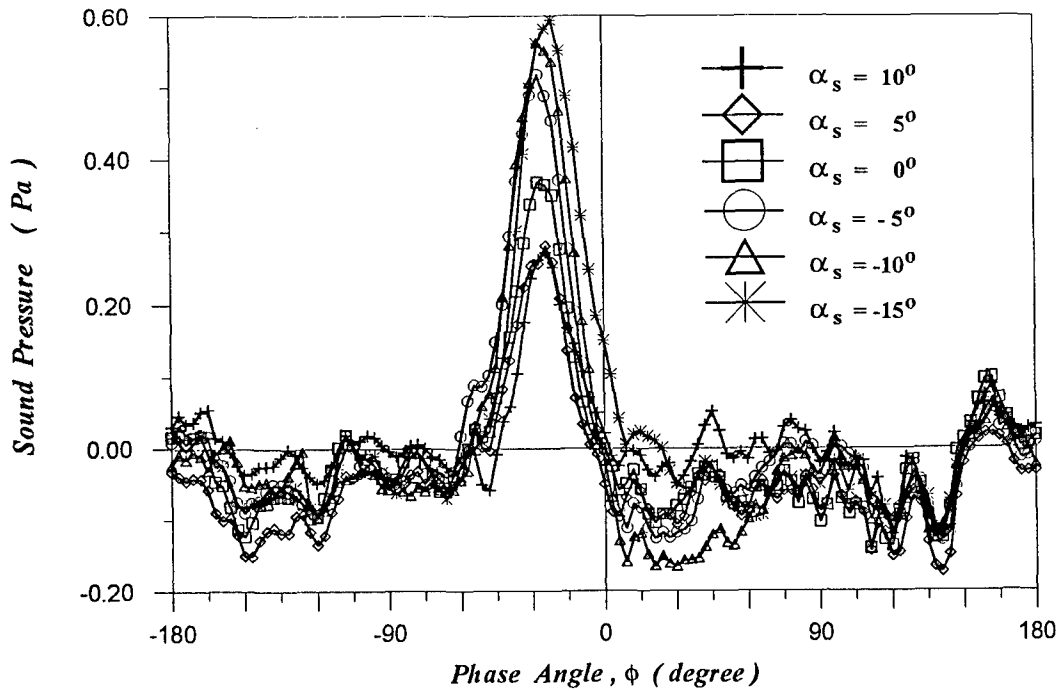


Fig. 3-1(d) ($U_0 = 4.66$ m/s, $U_r@55\%R = 15.29$ m/s : $\beta_e = 9.05^\circ$, $U_t@55\%R = 15.98$ m/s.)

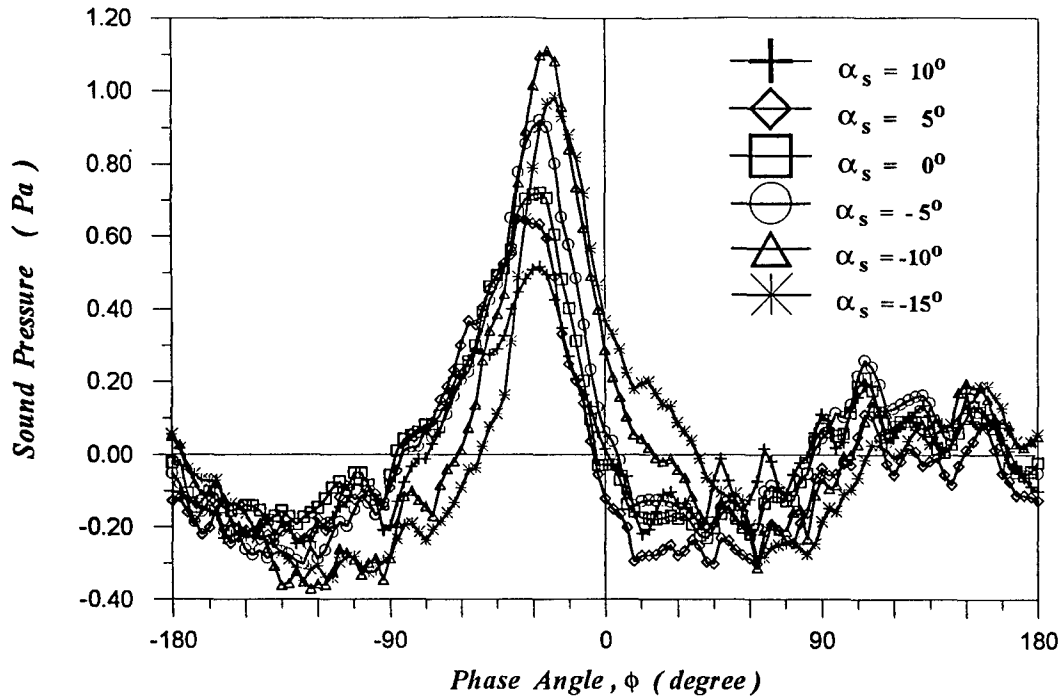


Fig. 3-1(e) ($U_0 = 4.66$ m/s, $U_r@55\%R = 19.11$ m/s: $\beta_e = 12.30^\circ$, $U_r@55\%R = 19.67$ m/s.)

Fig. 3-1. Noise signatures measured at a constant freestream speed, 4.66 m/s, with five different rotor's speed at 55%R: (a) 6.11, (b) 7.65, (c) 12.23, (d) 15.29 and (e) 19.11 m/s, respectively. The resultant local incident velocities, U_i , are (a) 7.68, (b) 8.96, (c) 13.09, (d) 15.98, and (e) 19.67 m/s, while their corresponding rotor's effective AoA, β_e , are (a) -11.33° , (b) -5.35° , (c) 5.14° , (d) 9.05° and (e) 12.30° , respectively.

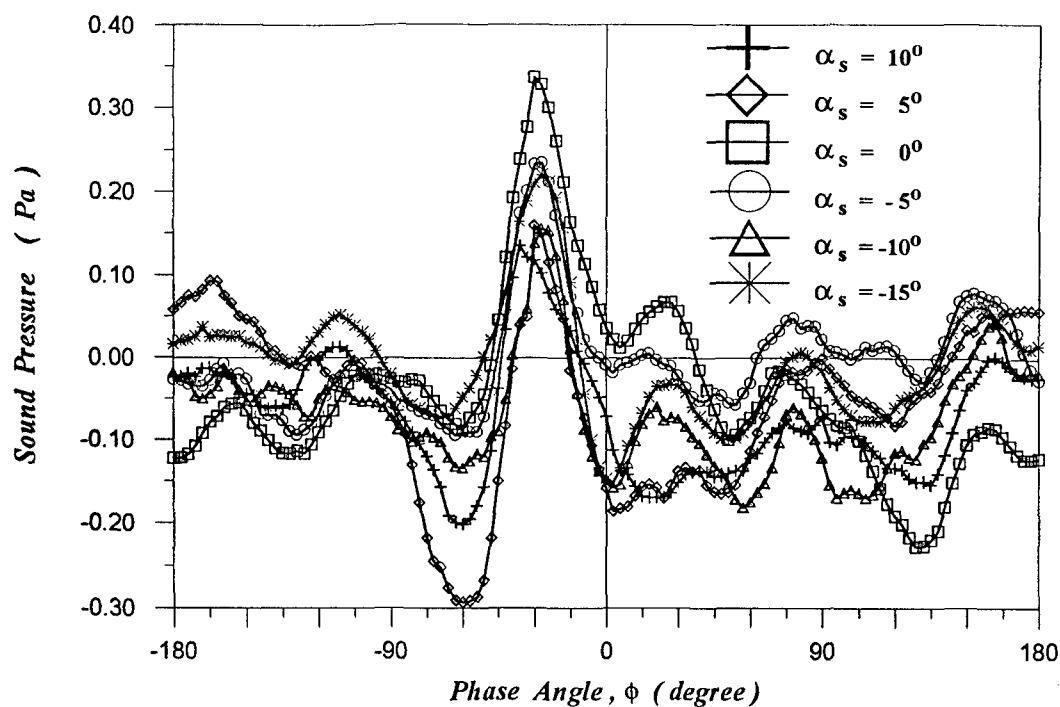


Fig. 3-2(a) ($U_0 = 5.62$ m/s, $U_r@55\%R = 6.11$ m/s : $\beta_e = -16.61^\circ$, $U_f@55\%R = 8.30$ m/s.)

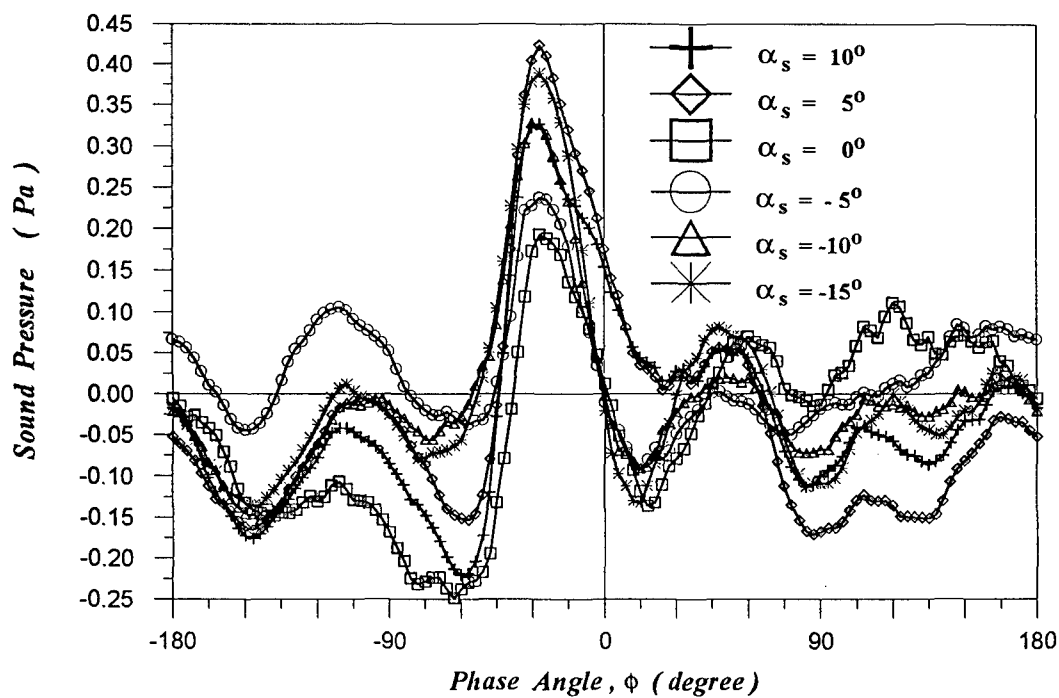


Fig. 3-2(b) ($U_0 = 5.62$ m/s, $U_r@55\%R = 7.65$ m/s : $\beta_e = -10.30^\circ$, $U_f@55\%R = 9.49$ m/s.)

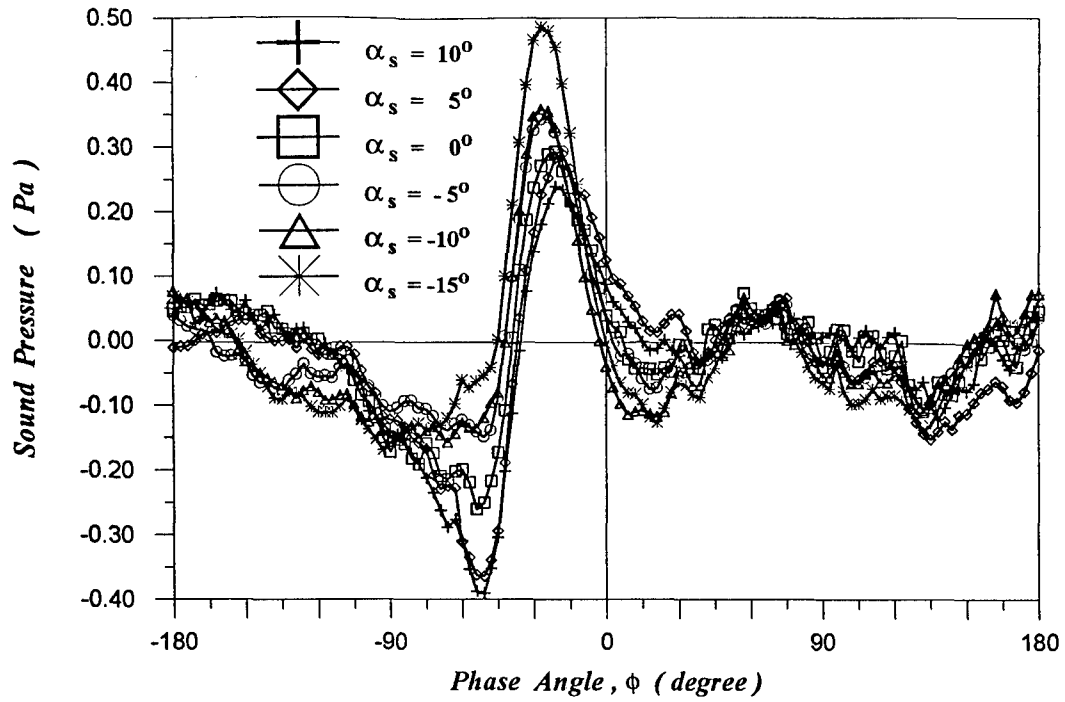


Fig. 3-2(c) ($U_0 = 5.62$ m/s, $U_r@ 55\%R = 12.23$ m/s : $\beta_c = 1.32^\circ$, $U_t@ 55\%R = 13.46$ m/s.)

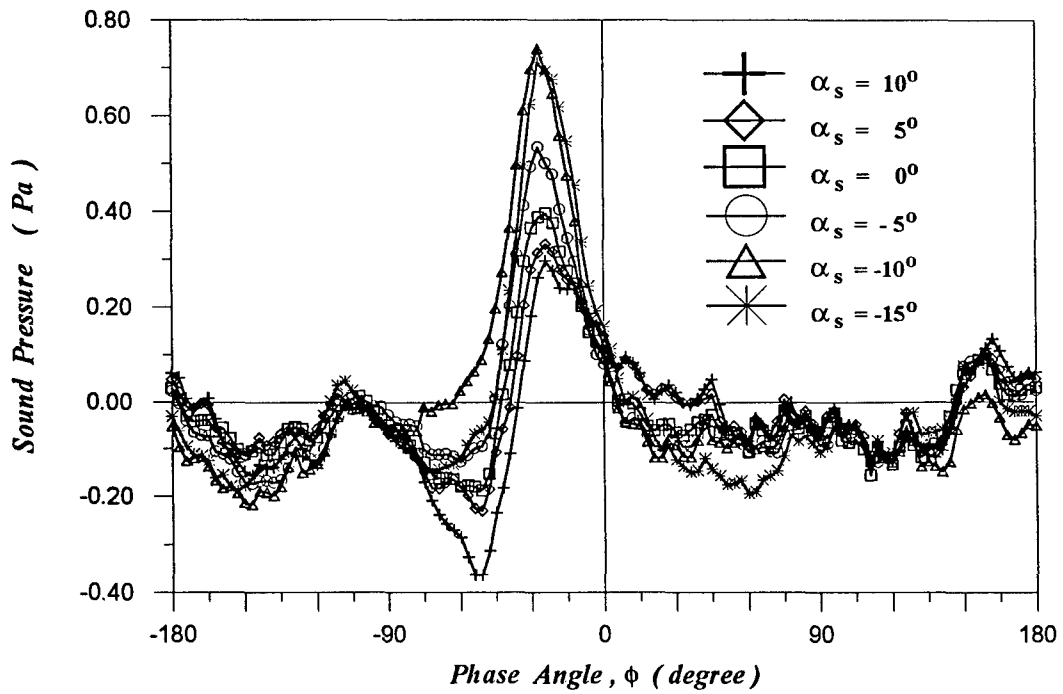


Fig. 3-2(d) ($U_0 = 5.62$ m/s, $U_r@ 55\%R = 15.29$ m/s : $\beta_c = 5.82^\circ$, $U_t@ 55\%R = 16.29$ m/s.)

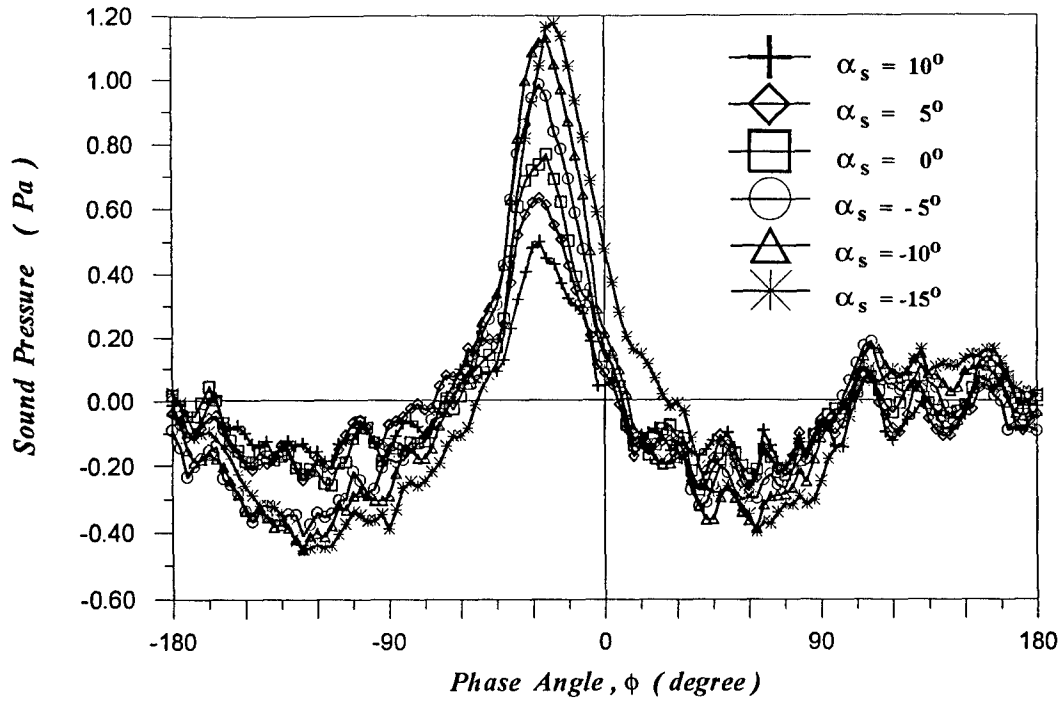


Fig. 3-2(e) ($U_0 = 5.62$ m/s, $U_r@55\%R = 19.11$ m/s : $\beta_e = 9.61^\circ$, $U_r@55\%R = 19.92$ m/s.)

Fig. 3-2. Noise signatures measured at a constant freestream speed, 5.62 m/s, with five different rotor's speed at 55%R: (a) 6.11, (b) 7.65, (c) 12.23, (d) 15.29 and (e) 19.11 m/s, respectively. The resultant local incident velocities, U_i , are (a) 8.30, (b) 9.49, (c) 13.46, (d) 16.29, and (e) 19.92 m/s, while their corresponding rotor's effective AoA, β_e , are (a) -16.61° , (b) -10.30° , (c) 1.32° , (d) 5.82° and (e) 9.61° , respectively.

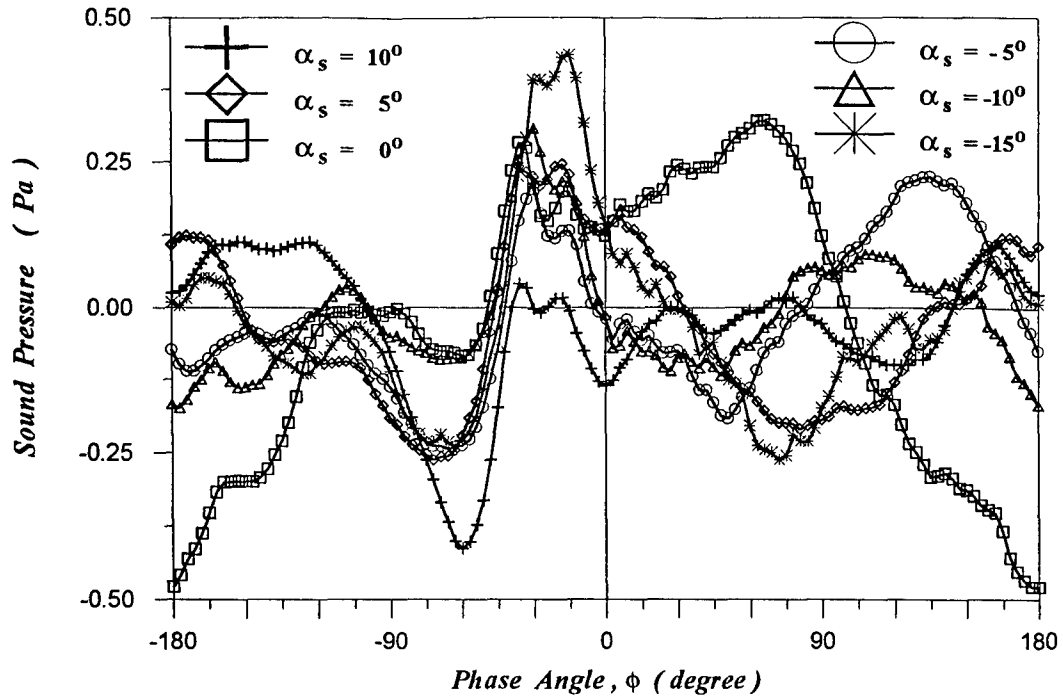


Fig. 3-3(a) ($U_0 = 8.43$ m/s, $U_r@55\%R = 6.11$ m/s : $\beta_c = -28.07^\circ$, $U_t@55\%R = 10.41$ m/s.)

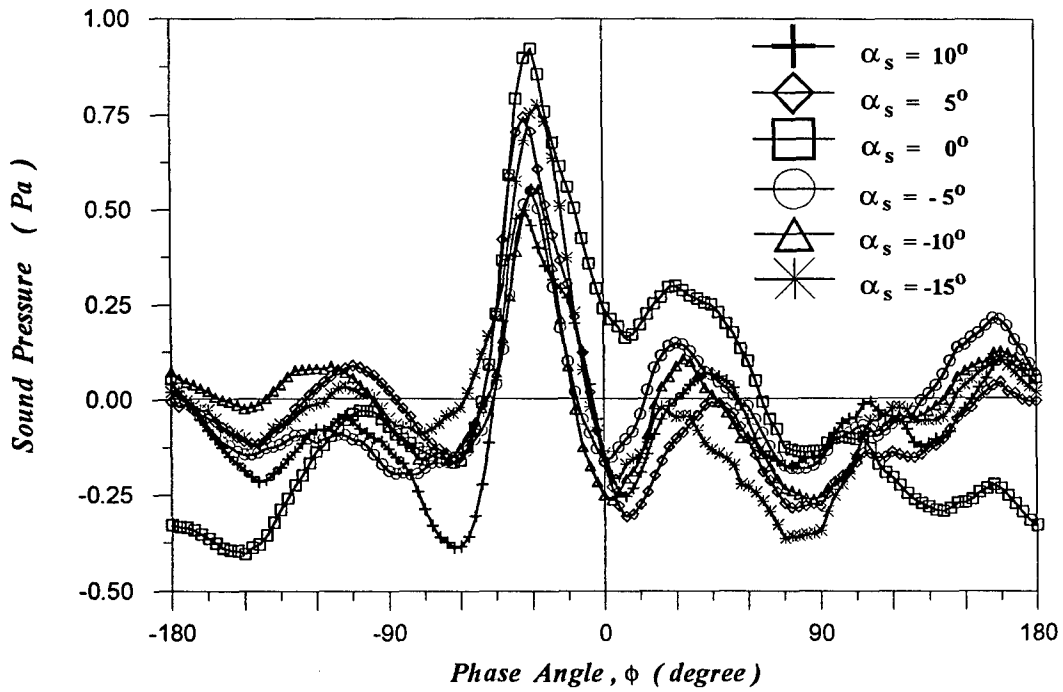


Fig. 3-3(b) ($U_0 = 8.43$ m/s, $U_r@55\%R = 7.65$ m/s : $\beta_c = -21.78^\circ$, $U_t@55\%R = 11.38$ m/s.)

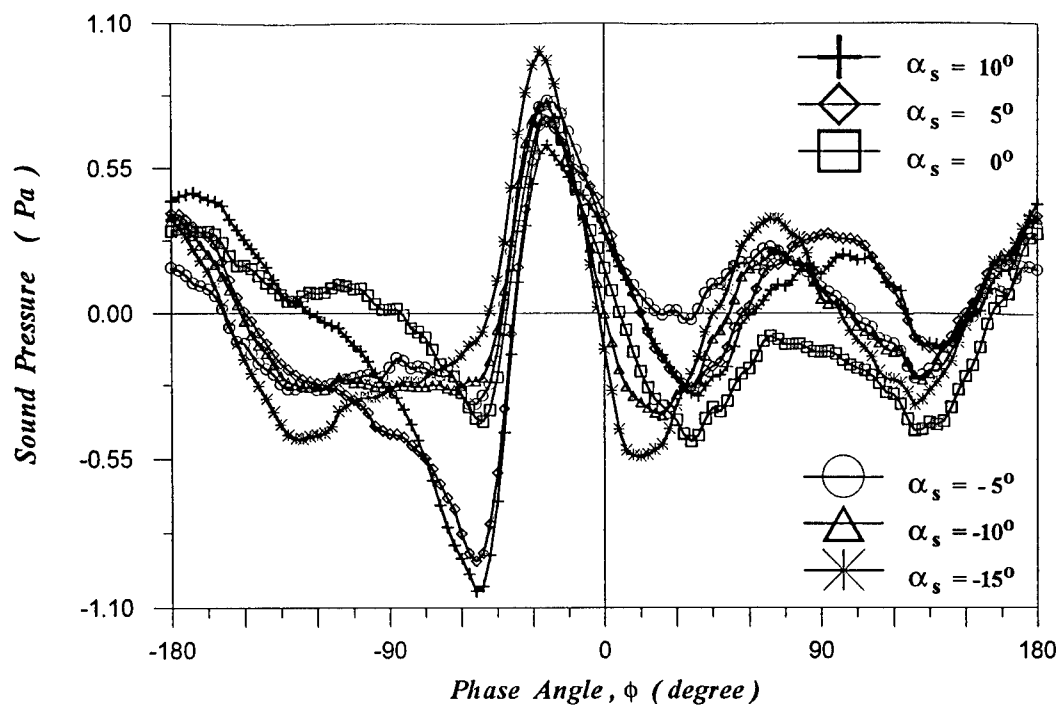


Fig. 3-3(c) ($U_0 = 8.43$ m/s, $U_r@ 55\%R = 12.23$ m/s : $\beta_e = -8.58^\circ$, $U_t@ 55\%R = 14.85$ m/s.)

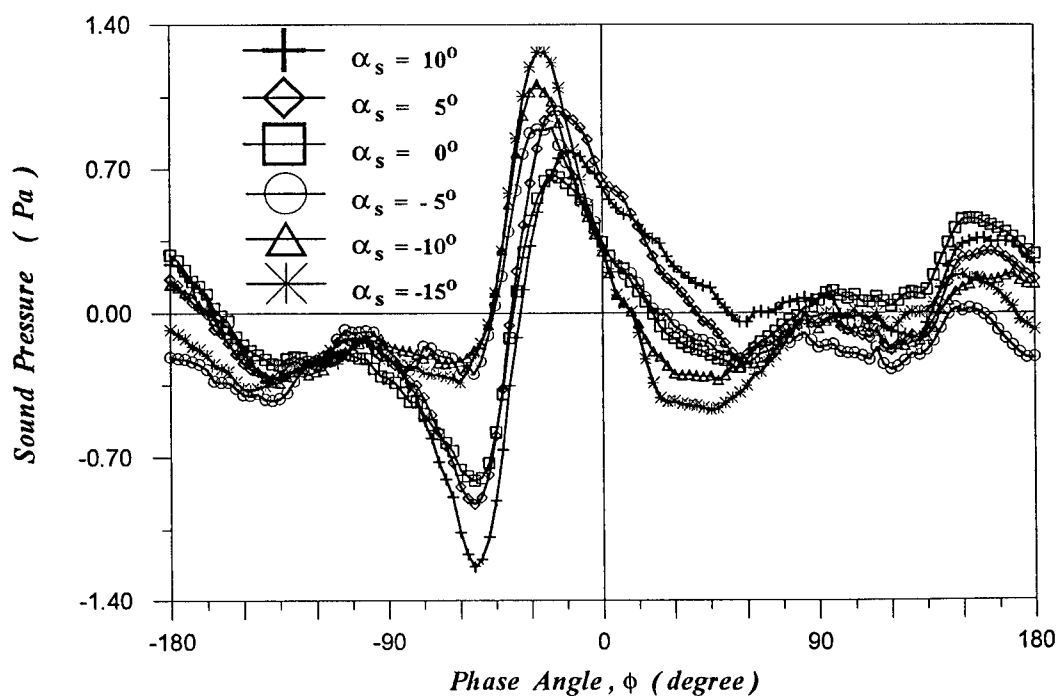


Fig. 3-3(d) ($U_0 = 8.43$ m/s, $U_r@ 55\%R = 15.29$ m/s : $\beta_e = -2.87^\circ$, $U_t@ 55\%R = 17.46$ m/s.)

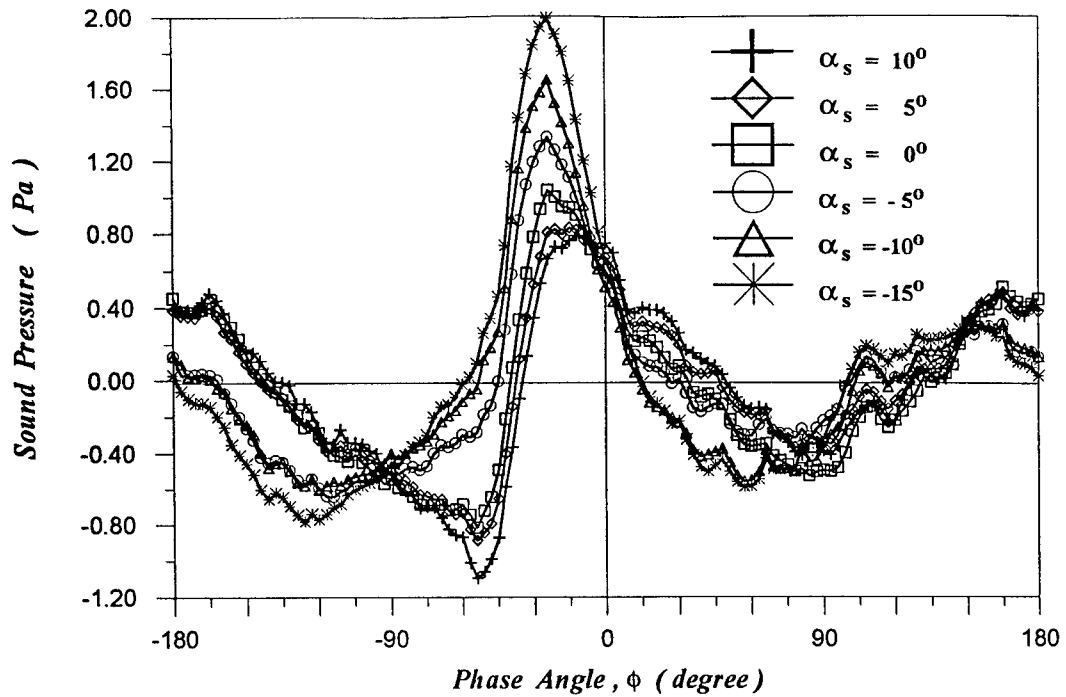


Fig. 3-3(e) ($U_0 = 8.43$ m/s , $U_r@ 55\%R = 19.11$ m/s : $\beta_e = 2.20^\circ$, $U_t@ 55\%R = 20.89$ m/s.)

Fig. 3-3. Noise signatures measured at a constant freestream speed, 8.43 m/s, with five different rotor's speed at 55%R: (a) 6.11, (b) 7.65, (c) 12.23, (d) 15.29 and (e) 19.11 m/s, respectively. The resultant local incident velocities, U_i , are (a) 10.41, (b) 11.38, (c) 14.85, (d) 17.46, and (e) 20.89 m/s, while their corresponding rotor's effective AoA, β_e , are: (a) -28.07° , (b) -21.78° , (c) -8.58° , (d) -2.87° and (e) 2.20° , respectively.

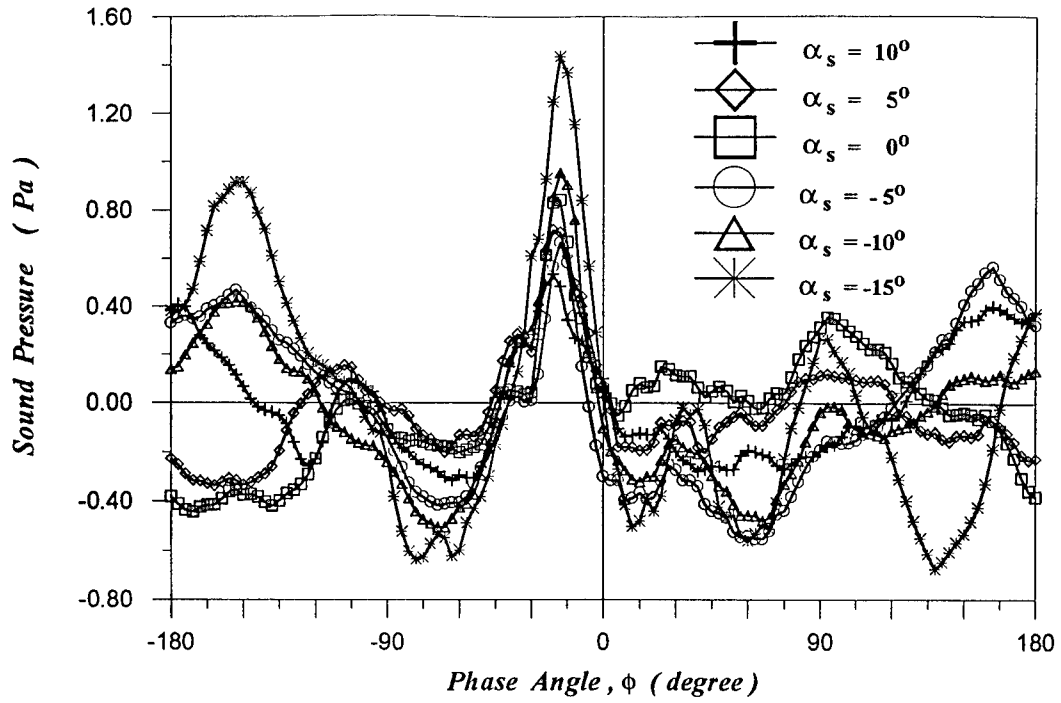


Fig. 3-4(a) ($U_0 = 11.24$ m/s, $U_f@ 55\%R = 6.11$ m/s : $\beta_c = -35.47^\circ$, $U_f@ 55\%R = 12.79$ m/s.)

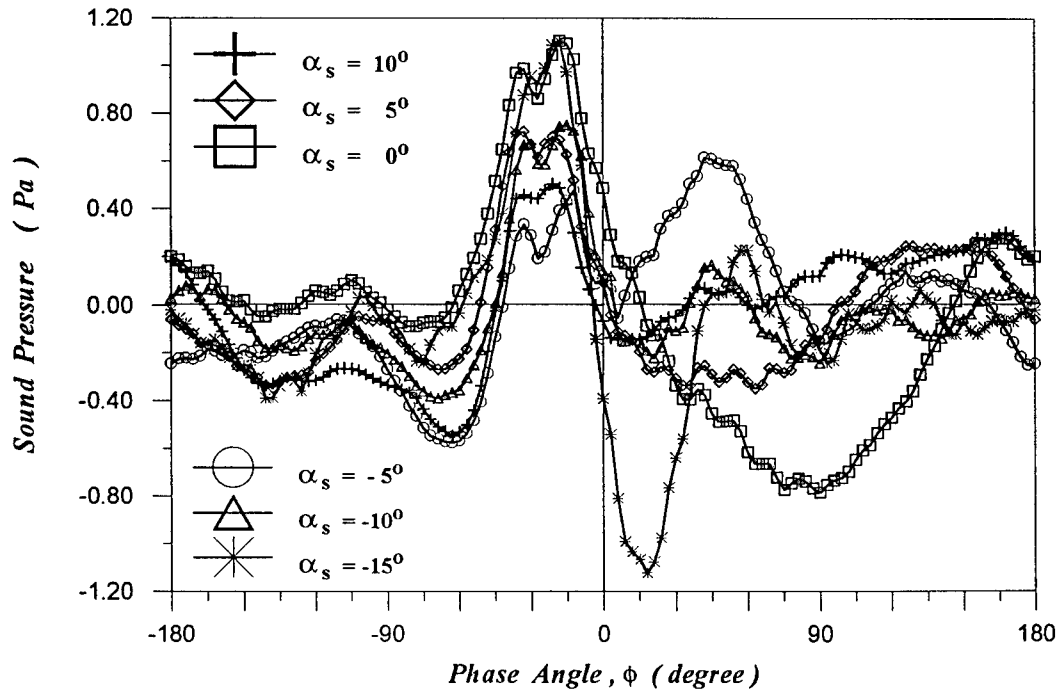


Fig. 3-4(b) ($U_0 = 11.24$ m/s, $U_f@ 55\%R = 7.65$ m/s : $\beta_c = -29.76^\circ$, $U_f@ 55\%R = 13.60$ m/s.)

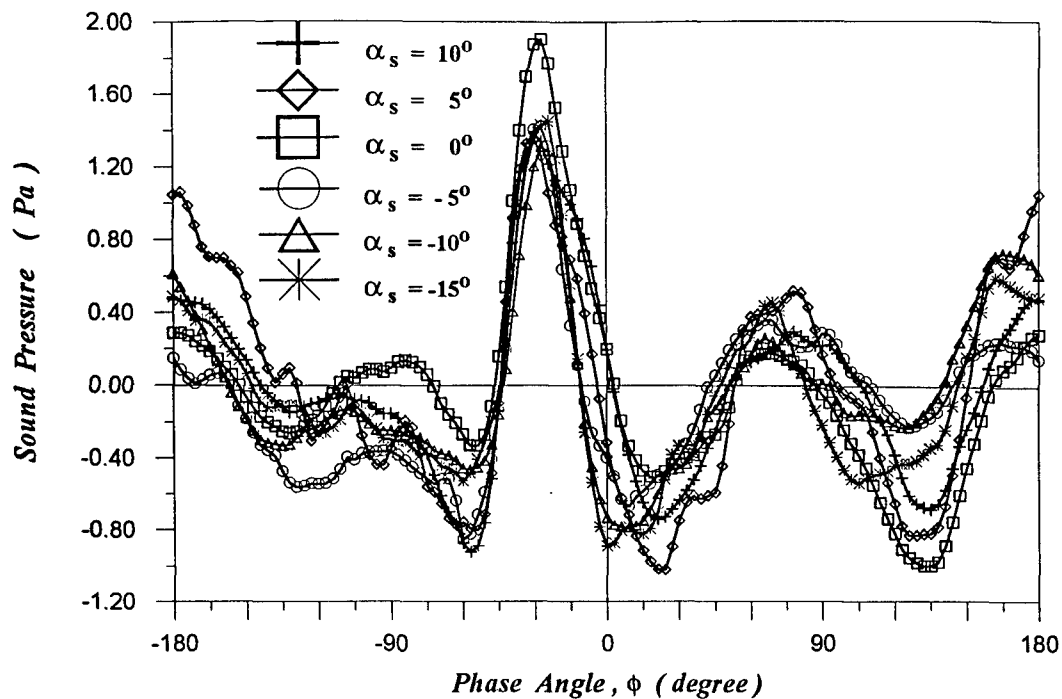


Fig. 3-4(c) ($U_0 = 11.24$ m/s, $U_r@55\%R = 12.23$ m/s: $\beta_e = -16.58^\circ$, $U_t@55\%R = 16.61$ m/s.)

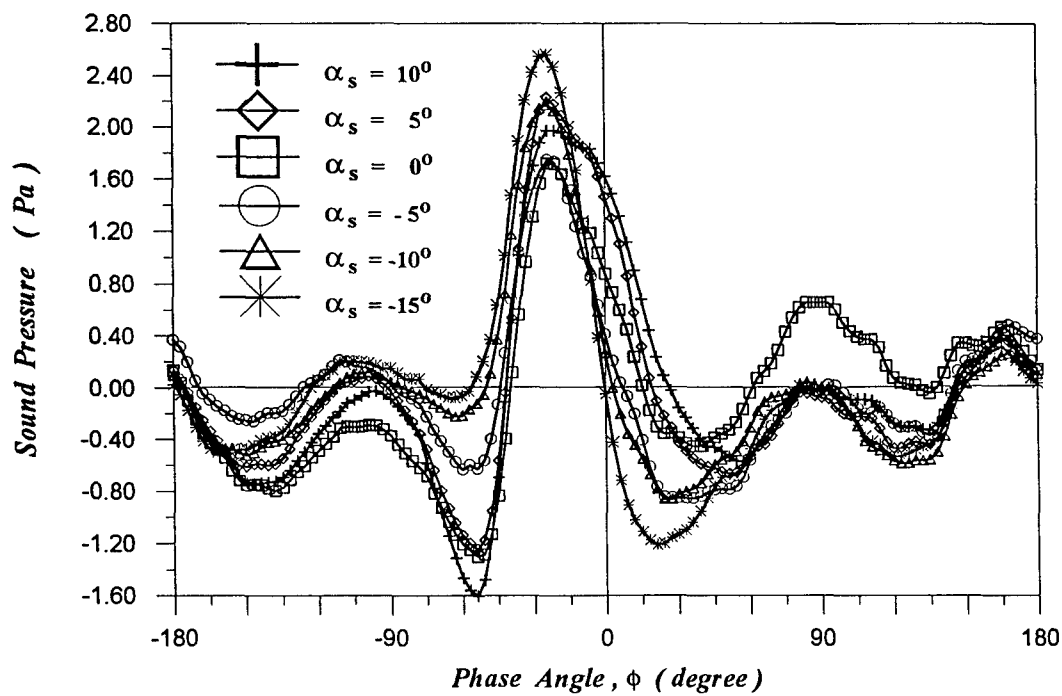


Fig. 3-4(d) ($U_0 = 11.24$ m/s, $U_r@55\%R = 15.29$ m/s: $\beta_e = -10.32^\circ$, $U_t@55\%R = 18.98$ m/s.)

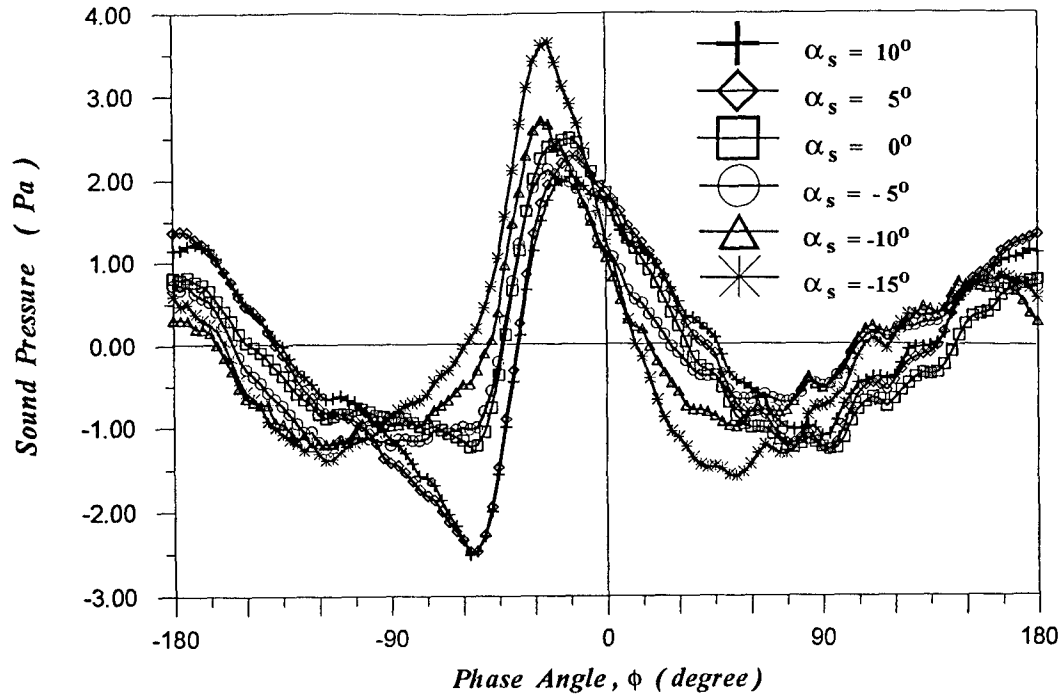


Fig. 3-4(e) ($U_0 = 11.24$ m/s, $U_r@55\%R = 19.11$ m/s: $\beta_e = -4.46^\circ$, $U_t@55\%R = 22.17$ m/s.)

Fig. 3-4. Noise signatures measured at a constant freestream speed, 11.24 m/s, with five different rotor's speed at 55%R: (a) 6.11, (b) 7.65, (c) 12.23, (d) 15.29 and (e) 19.11 m/s, respectively. The resultant local incident velocities, U_i , are (a) 12.79, (b) 13.60, (c) 16.61, (d) 18.98, and (e) 22.17 m/s, while their corresponding rotor's effective AoA, β_e , are: (a) -35.47° , (b) -29.76° , (c) -16.58° , (d) -10.32° and (e) -4.46° , respectively.

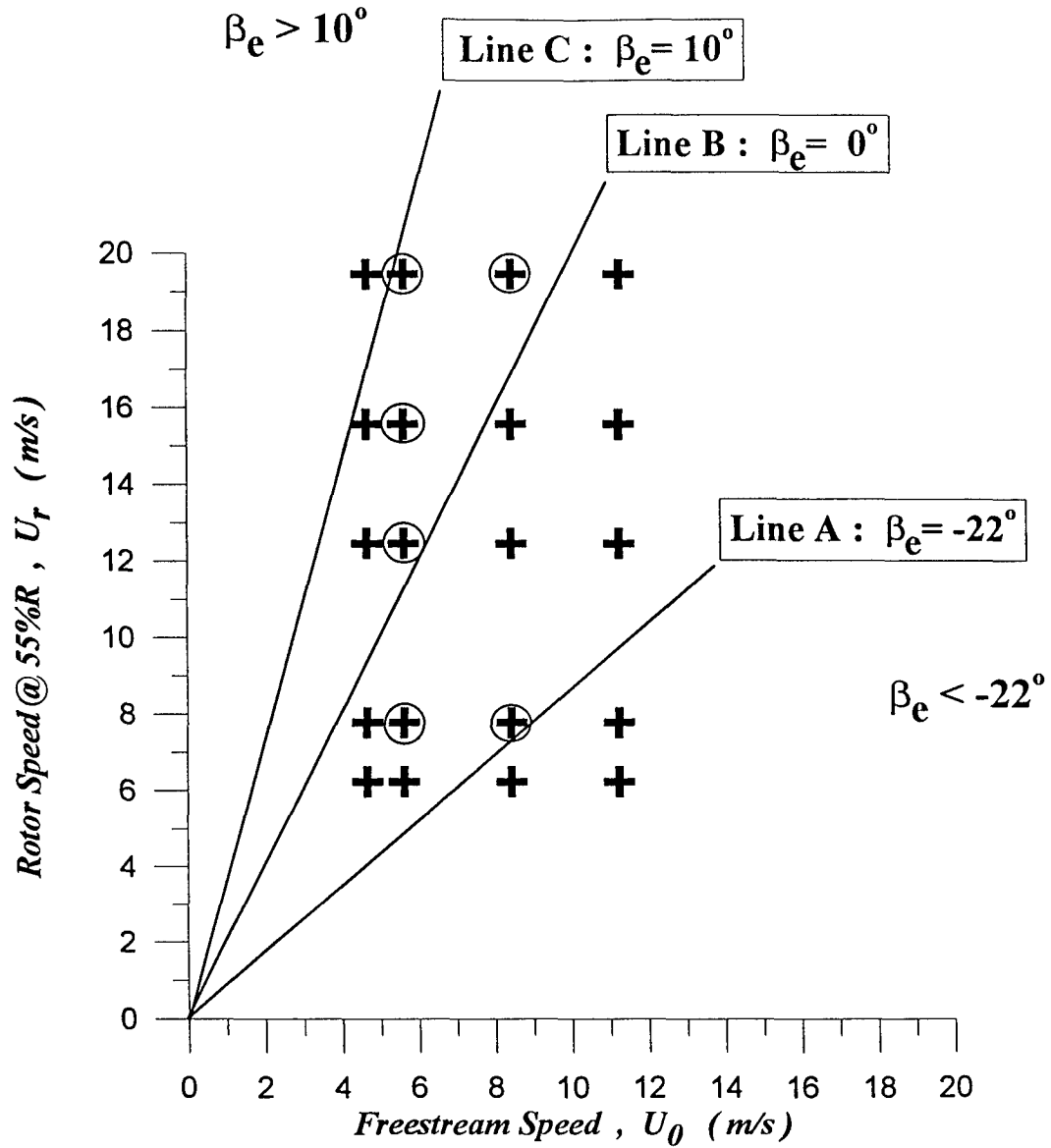


Fig. 3-5. A schematic classification by β_e on a U_0 - U_r plot: along Line A, $\beta_e = -22^\circ$; along Line B, $\beta_e = 0^\circ$; and, along Line C, $\beta_e = 10^\circ$. The cross symbol represents the operating-condition setup for noise measurements, while the circle symbols are related to the setup of surface pressure and velocity measurements in the following chapters.

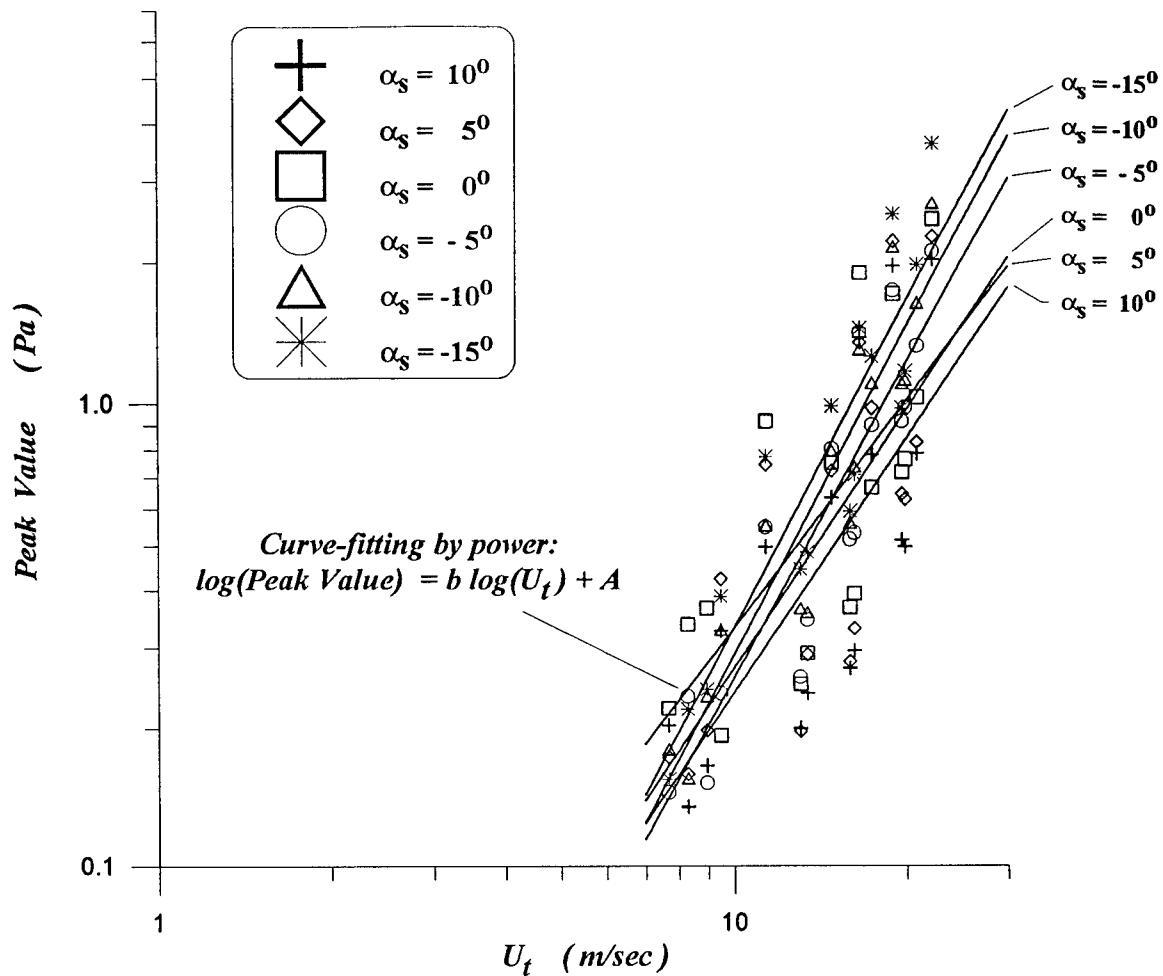


Fig. 3-6. Peak values of noise vs. the resultant speed, U_t , for cases: $\beta_t > -22^\circ$. For a fixed stator's AoA, the peak-value data are *curve-fitted by power*, $\log(\text{Peak Value}) = b \log(U_t) + A$ or $(\text{Peak Value}) = aU_t^b$, where power b represents the slope of each line in the log-log plot. Note that an average value of the power b 's is 2 for U_t .

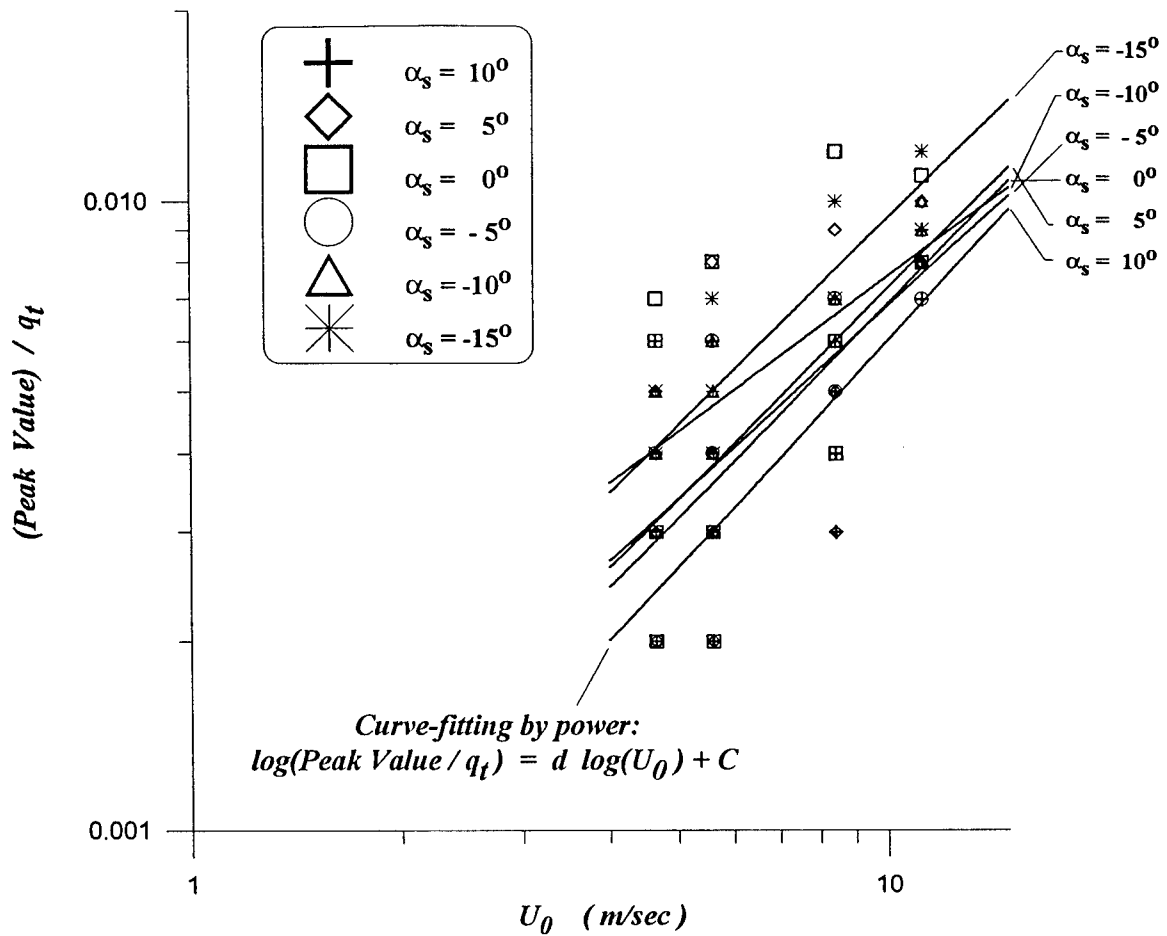


Fig. 3-7. Non-dimensionalized peak values of noise vs. the freestream speed, U_0 , for cases: $\beta_s > -22^\circ$. For a fixed stator's AoA, the peak-value data are *curve-fitted by power*, $\log(\text{Peak Value} / q_t) = d \log(U_0) + C$ or $(\text{Peak Value} / q_t) = c U_0^d$, where power d represents the slope of each line in the log-log plot, where q_t is the local dynamic pressure defined as $\frac{1}{2} \rho U_t^2$ and U_t is the resultant speed. Note that an average value of the power d 's is 1 for U_0 .

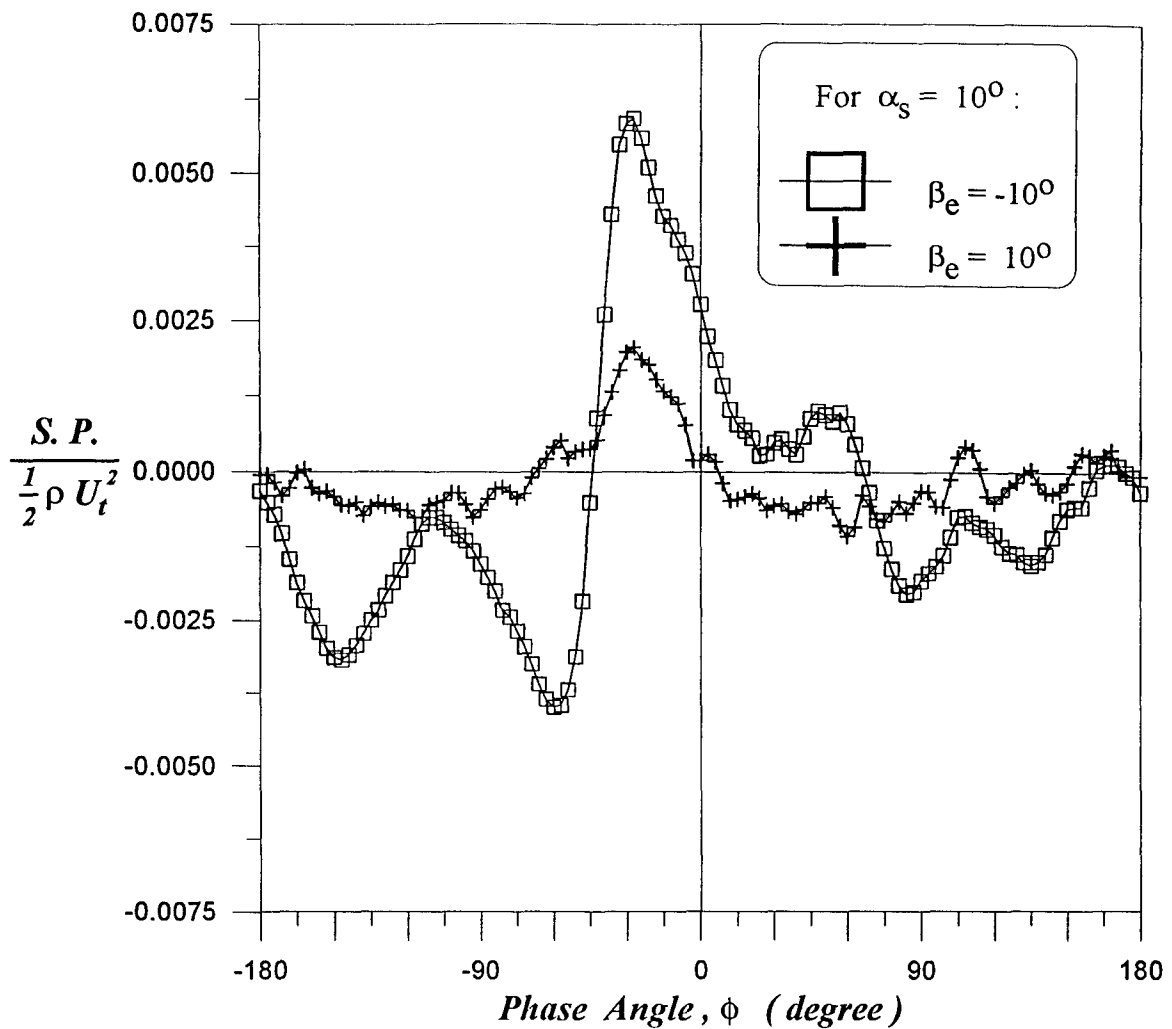


Fig. 3-8. Two typical noise patterns in cases: $\beta_e = \pm 10^\circ$, for $\alpha_s = 10^\circ$. For the case $\beta_e = -10^\circ$, the noise reaches a valley at $\phi = -60^\circ$, and then rises abruptly to a peak at $\phi = -30^\circ$. However, for the case $\beta_e = 10^\circ$, the noise rises gradually from a valley at $\phi = -90^\circ$, and then, after reaching a higher-noise level at $\phi = -48^\circ$, increases rapidly to a peak at $\phi = -30^\circ$.

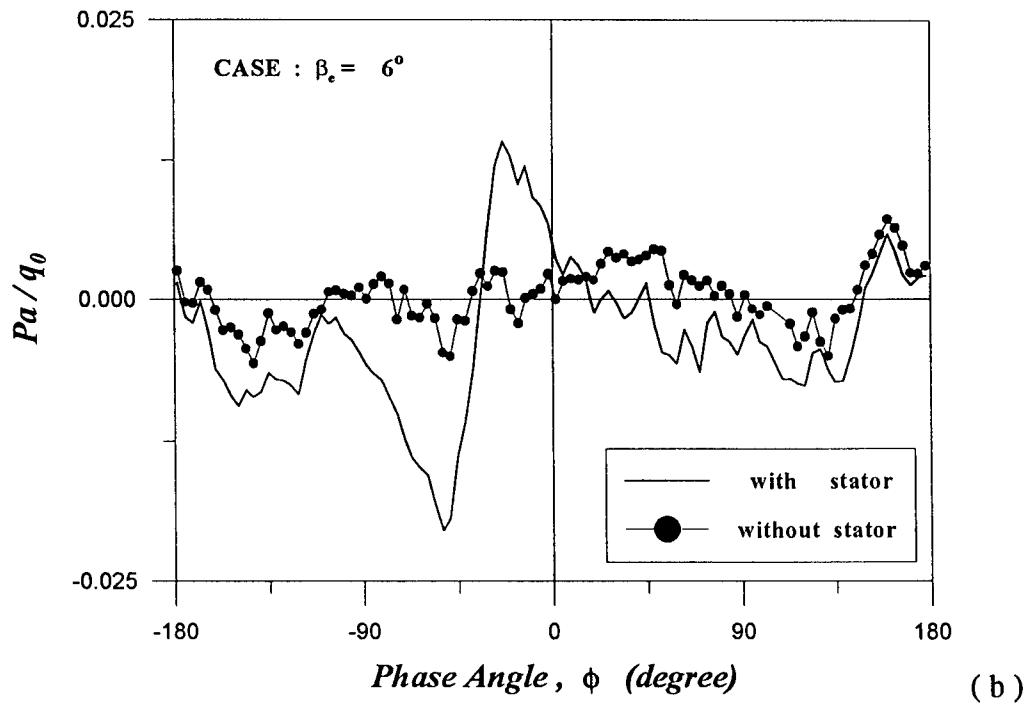
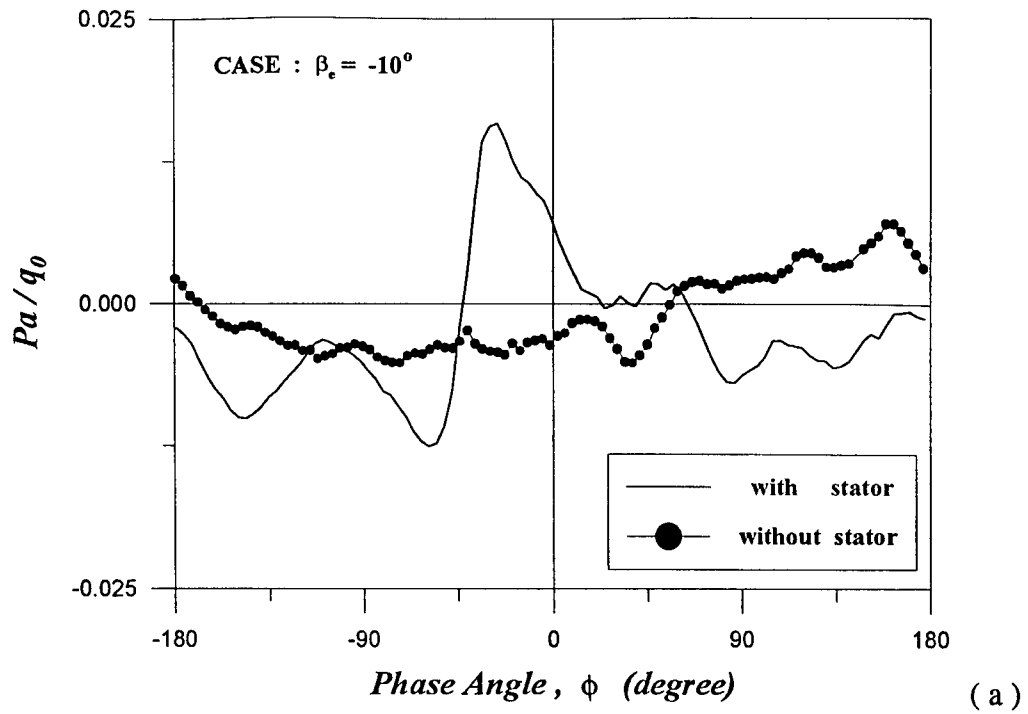
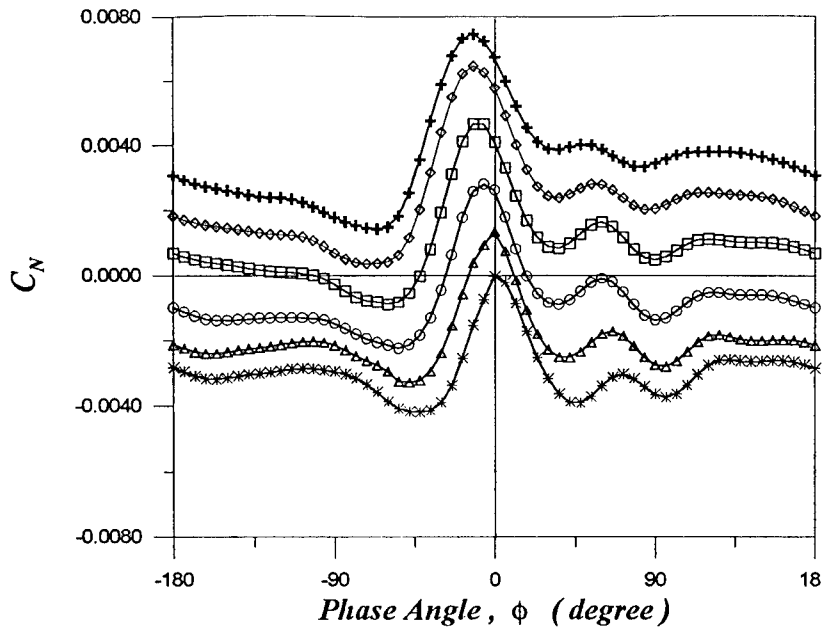
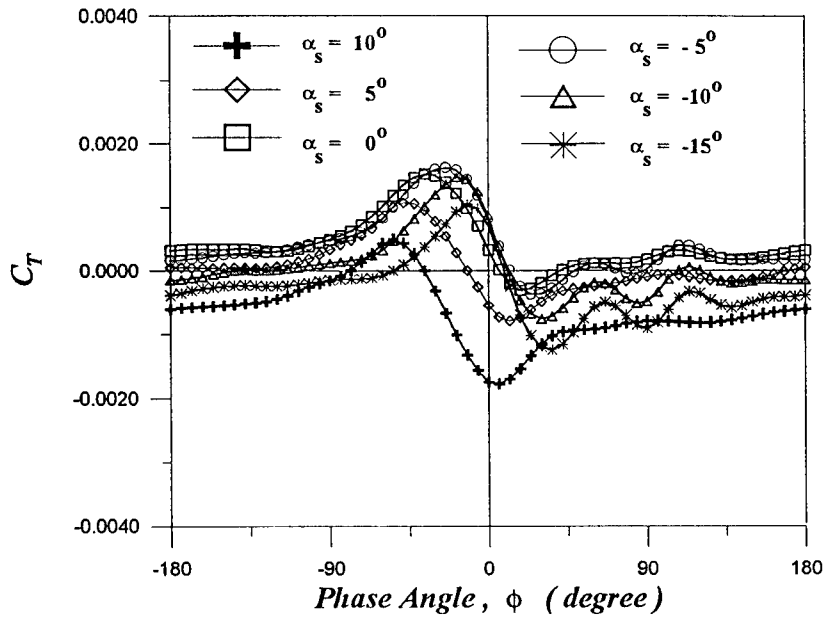


Fig.3-9. Noise signatures *with* and *without* the presence of stator for both cases: $\beta_e =$ (a) -10.30° and (b) 5.82° .



(a)



(b)

Fig. 4-2. Time traces of (a) the normal force coefficient, C_N , and (b) the tangential force coefficient, C_T : for $\beta_e = -21.78^\circ$ and with six stator's AoA α_s 's.

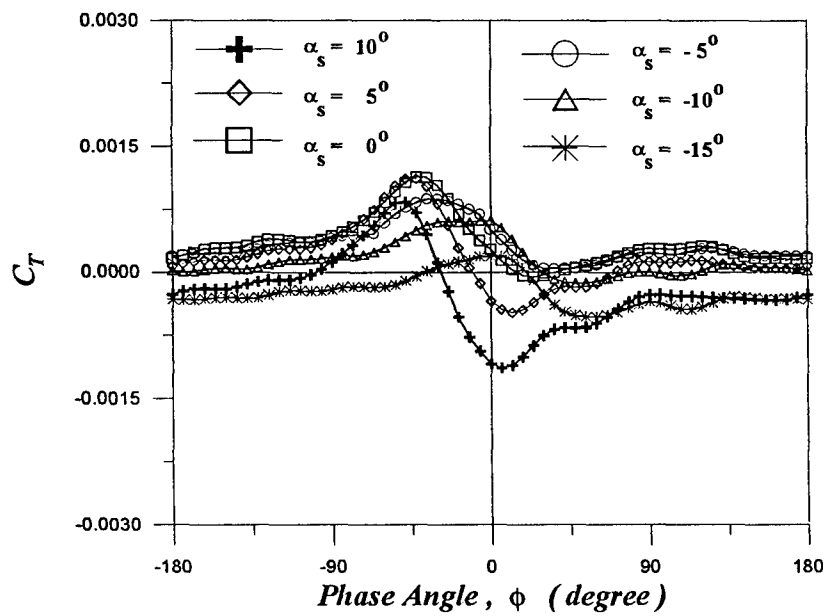
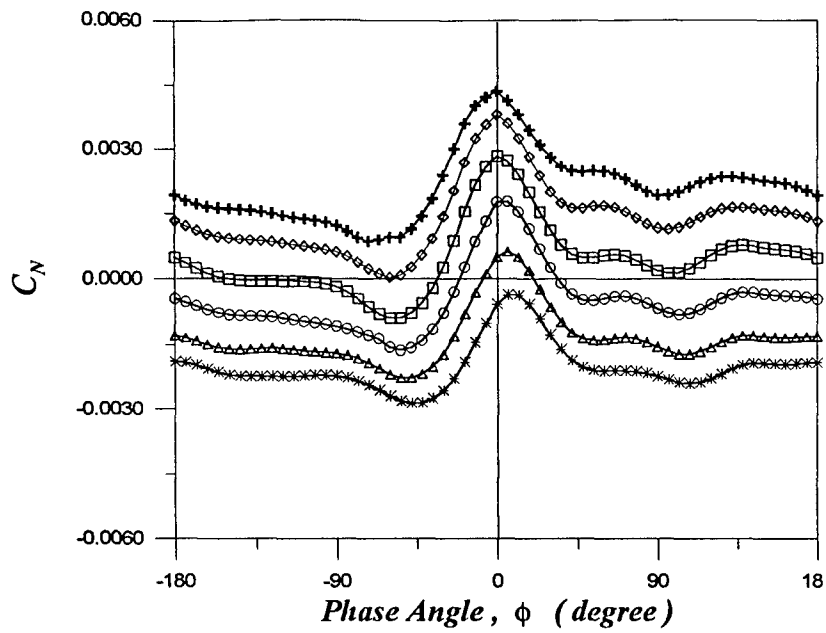
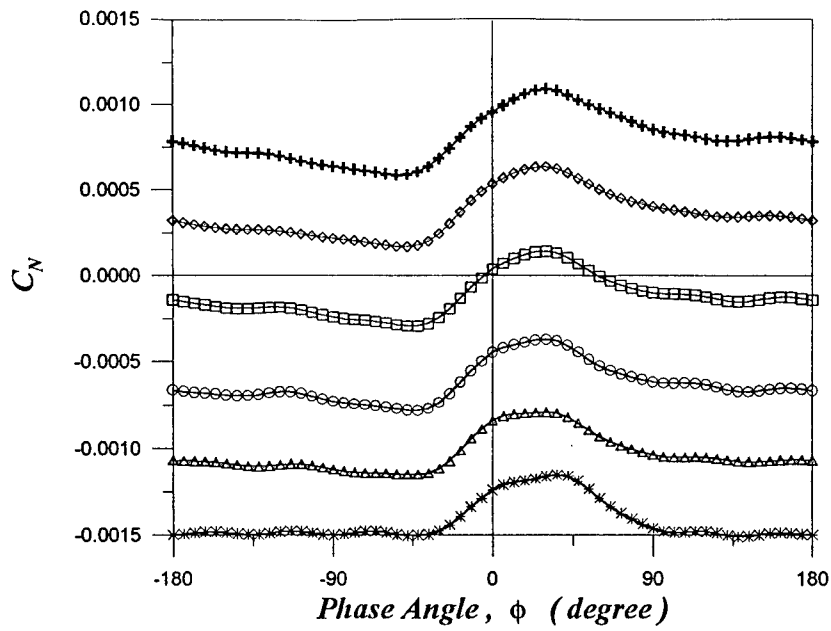
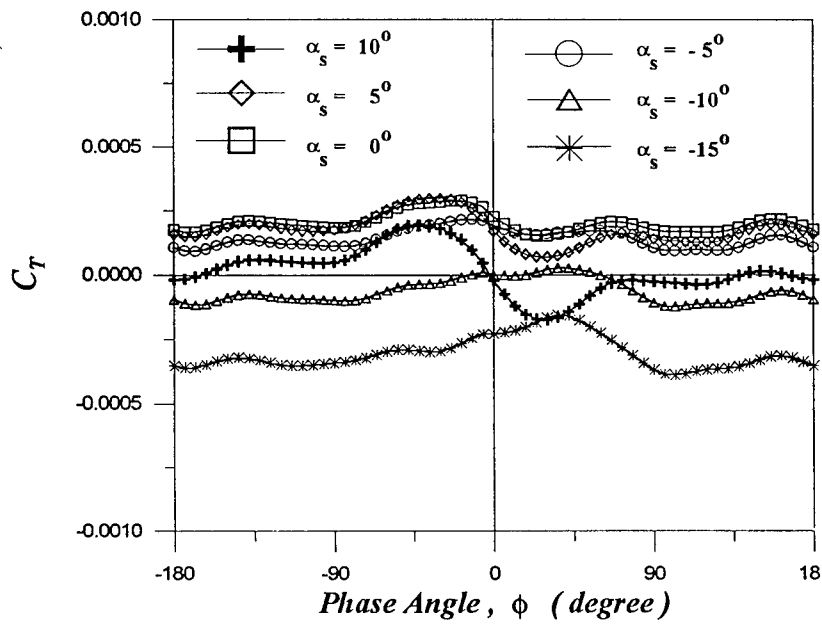


Fig. 4-3. Time traces of (a) the normal force coefficient, C_N , and (b) the tangential force coefficient, C_T : for $\beta_t = -10.30^\circ$ and with six stator's AoA α_s 's.

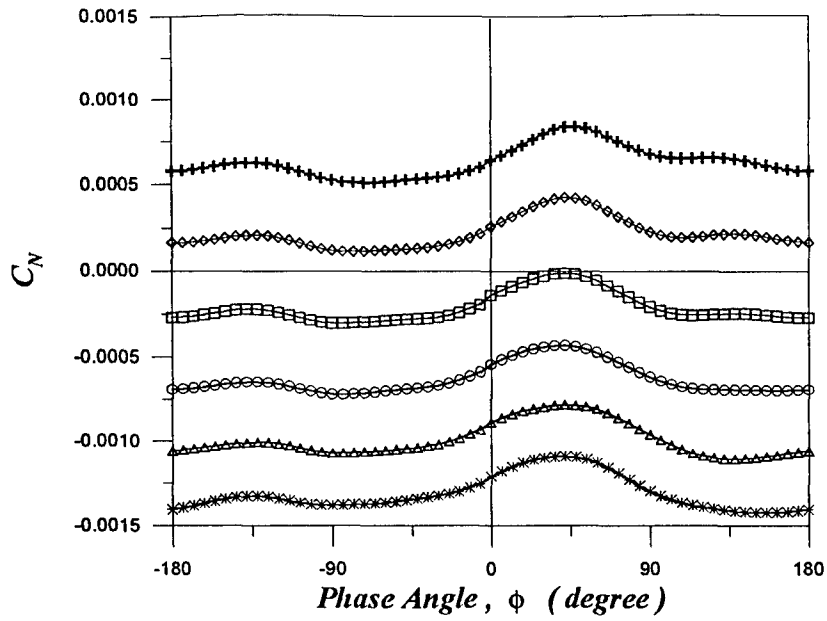


(a)

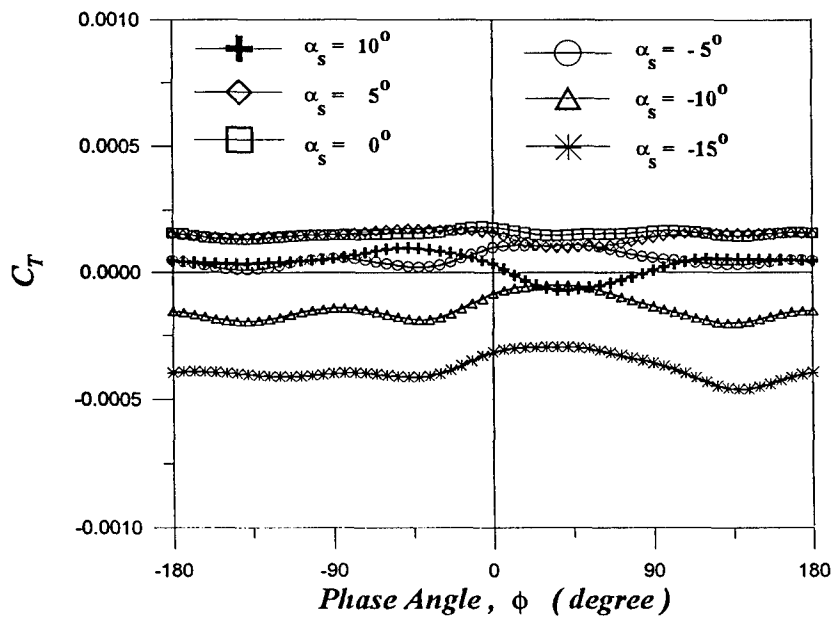


(b)

Fig. 4-4. Time traces of (a) the normal force coefficient, C_N , and (b) the tangential force coefficient, C_T : for $\beta_e = 1.32^\circ$ and with six stator's AoA α_s 's.

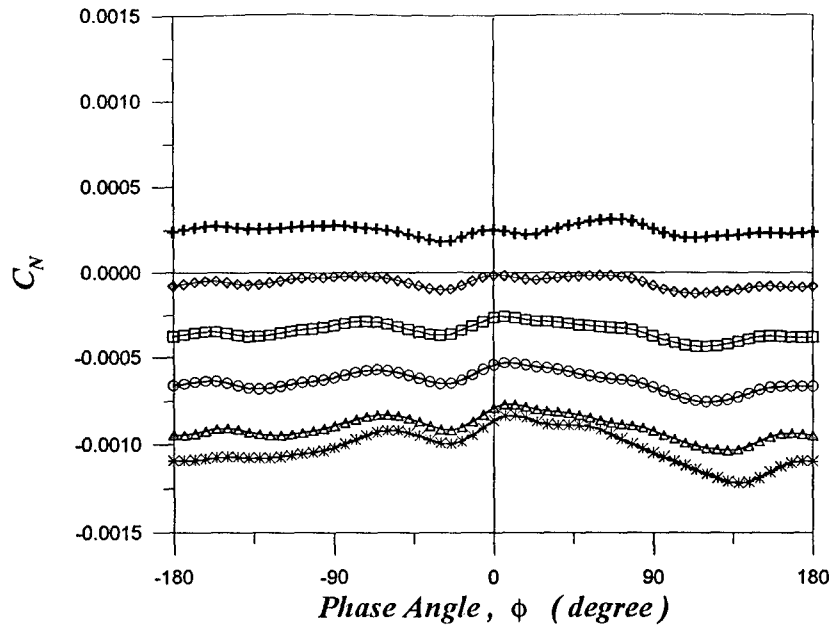


(a)

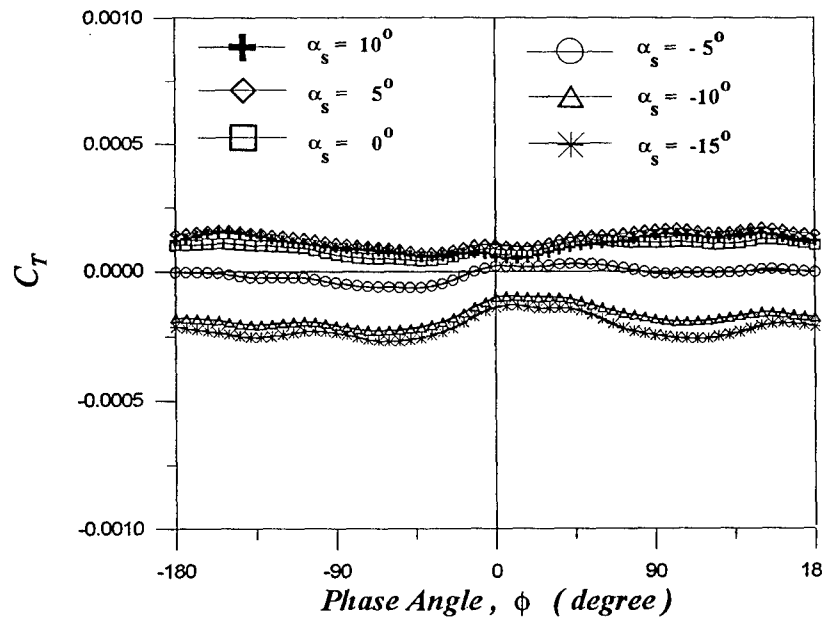


(b)

Fig. 4-5. Time traces of (a) the normal force coefficient, C_N , and (b) the tangential force coefficient, C_T : for $\beta_e = 2.20^\circ$ and with six stator's AoA α_s 's.

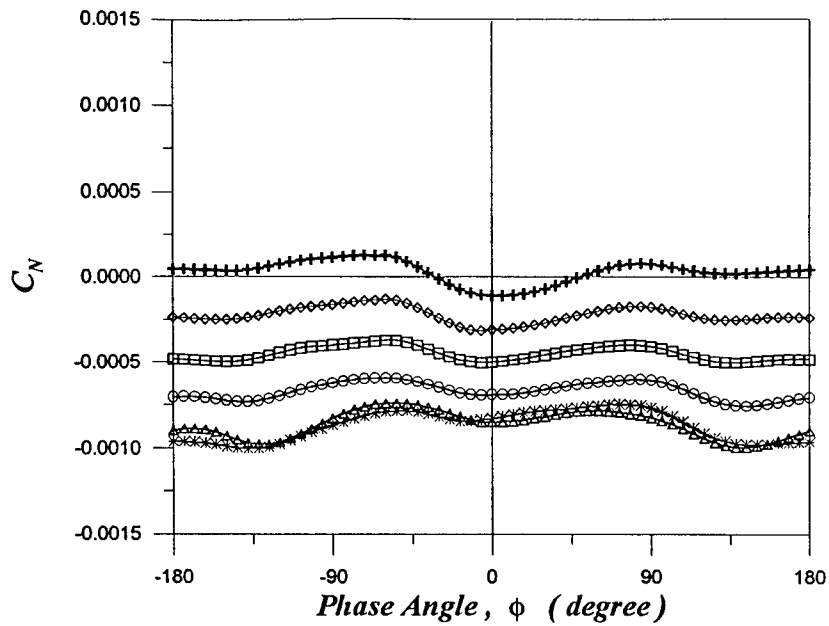


(a)

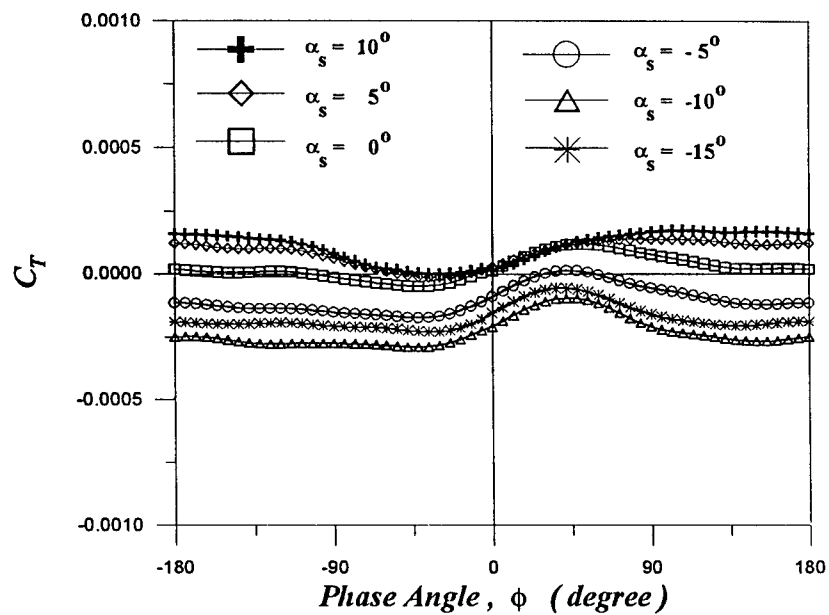


(b)

Fig. 4-6. Time traces of (a) the normal force coefficient, C_N , and (b) the tangential force coefficient, C_T : for $\beta_t = 5.82^\circ$ and with six stator's AoA α_s 's.

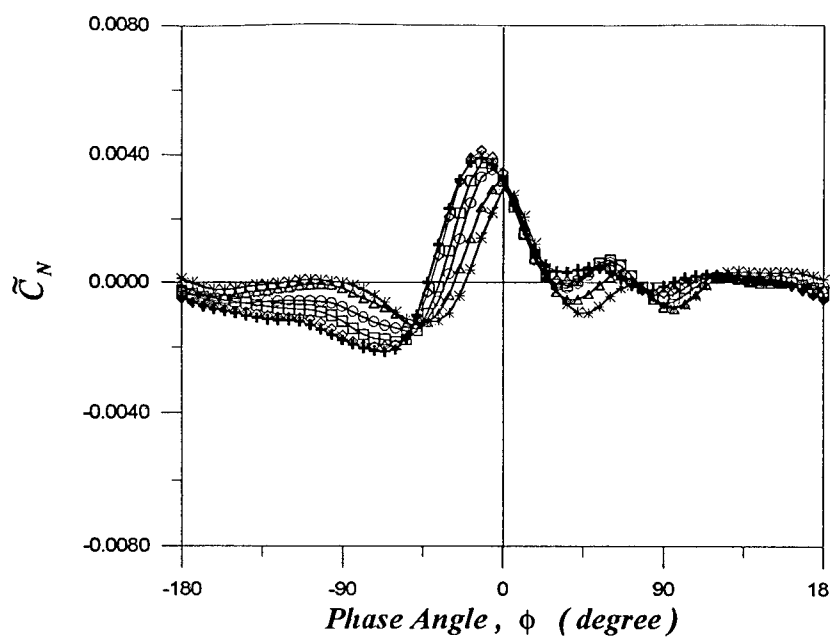


(a)

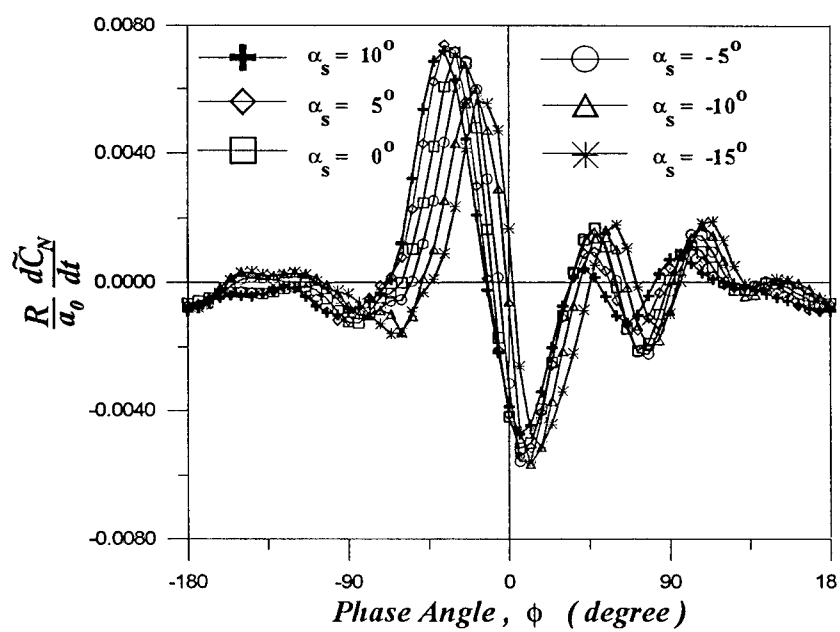


(b)

Fig. 4-7. Time traces of (a) the normal force coefficient, C_N , and (b) the tangential force coefficient, C_T : for $\beta_c = 9.61^\circ$ and with six stator's AoA α_s 's.

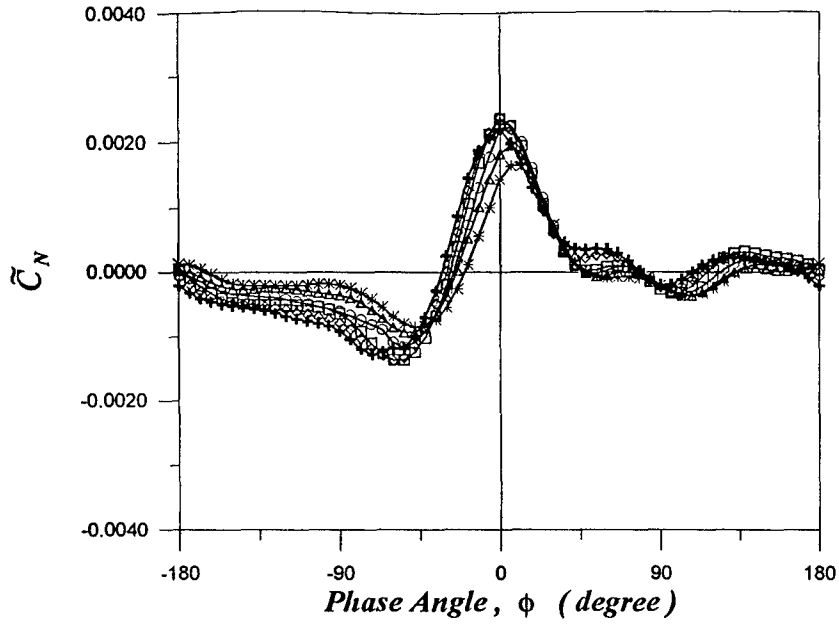


(a)

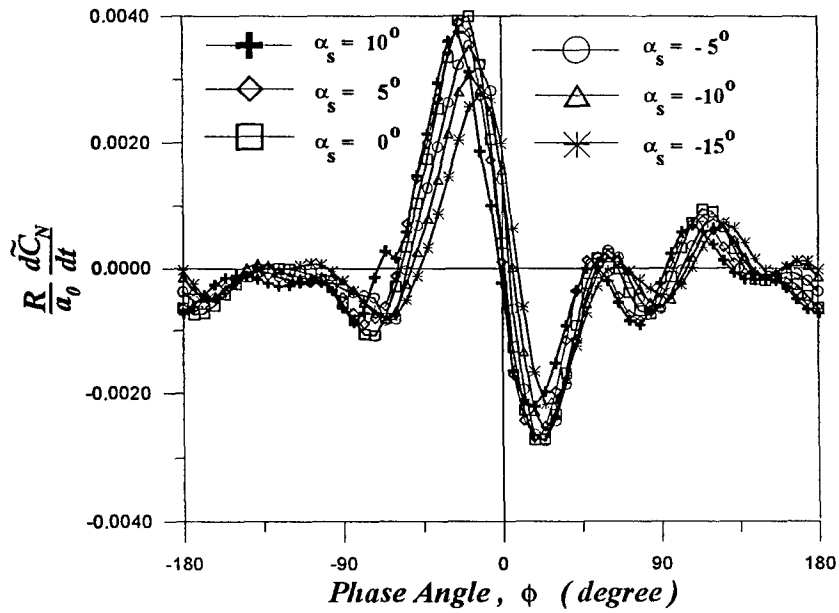


(b)

Fig. 4-8. Time traces of (a) \tilde{C}_N and (b) $\frac{R}{a_0} \frac{d\tilde{C}_N}{dt}$: for $\beta_e = -21.78^\circ$ and at six stator's AoA α_s 's.



(a)



(b)

Fig. 4-9. Time traces of (a) \tilde{C}_N and (b) $\frac{R}{a_0} \frac{d\tilde{C}_N}{dt}$: for $\beta_t = -10.30^\circ$ and at six stator's AoA α_s 's.

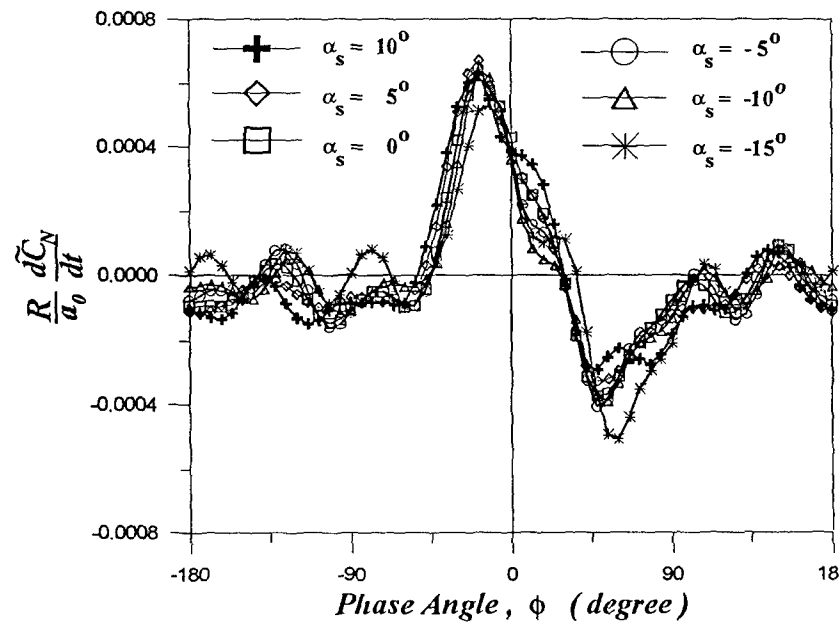
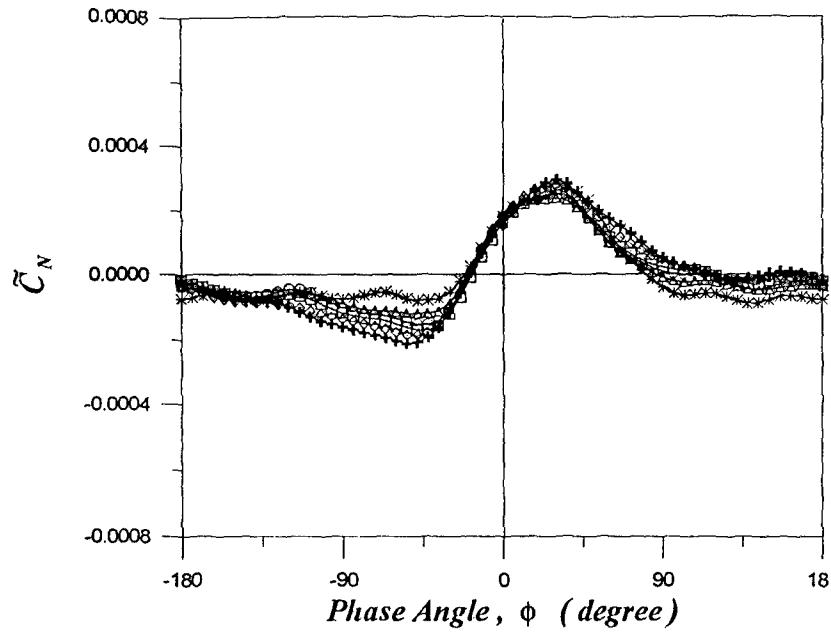
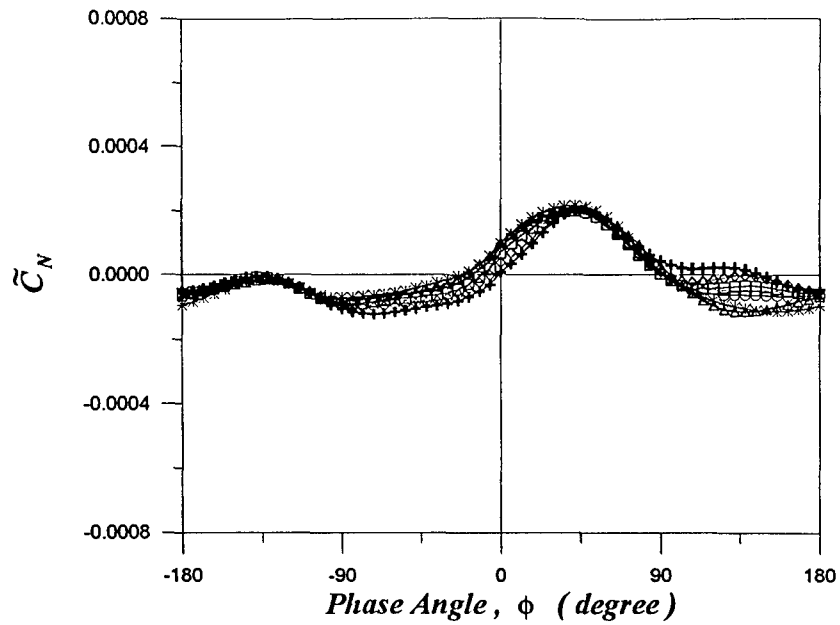
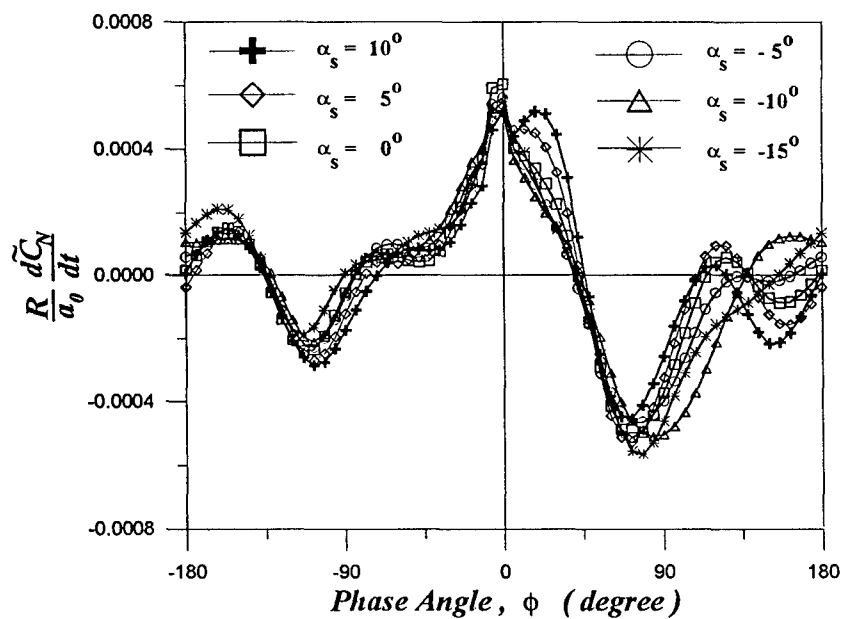


Fig. 4-10. Time traces of (a) \tilde{C}_N and (b) $\frac{R}{a_0} \frac{d\tilde{C}_N}{dt}$: for $\beta_e = 1,32^\circ$ and at six stator's AoA α_s 's.



(a)



(b)

Fig. 4-11. Time traces of (a) \tilde{C}_N and (b) $\frac{R}{a_0} \frac{d\tilde{C}_N}{dt}$: for $\beta_e = 2.20^\circ$ and at six stator's AoA α_s 's.

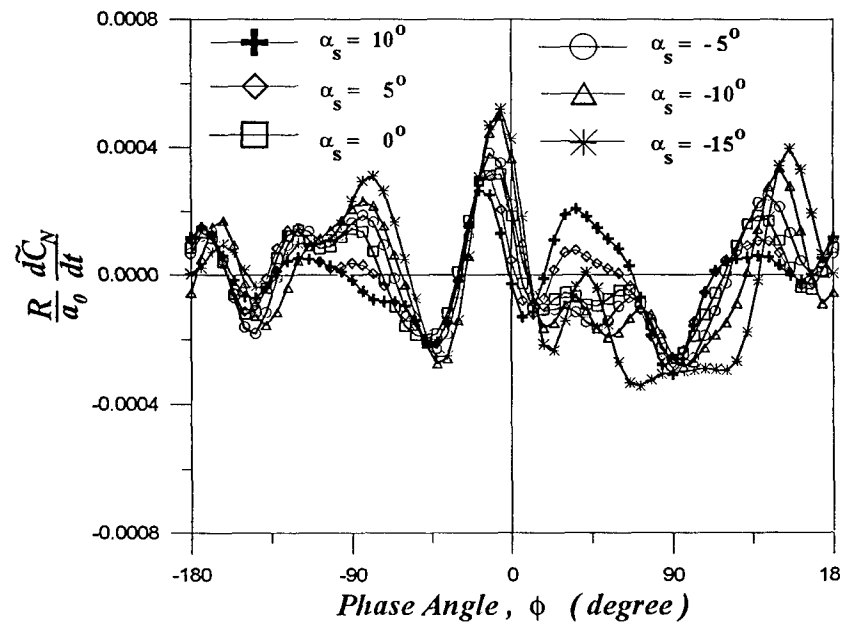
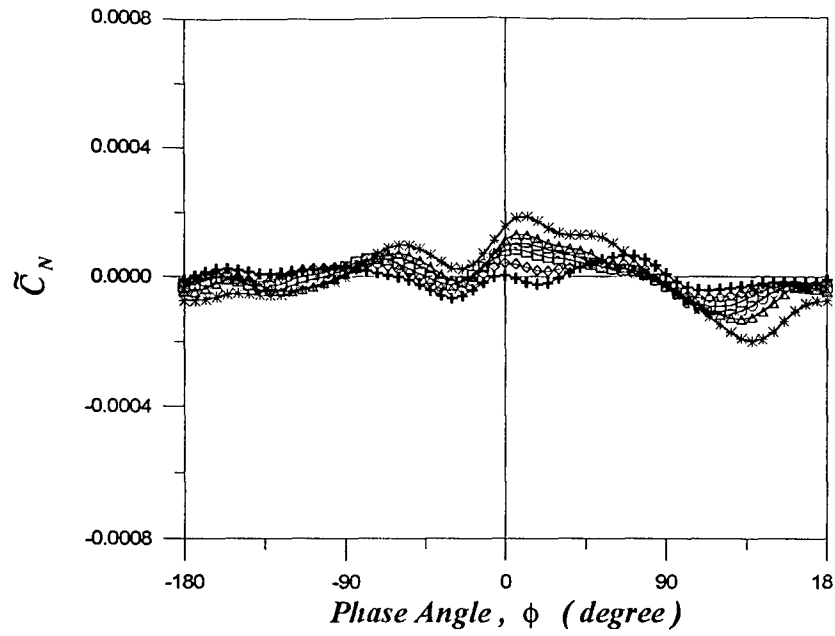
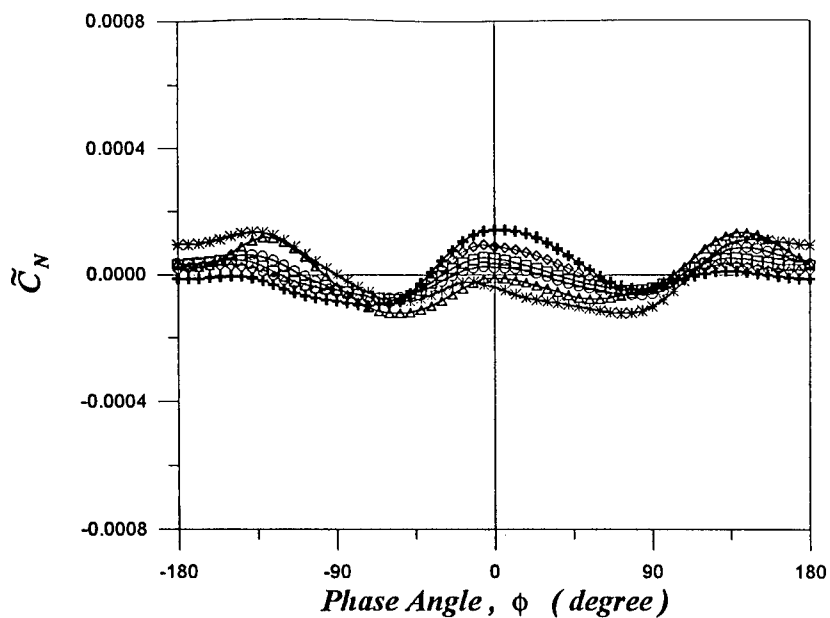
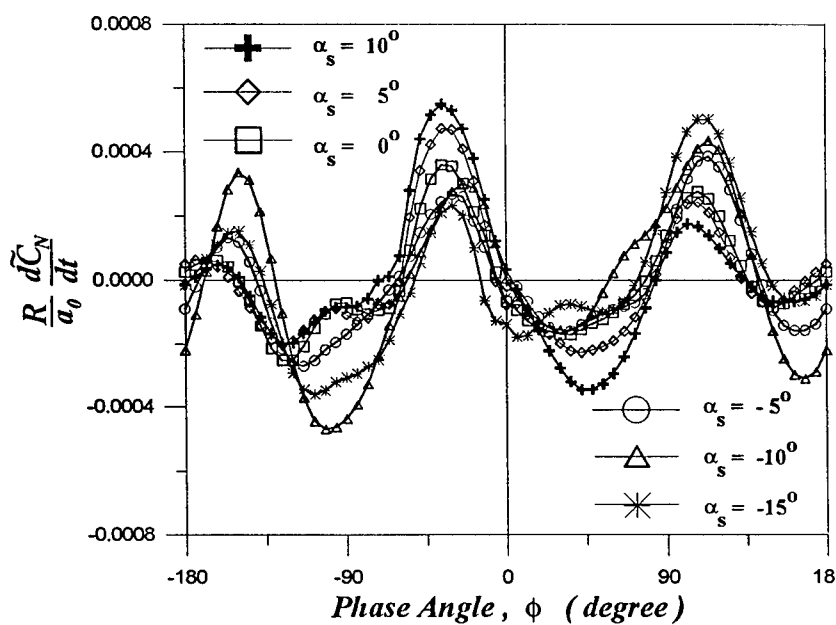


Fig. 4-12. Time traces of (a) \tilde{C}_N and (b) $\frac{R}{a_0} \frac{d\tilde{C}_N}{dt}$: for $\beta_e = 5.82^\circ$ and at six stator's AoA α_s 's.



(a)



(b)

Fig. 4-13. Time traces of (a) \tilde{C}_N and (b) $\frac{R}{a_0} \frac{d\tilde{C}_N}{dt}$: for $\beta_e = 9.61^\circ$ and at six stator's AoA α_s 's.

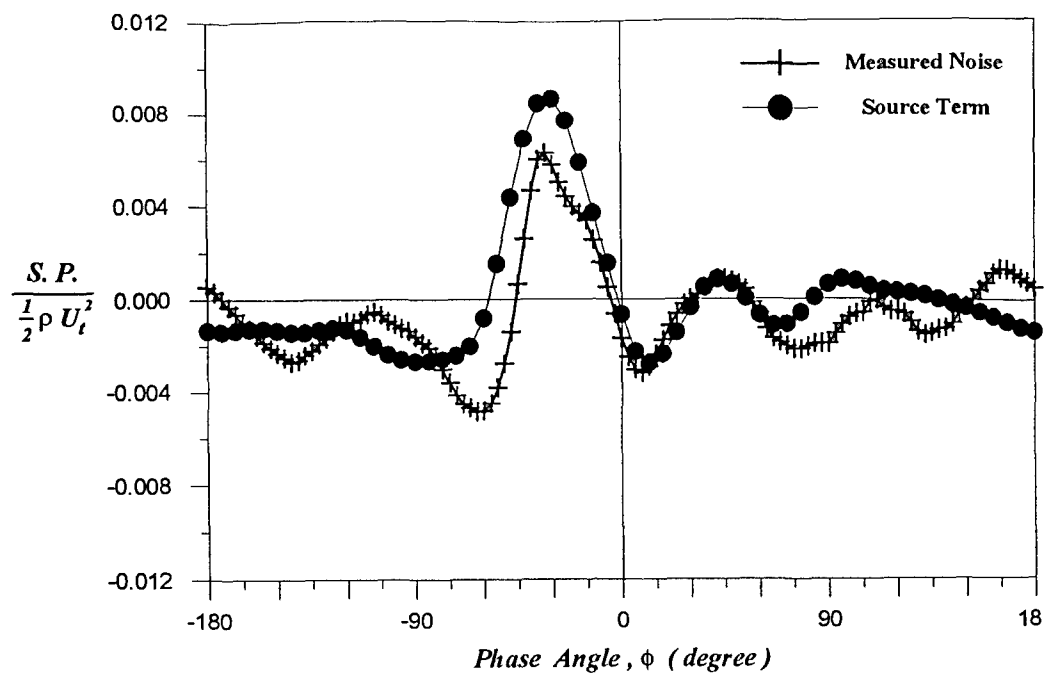


Fig. 4-14(a) ($\alpha_s = 10^\circ$, $\beta_e @ 55\%R = -21.78^\circ$, $U_t @ 55\%R = 11.38$ m/s.)

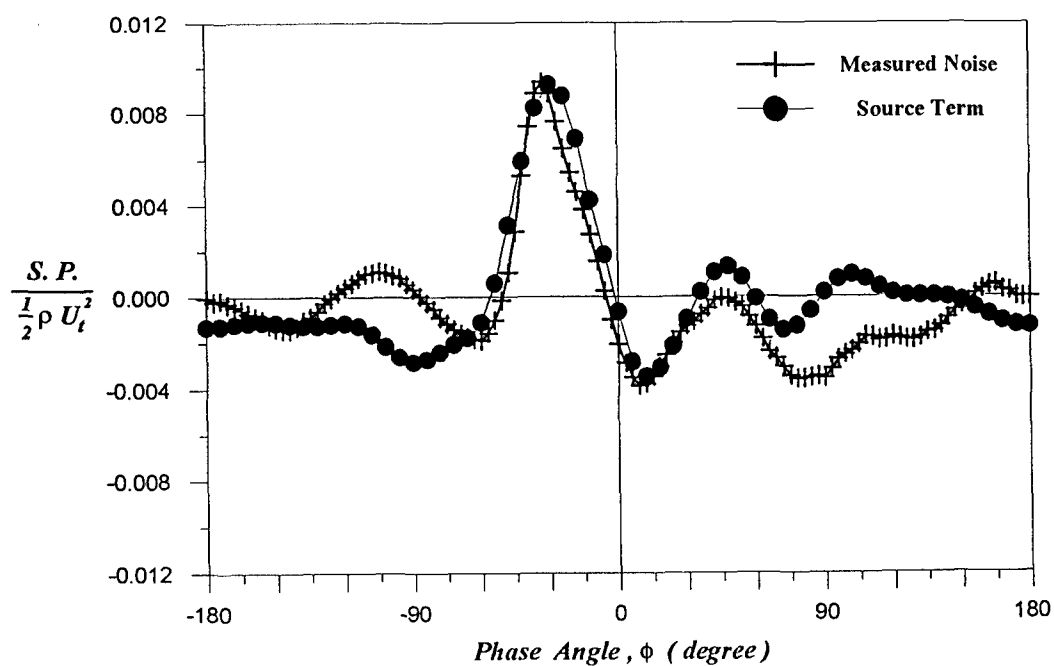


Fig. 4-14(b) ($\alpha_s = 5^\circ$, $\beta_e @ 55\%R = -21.78^\circ$, $U_t @ 55\%R = 11.38$ m/s.)

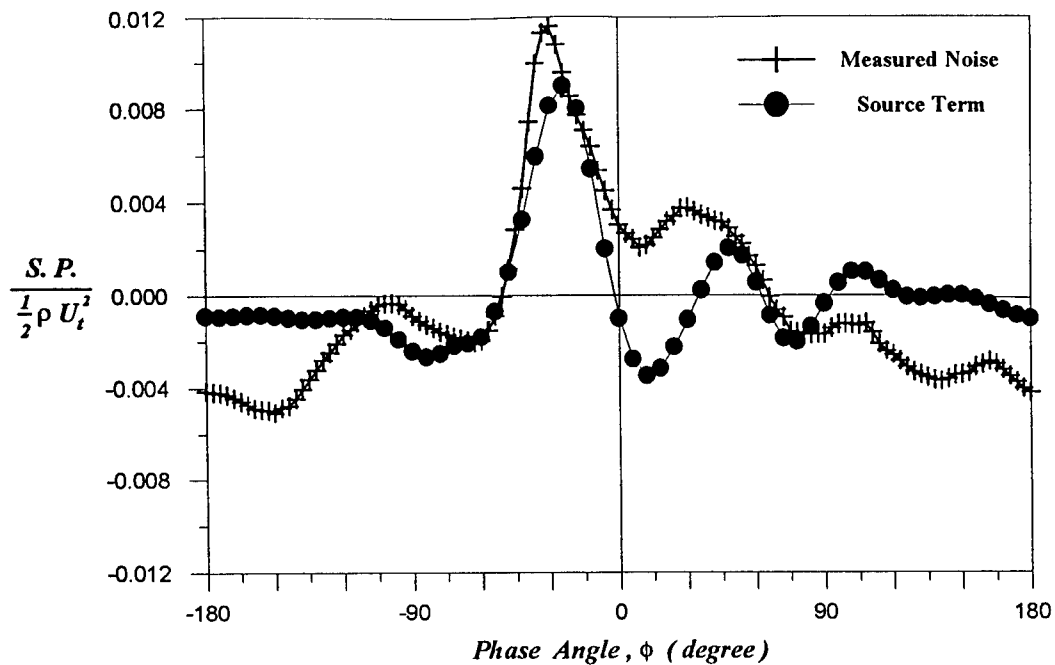


Fig. 4-14(c) ($\alpha_s = 0^\circ$, $\beta_e @ 55\%R = -21.78^\circ$, $U_t @ 55\%R = 11.38$ m/s.)

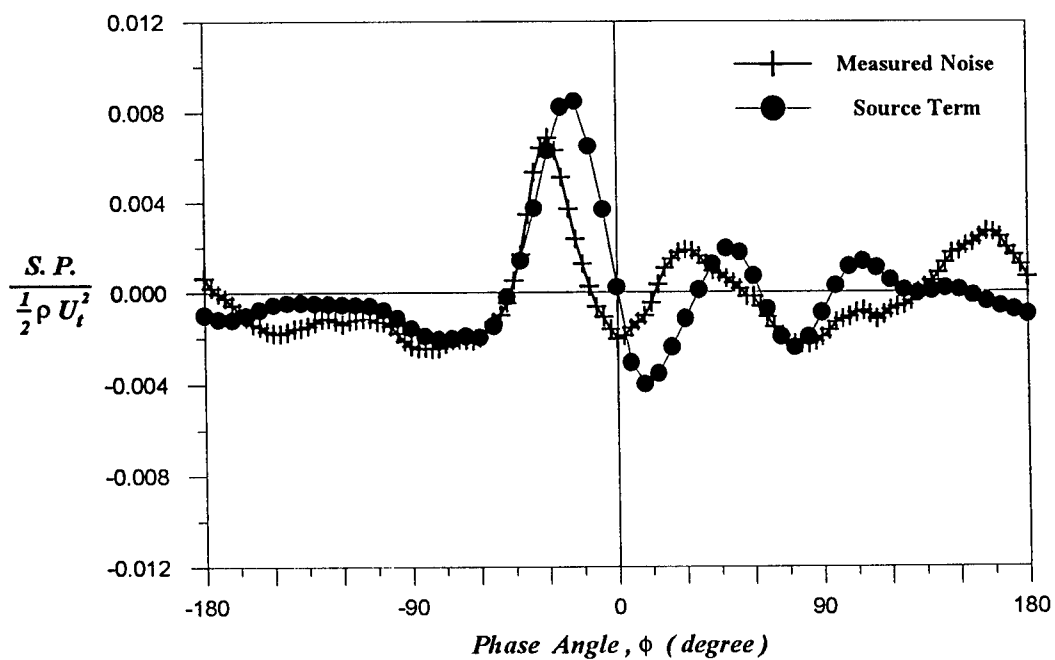


Fig. 4-14(d) ($\alpha_s = -5^\circ$, $\beta_e @ 55\%R = -21.78^\circ$, $U_t @ 55\%R = 11.38$ m/s.)

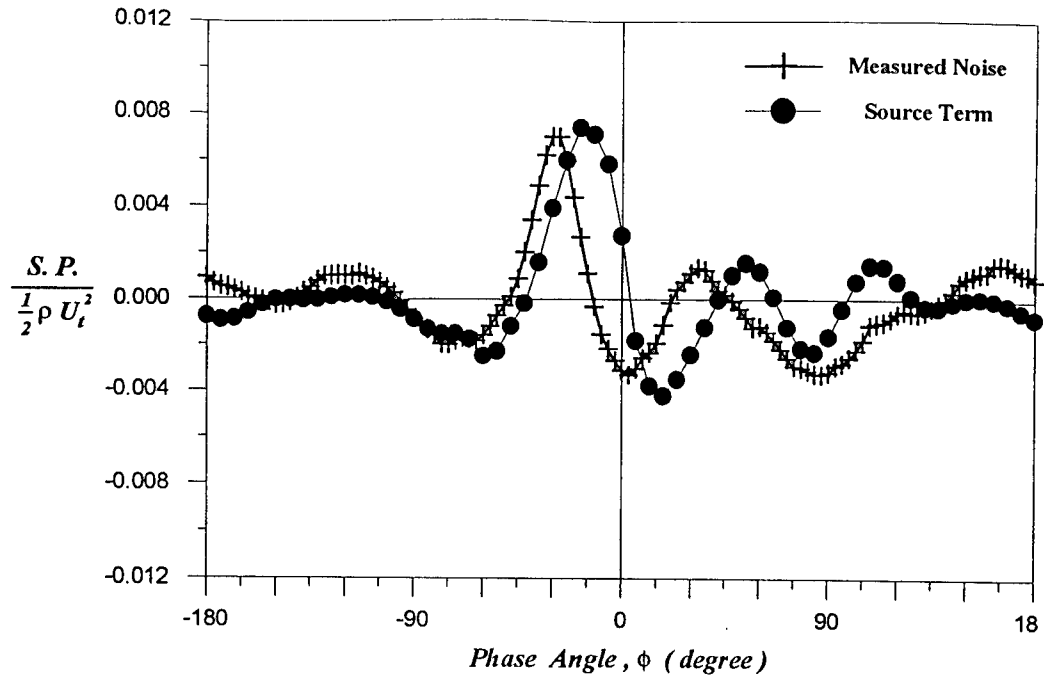


Fig. 4-14(e) ($\alpha_s = -10^\circ$, $\beta_e @ 55\%R = -21.78^\circ$, $U_t @ 55\%R = 11.38$ m/s.)

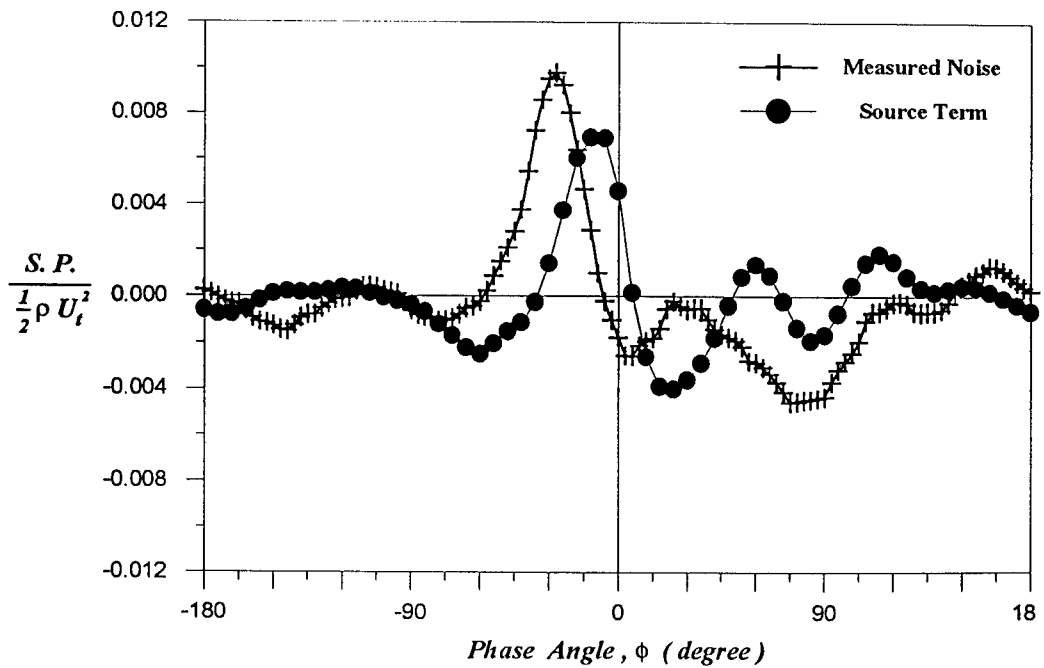


Fig. 4-14(f) ($\alpha_s = -15^\circ$, $\beta_e @ 55\%R = -21.78^\circ$, $U_t @ 55\%R = 11.38$ m/s.)

Fig. 4-14. Measured noise vs. source term : for $\beta_e = -21.78^\circ$ with α_s at (a) 10° , (b) 5° , (c) 0° , (d) -5° , (e) -10° and (f) -15° , respectively.

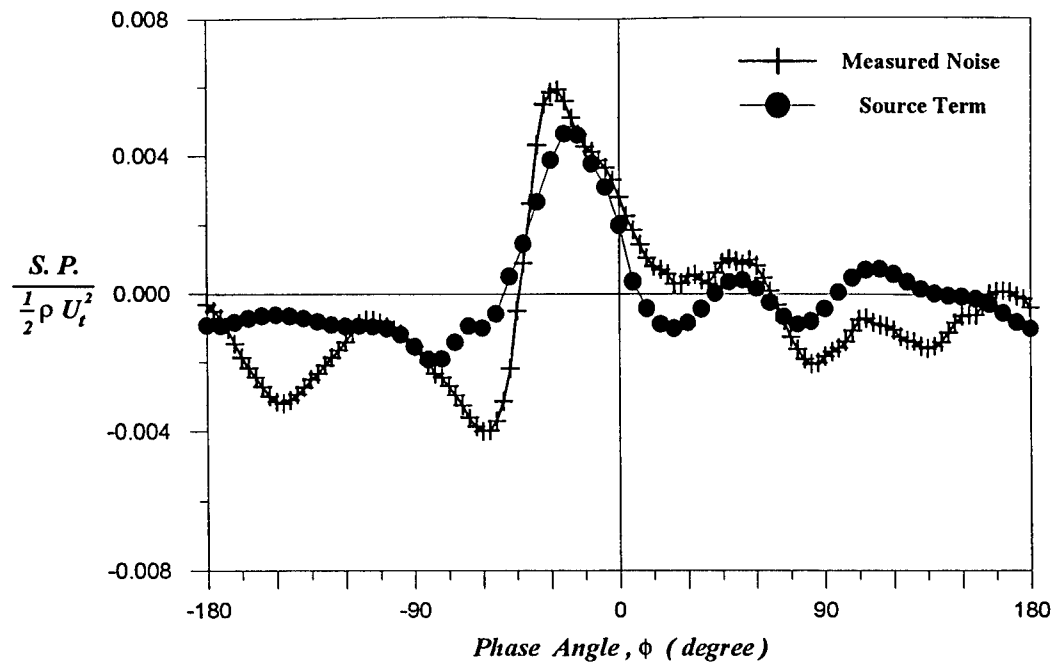


Fig. 4-15(a) ($\alpha_s = 10^\circ$, $\beta_e @ 55\%R = -10.30^\circ$, $U_t @ 55\%R = 9.49$ m/s.)

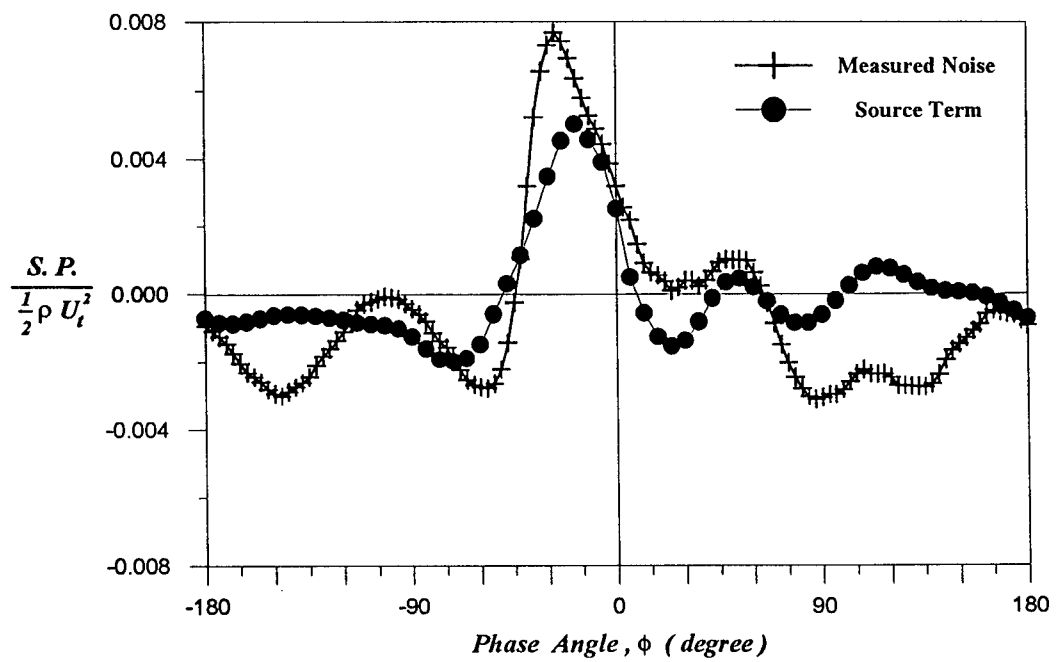


Fig. 4-15(b) ($\alpha_s = 5^\circ$, $\beta_e @ 55\%R = -10.30^\circ$, $U_t @ 55\%R = 9.49$ m/s.)

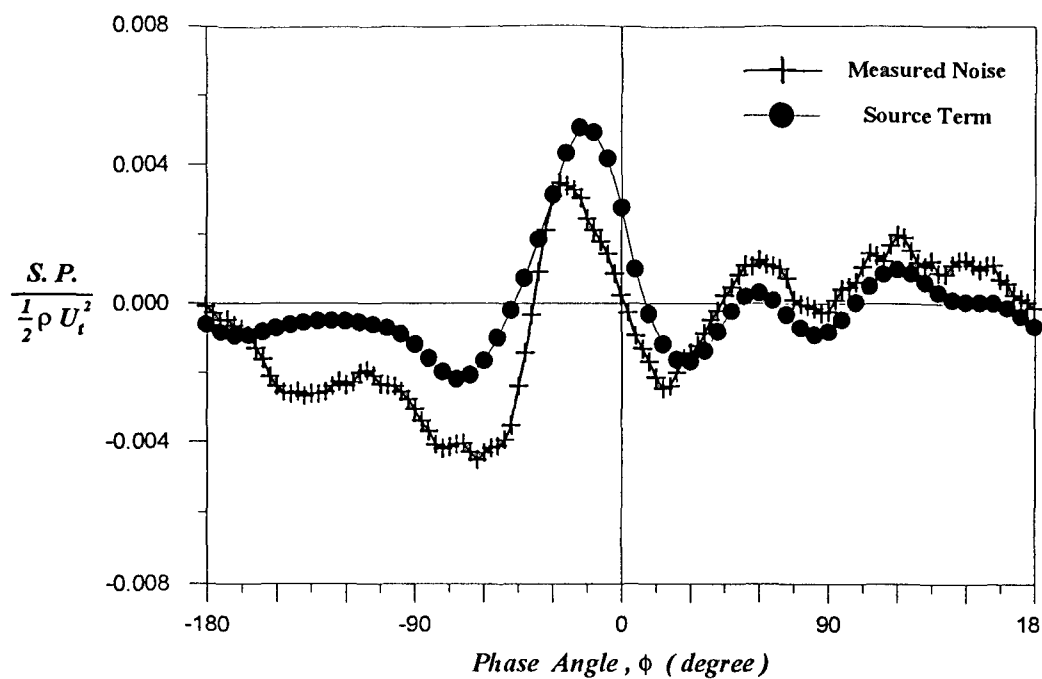


Fig. 4-15(c) ($\alpha_s = 0^\circ$, $\beta_e @ 55\%R = -10.30^\circ$, $U_t @ 55\%R = 9.49$ m/s.)

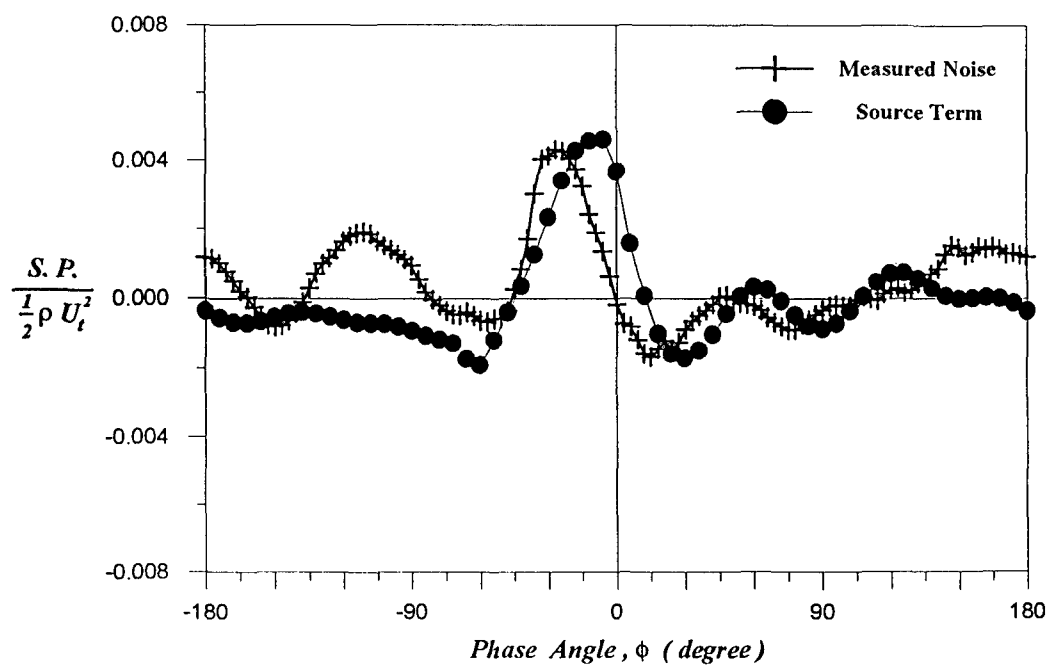


Fig. 4-15(d) ($\alpha_s = -5^\circ$, $\beta_e @ 55\%R = -10.30^\circ$, $U_t @ 55\%R = 9.49$ m/s.)

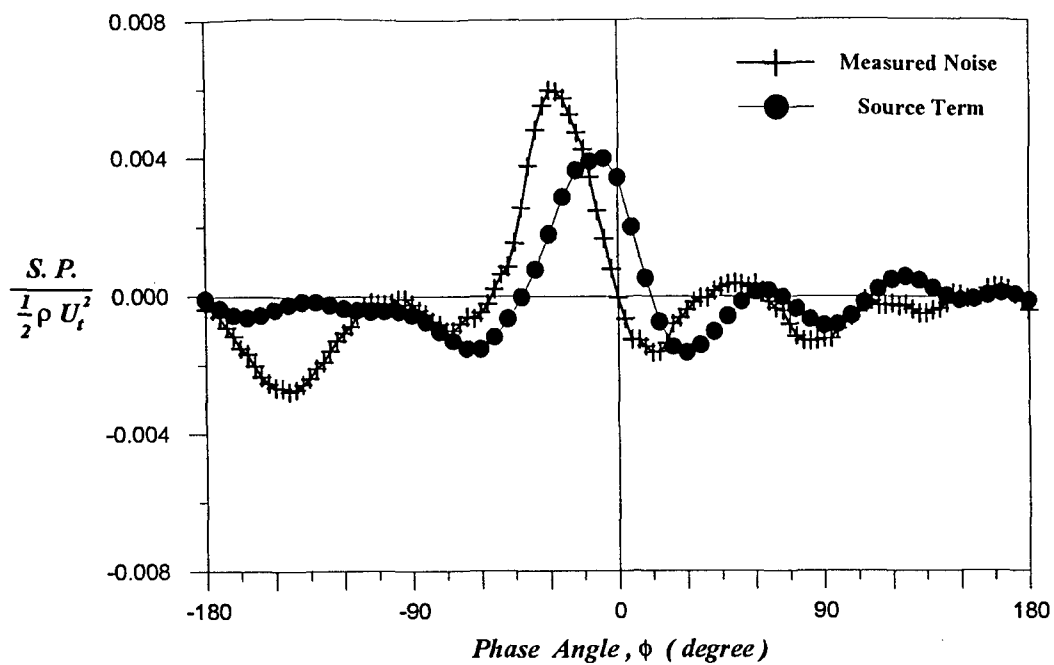


Fig. 4-15(e) ($\alpha_s = -10^\circ$, $\beta_e @ 55\%R = -10.30^\circ$, $U_t @ 55\%R = 9.49$ m/s.)

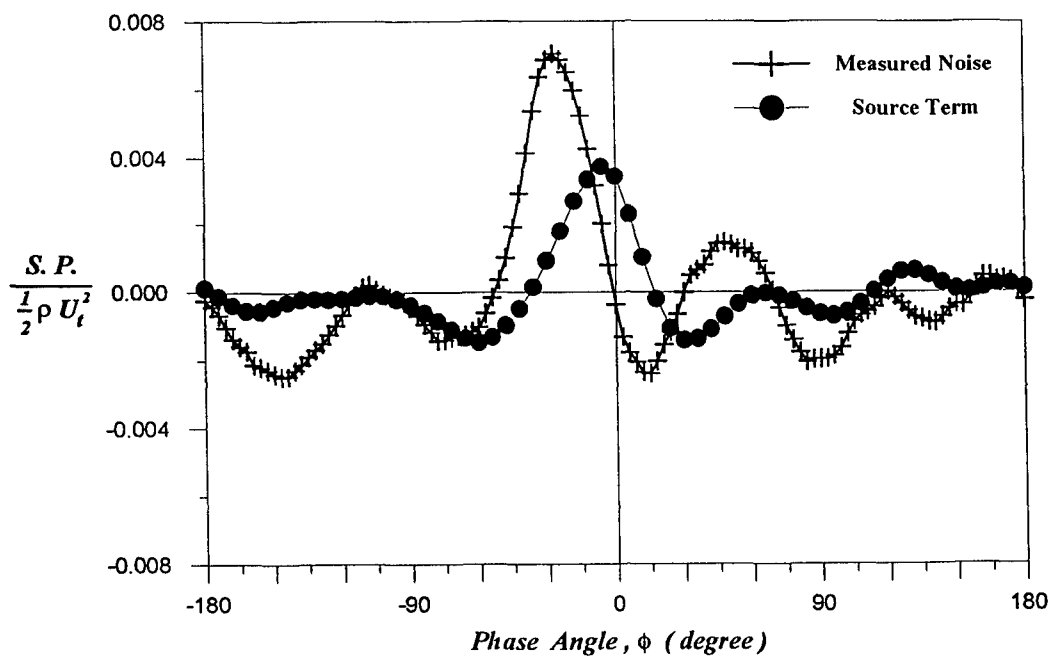


Fig. 4-15(f) ($\alpha_s = -15^\circ$, $\beta_e @ 55\%R = -10.30^\circ$, $U_t @ 55\%R = 9.49$ m/s.)

Fig. 4-15. Measured noise vs. source term : for $\beta_e = -10.30^\circ$ with α_t at (a) 10° , (b) 5° , (c) 0° , (d) -5° , (e) -10° and (f) -15° , respectively.

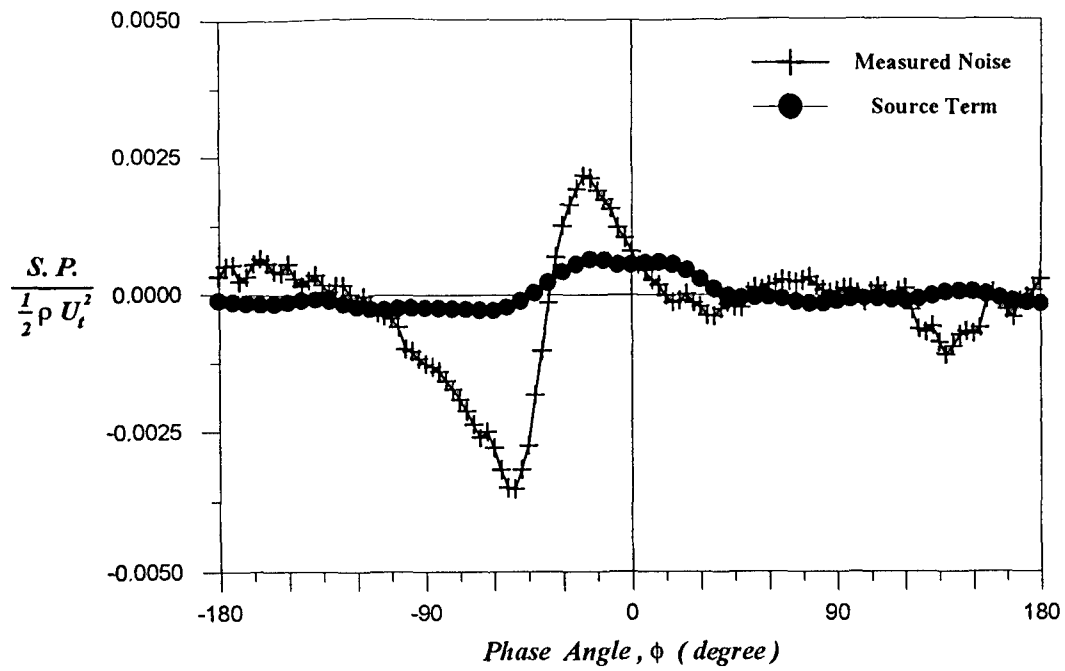


Fig. 4-16(a) ($\alpha_s = 10^\circ$, $\beta_e @ 55\%R = 1.32^\circ$, $U_t @ 55\%R = 13.46$ m/s.)

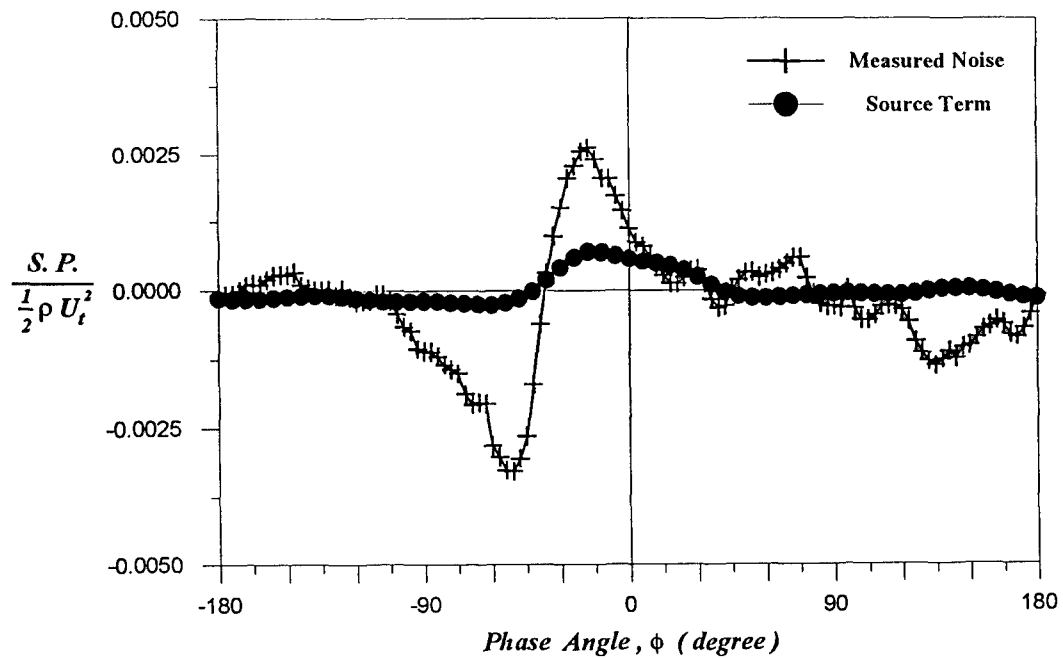


Fig. 4-16(b) ($\alpha_s = 5^\circ$, $\beta_e @ 55\%R = 1.32^\circ$, $U_t @ 55\%R = 13.46$ m/s.)

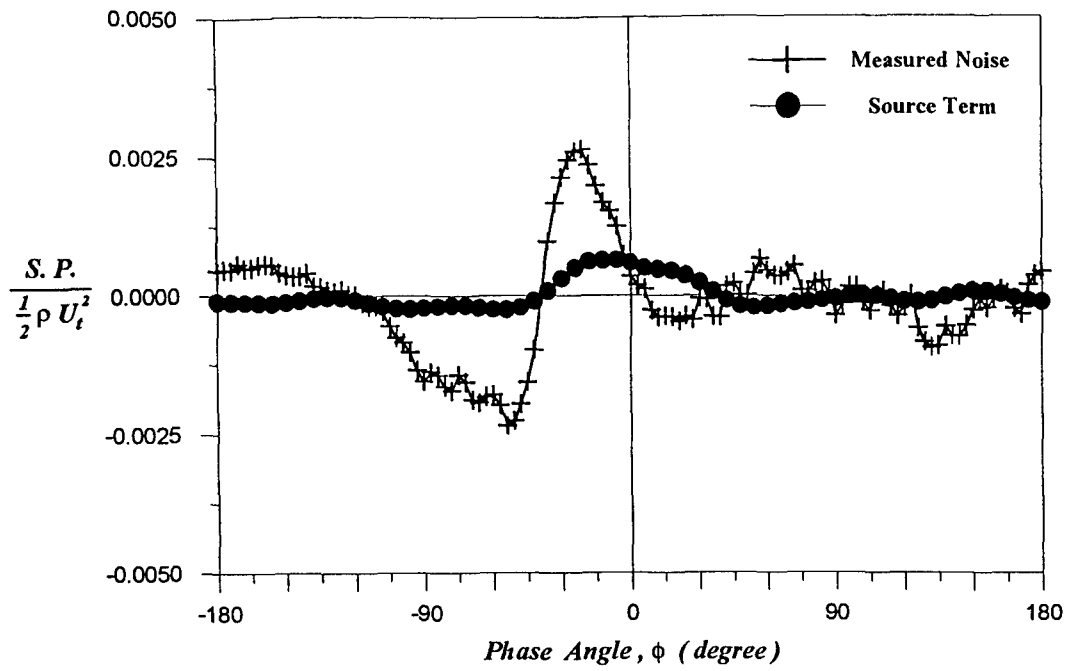


Fig. 4-16(c) ($\alpha_s = 0^\circ$, $\beta_e @ 55\%R = 1.32^\circ$, $U_t @ 55\%R = 13.46$ m/s.)

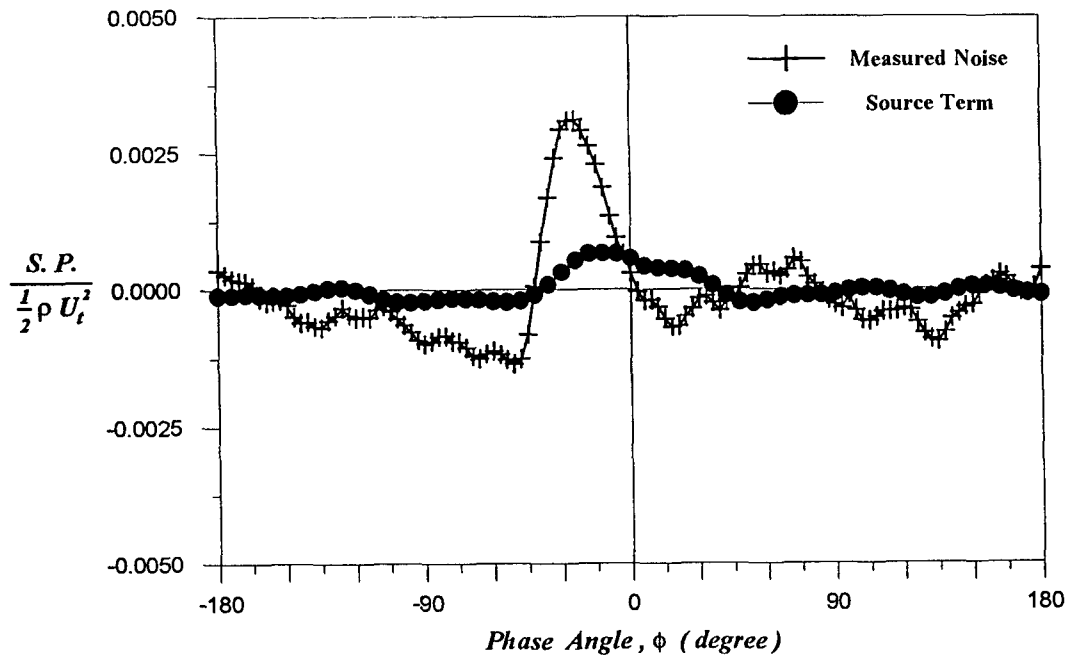


Fig. 4-16(d) ($\alpha_s = -5^\circ$, $\beta_e @ 55\%R = 1.32^\circ$, $U_t @ 55\%R = 13.46$ m/s.)

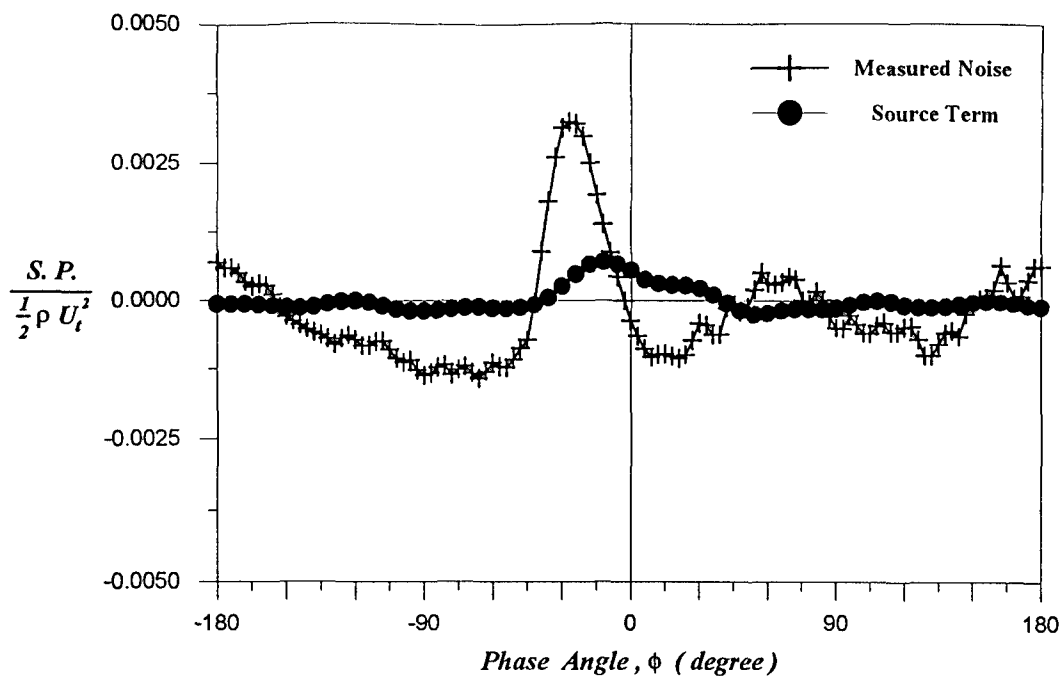


Fig. 4-16(e) ($\alpha_s = -10^\circ$, $\beta_e @ 55\%R = 1.32^\circ$, $U_t @ 55\%R = 13.46$ m/s.)

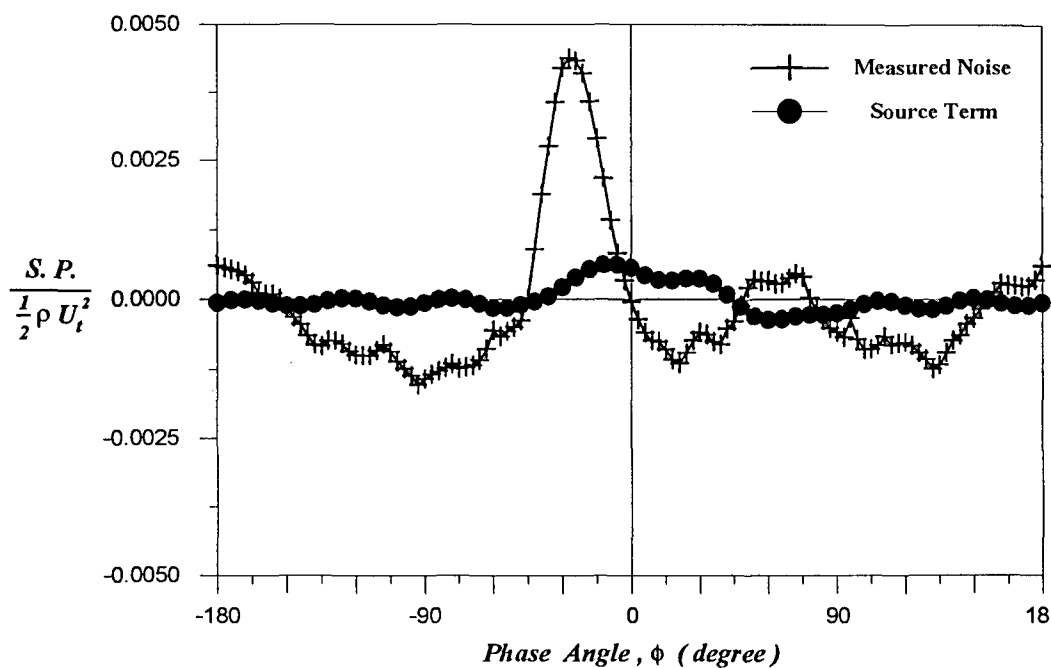


Fig. 4-16(f) ($\alpha_s = -15^\circ$, $\beta_e @ 55\%R = 1.32^\circ$, $U_t @ 55\%R = 13.46$ m/s.)

Fig. 4-16. Measured noise vs. source term : for $\beta_e = 1.32^\circ$ with α_s at (a) 10° , (b) 5° , (c) 0° , (d) -5° , (e) -10° and (f) -15° , respectively.

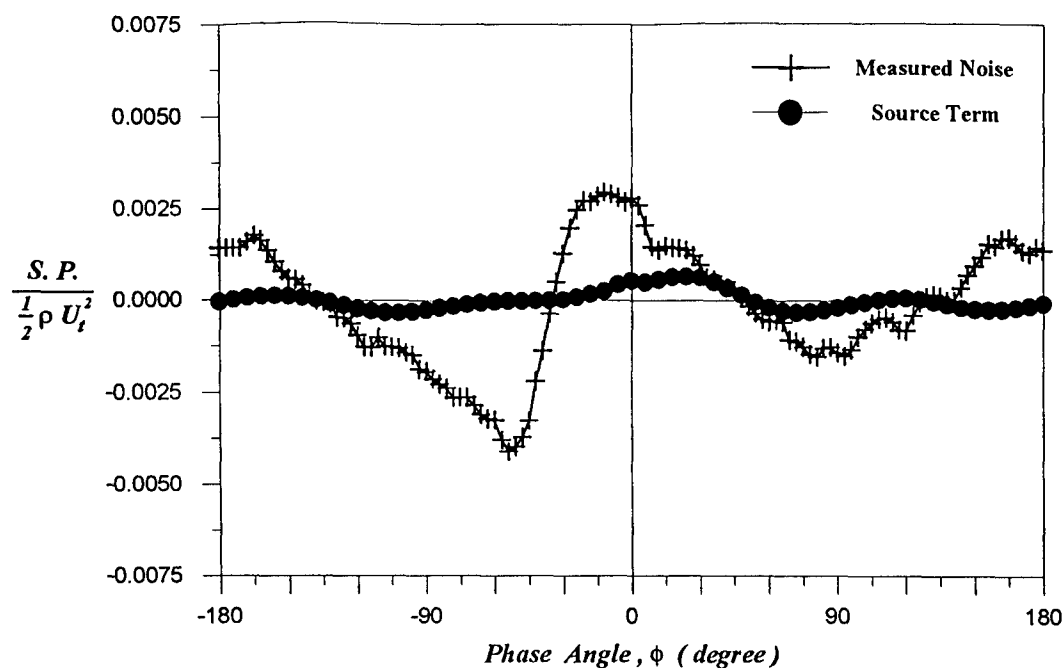


Fig. 4-17(a) ($\alpha_s = 10^\circ$, $\beta_e @ 55\%R = 2.20^\circ$, $U_t @ 55\%R = 20.89$ m/s.)

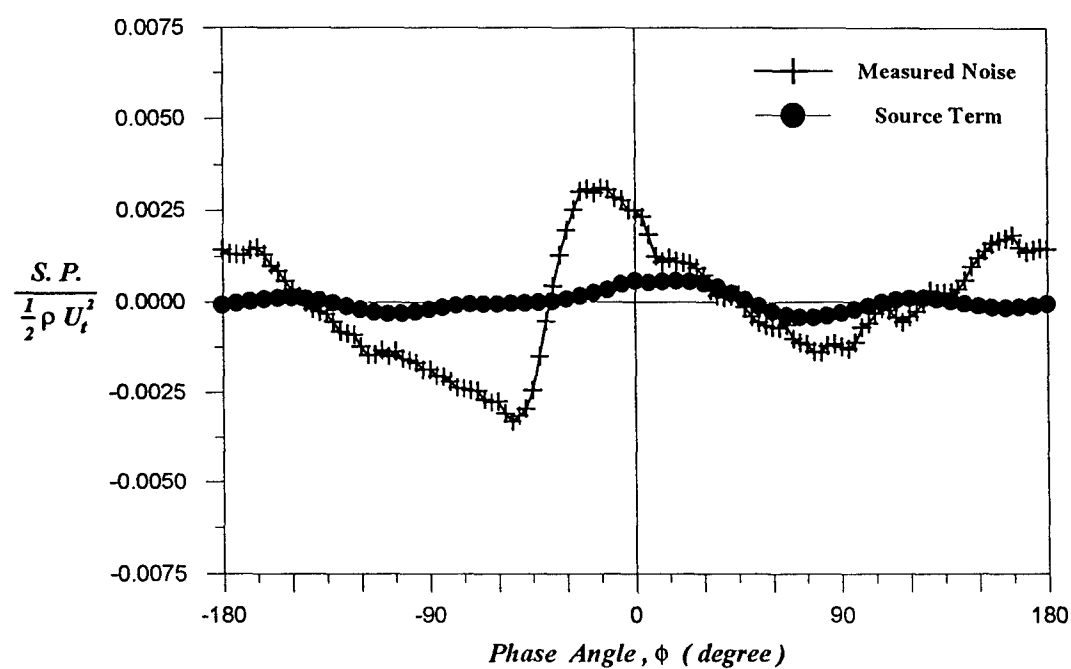


Fig. 4-17(b) ($\alpha_s = 5^\circ$, $\beta_e @ 55\%R = 2.20^\circ$, $U_t @ 55\%R = 20.89$ m/s.)

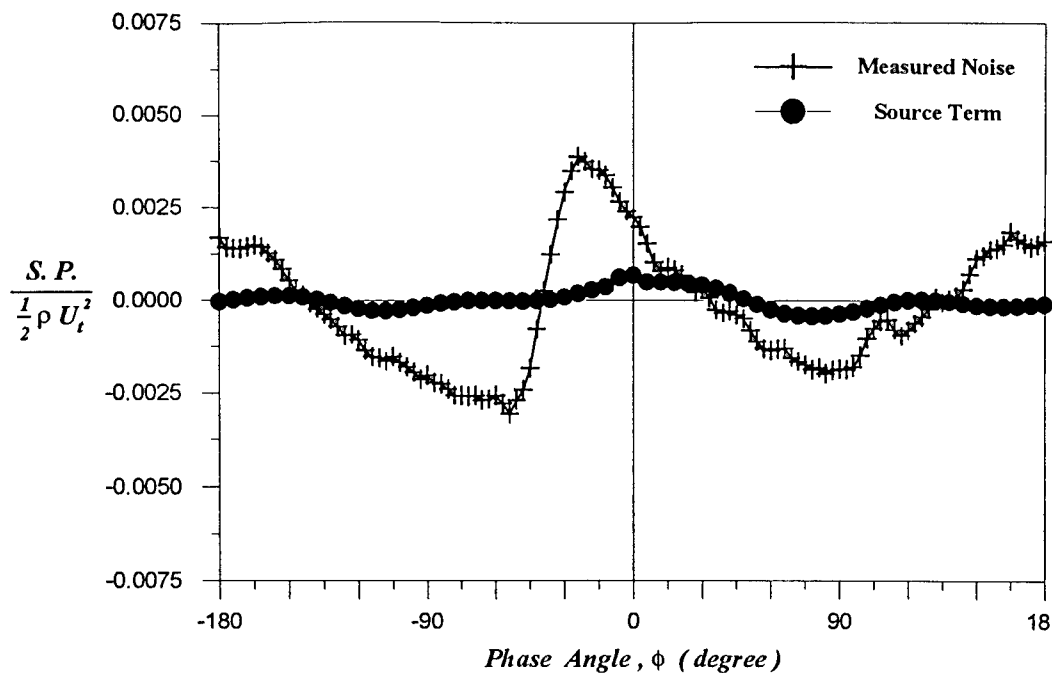


Fig. 4-17(c) ($\alpha_s = 0^\circ$, $\beta_c @ 55\%R = 2.20^\circ$, $U_t @ 55\%R = 20.89$ m/s.)

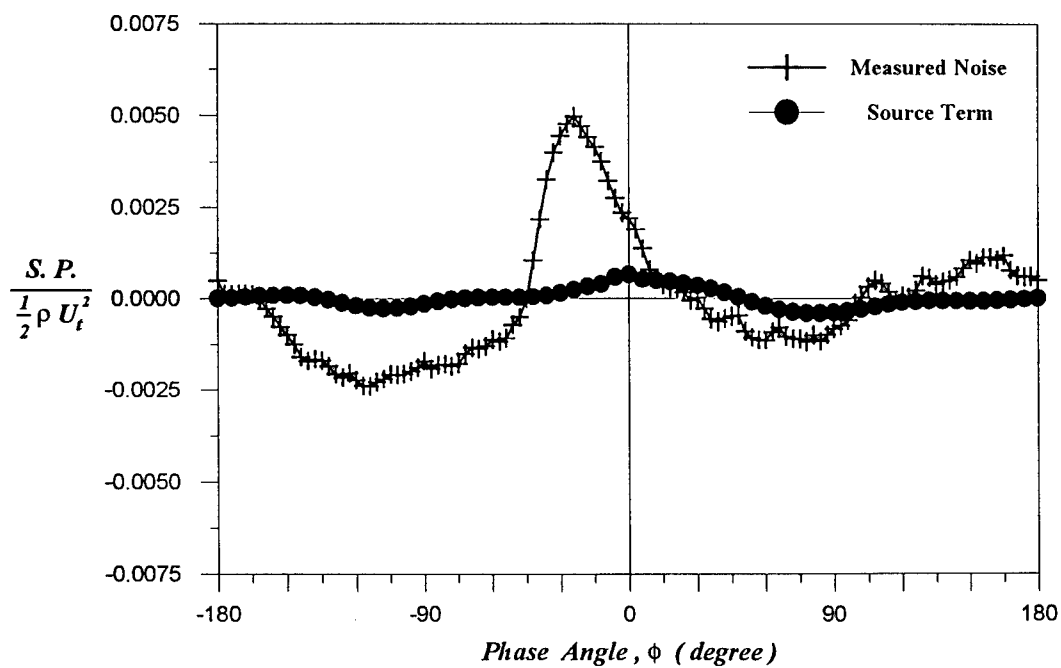


Fig. 4-17(d) ($\alpha_s = -5^\circ$, $\beta_c @ 55\%R = 2.20^\circ$, $U_t @ 55\%R = 20.89$ m/s.)

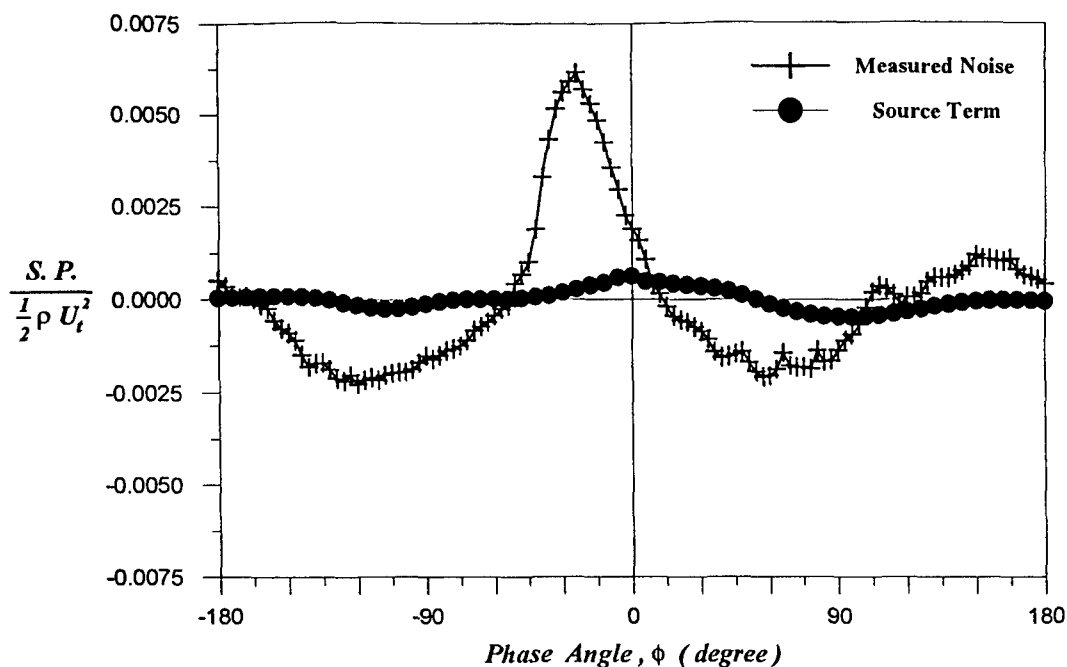


Fig. 4-17(e) ($\alpha_s = -10^\circ$, $\beta_e @ 55\%R = 2.20^\circ$, $U_t @ 55\%R = 20.89$ m/s.)

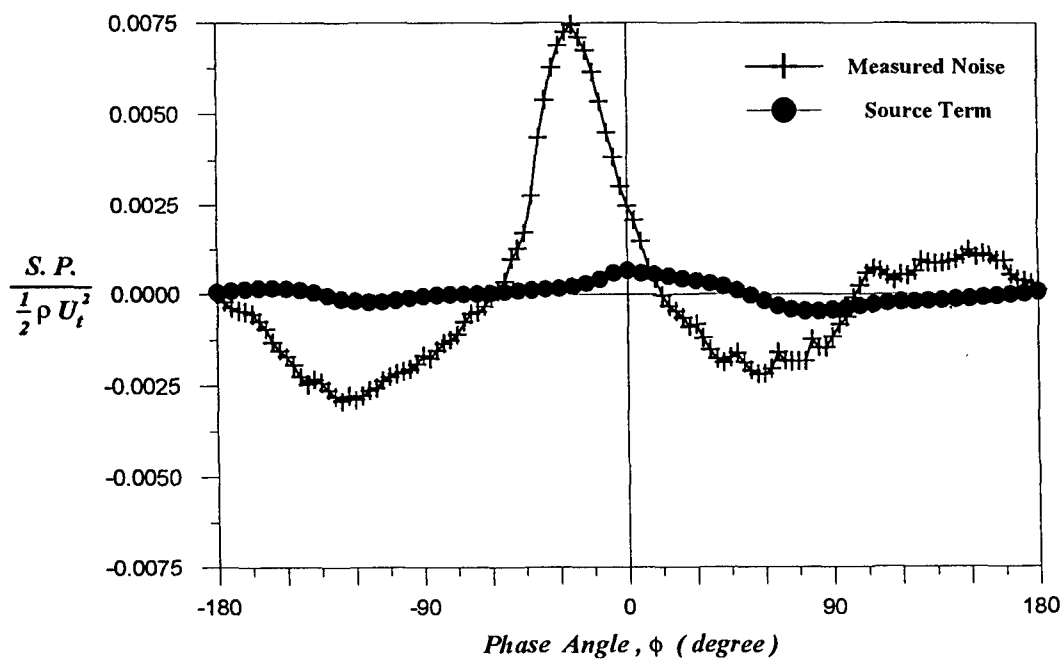


Fig. 4-17(f) ($\alpha_s = -15^\circ$, $\beta_e @ 55\%R = 2.20^\circ$, $U_t @ 55\%R = 20.89$ m/s.)

Fig. 4-17. Measured noise vs. source term : for $\beta_e = 2.20^\circ$ with α_s at (a) 10° , (b) 5° , (c) 0° , (d) -5° , (e) -10° and (f) -15° , respectively.

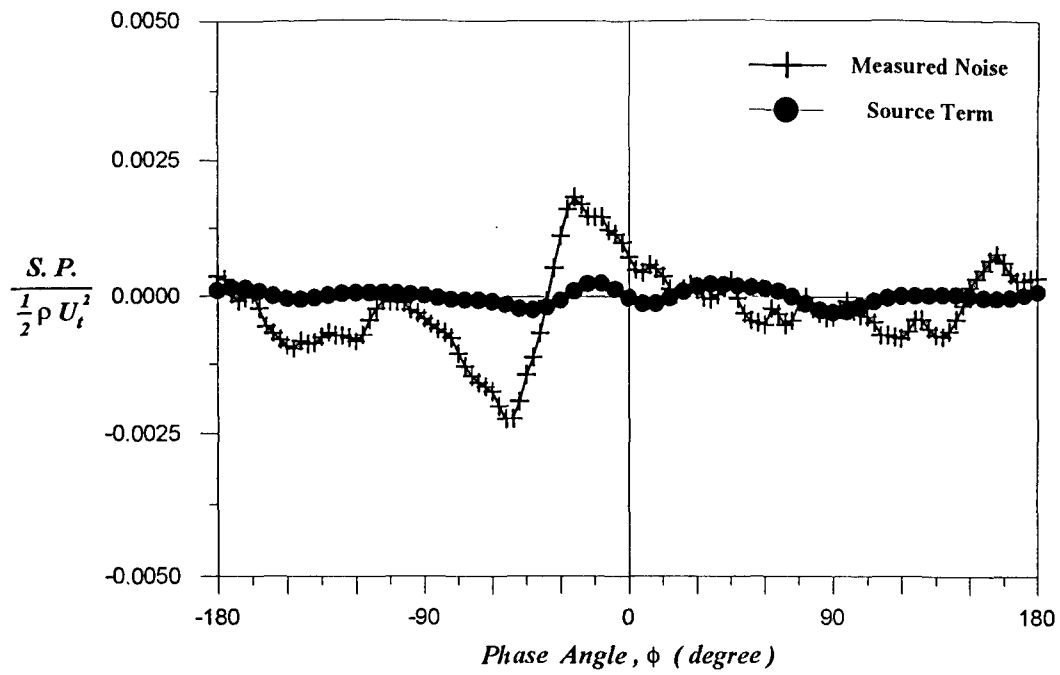


Fig. 4-18(a) ($\alpha_s = 10^\circ$, $\beta_e @ 55\%R = 5.82^\circ$, $U_f @ 55\%R = 16.29$ m/s.)

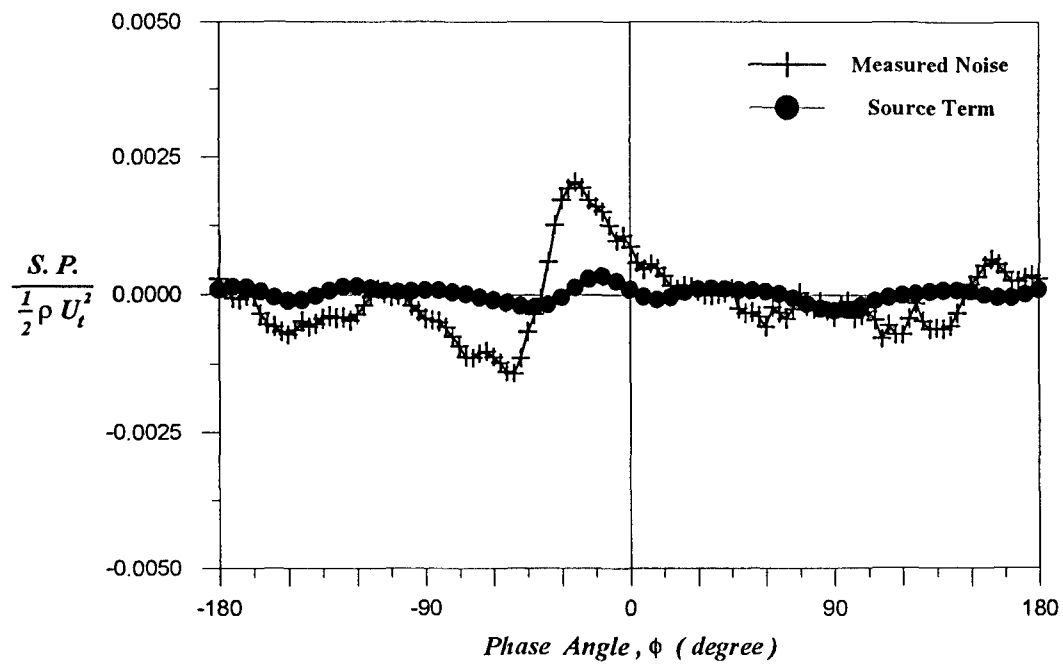


Fig. 4-18(b) ($\alpha_s = 5^\circ$, $\beta_e @ 55\%R = 5.82^\circ$, $U_f @ 55\%R = 16.29$ m/s.)

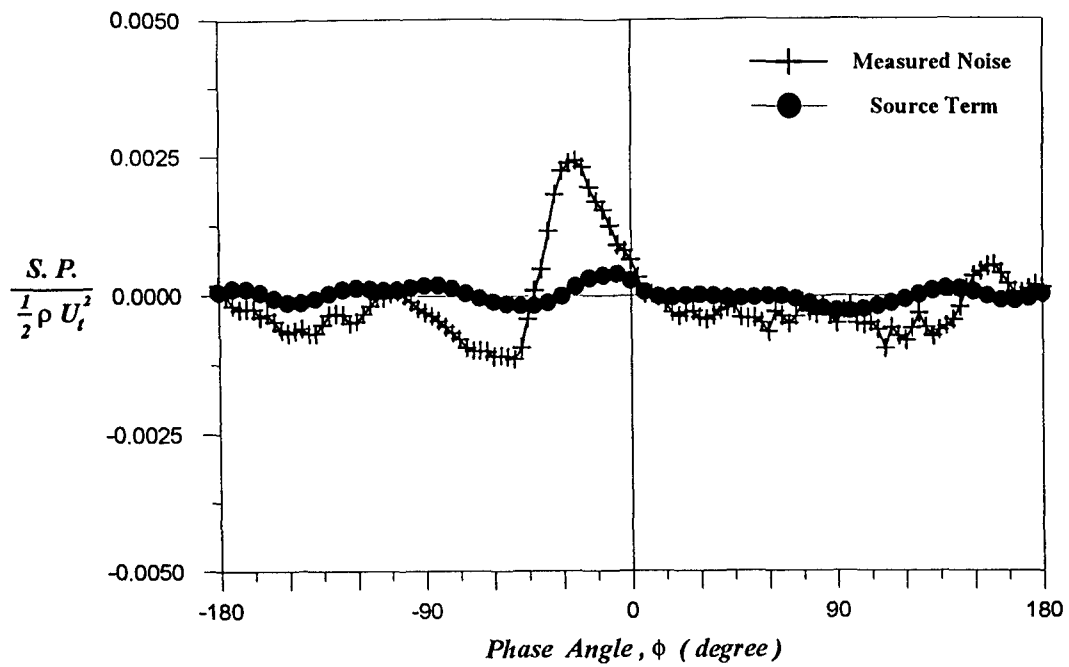


Fig. 4-18(c) ($\alpha_s = 0^\circ$, $\beta_e @ 55\%R = 5.82^\circ$, $U_t @ 55\%R = 16.29$ m/s.)

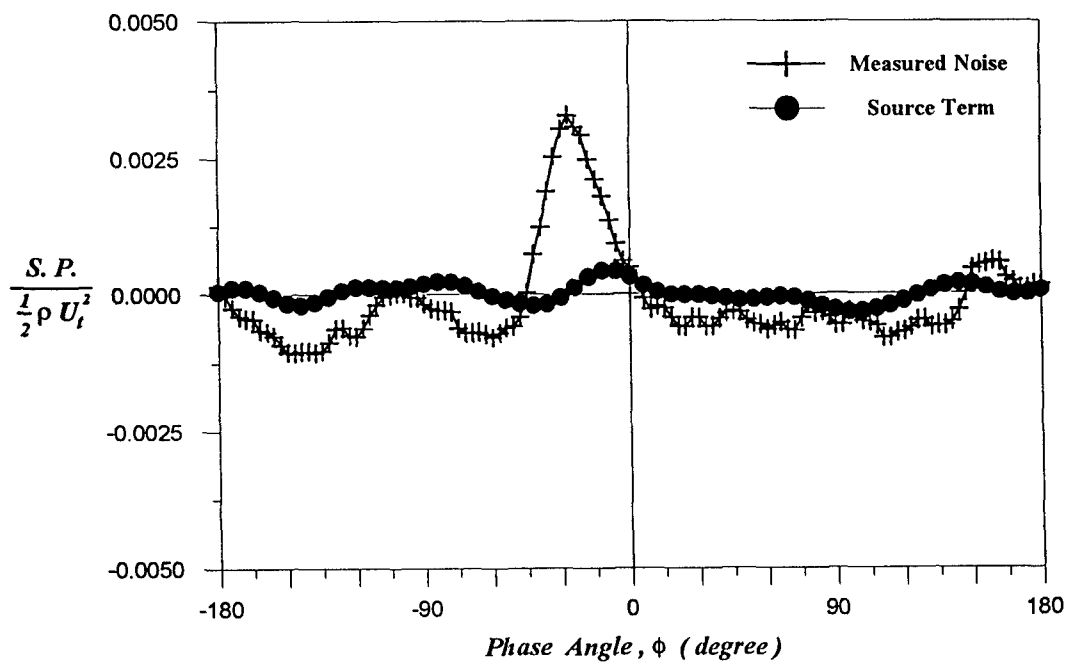


Fig. 4-18(d) ($\alpha_s = -5^\circ$, $\beta_e @ 55\%R = 5.82^\circ$, $U_t @ 55\%R = 16.29$ m/s.)

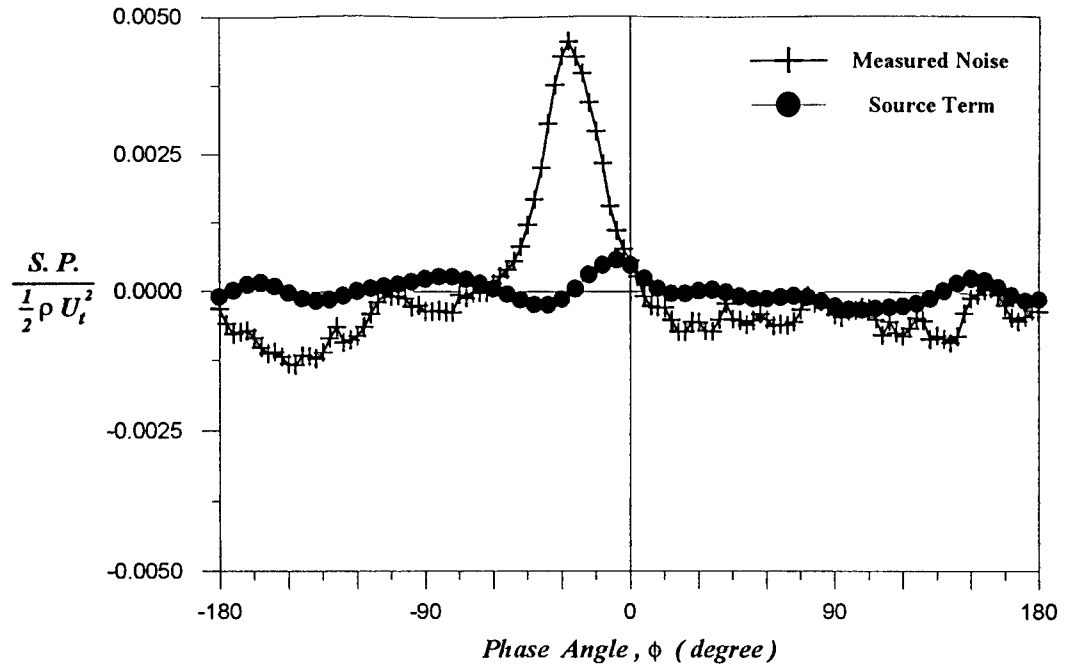


Fig. 4-18(e) ($\alpha_s = -10^\circ$, $\beta_e @ 55\%R = 5.82^\circ$, $U_t @ 55\%R = 16.29$ m/s.)

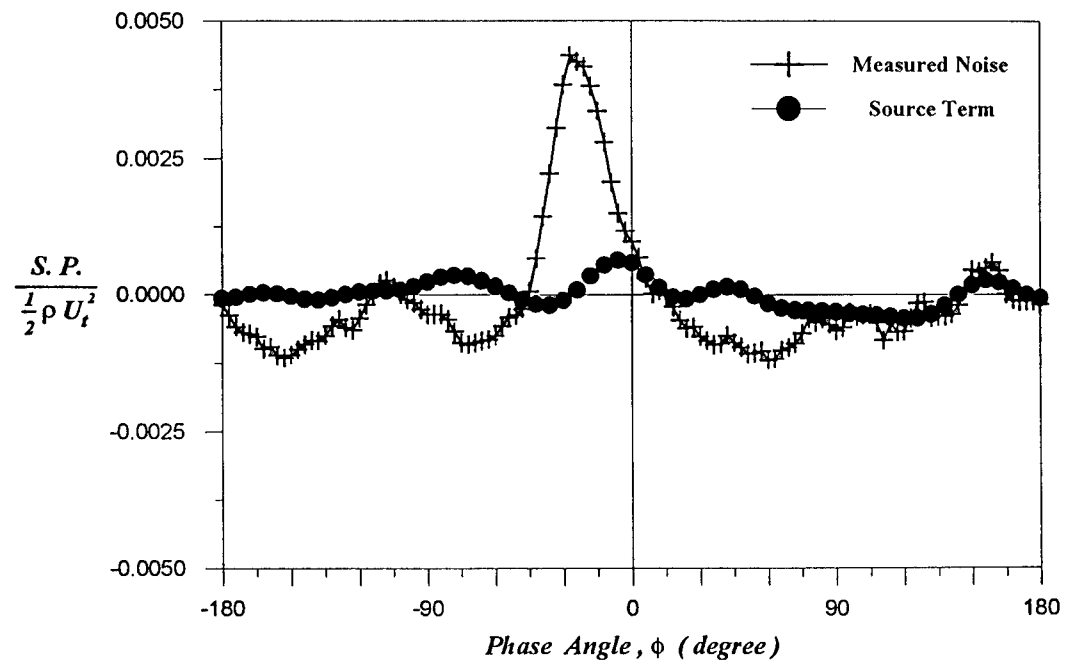


Fig. 4-18(f) ($\alpha_s = -15^\circ$, $\beta_e @ 55\%R = 5.82^\circ$, $U_t @ 55\%R = 16.29$ m/s.)

Fig. 4-18. Measured noise vs. source term : for $\beta_e = 5.82^\circ$ with α_s at (a) 10° , (b) 5° , (c) 0° , (d) -5° , (e) -10° and (f) -15° , respectively.

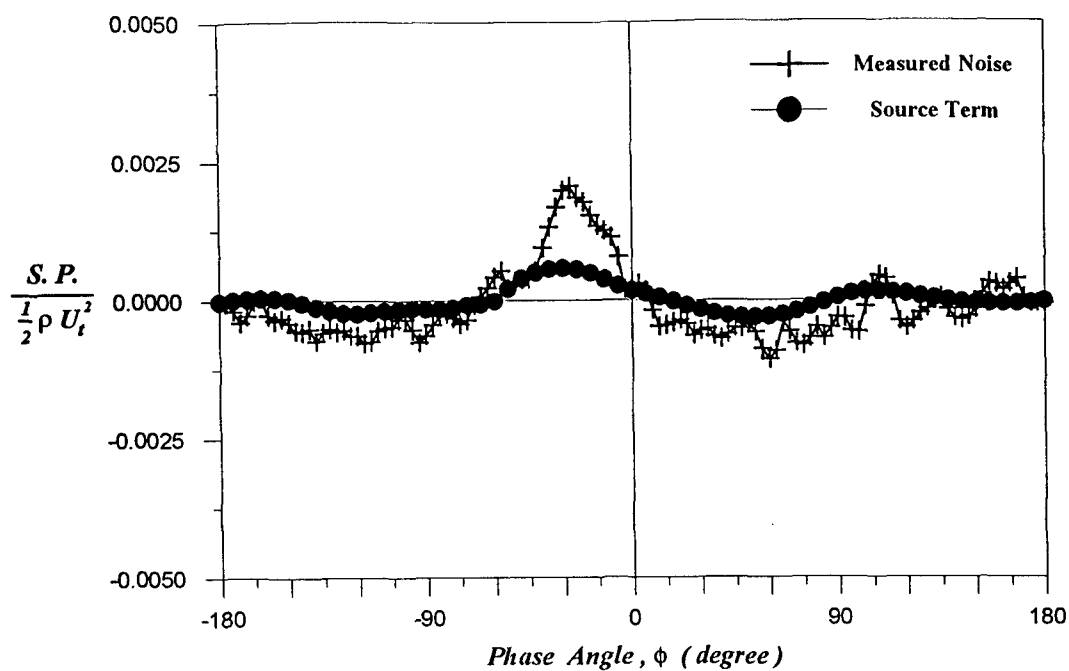


Fig. 4-19(a) ($\alpha_s = 10^\circ$, $\beta_e @ 55\%R = 9.61^\circ$, $U_t @ 55\%R = 19.92$ m/s.)

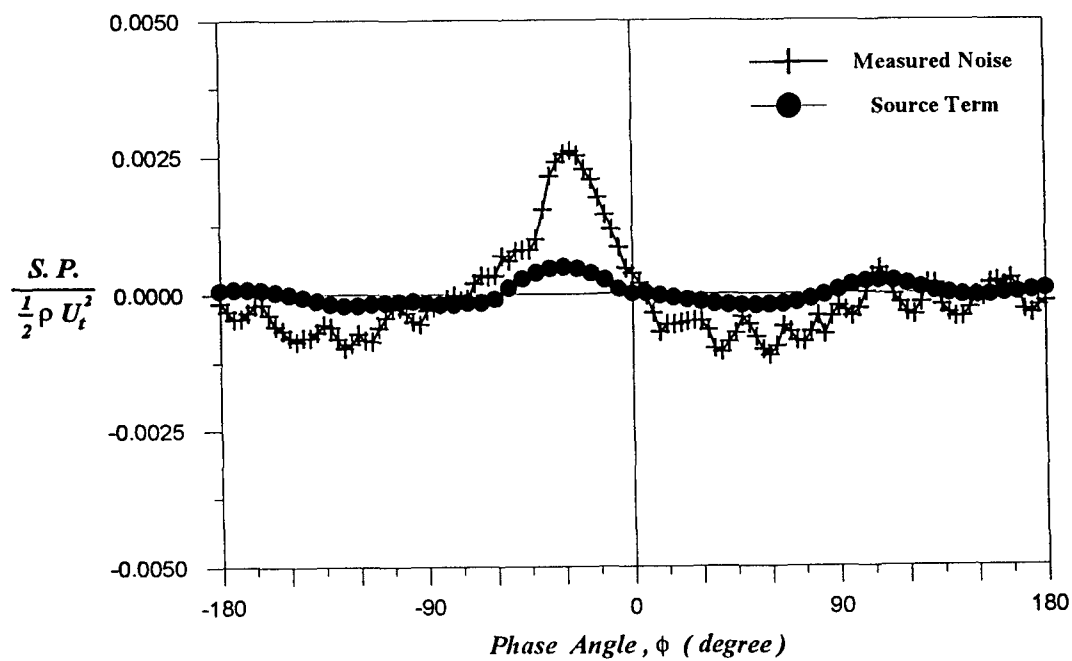


Fig. 4-19(b) ($\alpha_s = 5^\circ$, $\beta_e @ 55\%R = 9.61^\circ$, $U_t @ 55\%R = 19.92$ m/s.)

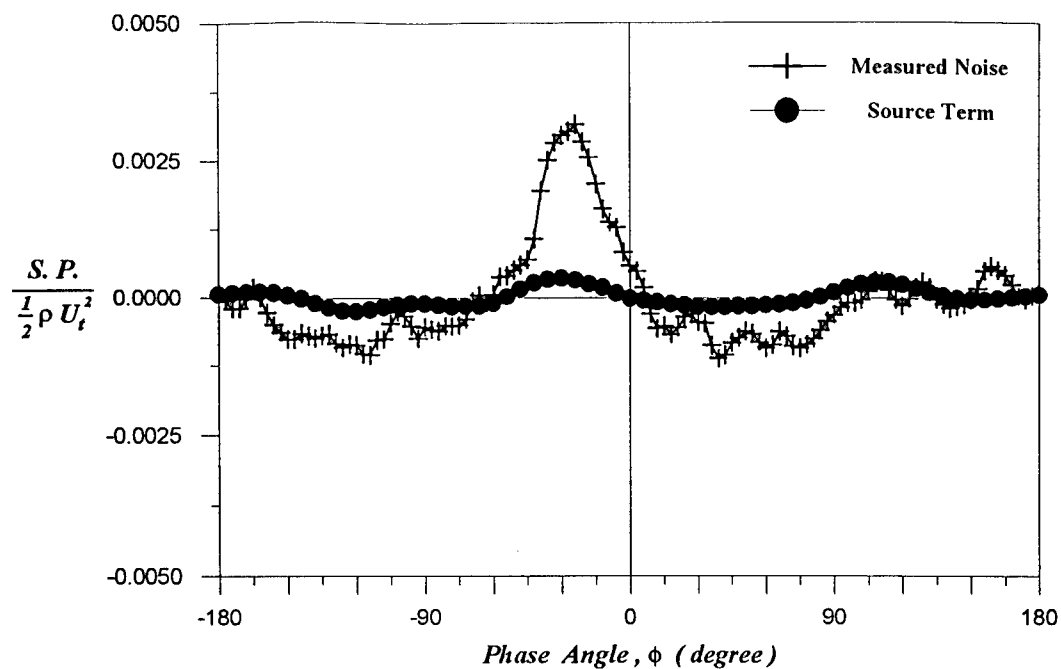


Fig. 4-19(c) ($\alpha_s = 0^\circ$, $\beta_c @ 55\%R = 9.61^\circ$, $U_t @ 55\%R = 19.92$ m/s.)

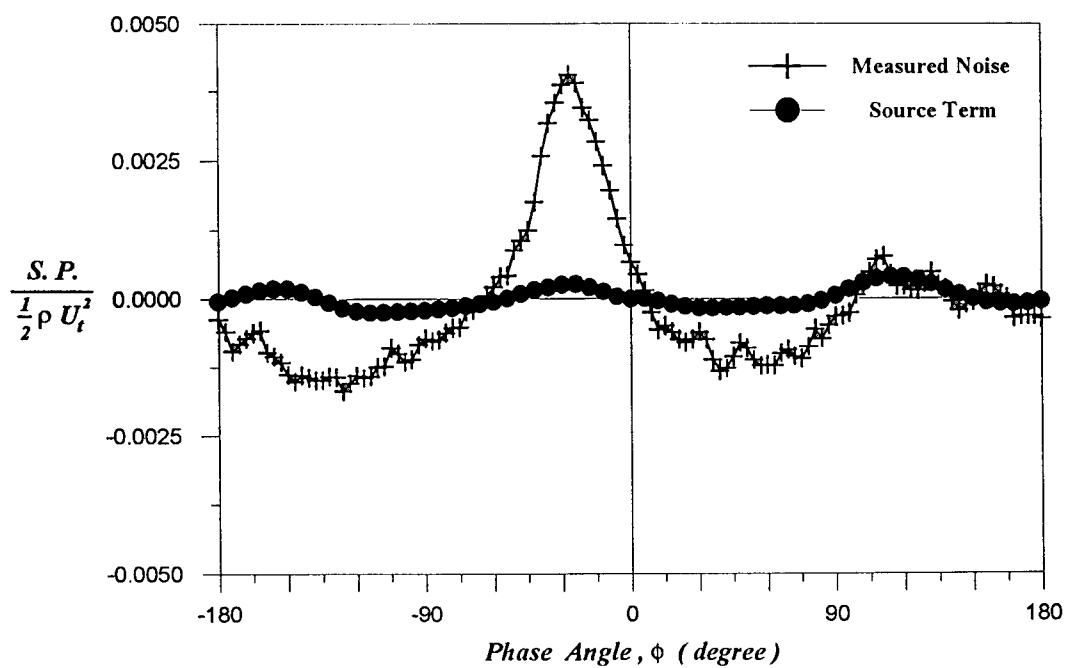


Fig. 4-19(d) ($\alpha_s = -5^\circ$, $\beta_c @ 55\%R = 9.61^\circ$, $U_t @ 55\%R = 19.92$ m/s.)

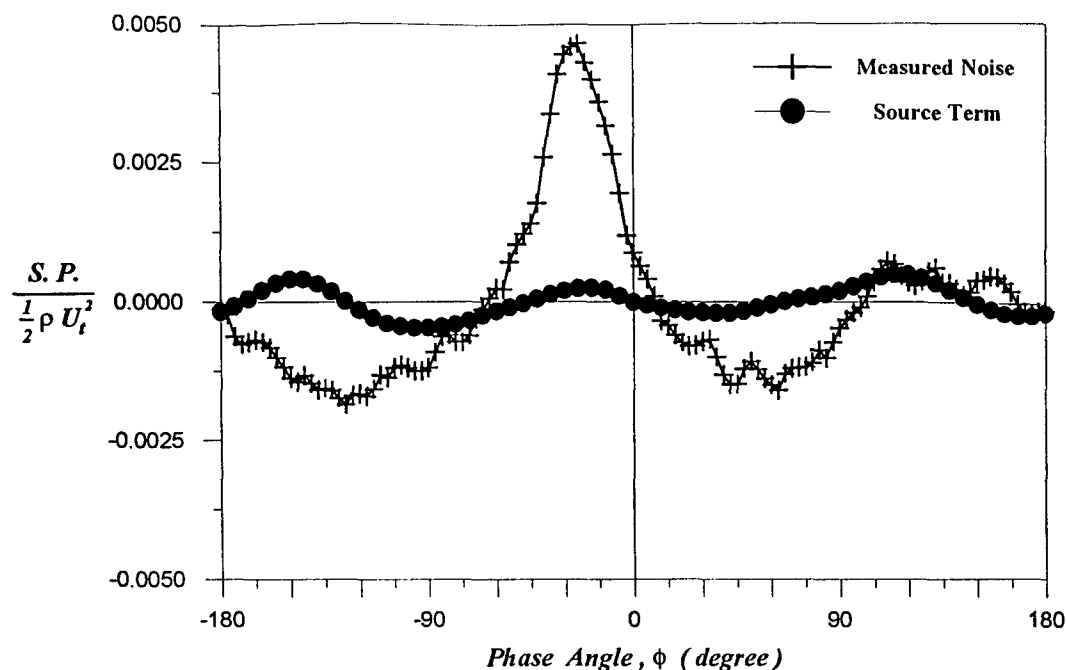


Fig. 4-19(e) ($\alpha_s = -10^\circ$, $\beta_e @ 55\%R = 9.61^\circ$, $U_t @ 55\%R = 19.92$ m/s.)

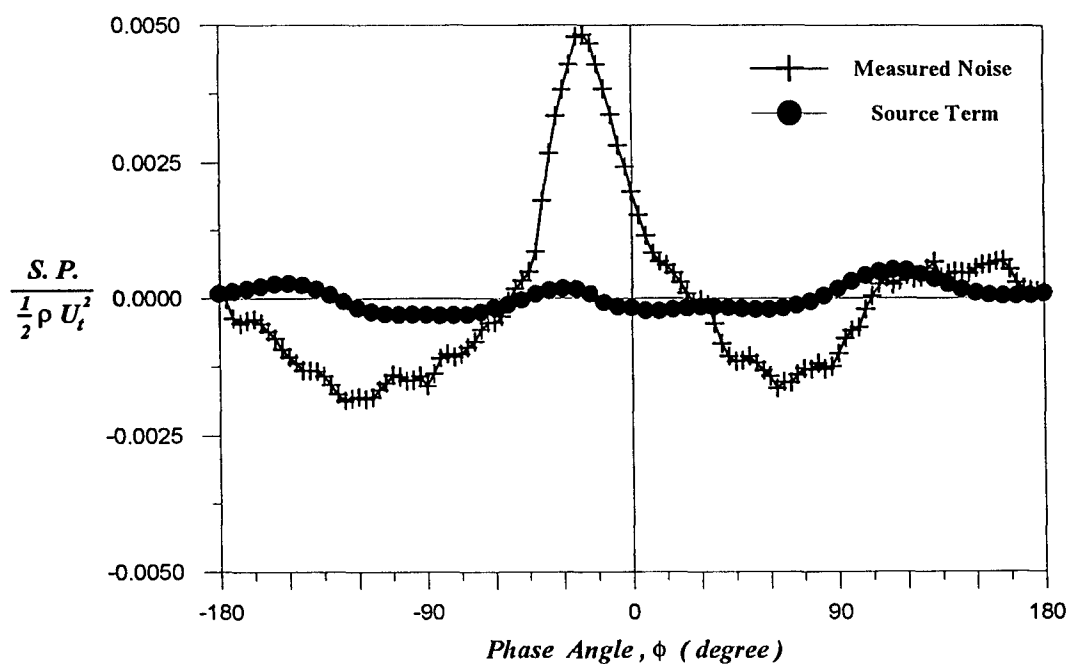
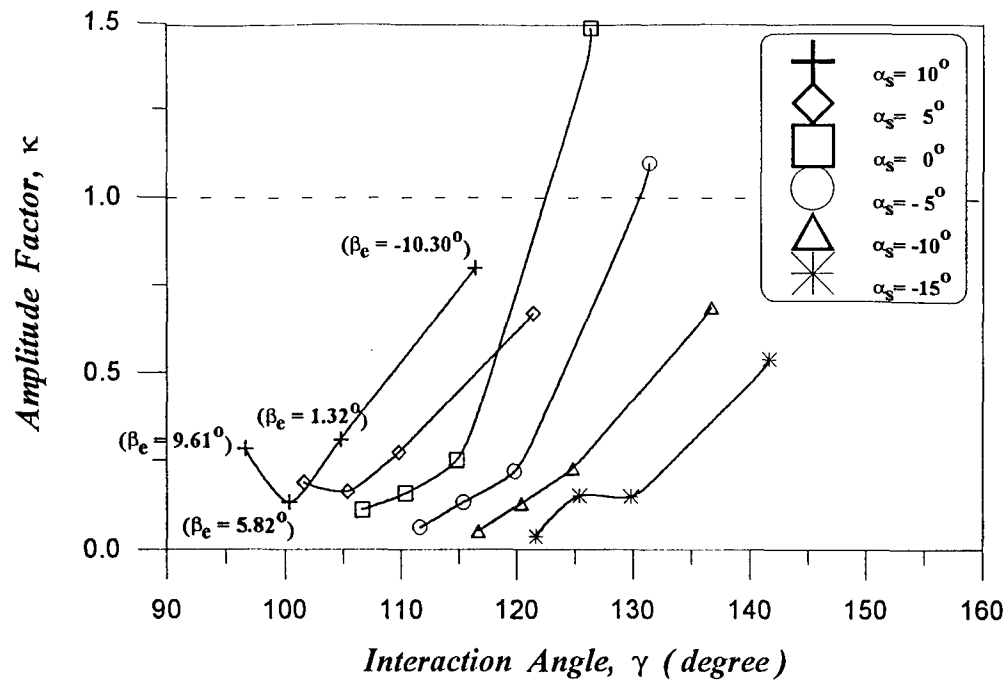
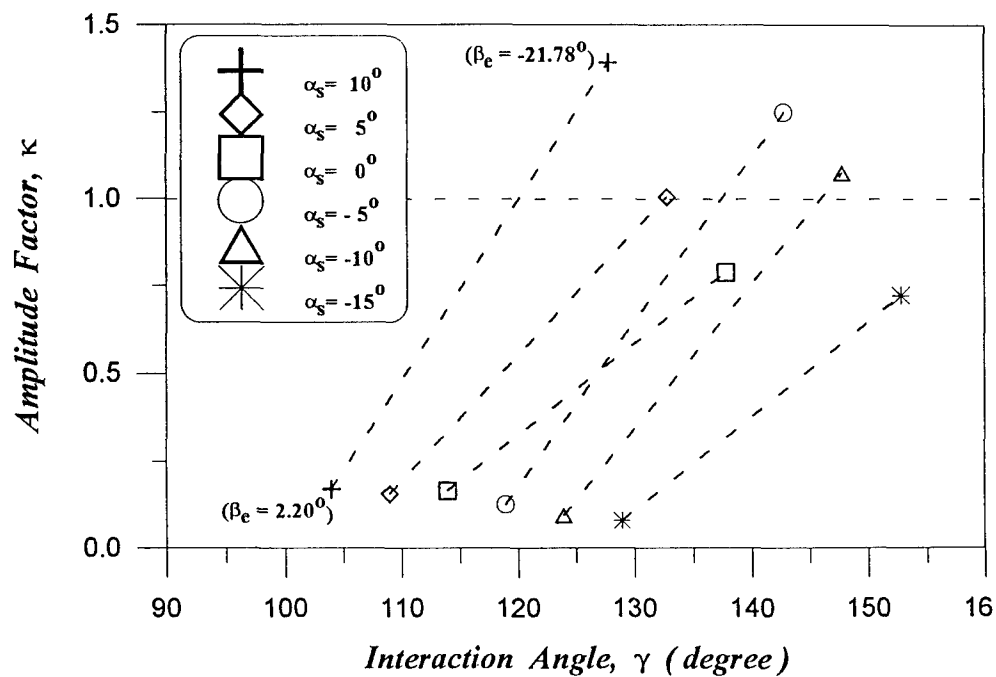


Fig. 4-19(f) ($\alpha_s = -15^\circ$, $\beta_e @ 55\%R = 9.61^\circ$, $U_t @ 55\%R = 19.92$ m/s.)

Fig. 4-19. Measured noise vs. source term : for $\beta_e = 9.61^\circ$ with α_s at (a) 10° , (b) 5° , (c) 0° , (d) -5° , (e) -10° and (f) -15° , respectively.



(a) For $U_0 = 5.62$ m/s = const.



(b) For $U_0 = 8.43$ m/s = const.

Fig. 4-21. Amplitude factor, κ , vs. interaction angle, γ : plotted for two constant freestream speeds, U_0 , at (a) 5.62 m/s and (b) 8.43 m/s, respectively.

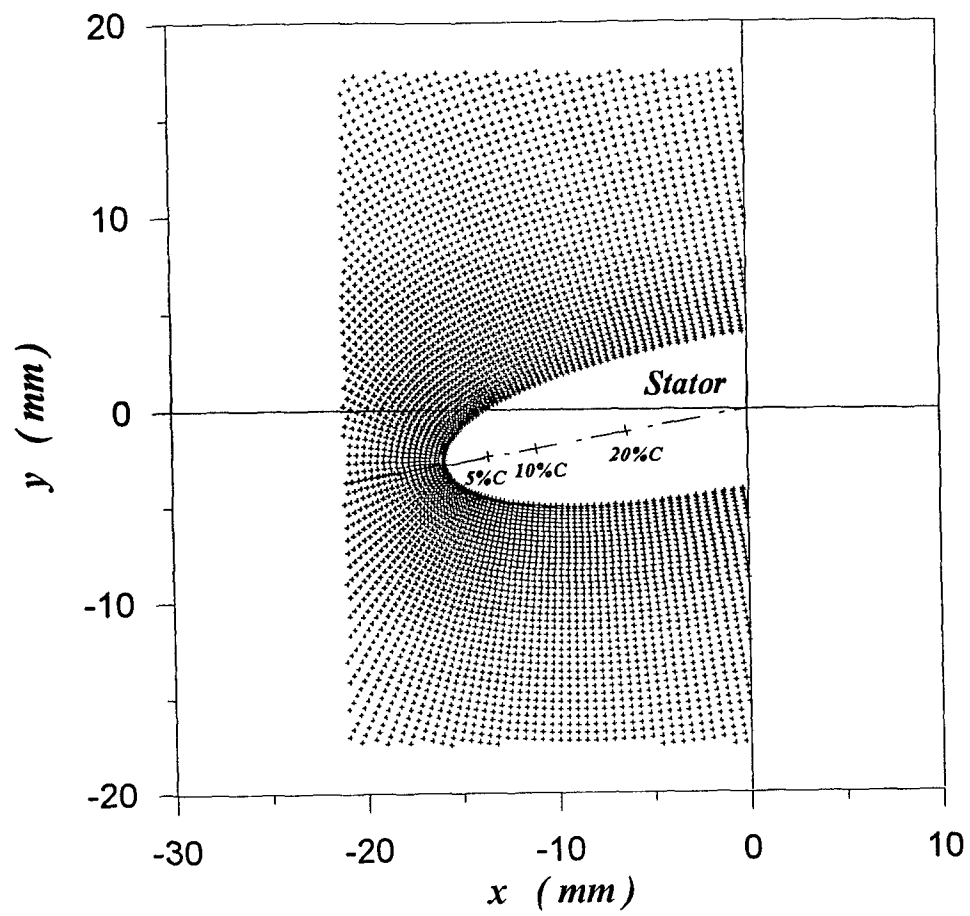


Fig. 5-1(a) $\alpha_s = 10^\circ$.

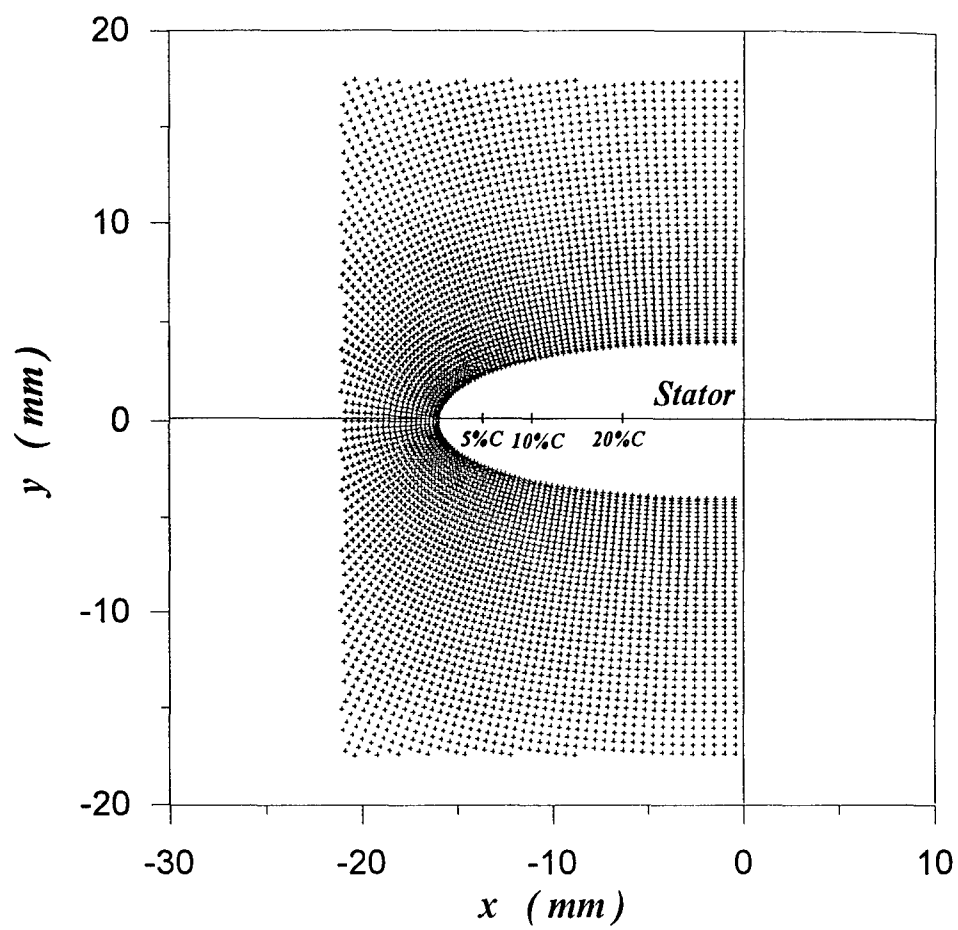


Fig. 5-1(b) $\alpha_s = 0^\circ$.

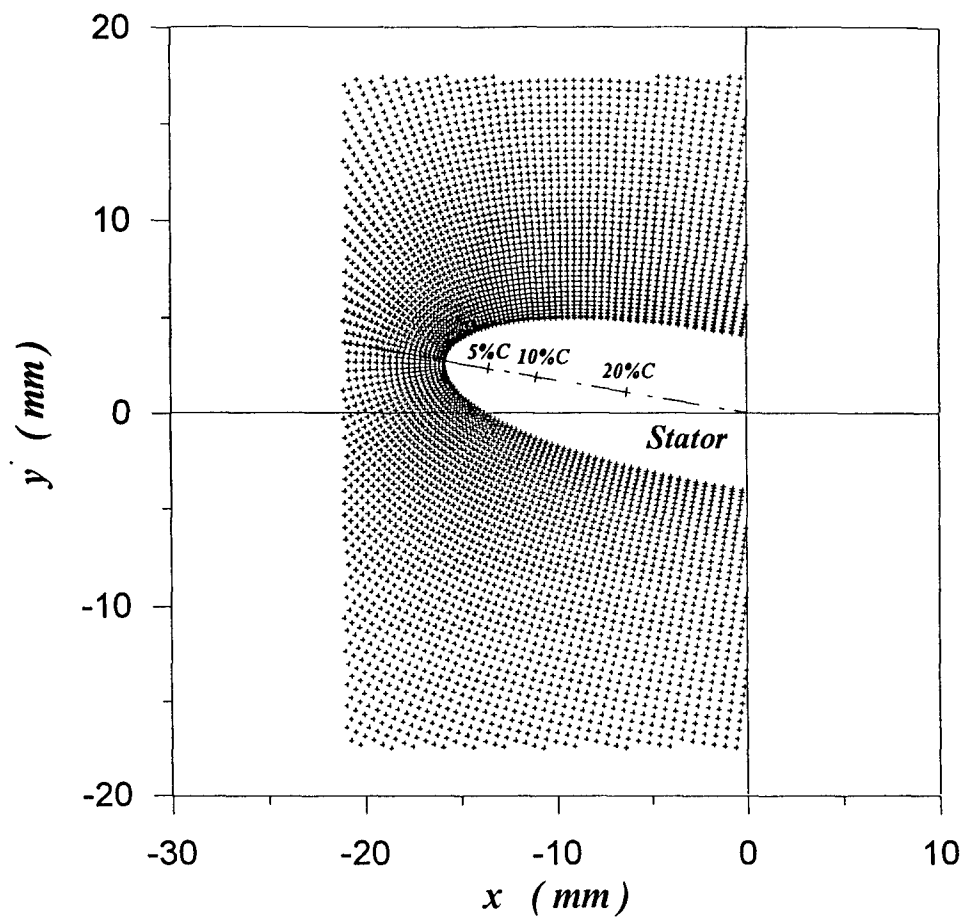


Fig. 5-1(c) $\alpha_i = -10^\circ$.

Fig. 5-1. 4,500 hot-wire stations around the stator from the leading edge to 32% chord length with stator's AoA α_i at (a) 10° , (b) 0° and (c) -10° , respectively. The stator's chord length is 50 mm.

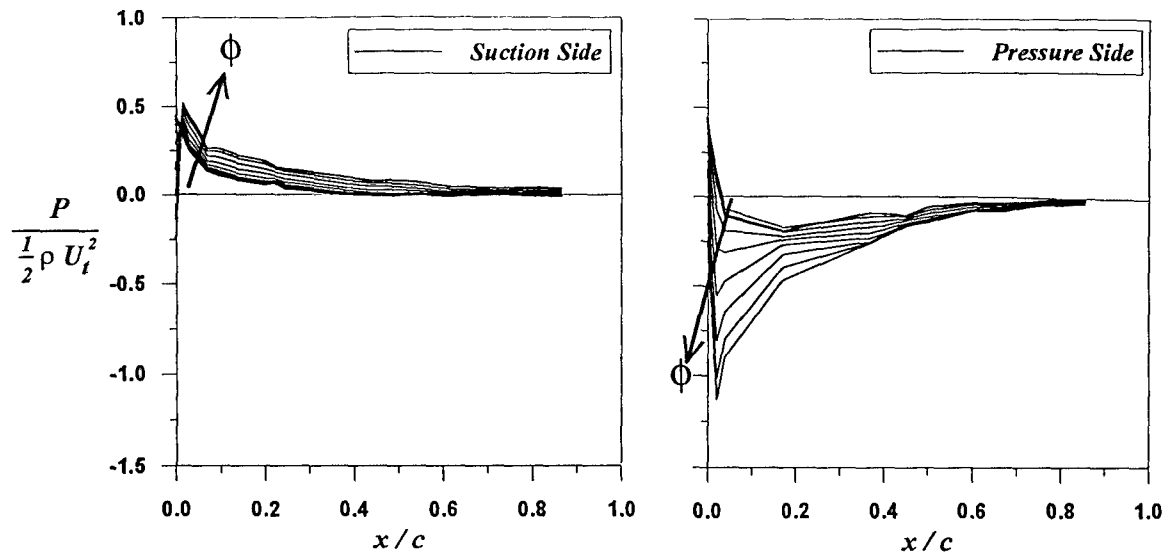


Fig. 5-2 (a) $-60^\circ < \phi < -12^\circ$: $\alpha_s = 10^\circ$, $\beta_e = -10.30^\circ$, $U_t = 9.49$ m/s.

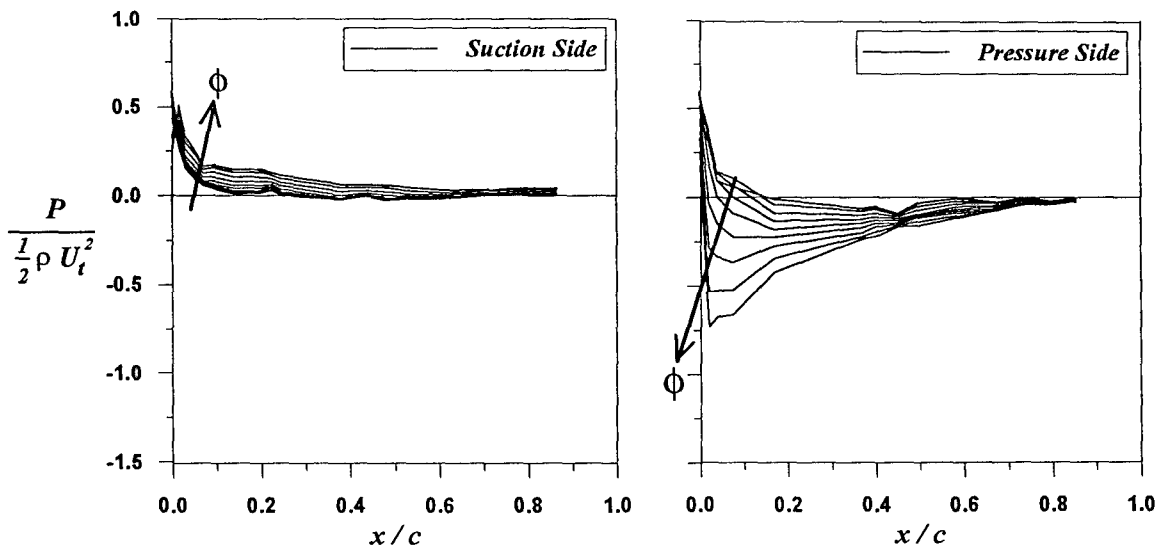


Fig. 5-2 (b) $-60^\circ < \phi < -12^\circ$: $\alpha_s = 5^\circ$, $\beta_e = -10.30^\circ$, $U_t = 9.49$ m/s.

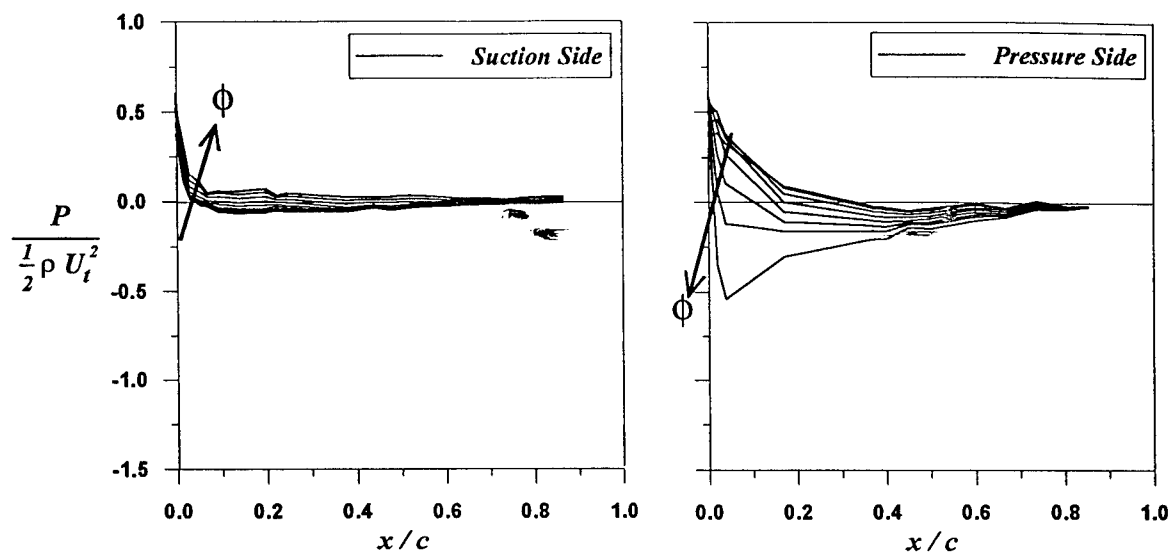


Fig. 5-2 (c) $-60^\circ < \phi < -12^\circ$: $\alpha_s = 0^\circ$, $\beta_e = -10.30^\circ$, $U_t = 9.49$ m/s.

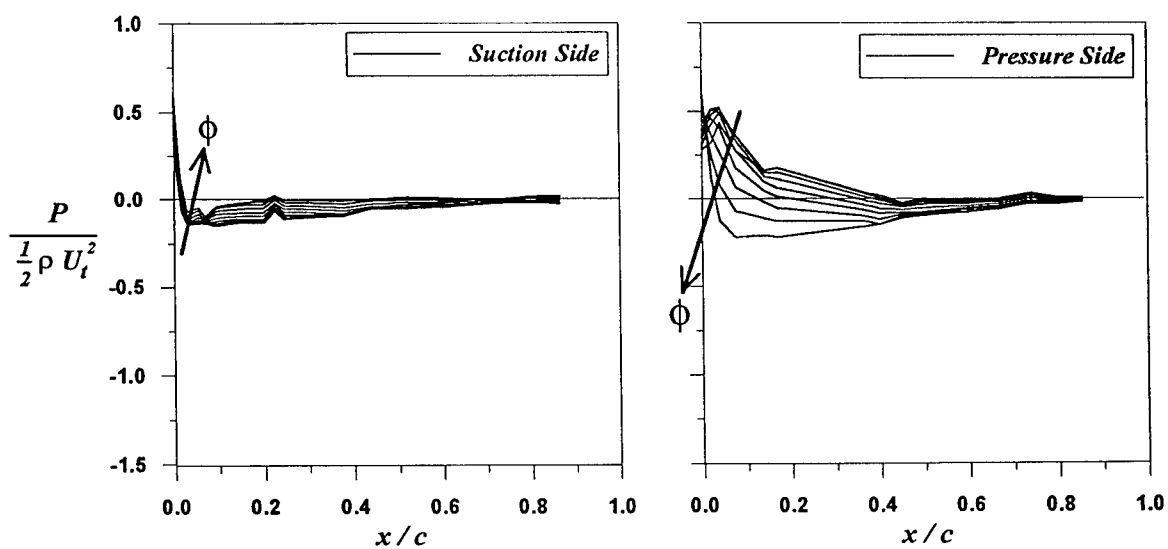


Fig. 5-2 (d) $-60^\circ < \phi < -12^\circ$: $\alpha_s = -5^\circ$, $\beta_e = -10.30^\circ$, $U_t = 9.49$ m/s.

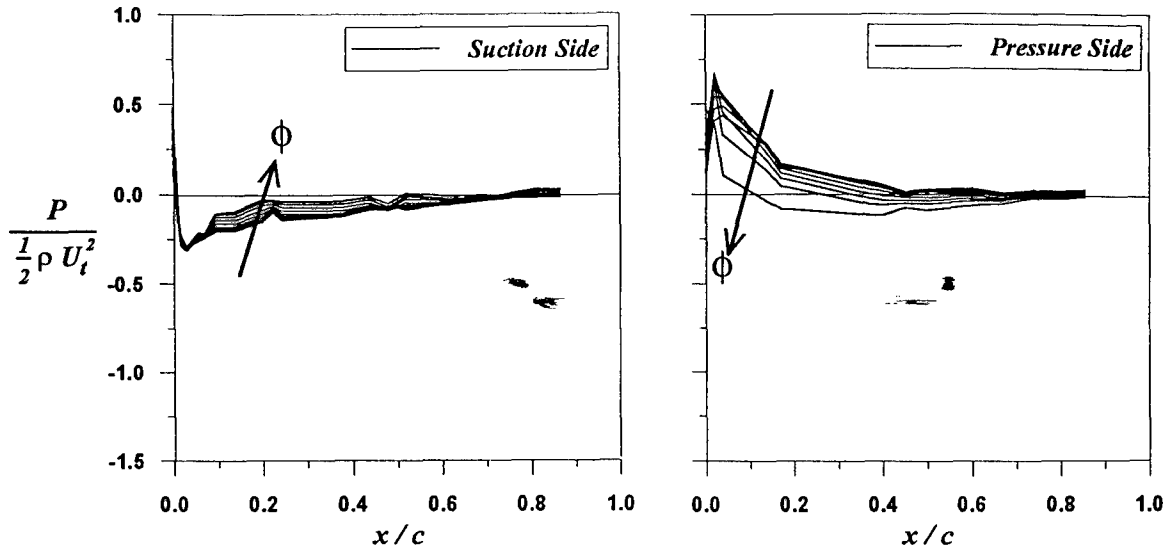


Fig. 5-2 (e) $-60^\circ < \phi < -12^\circ$: $\alpha_s = -10^\circ$, $\beta_e = -10.30^\circ$, $U_t = 9.49$ m/s.

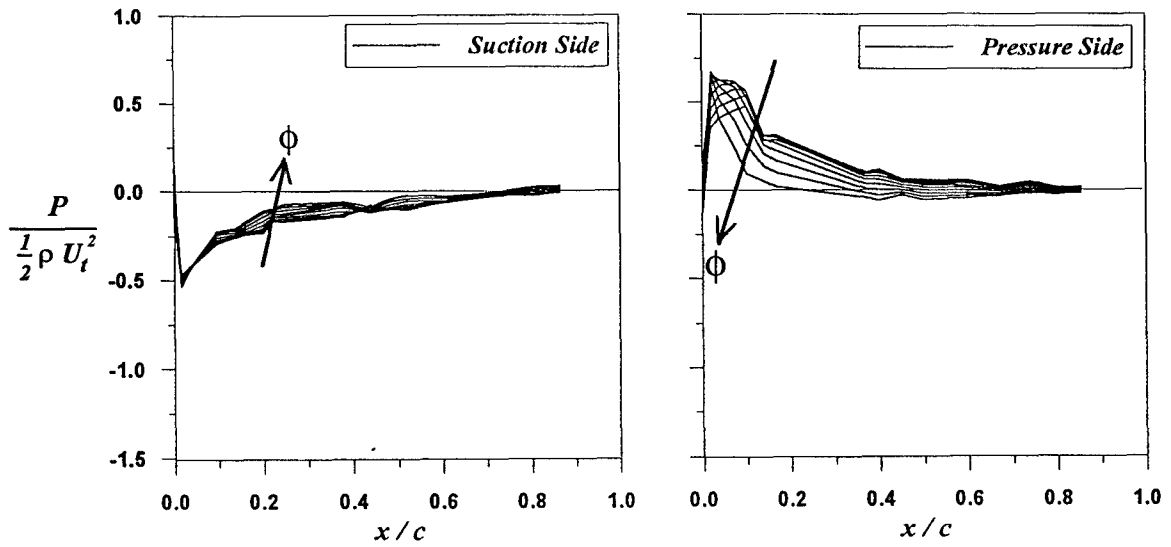


Fig. 5-2 (f) $-60^\circ < \phi < -12^\circ$: $\alpha_s = -15^\circ$, $\beta_e = -10.30^\circ$, $U_t = 9.49$ m/s.

Fig. 5-2. Non-dimensionalized pressure distributions on both sides of the stator with stator's AoA, α_s : (a) 10° , (b) 5° , (c) 0° , (d) -5° , (e) -10° , and -15° , respectively, for $\beta_e = -10.30^\circ$ and during $-60^\circ \leq \phi \leq -12^\circ$. Note that $U_t = 9.49$ m/s with $U_o = 5.62$ m/s and U_r at 55%R = 7.65 m/s.

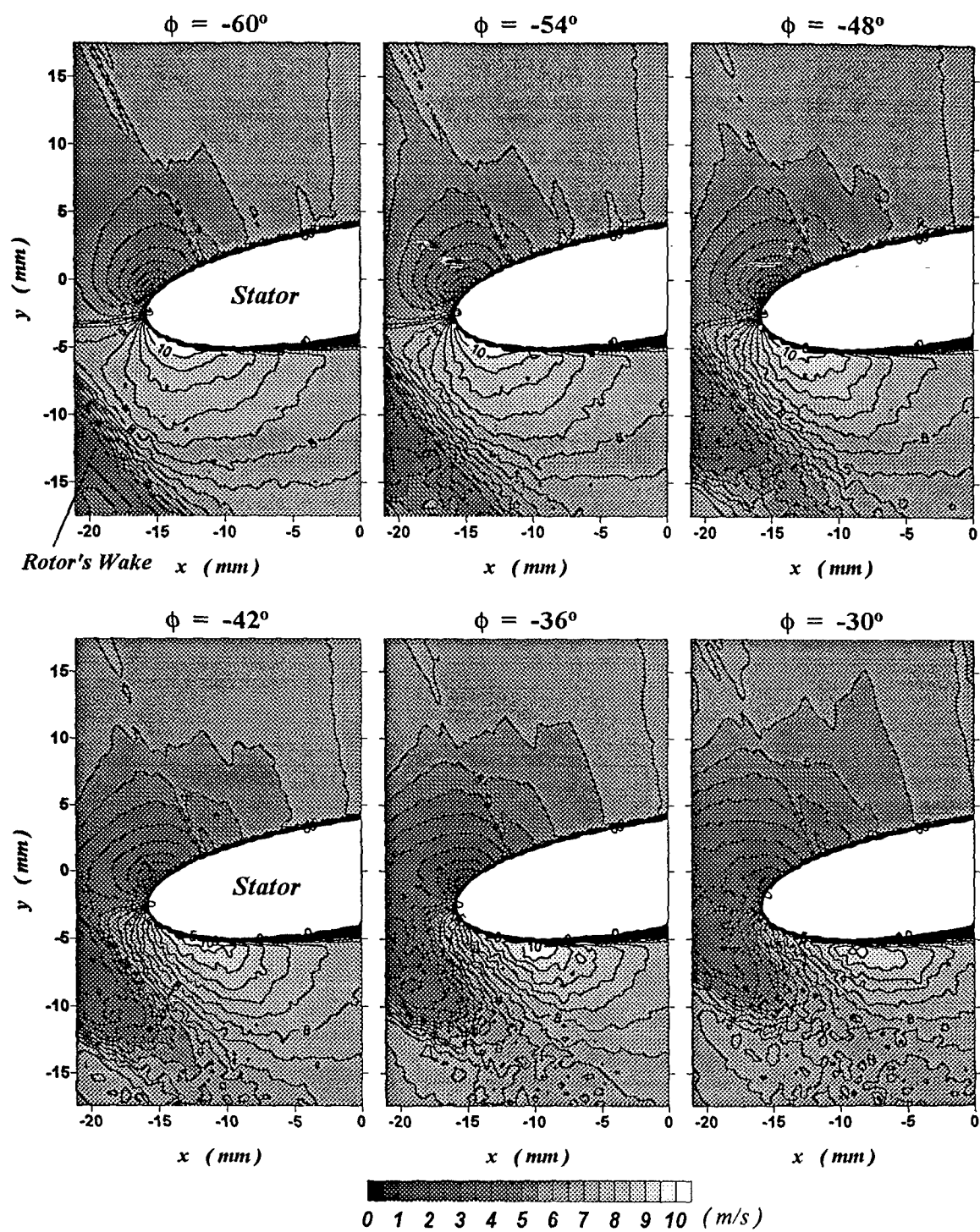


Fig. 5-3. (Caption on next page.)

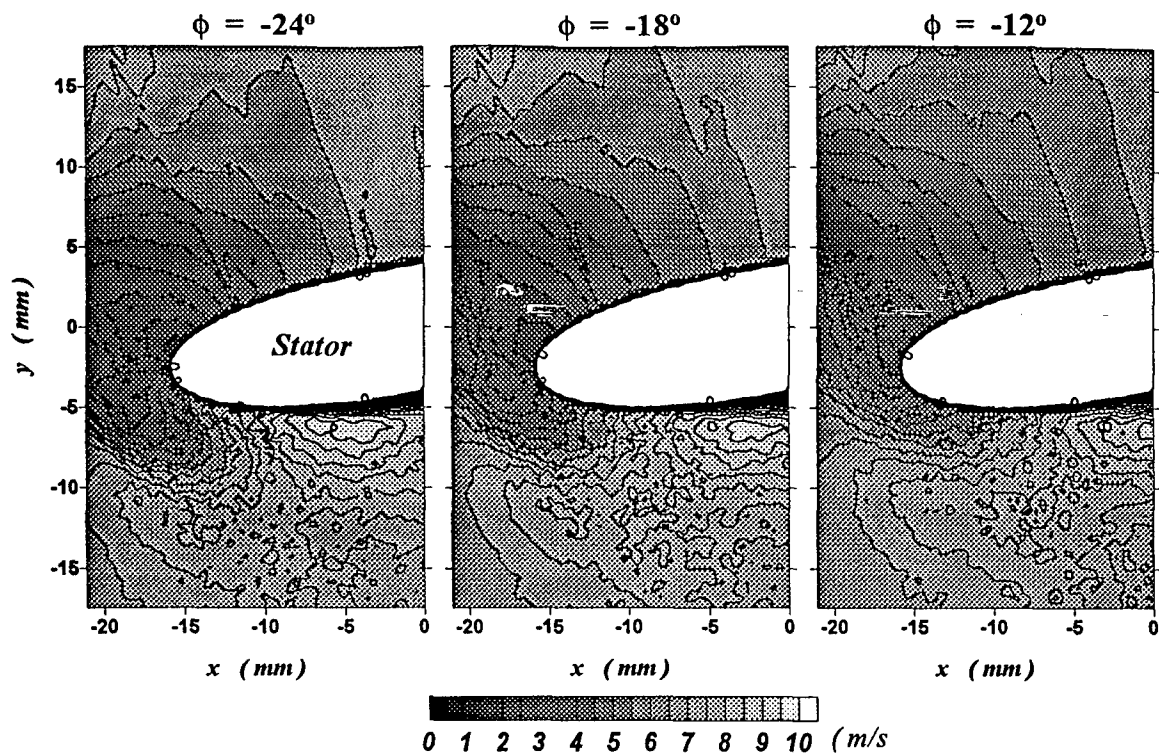


Fig. 5-3. History of velocity contours around the stator's leading edge during $-60^\circ \leq \phi \leq -12^\circ$, with stator's AoA α_s at 10° , for $\beta_s = -10.30^\circ$ and $U_i = 9.49 \text{ m/s}$ at 55%R. Note that $U_o = 5.62 \text{ m/s}$ and U_r at 55%R = 7.65 m/s .

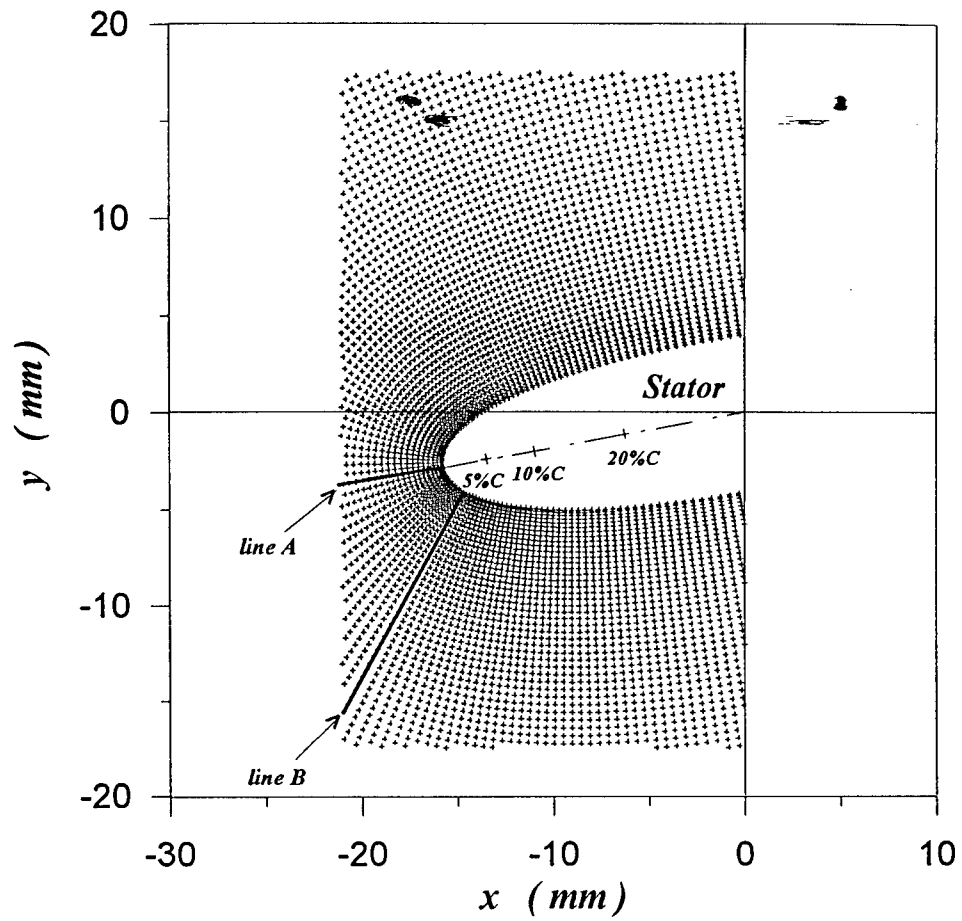


Fig. 5-4(a) Two specific lines (*Lines A and B*) normal to the stator surface at the leading edge and 2%C on the pressure side, respectively, for inspecting the stator's boundary-layer variation.

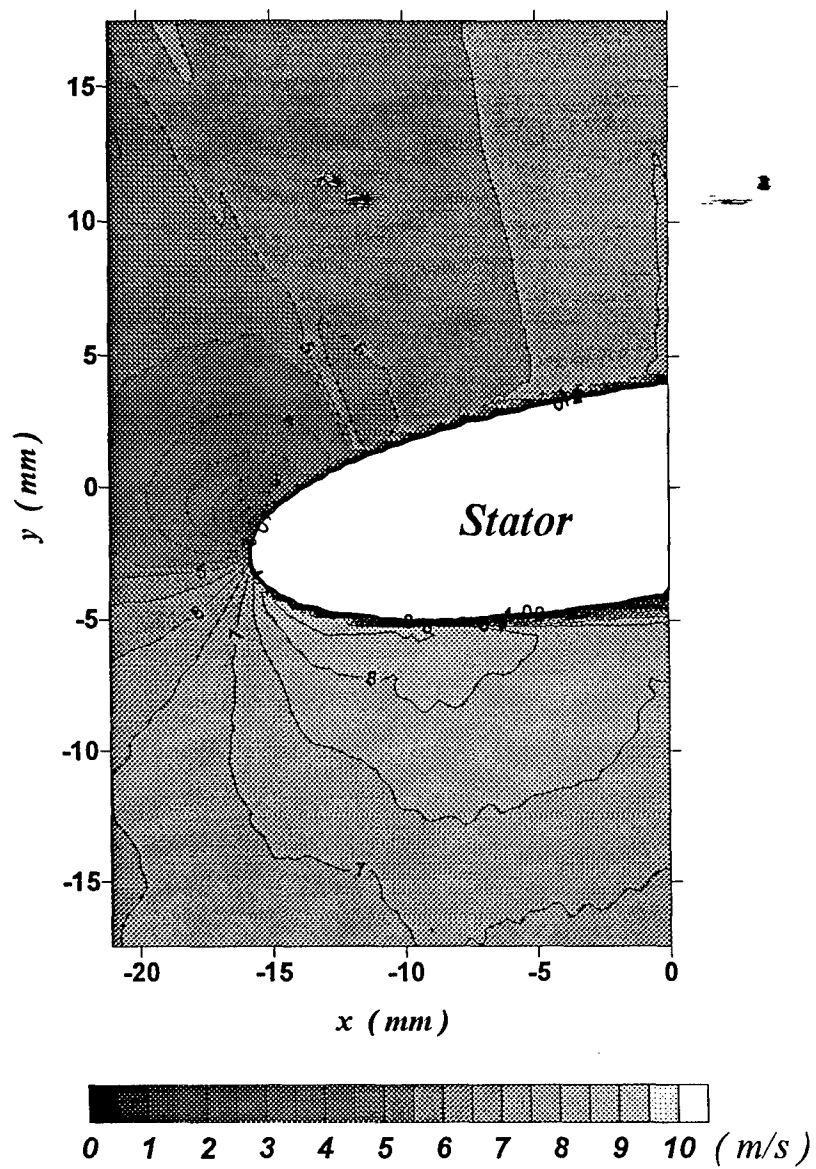


Fig. 5-4(b) The velocity contour at $\phi = \pm 180^\circ$ for $\beta_t = -10.30^\circ$ and $\alpha_s = 10^\circ$.

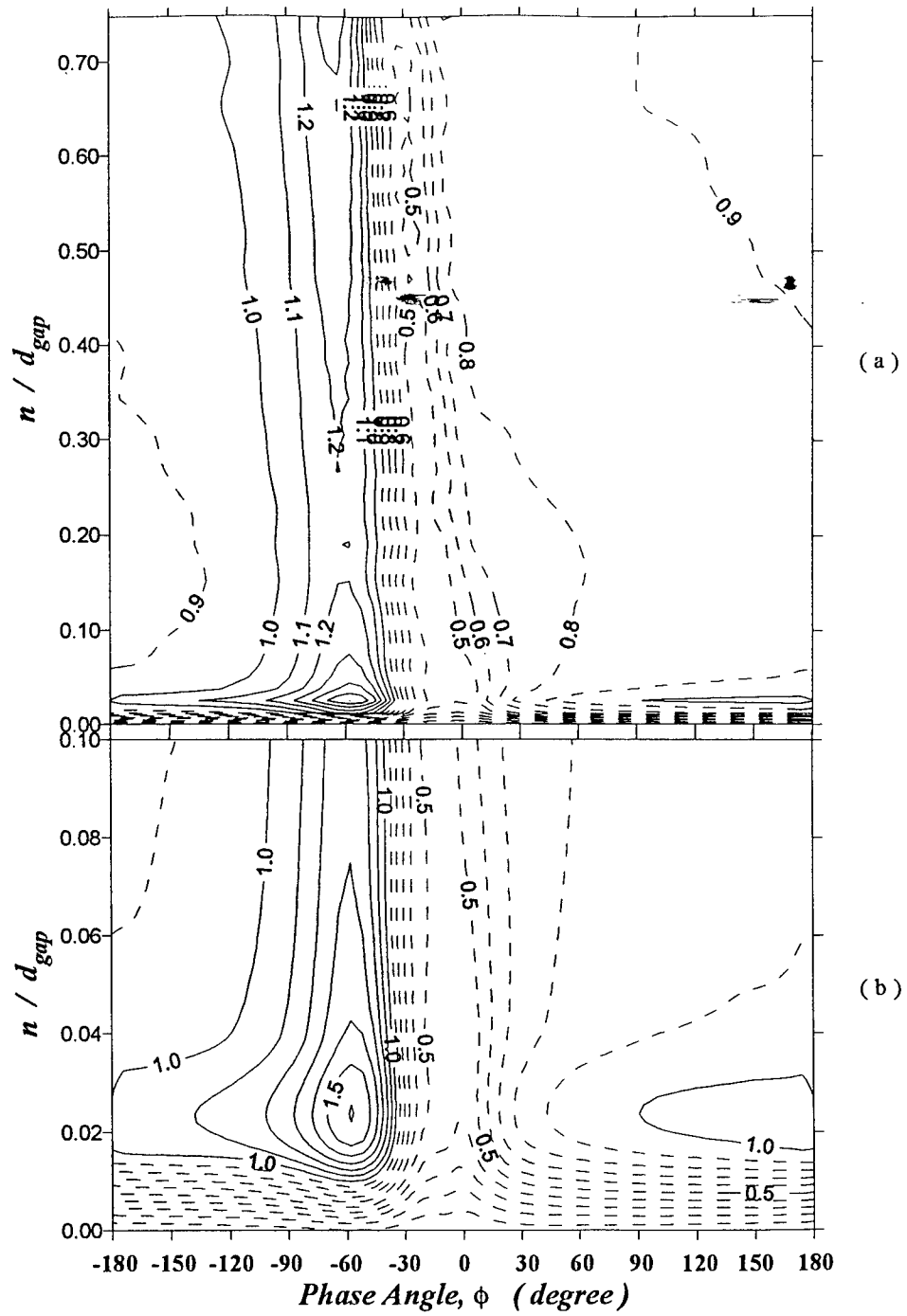


Fig. 5-5 (a) & (b) Temporal variation of the velocity field for $\beta_t = -10.30^\circ$ and $\alpha_t = 10^\circ$: (a) $0.75 d_{gap}$ and (b) $0.1 d_{gap}$ above the stator's leading edge along Line A in Fig. 5-4(a). Note that $d_{gap} = 0.71$ cm.

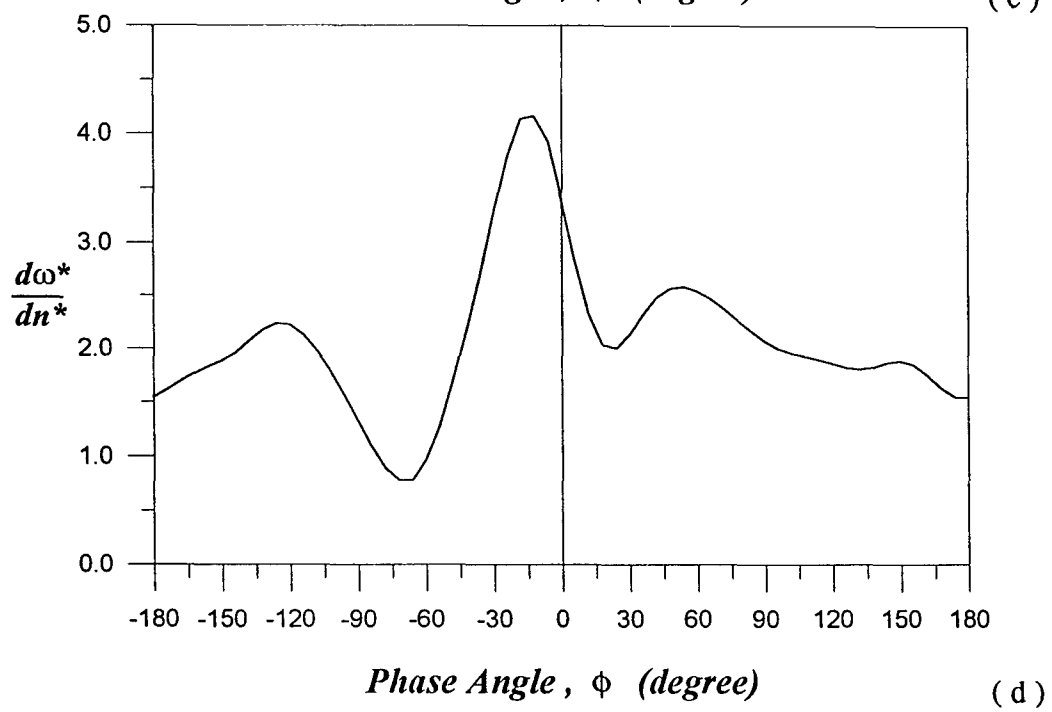
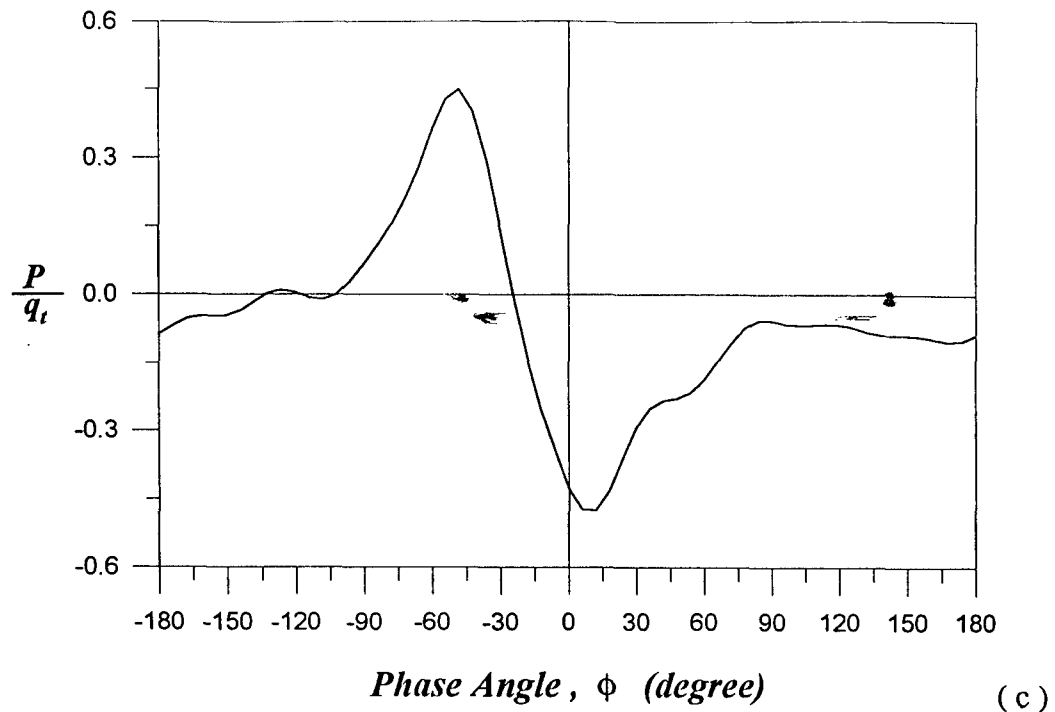


Fig. 5-5 (c) & (d) Time trace of surface pressure and vorticity gradient at the stator's leading edge for $\beta_s = -10.30^\circ$ and $\alpha_s = 10^\circ$.

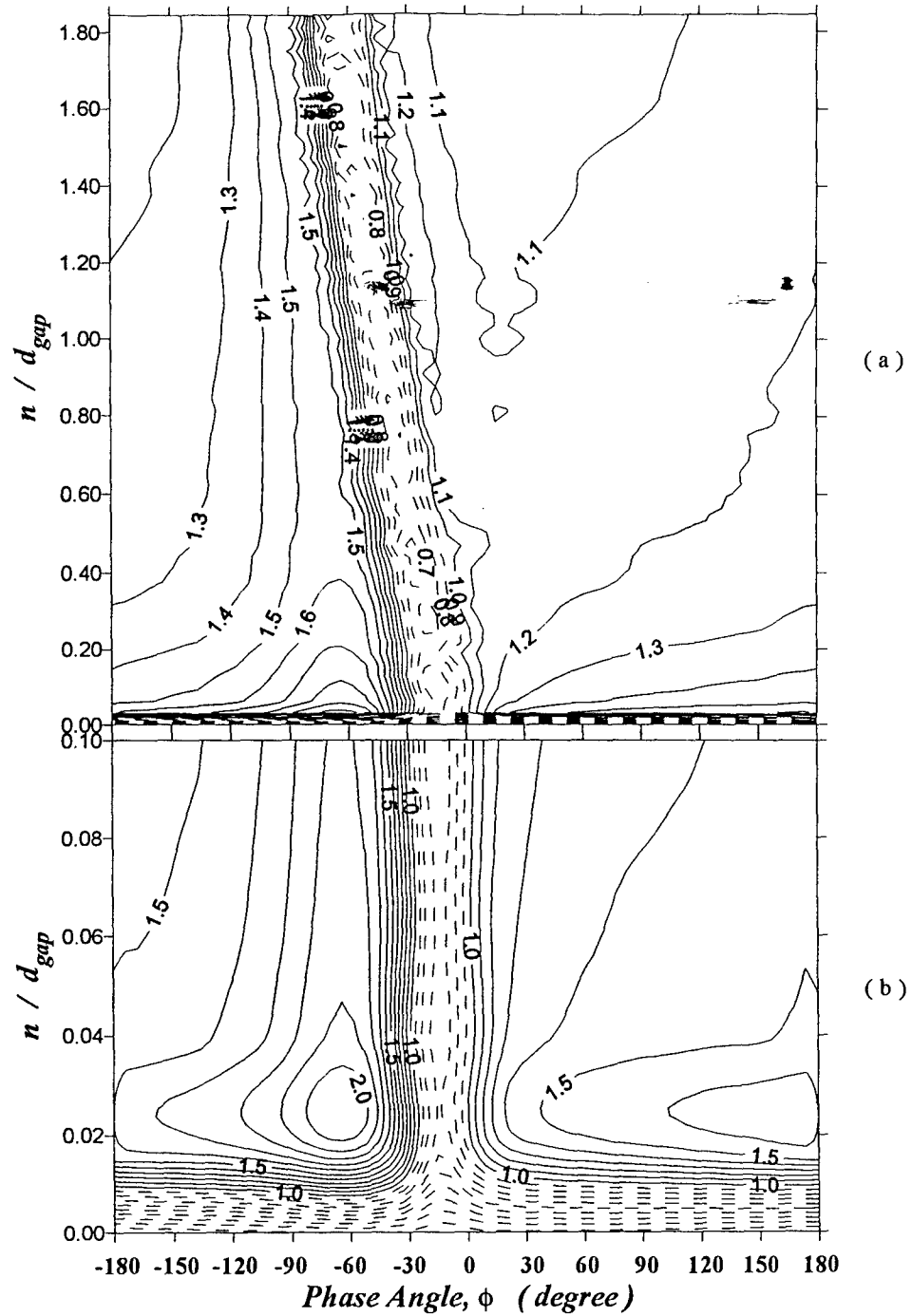


Fig. 5-6 (a) & (b) Temporal variation of the velocity field for $\beta_t = -10.30^\circ$ and $\alpha_t = 10^\circ$:
 (a) $1.85 d_{gap}$ and (b) $0.1 d_{gap}$ above the point at 2%C on stator's pressure side along Line B
 in Fig.5-4(a). Note that $d_{gap} = 0.71\text{cm}$.

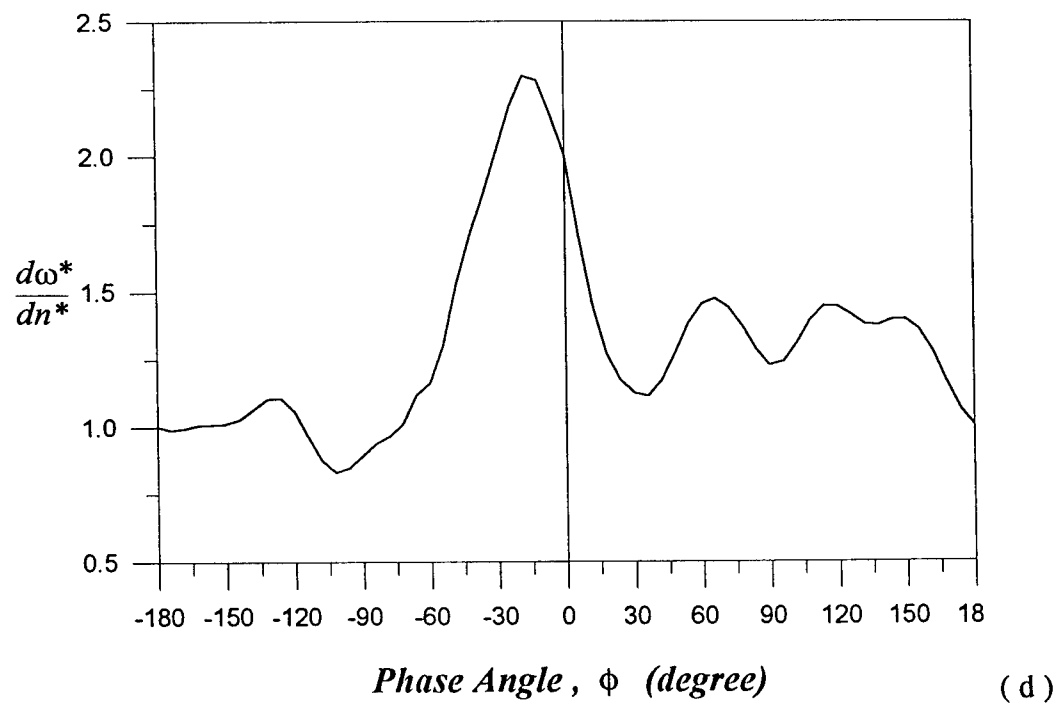
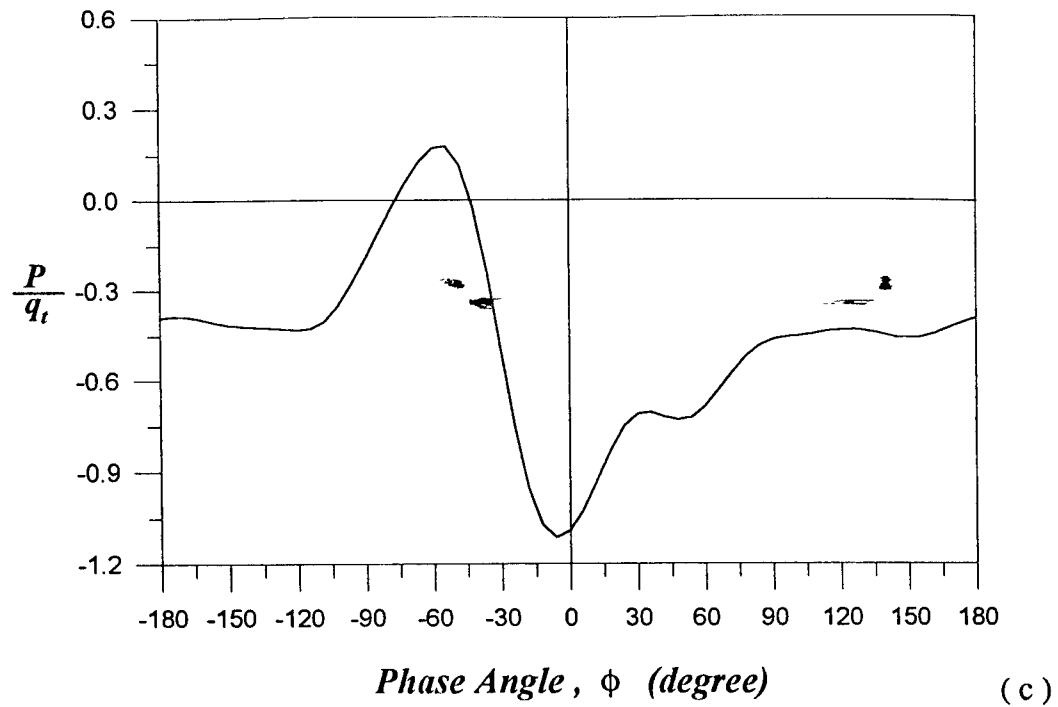


Fig. 5-6 (c) & (d) Time trace of surface pressure and vorticity gradient at the point of 2%C on the stator's pressure side for $\beta_c = -10.30^\circ$ and $\alpha_c = 10^\circ$.




Fig. 5-7. A schematic description of the flow-interaction process for $\beta_r = -10.30^\circ$ and $\alpha_r = 10^\circ$: (a) a narrow flow margin formed by the rotor's approach in $-90^\circ < \phi < -48^\circ$, and (b) the rotor's wake impinging on the stator's leading-edge portion during $-48^\circ < \phi < -30^\circ$.

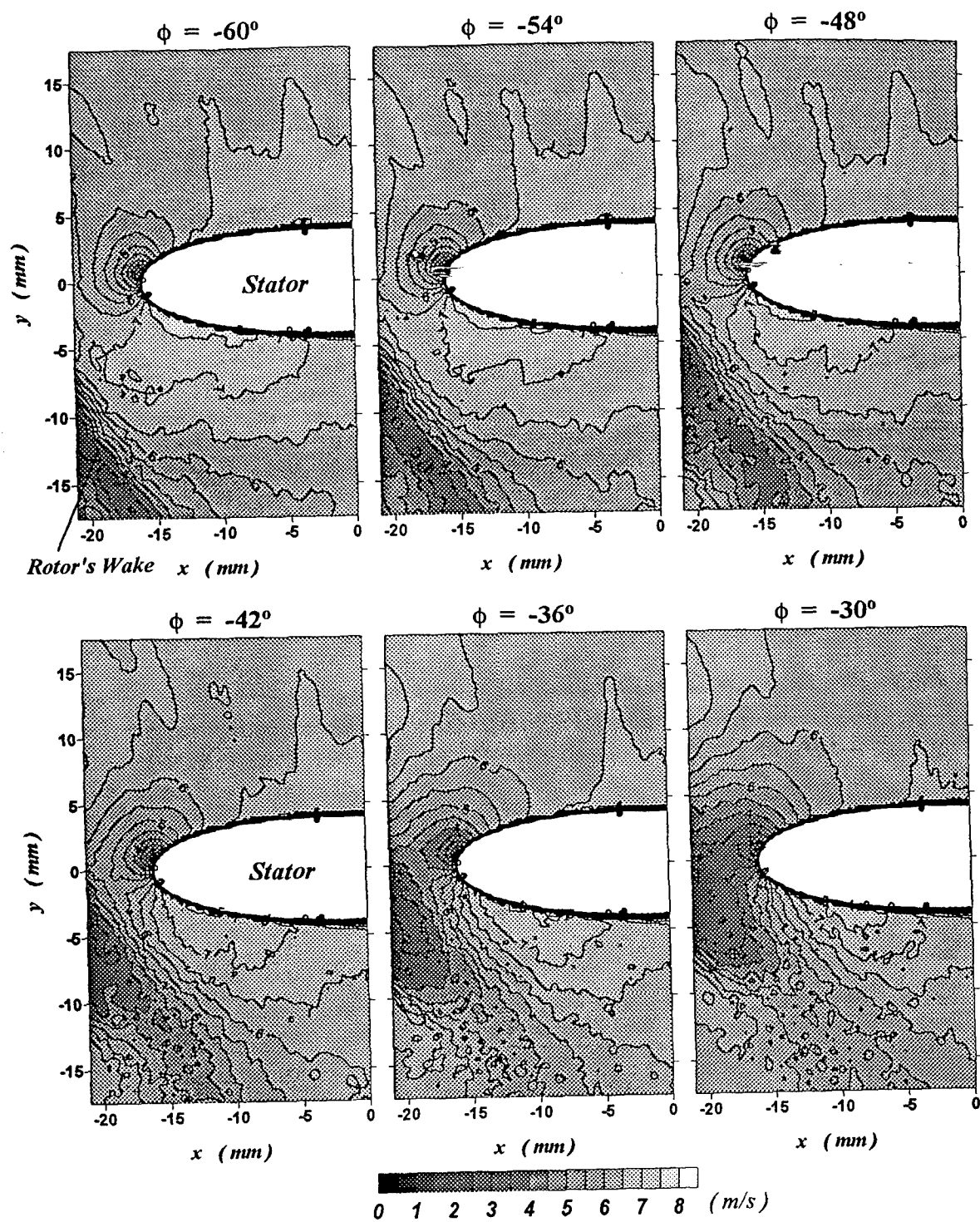


Fig. 5-8. (Caption on next page.)

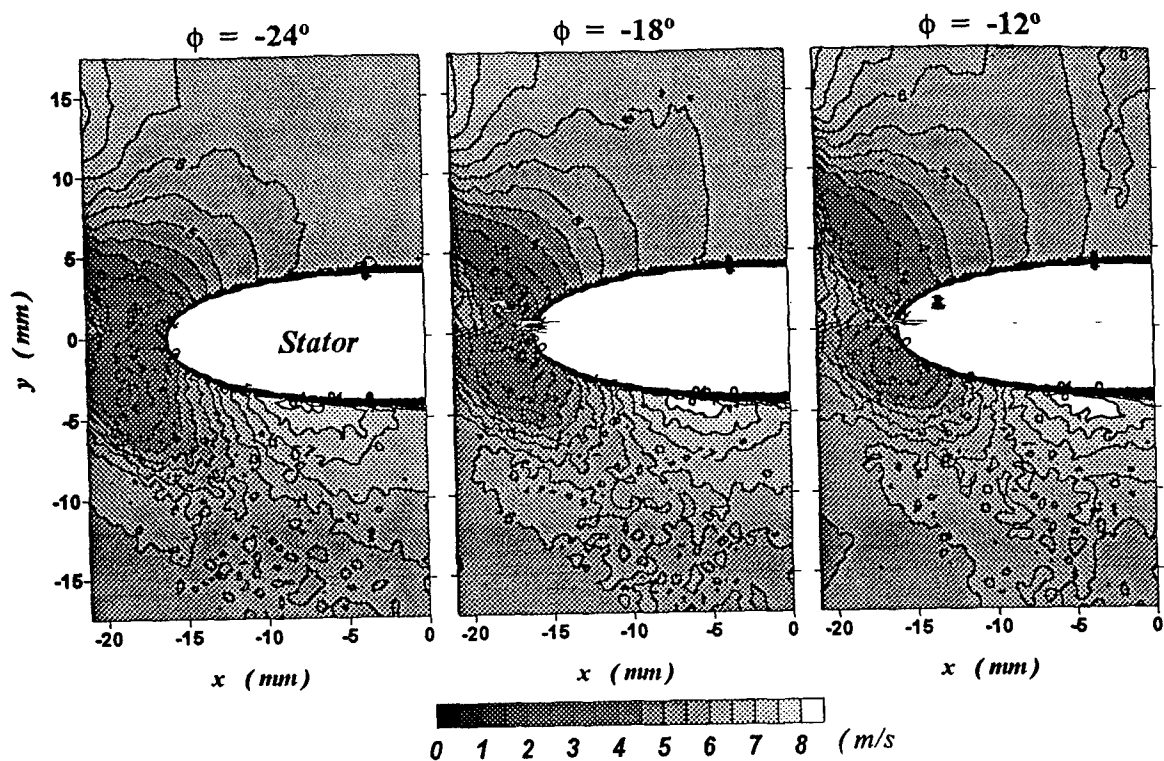


Fig. 5-8. History of velocity contours around the stator's leading edge during $-60^\circ \leq \phi \leq -12^\circ$, with stator's AoA α_s at 0° , for $\beta_s = -10.30^\circ$ and $U_i = 9.49$ m/s at 55%R. Note that $U_o = 5.62$ m/s and U_i at 55%R = 7.65 m/s.

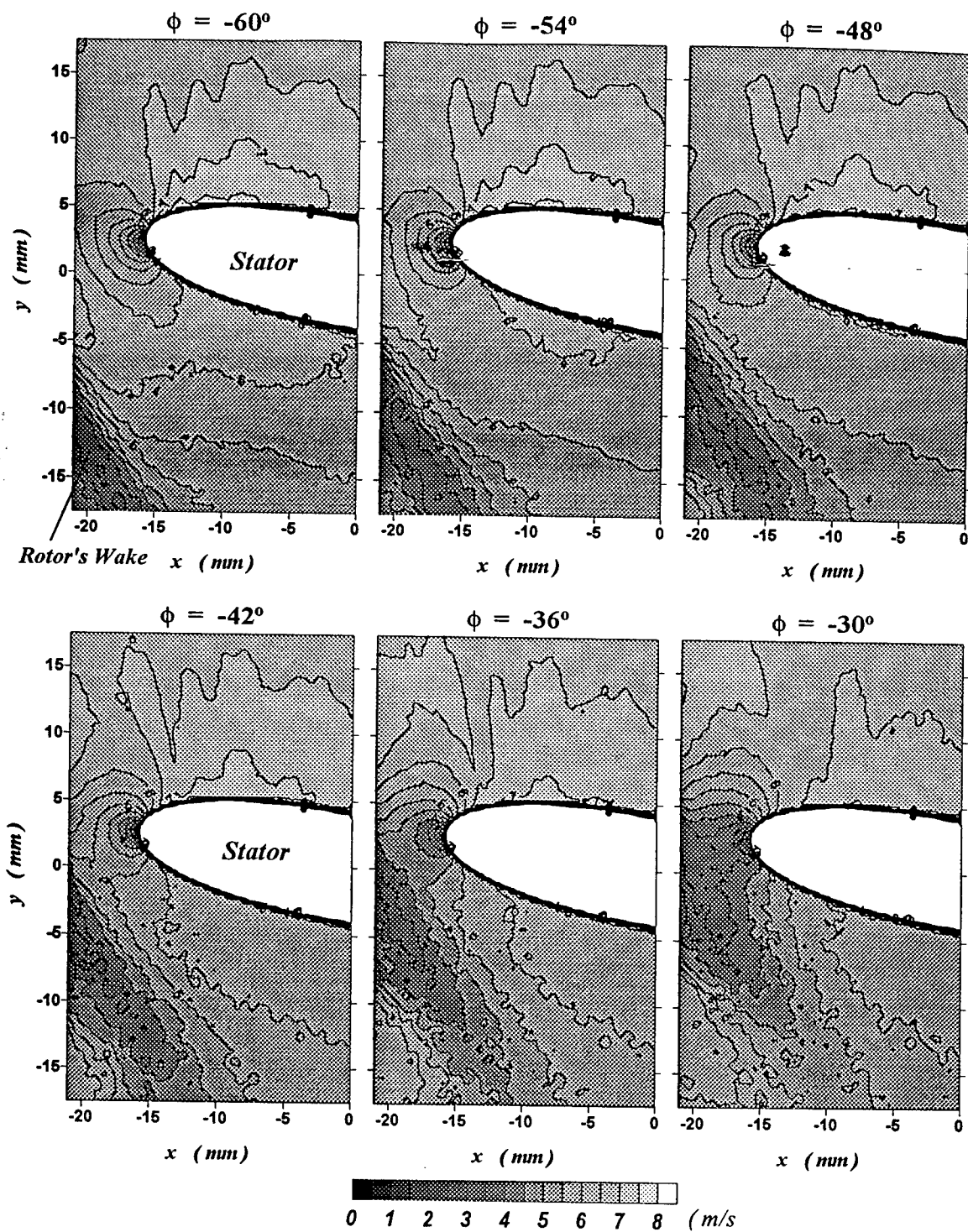


Fig. 5-9. (Caption on next page.)

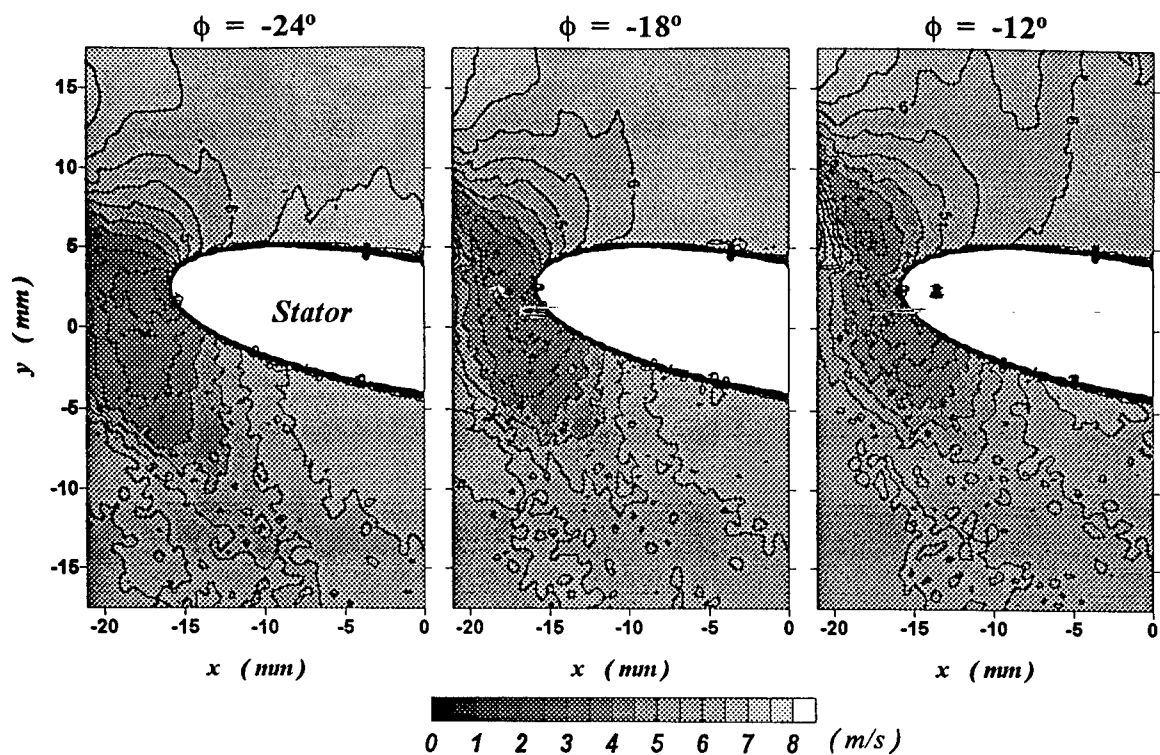


Fig. 5-9. History of velocity contours around the stator's leading edge during $-60^\circ \leq \phi \leq -12^\circ$, with stator's AoA α_s at -10° , for $\beta_t = -10.30^\circ$ and $U_t = 9.49 \text{ m/s}$ at 55%R. Note that $U_o = 5.62 \text{ m/s}$ and U_t at 55%R = 7.65 m/s .

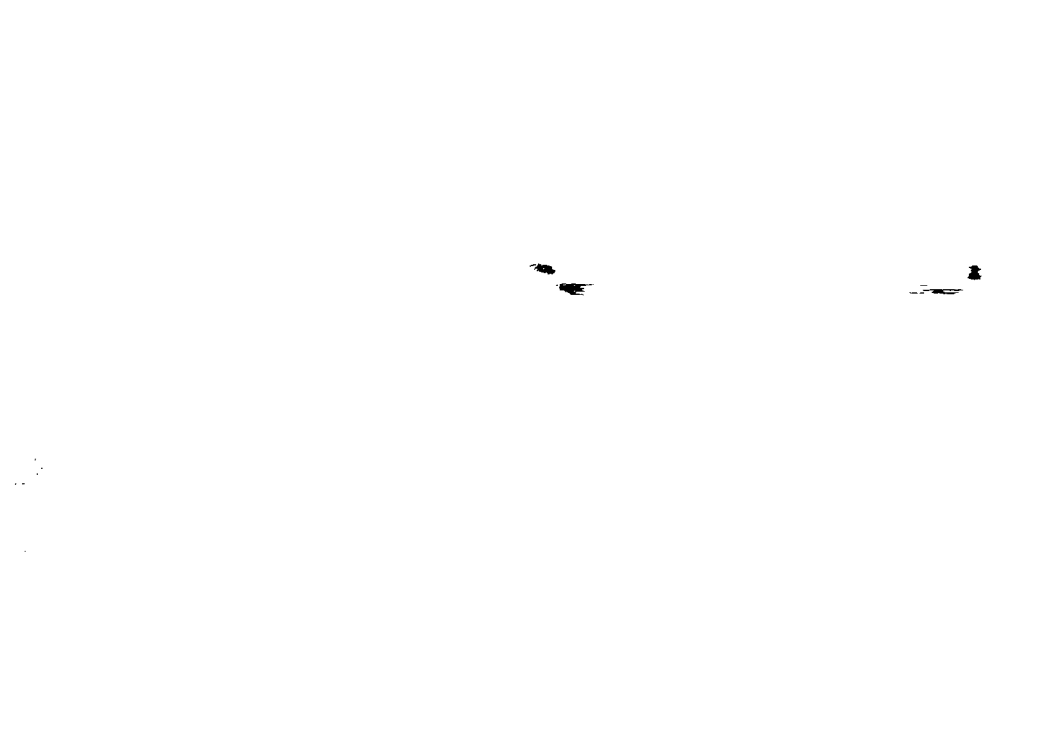


Fig. 5-10. A local coordinate system, s - n - z , on the stator surface.

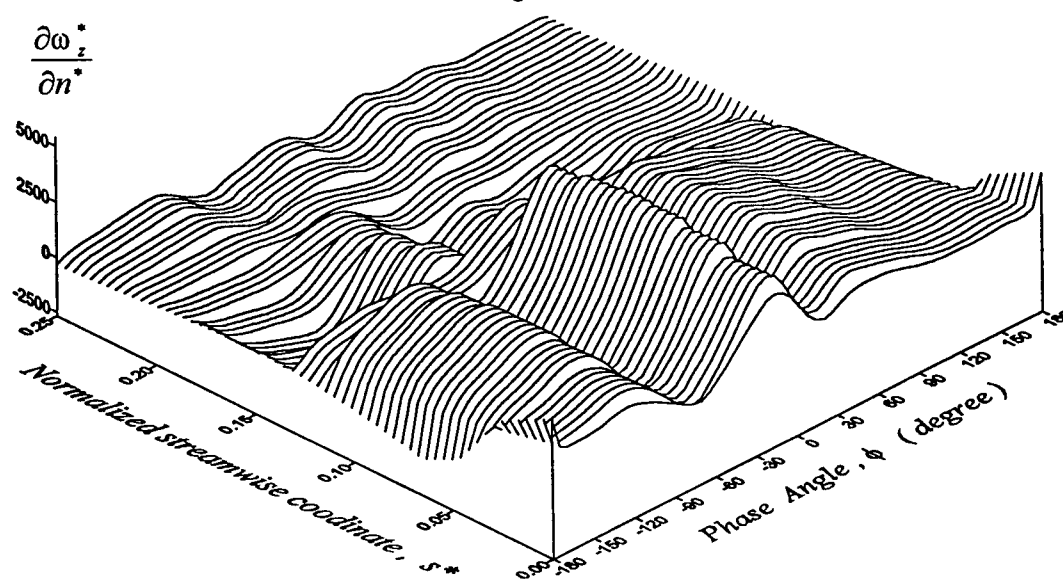
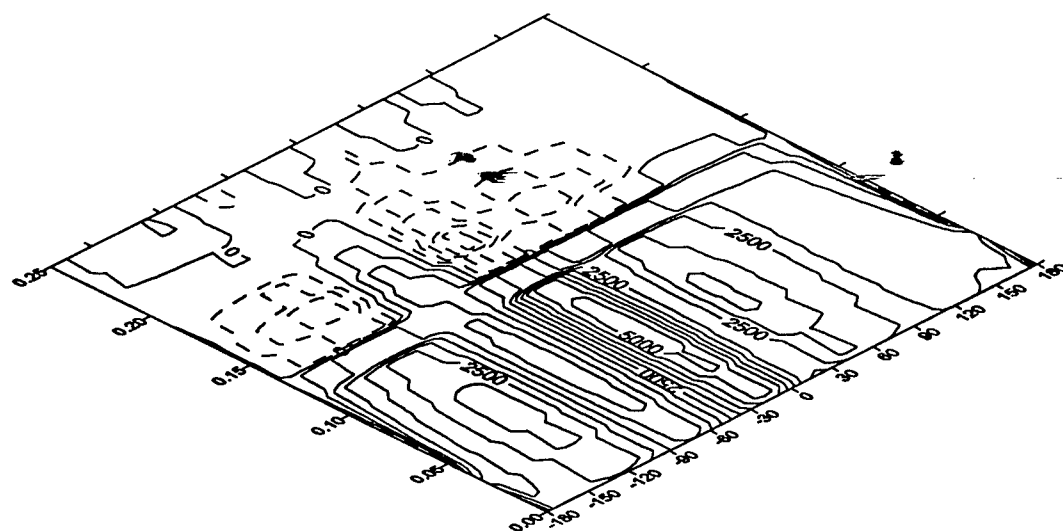


Fig. 5-11 (a)

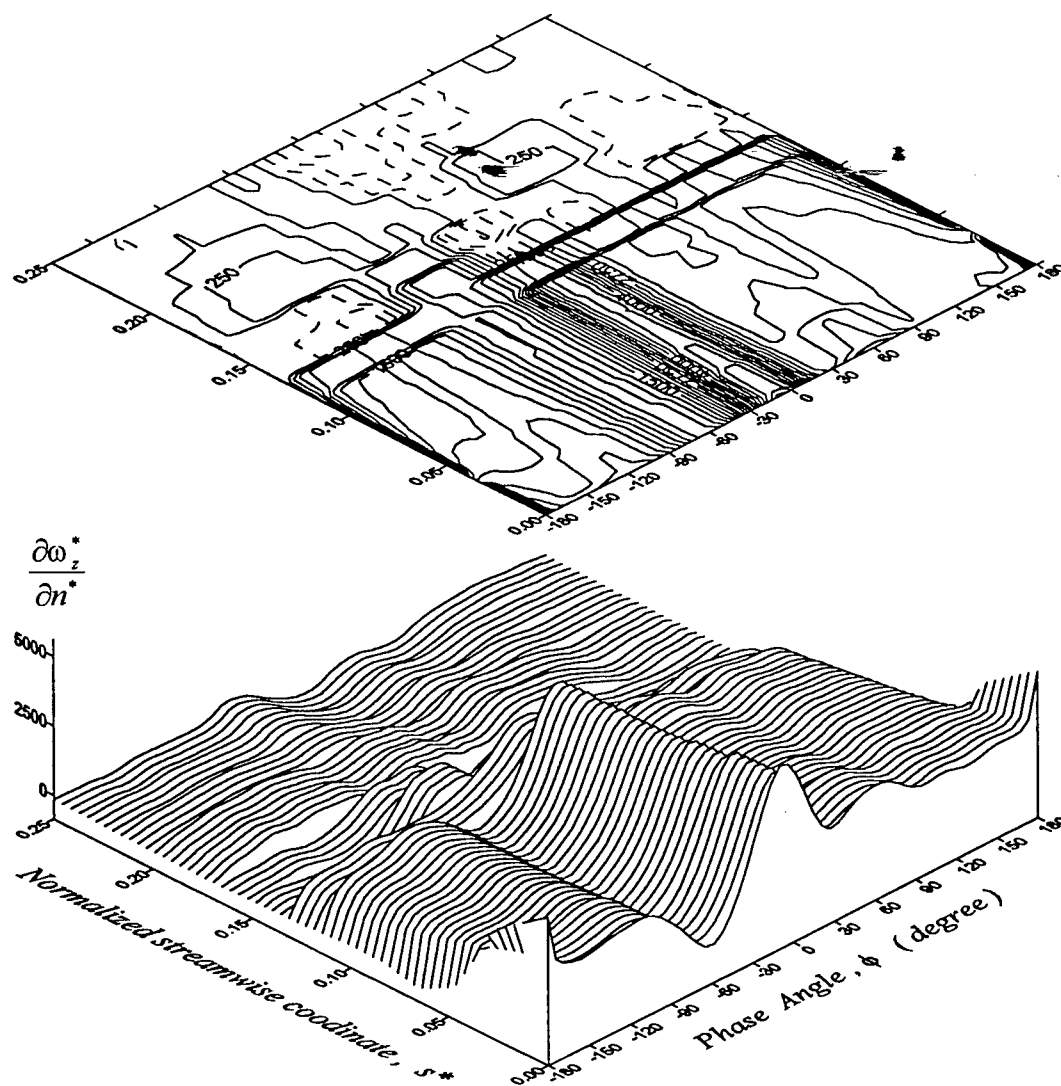


Fig. 5-11 (b)

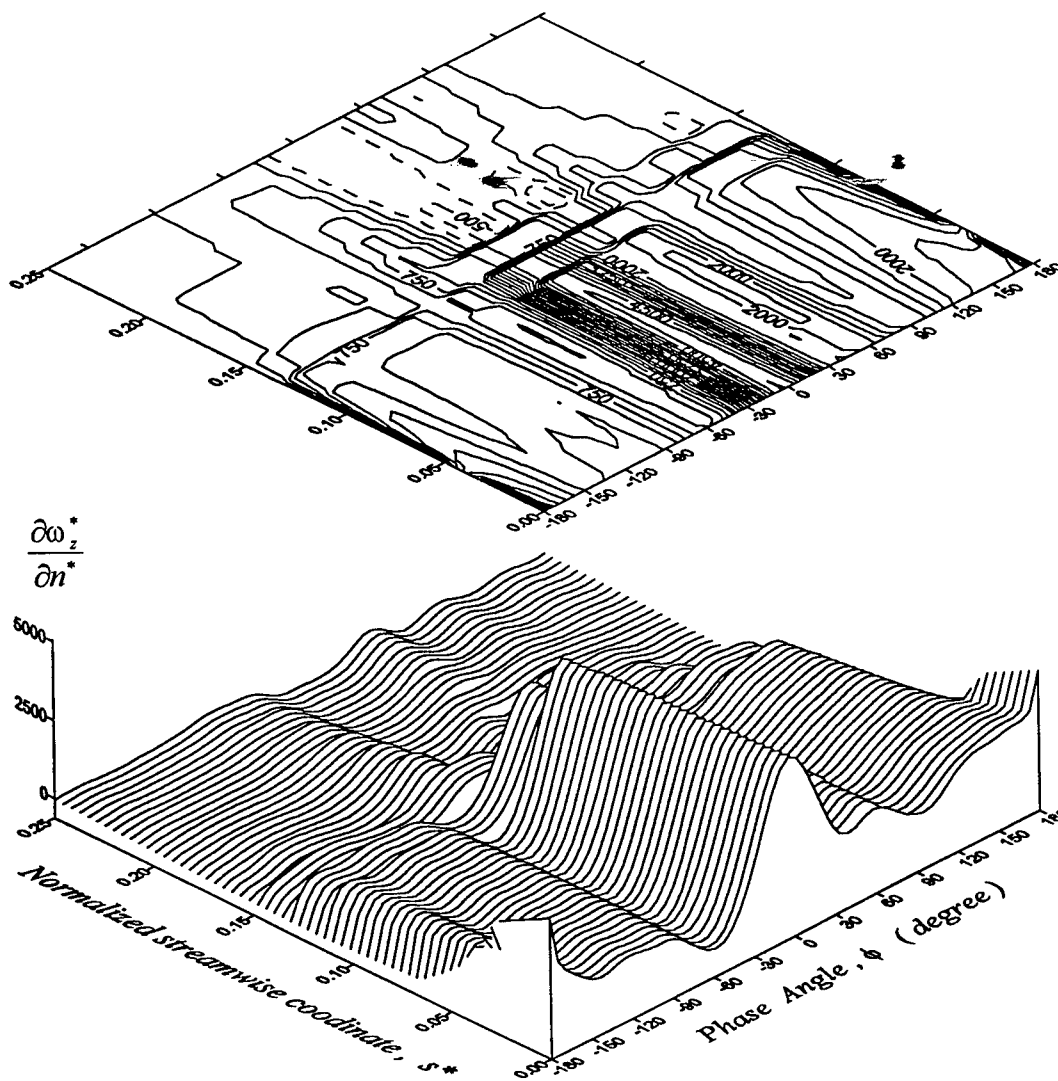


Fig. 5-11 (c)

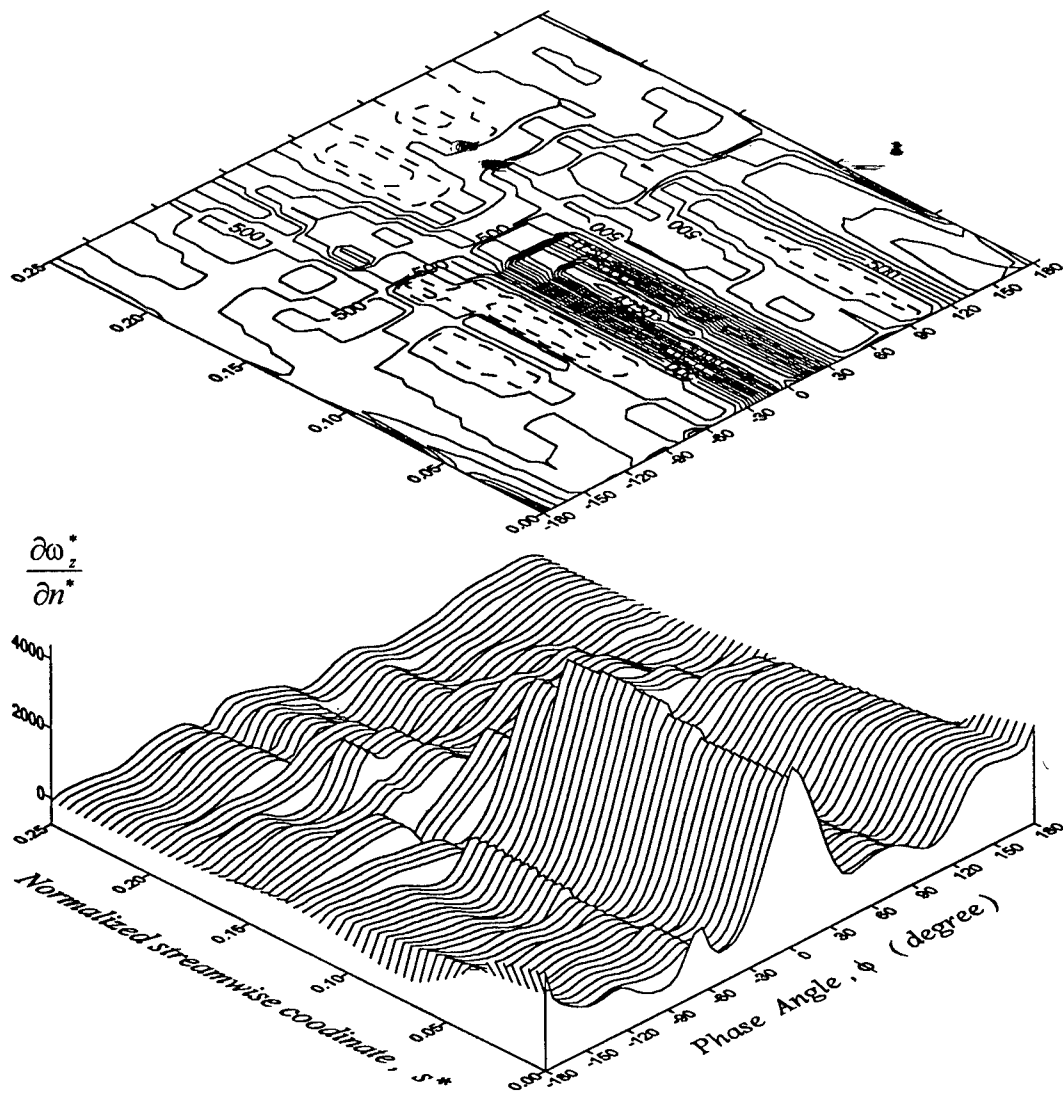


Fig. 5-11 (d)

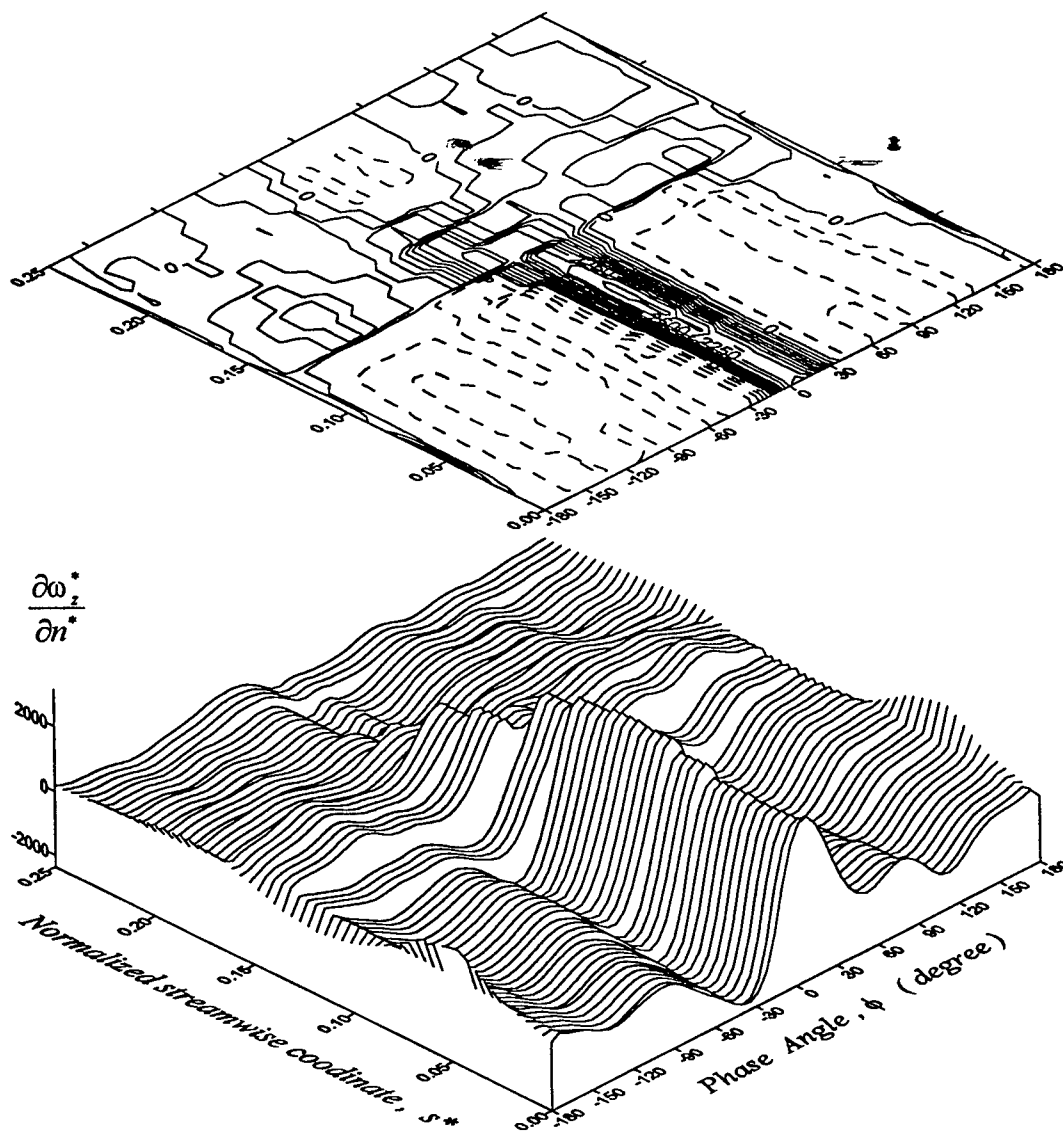


Fig. 5-11 (e)

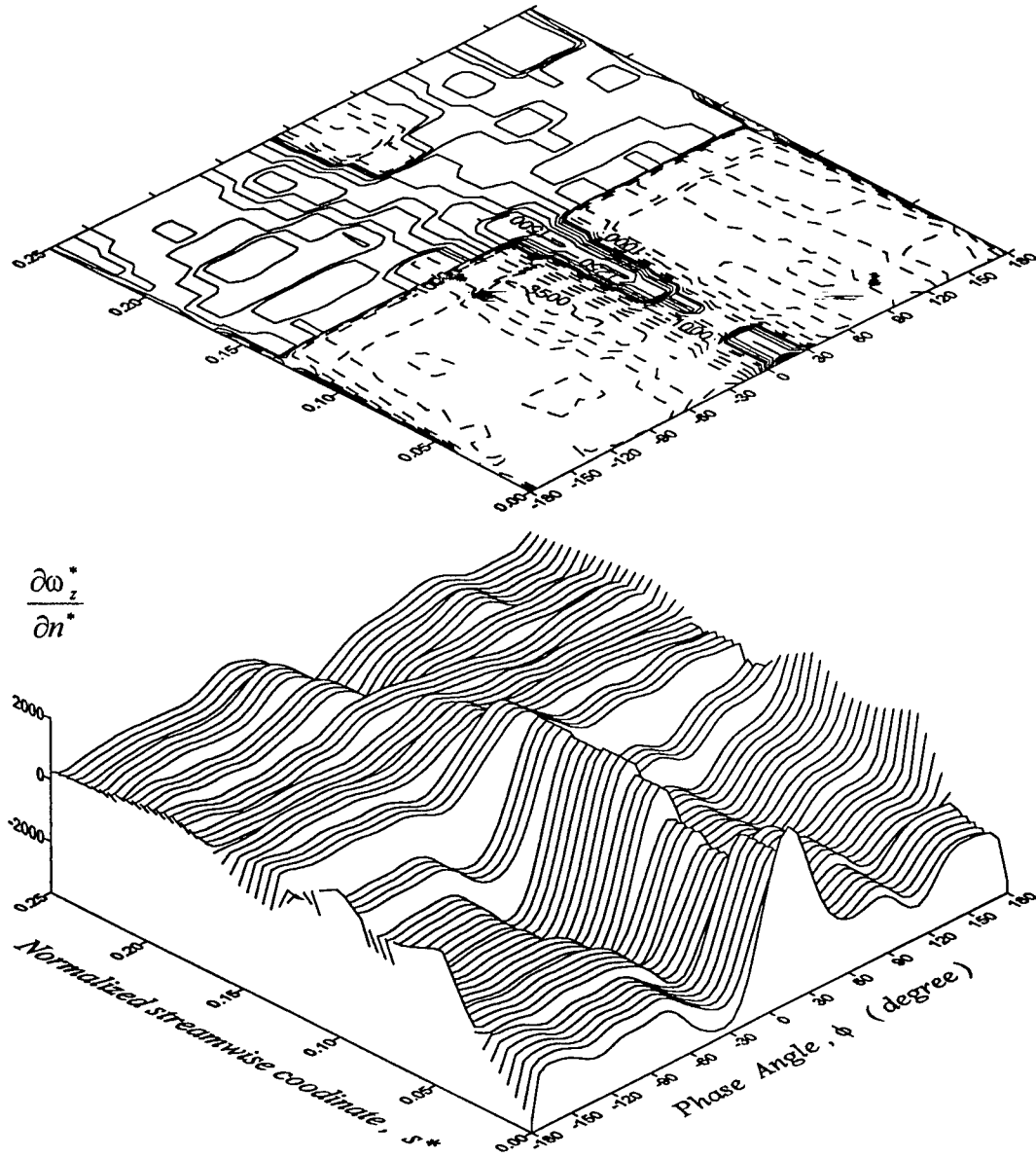


Fig. 5-11 (f)

Fig. 5-11. The contour and surface plots of the normalized vorticity gradient, $\frac{\partial \omega_z^*}{\partial n^*} (= -\frac{d_{gap}^2}{U_t} \frac{\partial p}{\partial s})$, for $\beta_t = -10.30^\circ$ and $\alpha_t =$ (a) 10° , (b) 5° , (c) 0° , (d) -5° , (e) -10° and (f) -15° , respectively. The *dashed contour lines* show the values which are *less than zero*.

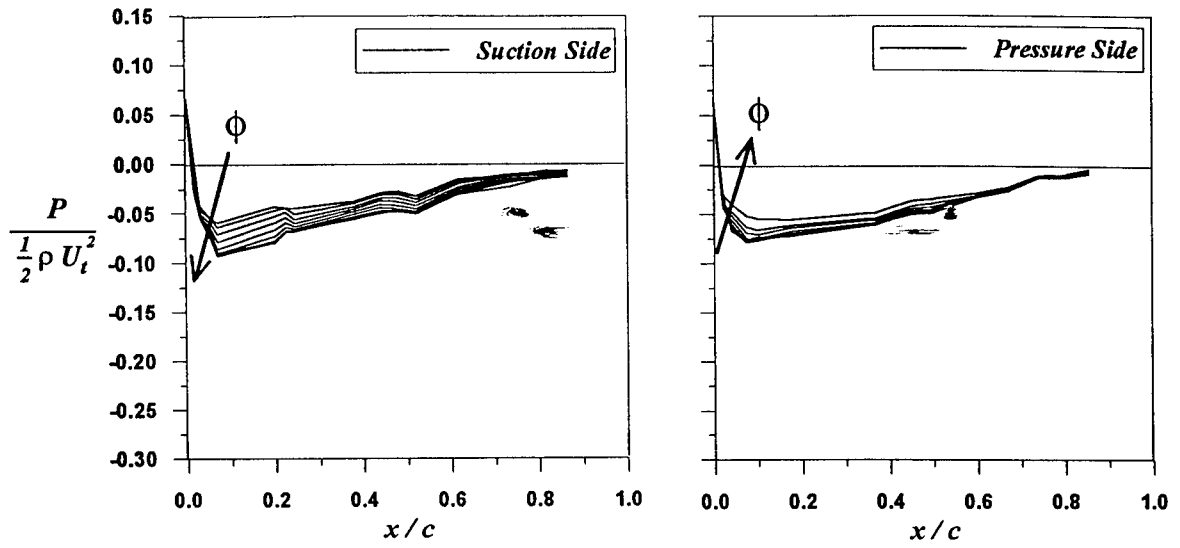


Fig. 5-13(a) $-60^\circ < \phi < -12^\circ$: $\alpha_s = 10^\circ$, $\beta_e = 9.61^\circ$, $U_t = 19.92$ m/s.

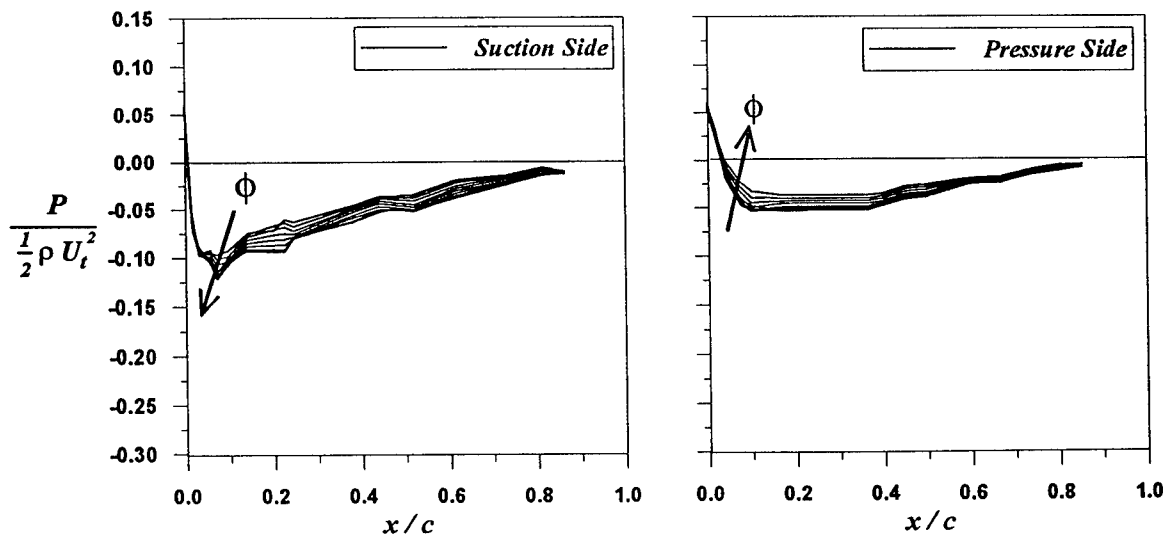


Fig. 5-13(b) $-60^\circ < \phi < -12^\circ$: $\alpha_s = 5^\circ$, $\beta_e = 9.61^\circ$, $U_t = 19.92$ m/s.

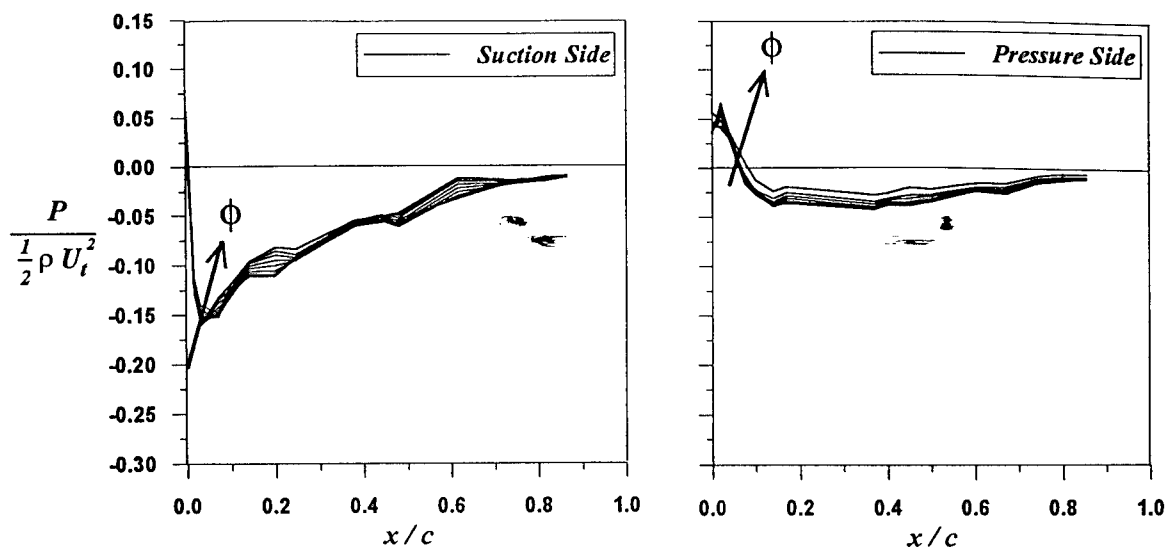


Fig. 5-13(c) $-60^\circ < \phi < -12^\circ$: $\alpha_s = 0^\circ$, $\beta_e = 9.61^\circ$, $U_t = 19.92$ m/s.

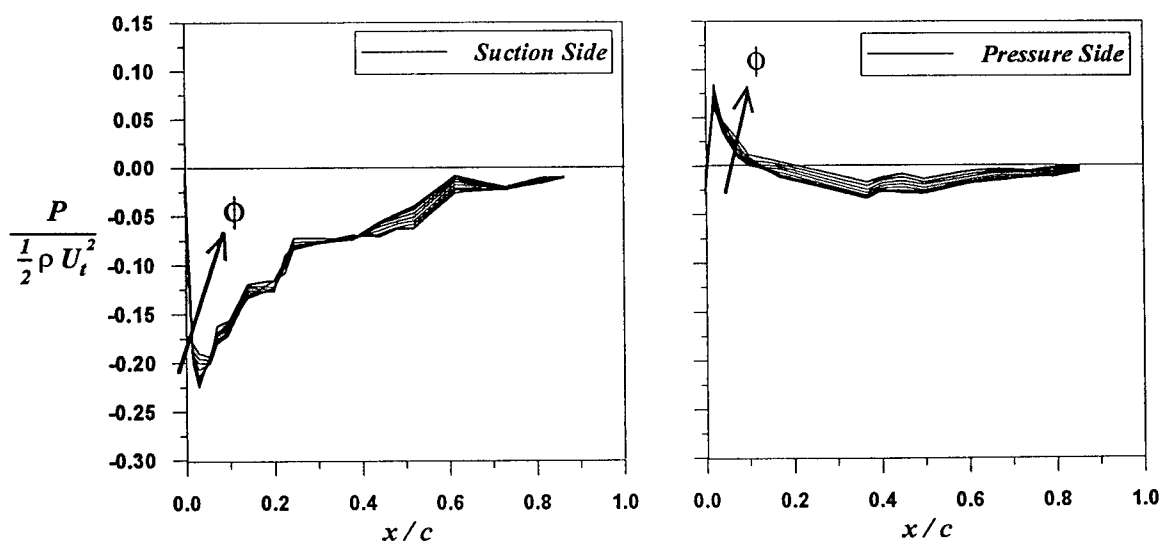


Fig. 5-13(d) $-60^\circ < \phi < -12^\circ$: $\alpha_s = -5^\circ$, $\beta_e = 9.61^\circ$, $U_t = 19.92$ m/s.

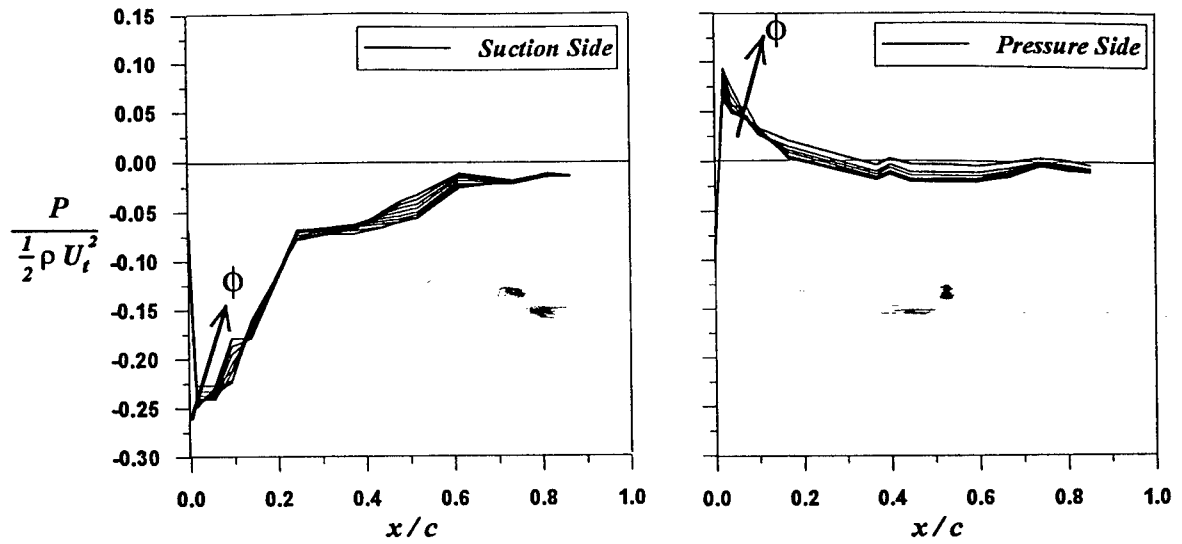


Fig. 5-13(e) $-60^\circ < \phi < -12^\circ$: $\alpha_s = -10^\circ$, $\beta_e = 9.61^\circ$, $U_t = 19.92$ m/s.

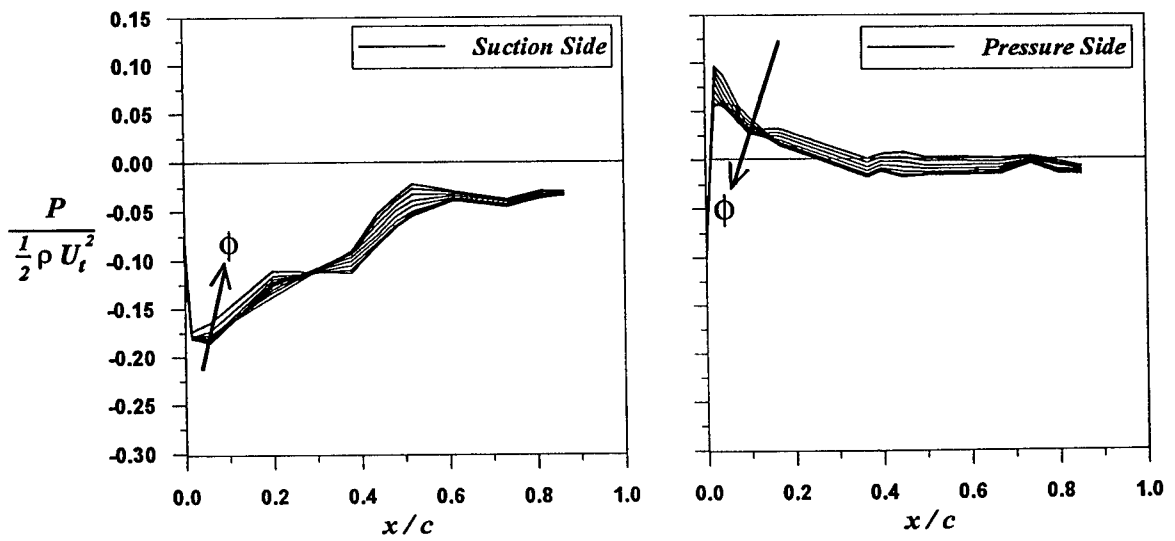


Fig. 5-13(f) $-60^\circ < \phi < -12^\circ$: $\alpha_s = -15^\circ$, $\beta_e = 9.61^\circ$, $U_t = 19.92$ m/s.

Fig. 5-13. Non-dimensionalized pressure distributions on both sides of the stator with stator's AoA, α_s : (a) 10° , (b) 5° , (c) 0° , (d) -5° , (e) -10° , and -15° , respectively, for $\beta_e = 9.61^\circ$ and during $-60^\circ \leq \phi \leq -12^\circ$. Note that $U_t = 19.92$ m/s with $U_o = 5.62$ m/s and U_t at $55\%R = 19.11$ m/s.

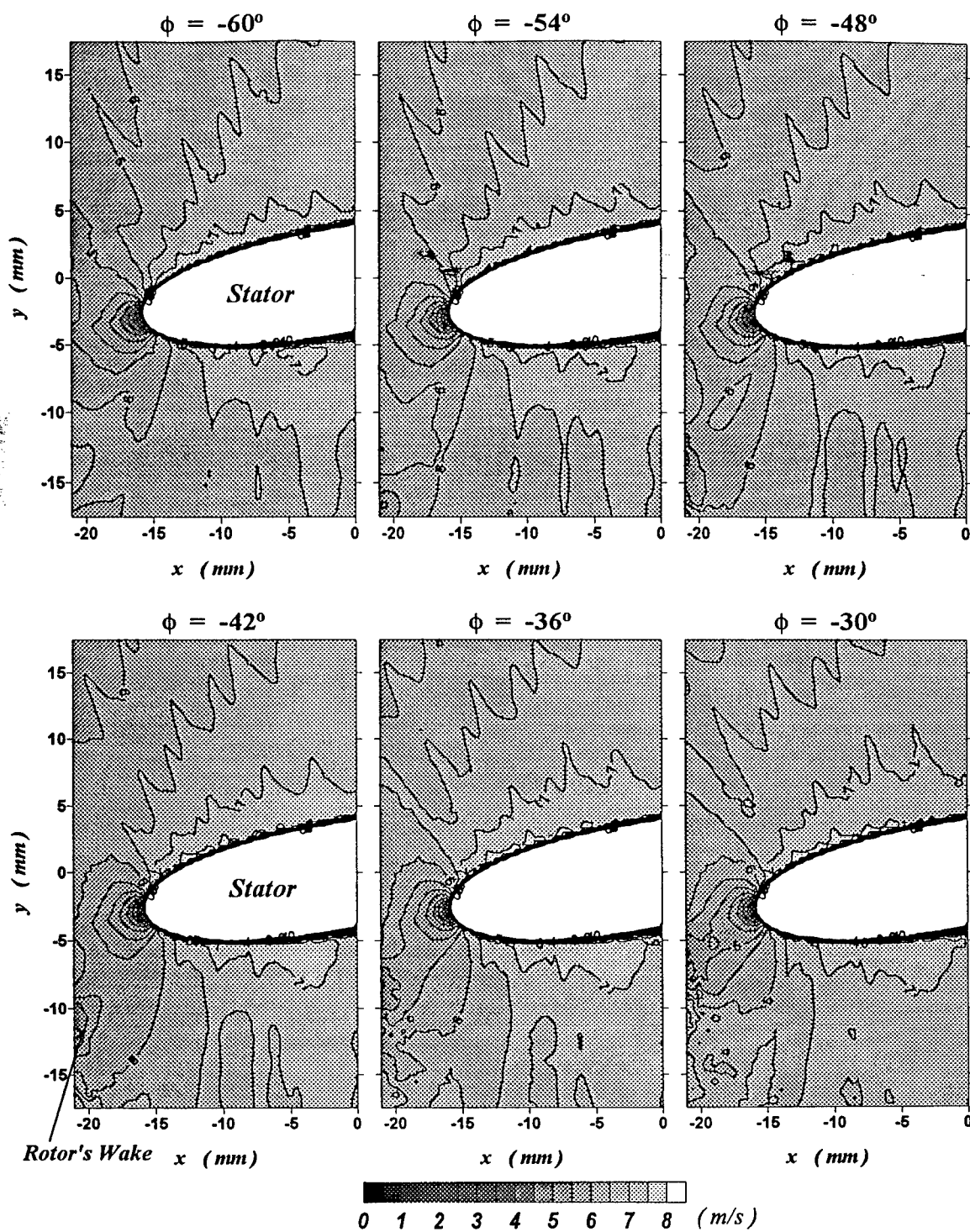


Fig. 5-14. (Caption on next page.)

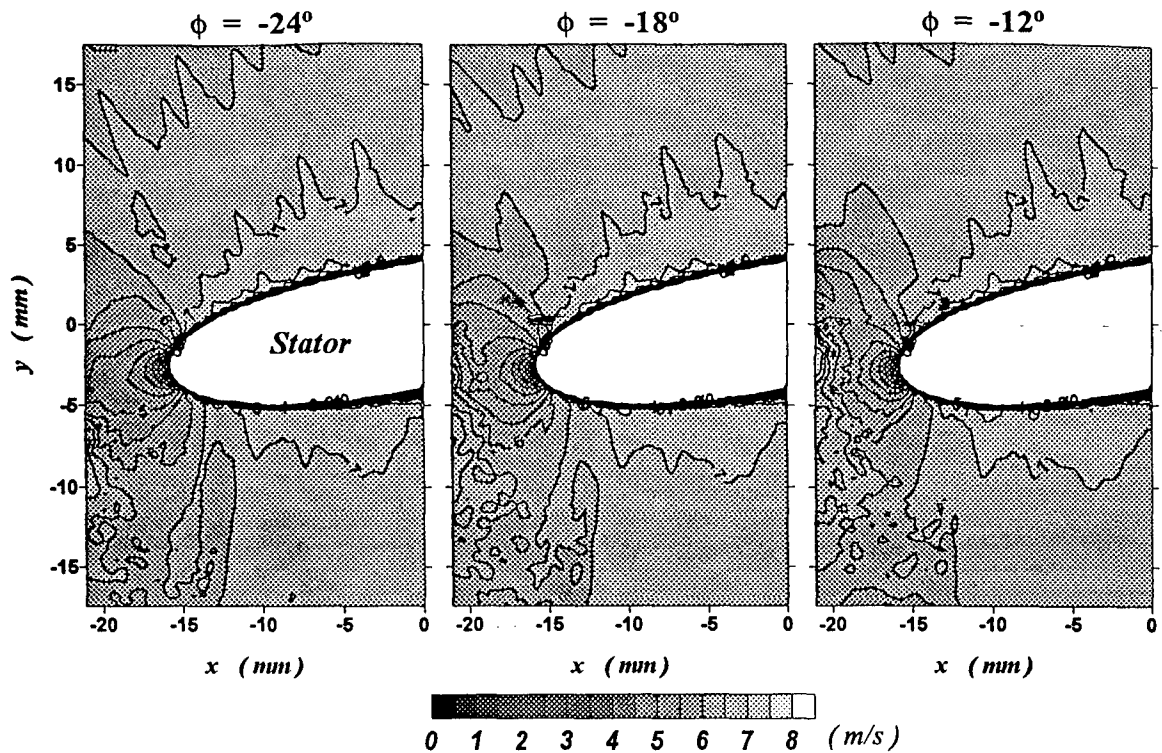


Fig. 5-14. History of velocity contours around the stator's leading edge during $-60^\circ \leq \phi \leq -12^\circ$, with stator's AoA α_i at 10° , for $\beta_i = 9.61^\circ$ and $U_i = 19.92 \text{ m/s}$ at 55%R. Note that $U_o = 5.62 \text{ m/s}$ and U_i at 55%R = 19.11 m/s .

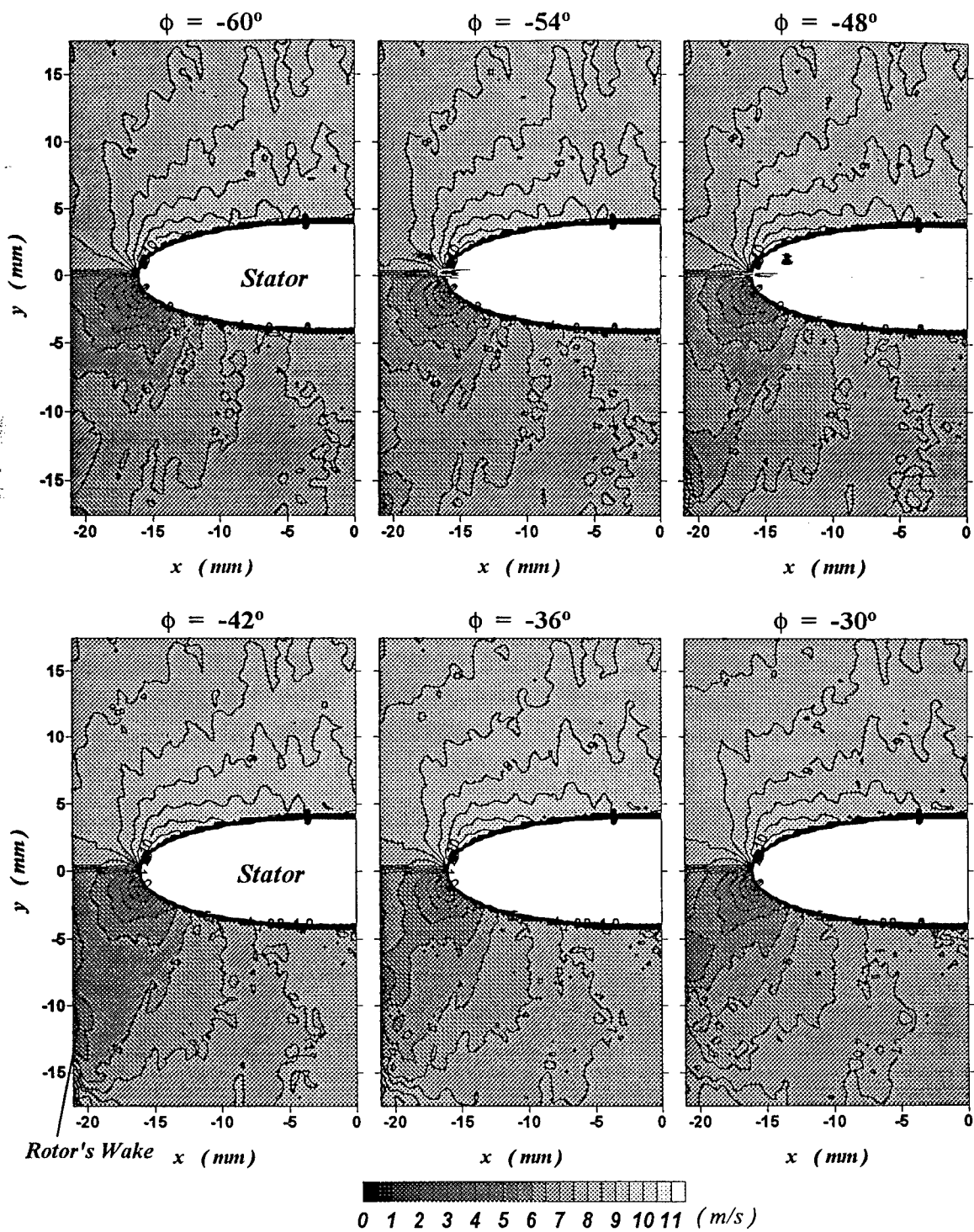


Fig. 5-15. (Caption on next page.)

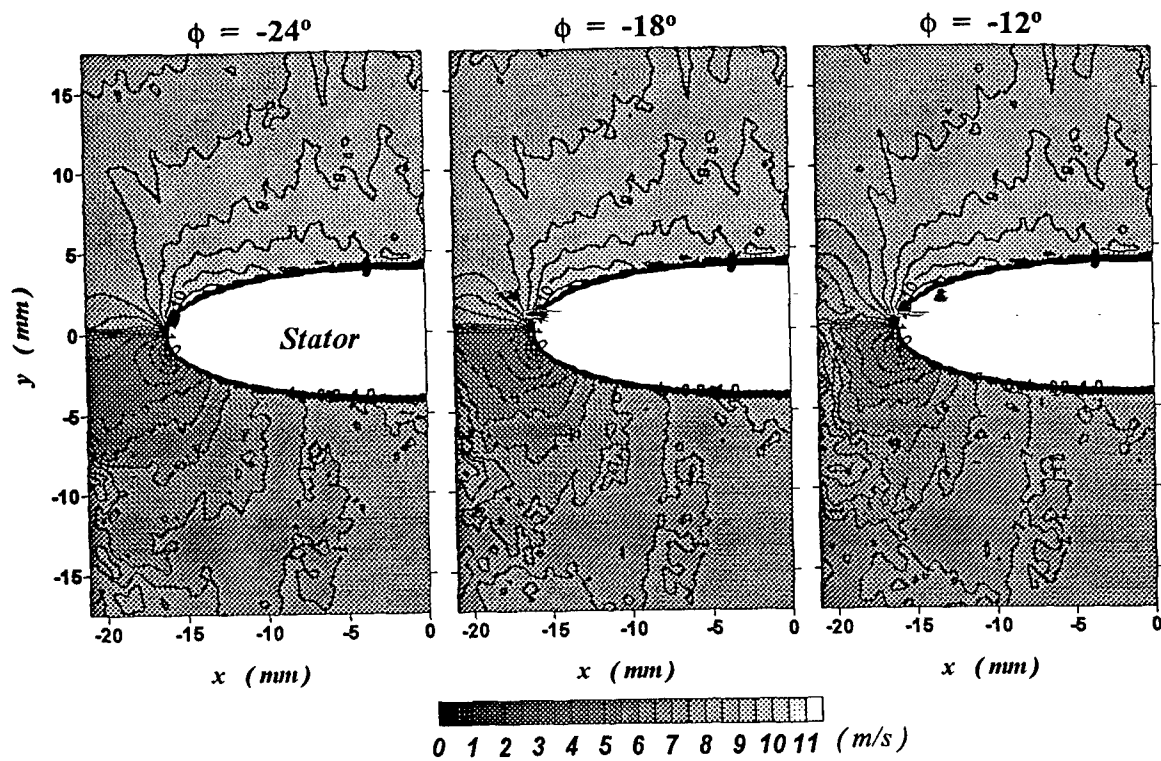


Fig. 5-15. History of velocity contours around the stator's leading edge during $-60^\circ \leq \phi \leq -12^\circ$, with stator's AoA α_s at 0° , for $\beta_s = 9.61^\circ$ and $U_i = 19.92$ m/s at 55%R. Note that $U_o = 5.62$ m/s and U_i at 55%R = 19.11 m/s.

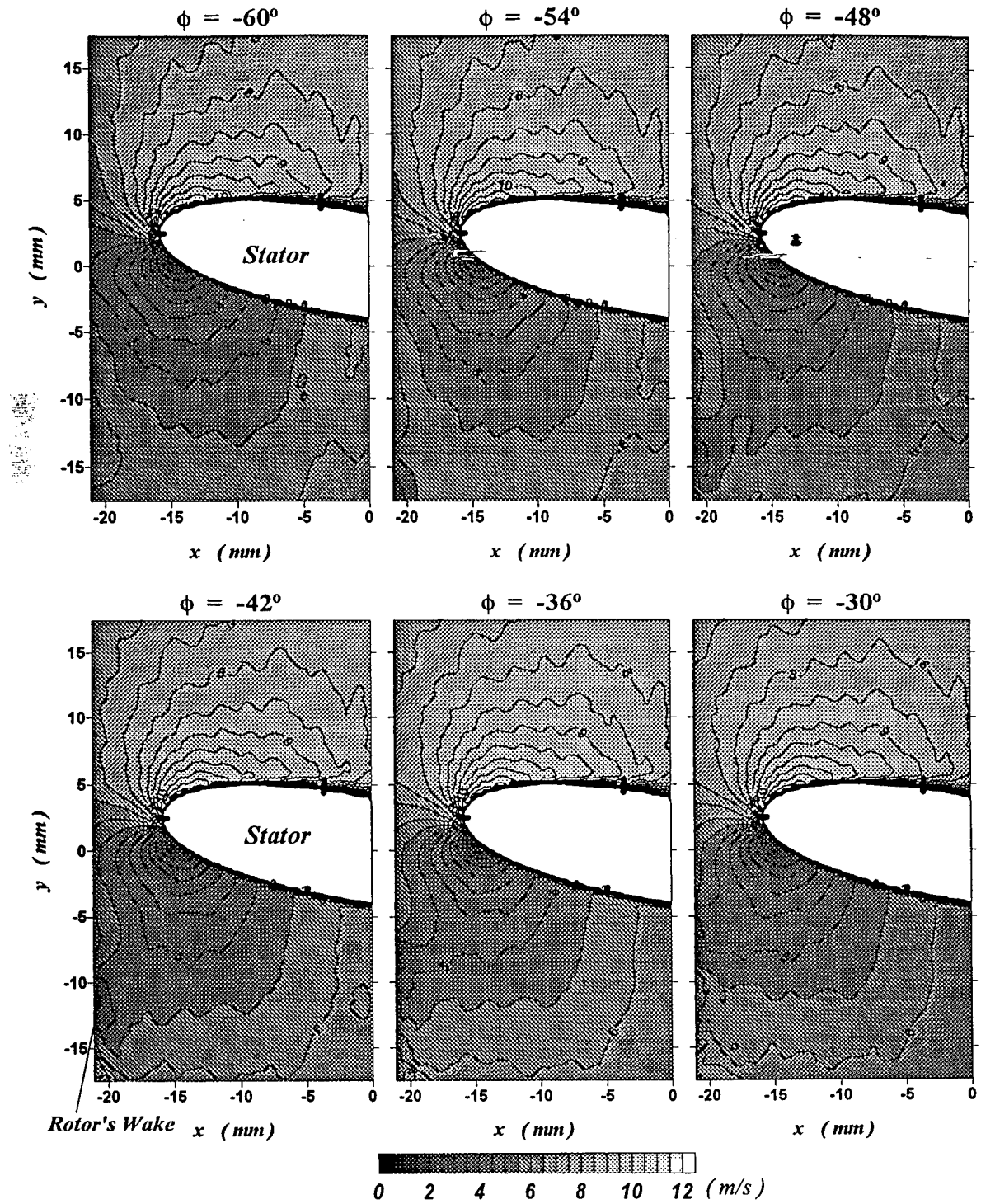


Fig. 5-16. (Caption on next page.)

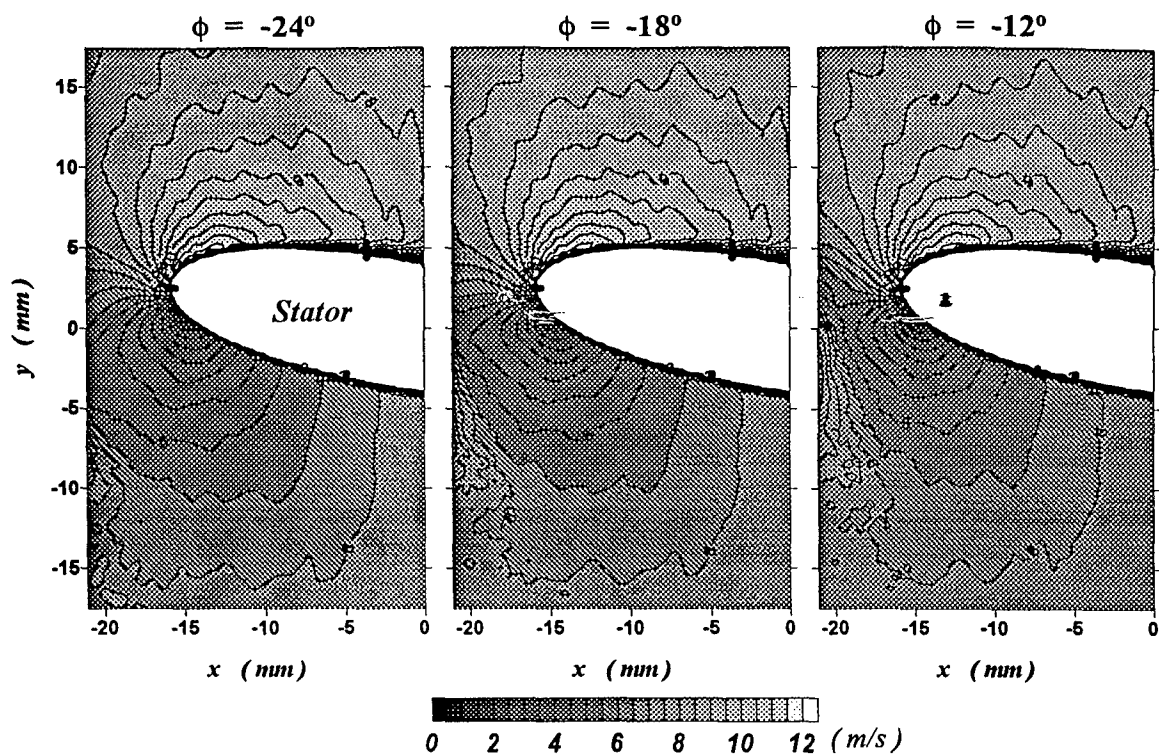


Fig. 5-16. History of velocity contours around the stator's leading edge during $-60^\circ \leq \phi \leq -12^\circ$, with stator's AoA α_i at -10° , for $\beta_i = 9.61^\circ$ and $U_i = 19.92 \text{ m/s}$ at 55%R. Note that $U_o = 5.62 \text{ m/s}$ and U_i at 55%R = 19.11 m/s.

REFERENCES

- [1] Bendat, J.S. and Piersol, A.G., "Random Data - Analysis and Measurement Procedures", 2nd ed., John Wiley & Sons Inc., 1986.
- [2] Blackwelder, R.F., "Hot-Wire and Hot-Film Anemometers", Methods of Experimental Physics: Fluid Dynamics, Vol.18, Part A, Academic Press Inc., New York, 1981.
- [3] Blake, W.K., "Mechanics of Flow-Induced Sound and Vibration." Volume II, Academic Press Inc., New York, 1986.
- [4] Brigham, E.O., "The Fast Fourier Transform and its Applications", 2nd ed., Prentice-Hall Inc., New Jersey, 1986.
- [5] Clark, P.J.F. and Ribner, H.S., "Direct Correlation of Fluctuating Lift with Radiated Sound for an Airfoil in Turbulent Flow", Journal of the Acoustical Society of America, 46, 802-805, 1969.
- [6] Curle, N., "The Influence of Solid Boundaries upon Aerodynamic Sound", Proceedings of Royal Society of London, Series A, 231, 505-514, 1955.
- [7] Didden, N. and Ho, C.-M., "Unsteady Separation in a Boundary Layer Produced by an Impinging Jet." Journal of Fluid Mechanics, 160, 235-256, 1985.
- [8] Ffowcs Williams, J.E. and Hawkings, D.L., "Theory Relating to the Noise of Rotating Machinery.", Journal of Sound and Vibration, 10, 10-21, 1969a.
- [9] Ffowcs Williams, J.E. and Hawkings, D.L., "Sound Generation by Turbulence and Surfaces in Arbitrary Motion", Philosophical Transactions of the Royal Society of London, Series A, 264, 321-342, 1969b.
- [10] Ffowcs Williams, J.E. and Hall, L.H., "Aerodynamic Sound Generation by Turbulent Flow in the Vicinity of a Scattering Half Plane", Journal of Fluid Mechanics, 40, part 4, 657-670, 1970.
- [11] Fujita, H. and Kovasznay, L. S. G., "Unsteady Lift and Radiated Sound from a Wake Cutting Airfoil", AIAA Journal, 12, 1216-1221, 1974.
- [12] Goldstein, M.E., "Aeroacoustics", McGraw-Hill Inc., New York, 1976.
- [13] Goldstein, R.J., "Fluid Mechanics Measurements", Hemisphere Pub. Corp., Washington, 1983.
- [14] Hanson, D.B., "Unified Analysis of Fan Stator Noise.", Journal of the Acoustical Society of America, 54, 1571-1591, 1973.
- [15] Ho, C.-M. and Kovasznay, L. S. G., "Sound Generated by a Single Cambered Blade in Wake Cutting", AIAA J., 14, 763-766, 1976a.
- [16] Ho, C.-M. and Kovasznay, L.S.G., "Propagation of a Coherent Acoustic Wave through a Turbulent Shear Flow", Journal of the Acoustical Society of America, 60, 40-45, 1976b.
- [17] Hu, C.-H. and Ho, C.-M., "Experimental Data and Results of Rotor-Stator Interaction Noise in an Incompressible Pipe Flow.", MAE Department, University of California, Los Angeles, California, 1997.

- [18] Kaji, S. and Okazaki, T., "Generation of Sound by Rotor-Stator interaction", Journal of Sound and Vibration, 13, 281-307, 1970.
- [19] Lighthill, M.J., "On Sound Generated Aerodynamically. I. General Theory", Proceedings of the Royal Society of London, Series A, 211, 564-687, 1952.
- [20] Lighthill, M.J., "On Sound Generated Aerodynamically. II. Turbulence as a Source of Sound", Proceedings of the Royal Society of London, Series A, 222, 1-32, 1954.
- [21] Lighthill, M.J., "The Bakerian Lecture, 1961, Sound Generated Aerodynamically", Proceedings of the Royal Society of London, Series A, 267, 147-182, 1962.
- [22] Lighthill, M.J., in "Laminar Boundary Layers." edited by L. Rosenhead, Oxford, 1963.
- [23] Lighthill, M.J., "Waves in Fluids", Cambridge University Press, 1978.
- [24] McClellan, J. H., Parks, T. W. and Rabiner, L. R., "A Computer Program for Designing Optimum FIR Linear Phase Digital Filters", Selected Papers in Digital Signal Processing II, IEEE Press, 97-117, 1975.
- [25] Meecham, W.C., "Surface and Volume Sound from Boundary Layers", Journal of the Acoustical Society of America, 37, 516-522, 1965.
- [26] Myers, M.R. and Kerschen, E.J., "Influence of Incidence Angle on Sound Generation by Airfoils Interacting with High-Frequency Gusts.", Journal of Fluid Mechanics, 292, 271-304, 1995.
- [27] Panton, R. L., "Incompressible Flow", John Wiley & Sons Inc., New York, 334-341, 1984.
- [28] Pierce, A.D., "Acoustics - an Introduction to Its Physical Principles and Applications", Acoustical Society of America, 1989.
- [29] Powell, A., "Aerodynamic Noise and the Plane Boundary", Journal of the Acoustical Society of America, 32, 982-990, 1960.
- [30] Pridmore-Brown, D.C., "Sound Propagation in a Temperature- and Wind-Stratified Medium." Journal of the Acoustical Society of America, 34, 438-443, 1962.
- [31] Proakis, J.G. and Manolakis, D.G., "Digital Signal Processing - Principles, Algorithms, and Applications.", 2nd ed., Macmillan Co., New York, 1992.
- [32] Rabiner, L.R., McClellan, J.H. and Parks, T.W., "FIR Digital Filter Design Techniques Using Weighted Chebyshev Approximation", Selected Papers in Digital Signal Processing II, IEEE Press, 81-96, 1975.
- [33] Rabiner, L.R. and Gold, B., "Theory and Application of Digital Signal Processing", Prentice-Hall, Inc., New Jersey, 1975.
- [34] Reynolds, W.C. and Carr, L.W., "Review of Unsteady, Driven, Separated Flows", AIAA paper No. 85-0527, 1985.
- [35] Shih, C. and Ho, C.-M., "Vorticity Balance and Time Scales of a Two-Dimensional Airfoil in an Unsteady Free Stream", Physics of Fluids, 6, 710-723, 1994.
- [36] Siddon, T.E., "Surface Dipole Strength by Cross-Correlation Method", Journal of the Acoustical Society of America, 53, 619-633, 1973.
- [37] Simonich, J., Lavrich, P., Sofrin, T. and Topol, D., "Active Aerodynamic Control of Wake-Airfoil Interaction Noise - Experiment", AIAA Journal, 31, 1761-1768, 1993.

- [38] Sugeng, F. and Fiedler, K., "An Experimental Investigation into Unsteady Blade Forces and Blade Losses in Axial Compressor Blade Cascade.", Transactions of the ASME, Journal of Engineering for Gas Turbines and Power, 108, 47-52, 1986.
- [39] Thompson, R.J., "Ray Theory for an Inhomogeneous Moving Medium.", Journal of the Acoustical Society of America, 51, 1675-1682, 1971.
- [40] Turton, R.K., "Principles of Turbomachinery", E.& F.N. Spon Ltd., New York, 1984.
- [41] Zandbergen, T., "Stator Vane Response due to the Impingement of the Wake of an Unloaded Rotor", AIAA Paper no.88-2814, 1988.